



Carl von Ossietzky Universität Oldenburg  
Fakultät II Informatik, Wirtschafts- und Rechtswissenschaften  
Department für Informatik

# **The InflateSAR Campaign**

## **Detecting Refugee Rubber Boats with SAR**

Von der Fakultät für Informatik, Wirtschafts- und Rechtswissenschaften der Carl von  
Ossietzky Universität Oldenburg  
zur Erlangung des Grades und Titels  
Doktors der Naturwissenschaften (Dr.rer.nat.)

angenommene Dissertation von  
**Peter Lanz**

---

Gutachter

Prof. Dr. Thomas Brinkhoff, Jade University of Applied Sciences Oldenburg

Prof. Dr. Frank Köster, Carl v. Ossietzky University of Oldenburg

Prof. apl. Dr. Matthias Möller, Otto-Friedrich-University of Bamberg

Tag der Disputation: 19.12.2023

## Zusammenfassung

Jüngste Forschungen im Bereich der Erkennung von maritimen Objekten mittels Radar mit synthetischer Apertur (Synthetic Aperture Radar; SAR) konzentrierten sich zumeist auf große, hauptsächlich aus metallischen Komponenten bestehende Schiffe. Der Fokus dieser Arbeit liegt auf wesentlich herausfordernderen Zielen, nämlich der Detektion von kleinen, aus Holz und Kunststoff bestehenden Schlauchbooten. Für die maritime Seenotrettung an den südlichen maritimen Grenzregionen Europas sind sie von großer Bedeutung, da sie in den letzten Jahren von Migranten und Geflüchteten genutzt wurden, um Europa zu erreichen. Diese Boote, mit bis zu 200 Personen belegt, sind in keiner Weise dazu geeignet das Mittelmeer oder andere große Gewässer zu überqueren und sind bereits bei der Abfahrt in Seenot. Der Aufbau einer satellitengestützten Infrastruktur für den maritimen Katastrophenschutz könnte Such- und Rettungsmissionen im Mittelmeer erheblich dabei helfen, Fluchtboote in Seenot schneller zu finden und die Anzahl an Todesfällen an Europas südlicher maritimer Grenze zu reduzieren. Die Motivation hinter dieser Arbeit ist es damit, die anhaltende humanitäre Krise im Mittelmeer und in anderen europäischen Grenzgewässern zu lindern.

Zu Beginn werden SAR Daten aus der ersten InflateSAR Kampagne, in der in 2017 mit Hilfe verschiedener Satellitenmissionen SAR-Daten in Einfach- und Dual-Polarisation eines originalen Fluchtboots gesammelt wurden, beschrieben und analysiert. Das Testgebiet für diese erste Kampagne war ein See in der Nähe von Berlin mit wenig Wellengang und gut einzuschätzenden, niedrigen Radar Rückstreuintensitäten. Die Aufnahmen umfassten eine Reihe von Experimenten, die Untersuchungen eines breiten Spektrums von Szenenparametern ermöglichen, wie etwa die Ausrichtung, die Besatzung und die Geschwindigkeit des Bootes. Ihr Einfluss hinsichtlich der Detektierbarkeit des Schlauchbootes unter verschiedenen Sensorparametern wie Polarimetrie, räumliche Auflösung und Einfallswinkel wird bewertet und untersucht. Die Ergebnisse zeigen, dass die TerraSAR-X Spotlight- und Stripmap Modi unter bestimmten Umständen geeignet sind, diese Art von Booten in Notfällen potenziell zu erkennen. Ein niedriger Einfallswinkel und die Cross-Polarisation verringern die Chance einer erfolgreichen Identifizierung, während ein mit Menschen besetztes Schlauchboot, das orthogonal zur Sichtlinie des Radarsensors ausgerichtet ist, am besten sichtbar zu sein scheint. Erste polarimetrische Analysen zeigen Unterschiede im polarimetrischen Verhalten des Bootes im Vergleich zur Wasseroberfläche des Sees. Schließlich werden verschiedene Metriken verwendet um zu diskutieren, ob und inwieweit die Ergebnisse auf Daten der realen Situation auf dem offenen Meer bei verschiedenen Wellengängen übertragbar sind.

In einem zweiten Schritt dient die Datensammlung dazu, die Leistungsfähigkeit mehrerer etablierter automatischer Schiffsdetektoren zu vergleichen. Alle Detektoren werden mit einem beweglichen Suchfenster implementiert und verwenden lokale Statistiken der Rückstreuung der angrenzenden Wasseroberfläche. Unter den getesteten Detektoren befinden sich der intensitätsbasierte cell-averaging constant false alarm rate (CA-CFAR) Detektor, ein Sublook Detektor (Sublook-Korrelation) sowie sechs polarimetrische Detektoren (der Polarimetric

---

Whitening Filter, der Polarimetric Match Filter, der Polarimetric Notch Filter, ein Entropie-Detektor, ein Symmetrie-Detektor und der Intensity Dual-Polarization Ratio Anomaly Detector (iDPolRAD). Weiters wird eine neue Version des Volumenstreuung detektierenden iDPolRAD vorgestellt, die darauf abzielt Oberflächenstreuung zu erkennen wobei zwei Ansätze zur Kombination dieser beiden Algorithmen verglichen werden. Dadurch entstehen zwei neue hochleistungsfähige Detektoren. Die Ergebnisse werden mit Grenzwertoptimierungskurven (Receiver Operating Characteristic; ROC)-Kurven visualisiert, die es ermöglichen Detektoren unabhängig von der Schwellenwertauswahl zu vergleichen.

Für den letzten Teil der Forschung werden Multi-Plattform SAR-Daten in Dual- und Quad-Polarisation aus der zweiten Datenerfassungskampagne, die 2022 organisiert wurde, verwendet. Wie in der ersten Kampagne kommt ein 12 m langes Schlauchboot zum Einsatz das in einen See in der Nähe von Berlin platziert wird. Um ein realistischeres Szenario zu berücksichtigen, wird das Boot dieses Mal mit Material, das das Mikrowellen Rückstreuungsmuster von 80 Menschen simulieren soll, befüllt. Darüber hinaus wurde eine Sammlung von SAR-Archivbildern des offenen Meeres bei unterschiedlichen Seegangsbedingungen, kategorisiert nach Windrichtung (relativ zum Radar Blickrichtung), Einfallswinkel und Polarisation, zusammengestellt. Die Kombination dieser beiden Datensätze ermöglichte es uns die Bedingungen für ein mit Passagieren voll besetztes Schlauchboot auf dem offenen Meer bei verschiedenen Wellengangszenarien zu simulieren. Hiermit wurde eine Auswahl verschiedener Schiffsdetektoren getestet, für das Testobjekt adaptiert, neue Detektionsalgorithmen entwickelt und verschiedene Kombinationen von Detektoren (Detektorfusion) unter verschiedenen Sensor- und Szeneparametern (Polarisation, Windgeschwindigkeit, Windrichtung und Bootsausrichtung) verglichen. Diese Analyse führte zur Identifikation der jeweils besten Detektoren, speziell zugeschnitten auf verschiedene Situationen und Seegangsbedingungen.



## Abstract

Most of the recent research in the field of marine target detection with Synthetic Aperture Radar (SAR) has concentrated on large metal-made ships. The focus of this work is on the much more challenging targets represented by small rubber inflatables. They are of importance since, in recent years, they have largely been used by migrants to cross the Mediterranean Sea between Libya and Europe. These boats, packed with up to 200 people, are in no way suitable to cross the Mediterranean Sea or any other big water body and are in distress from the moment of departure. The establishment of a satellite-based surveillance infrastructure could considerably support search and rescue missions in the Mediterranean Sea, reduce the number of such boats which go missing and reduce the ever-increasing death toll. The motivation of this application-focused research is to develop detection algorithms with spaceborne SAR to mitigate the ongoing humanitarian crisis in Europe's maritime border regions.

At the beginning of the research stands the description and analysis of the data from the first acquisition campaign, in which multiple-platform SAR imagery from an original refugee inflatable was gathered. The test site for this campaign was a lake which provided low radar background clutter that is more predictable. The analysis considered a number of experiments, allowing for the investigation of a broad range of scene settings, such as the vessel's orientation, superstructure and movement. Their impact on the detectability of the inflatable under different sensor parameters, such as polarimetry, spatial resolution and incidence angle, is assessed. Results show that TerraSAR-X Spotlight and Stripmap modes offer good capabilities to potentially detect this type of rubber inflatable. Low incidence angles and cross-polarisation decrease the chance of successful identification, whereas a fully occupied inflatable, orthogonally oriented to the line of sight, seems to be more visible than an empty one oriented at  $45^\circ$ . The polarimetric analyses test the vessel's different polarimetric behaviour in comparison with that of the water surface, especially with respect to entropy. Finally, different metrics are used to discuss whether and to which extent the results are applicable to other open ocean datasets.

In a second step, the collected data is used to compare the performance of several automatic vessel detectors. The detectors trialled include the well-known intensity-based CA-CFAR, one sublook-based (sublook correlation) approach and six polarimetric-based (the Polarimetric Whitening Filter, the Polarimetric Match Filter, the Polarimetric Notch Filter, an entropy detector, a symmetry detector and the Intensity Dual-Polarisation Ratio Anomaly Detector (iDPolRAD)) approaches. Additionally, a new version of the volume detecting iDPolRAD, aimed at detecting surface anomalies, is introduced and the two approaches are compared to combine them in one algorithm, producing two new high-performance detectors. The results are visualised with receiver operating characteristic (ROC) curves, enabling a comparison of detectors independently of threshold selection.

---

For the last part of the research, multi-platform dual-pol and quad-pol data was collected in a second data acquisition campaign over a 12 m rubber inflatable in a test-bed lake in 2022. To simulate a real scenario, the vessel was prepared so that its backscattering emulated that of a vessel fully occupied with passengers. Further, a collection of SAR archive imagery from the open sea with different sea states, categorised by incidence angle and by polarisation was put together. These are used to emulate realistic conditions of a vessel, sitting in ocean waters and occupied with 80 passengers. This setup enables the testing of eight well-known vessel detection algorithms, to explore the capabilities of new detection algorithms and to benchmark different combinations of detectors (detector fusion) with respect to different sensor and scene parameters (e.g., the polarisation, wind speed, wind direction and boat orientation). The analysis culminated in the design of a detection system that is specifically tailored to accommodate different situations and sea states.

# Erklärung

Hiermit versichere ich, Peter Lanz, dass ich diese Arbeit selbstständig verfasst und keine anderen als die angegebenen Quellen und Hilfsmittel verwendet habe. Außerdem versichere ich, dass ich die allgemeinen Prinzipien wissenschaftlicher Arbeit und Veröffentlichung, wie sie in den Leitlinien guter wissenschaftlicher Praxis an der Carl von Ossietzky Universität Oldenburg und den DFG-Richtlinien festgelegt sind, befolgt habe. Des Weiteren habe ich im Zusammenhang mit dem Promotionsvorhaben keine kommerziellen Vermittlungs- oder Beratungsdienste in Anspruch genommen.

Date: 04/07/2023





Dedicated to everyone who won't look away.

It is an indictment of the state of our world.  
— Filippo Grandi, United Nations High Commissioner for Refugees, June 2023



## Acknowledgements

This research was enabled by the PhD program Safe Automation of Maritime Systems - SAMS, which was a joint PhD program of the University of Oldenburg, the Jade University of Applied Science and the research institute OFFIS. It was funded by the federal state of Lower Saxony, the DLR and the Jade University's research funding. It was facilitated by the radar satellite operators DLR, ESA, ASI and ICEYE for providing radar satellite imagery free of charge and by various providers (the Deutsche Wetterdienst, the Bundesamt für Seeschifffahrt und Hydrographie, the Leibniz-Institut für Gewässerökologie und Binnenfischerei and the Copernicus Marine Service) of weather and wave data free of charge.

I would like to thank my supervisors, friends, colleagues and all the helping hands and volunteers who made this journey very enjoyable.

Matthias, thank you for believing that I could deliver this PhD thesis when I had no prior training in radar remote sensing. Thomas, thank you for being a steadfast supporter over this long time and for always being positive and always contributing to make things possible. I also want to thank Thomas for inviting me into the Jade University and for providing space to discuss and work. Frank, thank you for your honest, believing and enriching attitude and for giving the right impulses in the right moments. I would also like to thank Frank for his positive impact to find co-financing in the later project stage. Armando, thank you for your kind guidance, the great thoughts and impulses and all the work you put into this project. I would like to thank Armando for inviting me to Scotland two times and for granting me access to his research group. And I want to thank Gerard who established the connection to Armando in the first place. Morgan, thank you very much for contributing to our last paper by organising a testing campaign and collecting the data to find out about how human do look like in radar imagery. I want to thank the contributors and organisers of the ESA trainings and the SAR summer school in Jena which are all free and highly recommendable and which gave me the chance to dive deeper into this field of research.

To friends and colleagues that in one way or another, in one place or another, stayed with me along the way. Paul, Timo, Paul, Fabian, Duncan and Frank for creating a welcoming and fun environment in Oldenburg. Duncan, thank you for working through the English proofreading process with great effort, curiosity and positiveness. Andre, Armando, Cristian, Victor, Vale, Nick, Alastair, Morgan and Erika for spending your time with me and giving me the chance to make new friends and experience Scotland during my two lab visits. I want to thank Martin, Vali and Jens, Holger, Andre, Alex, Lisa and Johann and all volunteers and helping hands who contributed to the first data collection campaign in 2017. Special thanks goes to Max, Timo and Anne who put much work into reparation and transport of the vessel, Sea-Watch e.V. who contributed the rubber inflatable, the people from the Zentrum für Politische Schönheit e.V. which helped gathering volunteers, Ortwin and Micha for the outboard engine, Schorschi who took care of the website, Lydia for graphics design and the SC Wiking who kindly provided an ideal mooring point. Many thank to Elisa, Holger, Indra,

---

Janek and the Wokule community who made the second data campaign a very pleasurable time for me, together with Judith, Julian and Alex, Holger, Bangi, Schorschi, Vali and Jonas, Kevin and Lilli, Jens, Christian, Felix, Martin and Sven, Martin and Saskia, Martin and Andreas.

Finally I want to thank my parents who were there all the time, my sister who was there in the most difficult moments and Judith, about whom I am grateful, glad and happy.



# Table of Contents

<b>Zusammenfassung</b>	<b>iii</b>
<b>Abstract</b>	<b>v</b>
<b>List of Figures</b>	<b>xvii</b>
<b>List of Tables</b>	<b>xxi</b>
<b>Symbols and Abbreviations</b>	<b>xxiii</b>
<b>1 Introduction</b>	<b>1</b>
1.1 Civil Search and Rescue at the Southern Maritime Borders . . . . .	3
1.2 Repoliticization of Migration . . . . .	4
1.3 'Peripheralisation' of Human Rights . . . . .	5
1.4 Motivation . . . . .	6
1.5 Objectives . . . . .	7
1.6 Structure . . . . .	8
<b>2 SAR and PolSAR</b>	<b>9</b>
2.1 SAR Missions and Capabilities . . . . .	10
2.2 SAR Principles . . . . .	10
2.2.1 SAR Resolution and Data Preprocessing . . . . .	14
2.2.2 SAR Image Focussing . . . . .	17
2.2.3 The Radar Equation . . . . .	19
2.2.4 The Speckle Phenomenon . . . . .	22
2.2.5 Radar Image Artefacts . . . . .	25
2.3 SAR Polarimetry . . . . .	26
2.3.1 Wave Polarimetry . . . . .	26
2.3.2 Scattering Polarimetry . . . . .	32
2.3.3 Scattering Mechanisms . . . . .	37
2.3.4 Polarimetric Response: Canonical Scattering Mechanisms . . . . .	38
2.3.5 Polarimetric Correlation Coefficients . . . . .	42
2.3.6 Polarimetric Decomposition . . . . .	43
2.3.6.1 Coherent Decompositions . . . . .	44
2.3.6.2 Eigenanalysis-based Decomposition . . . . .	46
2.3.6.3 Model-Based Decompositions . . . . .	53
2.3.7 The Dual-Pol Case . . . . .	57
2.3.7.1 Polarimetric Decomposition for the Dual-Pol Case . . . . .	59
2.4 Complex SAR Image Spectral Analysis . . . . .	62
2.5 Polarimetric Interferometric SAR . . . . .	64
<b>3 Object Detection in the Maritime Domain with SAR</b>	<b>67</b>
3.1 Microwave Scattering of the Sea Surface . . . . .	67
3.1.1 Sensor-Specific Parameters . . . . .	69
3.1.2 Scene-Specific Parameters . . . . .	70
3.1.3 Bragg Scattering . . . . .	74
3.2 Wind Field Estimation with SAR . . . . .	75

## TABLE OF CONTENTS

---

3.3	Detection Fundamentals . . . . .	77
3.3.1	Statistical Modelling of the Ocean Clutter . . . . .	77
3.3.2	Thresholding Schemes for (Semi-) Automatic Detection . . . . .	79
3.3.3	The Detection Problem . . . . .	81
3.4	Automatic Vessel Detection . . . . .	82
3.4.1	Vessel Detection Schemes . . . . .	82
3.4.1.1	Constant False Alarm Rate Detectors . . . . .	83
3.4.1.2	Sublook Correlation Techniques . . . . .	85
3.4.1.3	Polarimetric Entropy Detector . . . . .	86
3.4.1.4	Polarimetric Match Filter . . . . .	87
3.4.1.5	Polarimetric Whitening Filter . . . . .	88
3.4.1.6	Optimal Polarimetric Detector . . . . .	88
3.4.1.7	Polarimetric Symmetry Detector . . . . .	89
3.4.1.8	Geometrical Perturbation Polarimetric Notch Filter . . . . .	90
3.4.1.9	Intensity Dual-polarisation Ratio Anomaly Detector . . . . .	90
3.4.1.10	Maritime Moving Target Indication . . . . .	91
<b>4</b>	<b>The InflateSAR Campaign</b>	<b>93</b>
4.1	The Test Object . . . . .	94
4.2	Spaceborne SAR Data: Overview . . . . .	95
4.3	Evaluating SAR Identification Capabilities of Distressed Refugee Boats . . . . .	95
4.3.1	Introduction to Ship Detection . . . . .	96
4.3.2	A Scattering Model of an Inflatable Refugee Boat . . . . .	98
4.3.3	Data . . . . .	100
4.3.3.1	Data Collection Campaign . . . . .	100
4.3.3.2	First Inspection of the Backscattering of Inflatable Boats . . . . .	102
4.3.4	Methods . . . . .	111
4.3.4.1	Water Surface Clutter . . . . .	111
4.3.4.2	Identification Scheme . . . . .	113
4.3.4.3	Estimation of the Inflatable's Size . . . . .	114
4.3.5	Results . . . . .	116
4.3.5.1	Analysis of the Inflatable's Backscattering . . . . .	116
4.3.5.2	Assessment of Acquisition Parameters . . . . .	117
4.3.5.3	Analysis of Clutter Effects . . . . .	118
4.3.5.4	Polarimetric Analysis . . . . .	119
4.3.5.5	Emulating the Detectability at Higher Sea States . . . . .	122
4.3.6	Section Resume . . . . .	123
4.4	Testing SAR Vessel Detection Systems for Refugee Rubber Inflatables . . . . .	124
4.4.1	Vessel Detection Systems: Developments, Approaches and Methods . . . . .	125
4.4.2	Data and Methods . . . . .	128
4.4.3	Results . . . . .	133
4.4.3.1	Preliminary Analysis of Detectors . . . . .	133
4.4.3.2	Comparing Well-Known Detectors . . . . .	137
4.4.3.3	Comparing Resolution Modes . . . . .	137
4.4.3.4	Comparing Polarimetric Modes . . . . .	138
4.4.3.5	Assessing Filtering (Multilooking) . . . . .	138
4.4.3.6	Counting the Boat as a Single Object . . . . .	139
4.4.3.7	Comparing Incidence Angles . . . . .	140
4.4.3.8	Combining iDPolRAD Detectors . . . . .	141
4.4.3.9	Summary of Results Using TerraSAR-X Data . . . . .	141

4.4.3.10	Performance Tests Using Sentinel-1 Data . . . . .	142
4.4.4	Section Resume . . . . .	143
4.5	Developing Refugee Vessel Detection Capabilities with Polarimetric SAR . . . . .	144
4.5.1	Materials and Methods . . . . .	145
4.5.1.1	The Human Scattering Experiment . . . . .	145
4.5.1.2	Data Campaign and Data Collection . . . . .	147
4.5.1.3	Polarimetric Analysis of the Inflatable . . . . .	151
4.5.1.4	Detector Comparison and Detector Fusion . . . . .	153
4.5.2	Results . . . . .	156
4.5.2.1	Qualitative Inspection of High-Resolution Data . . . . .	156
4.5.2.2	Polarimetric Scattering Analysis . . . . .	157
4.5.2.3	Detector Testing . . . . .	159
4.5.2.4	Detector Fusion . . . . .	165
4.5.2.5	Estimation of the Detection Quality . . . . .	167
<b>5</b>	<b>Discussion and Conclusion</b>	<b>169</b>
5.1	Synthesis in the Context of Existing Literature . . . . .	169
5.2	Summary . . . . .	172
5.3	Outlook . . . . .	175
5.4	Concluding Remarks . . . . .	176
	<b>Bibliography</b>	<b>179</b>
	<b>Appendix A Dissemination Activities</b>	<b>207</b>



# List of Figures

1.1	The disaster Risk Management Cycle as proposed by the UN [1]. . . . .	1
1.2	Quantification and location of refugee streams over the last decades. . . . .	2
1.3	Missing people at European Southern Borders. . . . .	2
1.4	Recorded arrivals and deaths in the Mediterranean 2014–2022. . . . .	3
1.5	The vision for an early warning system. . . . .	6
2.1	The electromagnetic spectrum [26]. . . . .	11
2.2	Common radar imaging angles & terms [27]. . . . .	11
2.3	SAR imaging geometry [27]. . . . .	12
2.4	SAR projection surfaces. Source: [28]. . . . .	12
2.5	SAR azimuth resolution (adapted from [26]). . . . .	15
2.6	Schematic of a SAR image divided into resolution cells. From [33]. . . . .	16
2.7	Sequence of transmission and reception of EM pulses [36]. . . . .	17
2.8	The time variation of the received signal [36]. . . . .	17
2.9	Target dichotomy. . . . .	19
2.10	Normalisation areas for SAR backscatter [45]. . . . .	21
2.11	Origin of speckle [51]. . . . .	22
2.12	SAR geometric distortions (from [19]). . . . .	26
2.13	Coordinate system convention with $z$ as the propagation direction [69]. . . . .	27
2.14	The polarisation ellipse [71]. . . . .	28
2.15	Examples for different polarisation states: linearly horizontal/vertical polarised waves (LHP/LVP), linear $\pm 45^\circ$ polarised waves (L+45P/L-45P) and right/left circularly polarised waves (RCP/LCP). (adapted from [43, 75]). . . . .	29
2.16	Poincaré Sphere [71]. . . . .	31
2.17	Scattering on a flat transition between two dielectric, infinite, lossless and homogeneous media in oblique incidence [42]. . . . .	32
2.18	Surface scattering mechanisms [52]. . . . .	38
2.19	Scattering and surface structure [94]. . . . .	38
2.20	Canonical scatterers [42]. . . . .	39
2.21	The expected co-polarisation ratio and double-bounce/single bounce scattering ratio as a function of the incidence angle for fresh water [27] . . . . .	43
2.22	The scattering matrix classification scheme of the Cameron decomposition [123]. . . . .	45
2.23	The roll-invariant parameters $H$ , $A$ and $\bar{\alpha}$ [130] . . . . .	46
2.24	interpretation of the alpha angle [17] . . . . .	48
2.25	Different combinations of entropy and anisotropy [130]. . . . .	49
2.26	The $H/\alpha$ plane and subsections connected to physical properties for the full-pol scenario [136]. . . . .	50
2.27	Comparison between a Sentinel2 scene and the $H-\bar{\alpha}$ classification. . . . .	51
2.28	Comparison between the $H-A-\bar{\alpha}$ Wishart classification and the $H-\bar{\alpha}$ Wishart classification [74]. . . . .	52
2.29	Freeman Wishart Classification [142]. . . . .	52

2.30	Comparison of Eigenanalysis decomposition and Freeman/Durden Decomposition. Single bounce in blue, double bounce in red and volume in green [74]. . . . .	55
2.31	Illustration of the Yamaguchi four-components power decomposition scattering model [143]. . . . .	55
2.32	Comparison between Singh decomposition and Yamaguchi decomposition. Single bounce in blue, double bounce in red and volume in green [74]. . . . .	56
2.33	Three canonical scatterers in the $H-\bar{\alpha}$ planes with: (a) quad-polarisation, (b) dual co-pol (HH VV); (c) dual cross-pol (HV HH); (d) dual cross-pol (VH VV) [136]. . . . .	60
2.34	Scattering plot of the $H-\bar{\alpha}$ planes with: (a) quad-polarisation, (b) dual co-pol (HH VV); (c) dual cross-pol (HV HH); (d) dual cross-pol (VH VV) [136]. . . . .	60
2.35	The sublook generation process in range direction, based on [171] and [36]. . . . .	62
2.36	Along Track Interferometry (ATI) acquisition modes [179]. . . . .	64
3.1	NRCS values simulated by XMOD for various incidence angles and wind directions for VV-pol [205]. . . . .	69
3.2	Backscattering coefficients for water, wet soil and dry soil at different polarisation states ( $\Gamma_{\perp} = VV$ -pol, $\Gamma_{\parallel} = HH$ -pol) and incidence angles. . . . .	70
3.3	The relationship between the relative direction of the radar LoS and the wind vector (angle $\chi$ ) [43]. The example shows model data and measurements for HH-pol in X-band. . . . .	71
3.4	Scattering mechanisms for breaking surface gravity waves [219]. . . . .	73
3.5	Impact of rain on the ocean surface [226]. . . . .	74
3.6	Illustration of Bragg scattering [199]. . . . .	74
3.7	The detection problem (adapted from MIT Lincoln Laboratory, 2001). . . . .	80
3.8	The detection problem. . . . .	81
3.9	Moving Window approach. . . . .	83
3.10	The entropy (from red = 0 to blue = 1) of the calm water surface of the small lake test-bed of the first data acquisition campaign (©DLR 2017). . . . .	87
4.1	3D model of the test object, the rubber inflatable [305]. . . . .	94
4.2	Draught of the rubber inflatable (y-axis, in meters) with different numbers of passengers (x-axis) [305]. . . . .	94
4.3	The inflatable rubber boat. . . . .	98
4.4	Expected dominant scattering mechanisms at and around the inflatable depending on wetness and superstructure with X-band, an incidence angle of approx. $45^{\circ}$ , the boat being oriented $90^{\circ}$ to the LoS and a water wave height of about 4cm (Bragg waves). . . . .	99
4.5	Comparison of the vessel's size and the available data's pixel sizes. . . . .	101
4.6	The inflatable with 30 volunteers. . . . .	101
4.7	Subsets of two examples of dual-pol TerraSAR-X Stripmap scenes showing the lake Müggelsee and its surroundings. . . . .	103
4.8	The vessel's radar footprint in TSX-HS mode (©DLR, 2017) with indications for polarisation and special scene or sensor settings. . . . .	104
4.9	The vessel's radar footprint in TSX-SM mode (©DLR, 2017) with indications for polarisation and special scene or sensor settings. . . . .	105
4.10	The vessel's radar footprint in S1 Interferometric Wide (IW) swath mode (©ESA, 2017). . . . .	105
4.11	3D representations of the vessel's radar footprint in TSX-HS mode (©DLR, 2017) with indications for polarisation and special scene or sensor settings. . . . .	108

4.12	3D representations of the vessel’s radar footprint in TSX–SM mode (©DLR, 2017) with indications for polarisation and special scene or sensor settings. . . . .	111
4.13	3D representations of the vessel’s radar footprint in S1 Interferometric Wide (IW) swath mode (©ESA, 2017). . . . .	111
4.14	Wind speed (©IGB Berlin): impact on ocean clutter. . . . .	112
4.15	The water surface’s maximum backscatter and dispersion and its relation to different sensor parameters. . . . .	113
4.16	Examples of the vessel’s radar footprint in TSX–HS mode (©DLR, 2017). . . . .	114
4.17	Introducing a resizing factor ( $k$ ) to improve the estimation of the boat size. . . . .	115
4.18	Impacts of scene and sensor settings on the quality of identification. . . . .	117
4.19	Using dual–pol acquisitions to compare the quality of identification between HH and VV polarisation. The incidence angle increases from left to right. . . . .	118
4.20	Influences of selected scene settings and sensor settings on the TCR with respect to the water surface’s clutter behaviour. . . . .	119
4.21	A comparison of the inflatable’s and the water surface’s entropy and mean alpha $\bar{\alpha}$ with sensor settings and scene settings for co–polarised data. . . . .	120
4.22	A comparison of the inflatable’s and the water surface’s entropy and mean alpha $\bar{\alpha}$ with sensor settings and scene settings for cross–polarisation data. . . . .	121
4.23	Distinguishing the vessel and the water surface in the H– $\bar{\alpha}$ –space of co–polarised and cross–polarisation data. . . . .	122
4.24	The vessel’s maximum $\sigma^0$ (point-like symbols) for HH–pol and VV–pol compared to the water surface’s radar return estimations according to different wind scenarios (lines). . . . .	122
4.25	The vessel on its way to the test–bed lake. . . . .	128
4.26	Example images of sea truth masks. Left column: TSX SAR images (©DLR 2017) coloured according to each image’s statistics; centre column: pixel–based sea truth mask; right column: object–based sea truth mask. . . . .	130
4.27	New combinations of the polarimetric detectors Cross–iDPolRAD (volume detector) and Co–SiDPolRAD (surface detector). . . . .	132
4.28	Incidence angle: high; boat: inclined; mode: SM; polarisation: dual VH–pol and VV–pol (scale in meters, colour ramps are without units). . . . .	134
4.29	Incidence angle: high; boat: orthogonal, moving in azimuth; mode: SM; polarisation: dual HV–pol and HH–pol (scale in meters, colour ramps are without units). . . . .	135
4.30	Incidence angle: low; boat: orthogonal, non–moving; polarisation: low; mode: SM; dual HV–pol and HH–pol (scale in meters, colour ramps are without units). . . . .	136
4.31	Comparing resolution: ROC curves for different acquisition modes (Pixel–based, multilooked). . . . .	137
4.32	Comparing polarimetric modes: ROC curves for dual co–pol and cross–pol data in SM mode (pixel–based, multilooked). . . . .	138
4.33	Assessing multilooking: ROC curves for different TSX–modes (pixel–based, not multilooked). . . . .	138
4.34	Object detection: impact of the usage of a buffer around the boat on ROC curves for different TSX–modes (multilooked, false positives in log10 scale). . . . .	139
4.35	Impact of the incidence angle on the ROC curves for different acquisition modes (pixel–based, multilooked). . . . .	140
4.36	ROC curves for the iDPolRAD volume detector (green), its surface detecting variant (orange) and the two new combinations in dark blue (pixel–based, multilooked). . . . .	141
4.37	VDS performance test on S1 data (pixel–based, multilooked). . . . .	143

## LIST OF FIGURES

---

4.38	Example results (in dB) of the human backscattering experiments: H2×2 (left), C2×2×2 ( <b>centre</b> ) and S2×3 (right). The y-axes show the distance from the sensor in decimetres. . . . .	147
4.39	SAR data acquisition setup in the test-bed lake. . . . .	147
4.40	Radar signature of 2.1 m waves in the up/down direction, HH-pol TSX Stripmap (left) and its implications for the detection task (right) (©DLR 2014). . . . .	149
4.41	TSX dual-pol data collection of different wave heights and their mean backscattering intensity; one diagram for each polarisation. . . . .	151
4.42	A 350 × 350 m ground truth map after insertion of the positive true pixels (yellow) of four different acquisitions from the rubber inflatable. Purple pixels represent the ocean surface. . . . .	151
4.43	Detector melange flow diagram. . . . .	155
4.44	High-resolution ICEYE VV-pol of the vessel at different scenarios and its mean backscattering intensity with $\sigma_{\mu}^0$ as the mean backscattering of the lake surface (©ESA 2022). . . . .	156
4.45	Pauli R (double bounce) G (volume scattering) B (single bounce) composites for the orthogonal vessel at a medium incidence angle (©ASI 2022). . . . .	157
4.46	Cloude-Pottier decomposition results in a scale from red (high) to blue (low) for the orthogonal vessel at a medium incidence angle (©ASI 2022). . . . .	158
4.47	Yamaguchi Y4R RGB-composite showing symmetric (red), irregular/double-bounce (green) and non-symmetric (blue) scattering of the orthogonal vessel at a medium incidence angle (©ASI 2022). . . . .	159
4.48	Comparison of the detector AUCs for different wave heights for HH VV. . . . .	161
4.49	Comparison of the detector AUCs for different wave height for HV HH. . . . .	162
4.50	Comparison of the detector AUCs for different wave heights for VH VV. . . . .	162
4.51	Comparison of the mean AUCs for different wave heights at VH VV and HV HH for PolRatioOR, PolSym and PWF. . . . .	165
4.52	ROC curves of the PWF detector for HV HH data with different sea states and the vessel oriented orthogonally to the LoS. . . . .	165
4.53	ROC curves of the PWF detector for VH VV data with different sea states and the vessel oriented orthogonally to the LoS. . . . .	166
4.54	Comparison of the mean AUCs for different wave heights at HH VV for HT22AND and PWF. . . . .	166
4.55	ROC curves of the HT22AND detector for HH VV data with different sea states and the vessel oriented orthogonally to the LoS. . . . .	167
4.56	Detection quality estimation parameters TCR and estimated vessel size on the lake test bed. . . . .	168



# List of Tables

2.1	Cameron’s common symmetric elementary scattering types [129]. . . . .	46
4.1	SAR data collection according to acquisition mode, polarisation and incidence angles (low angles ‘L’, high angles ‘H’). . . . .	100
4.2	Pixel size in $m^2$ of available acquisition modes after resampling. . . . .	101
4.3	Data collection: available datasets per experiment type. . . . .	102
4.4	Wind speed and wind direction during the data collection. . . . .	102
4.5	Identification rate according to scene and sensor parameters: positive identification in % (datasets available, which suffer from increased clutter). . . . .	116
4.6	Available data according to acquisition mode and polarisation. . . . .	128
4.7	VDSs under test, applicable polarimetric channels and total number of samples (n) per detector. . . . .	131
4.8	Detectors’ performance comparison (pixel-based, multilooked). . . . .	142
4.9	The dielectric properties for a list of materials involved in the detection scenario at 20°C (* at 37°C) [413]. The value for sea water, given the typical salinity of the Mediterranean Sea, is about 38 g per kilo [414]. . . . .	146
4.10	Overview of the data collected for the boat on the lake with 80 simulated people.	148
4.11	TSX data parameter matrix of the ‘full’ inflatable on the lake. . . . .	148
4.12	Collection of TSX dual-pol ocean data, covering different wave directions, wave heights, polarimetric channel combinations and incidence angles. . . . .	150
4.13	Polarimetric decompositions and parameters. The Yamaguchi parameters had their orientation removed. . . . .	152
4.14	Overview of the vessel detection algorithms being tested and their parameterization. . . . .	154
4.15	Pauli scattering mechanisms (dimensionless, comparative quantities, normalized to 0->1). . . . .	157
4.16	The results of the Cloude–Pottier decomposition of the inflatable (dimensionless, comparative quantities, normalized to 0->1). . . . .	158
4.17	Yamaguchi Y4R decomposition (dimensionless, comparative quantities, normalised to 0->1). . . . .	158
4.18	Cameron decomposition (dimensionless, comparative quantities, normalised to 0->1). . . . .	159
4.19	The vessel-detection algorithm AUCs with different sensor parameters. . . . .	163
4.20	The vessel detection algorithm AUCs with high sea states (SPAN > -17 dB). . . . .	164
4.21	The vessel-detection algorithm AUCs with different orientations of the rubber vessel. . . . .	164



# Symbols and Abbreviations

$(\cdot)^*$	Matrix/vector conjugate	$\bar{\alpha}$	Mean alpha angle
$(\cdot)^T$	Matrix/vector transposition	$\Phi$	Absolute phase (polarisation ellipse)
$(\cdot)^{*T}$	Matrix/vector conjugate transpose (Hermitian)	$\phi$	Phase
$[C]$	Covariance matrix	$\phi_N$	Wind direction (CMOD)
$[J]$	Wave coherence vector/matrix	$\Psi$	Orientation angle (polarisation ellipse)
$[K]$	Kennaugh matrix	$\sigma$	Radar cross section RCS (radar equation)
$[M]$	Mueller matrix	$\sigma$	Standard deviation (statistics)
$[S]$	Sinclair scattering matrix	$\sigma^0$	normalised (or average) radar cross section (NRCS)
$[T]$	Coherency matrix	$\sigma_n$	Noise level
$\alpha$	Absolute phase angle (polarization ellipse)	$\tau$	Pulse length
$\beta^0$	Scattering coefficient radar brightness	$\theta$	Incidence angle
$\chi$	Ellipticity angle (polarization ellipse)	$\cdot$	Vector operator
$\delta$	Phase difference (polarization ellipse)	$\underline{\Omega}$	Lexicographic scattering vector
$\delta_p$	SAR penetration depth	$\underline{E}$	Jones vector
$\epsilon'$	Dielectric constant	$\underline{e}_i$	Eigenvector
$\epsilon''$	Dielectric loss factor	$\underline{E}_r$	The received (scattered) field
$\epsilon_0$	Permittivity of free space	$\underline{E}_t$	The emitted (incident) electric field
$\epsilon_c$	Complex dielectric permittivity	$\underline{E}_x$	Electric field
$\epsilon_r$	Relative dielectric permittivity	$\underline{g}$	Stokes vector
$\gamma$	Interferometric coherence	$\underline{H}$	Magnetic field vector (real)
$\gamma^0$	Scattering coefficient $\gamma$	$\underline{k}$	Target vector
$\hat{\alpha}, \hat{\beta}, \hat{\delta}, \hat{\gamma}$	Set of unitary parameters (Cloude & Pottier decomposition)	$\underline{k}_p$	Pauli scattering vector
$\lambda_i$	Eigenvalue	$\varphi$	Phase
$\lambda_r$	Wavelength of the radar system	$\varrho$	Complex polarisation ratio
$\lambda_s$	Wavelength of a water wave	$A$	Anisotropy
$\langle \cdot \rangle$	Average operator	$A_0$	Area of the SAR resolution cell
$\mu$	Mean (statistics)	$A_r$	The effective aperture of the antenna
$\omega$	Angular frequency	$B_{ATI}$	ATI baseline
		$B_{XTI}$	XTI baseline
		$BW_a$	Antenna beam width
		$f$	Frequency (time)
		$G_t$	The antenna gain in the direction of the target
		$h(t)$	Match filter
		$H_r$	Height of the radar platform
		$k_0$	Wavenumber of the illuminating wave
		$L$	Real antenna length
		$L_s$	Synthetic aperture antenna length
		$P_D$	Probability of detection
		$P_F$	Probability of false alarm
		$P_M$	Probability of missed detection
		$P_r$	Power of the scattered wave
		$P_t$	Power of the transmitted wave

## SYMBOLS AND ABBREVIATIONS

---

$R$	Slant range distance	$k$	Boltzmann's constant
$r_a$	SAR resolution in azimuth	LoS	Line of sight of the SAR sensor
$r_g$	SAR resolution in ground range	MMTI	Maritime moving target indication
$r_{RAR}$	Real aperture radar resolution	N	Nominal number of looks
$r_r$	SAR resolution in slant range	NEBN	Noise equivalent beta nought
$s(t)$	Transmitted EM pulse	NESZ	Noise equivalent sigma zero
$U_{10}$	Wind speed 10m above ground	p	Co-polarisation ratio
$u_s$	Local wind speed	PolInSAR	Polarimetric Interferometric SAR
$v_p$	Phase velocity	PolSAR	SAR polarimetry
A	Amplitude (polarisation ellipse)	PRF	Pulse repetition frequency
ATI	Along-track interferometry	q	Cross-polarisation ratio
B	Bandwidth of the SAR system	RAR	Real aperture radar systems
BSA	Backscatter Alignment convention	RCM	range cell migration
c	Speed of light	ROC	Receiver Operating Characteristic
CSG	COSMO-Skyimed Second Generation	S-1	SENTINEL-1
DEM	Digital elevation model	SAR	Synthetic Aperture Radar
DInSAR	Differential SAR interferometry	SLAR	side-looking aperture radars
DN	Digital number	SLC	Single look complex
DoP	Degree of polarization	SNR	Signal to noise ratio
EM	Electromagnetic	T	Total equivalent noise temperature
ENL	Equivalent (or effective) number of looks	TCR	Target to clutter ratio
FFT	Fast Fourier Transformation	TDX	TanDEM-X
FM	Frequency modulated	TomoSAR	SAR tomography
FPR	False positive rate (ROC)	TPR	True positive rate (ROC)
GMF	Geophysical Model Function	tr	Trace of a matrix
GTC	geocoded-terrain-corrected	TSX	TerraSAR-X
H	Entropy	v	SAR platform velocity
I	Intensity	XTI	Across-track interferometry
InSAR	SAR interferometry		
K	Linear FM chirp rate		

# 1

## Introduction

**I**n recent decades, Synthetic Aperture Radar (SAR) has emerged from being primarily interesting for theoretical science, engineering and development to a rather more application-driven branch of the remote sensing community. An important example that has raised public awareness and tested the practicability and applicability of SAR is disaster monitoring and mitigation. Satellite-based, aircraft-based or drone-based SAR sensors are predestined to perform disaster monitoring, mitigation and damage assessment due to their all-weather day-and-night imaging capability.

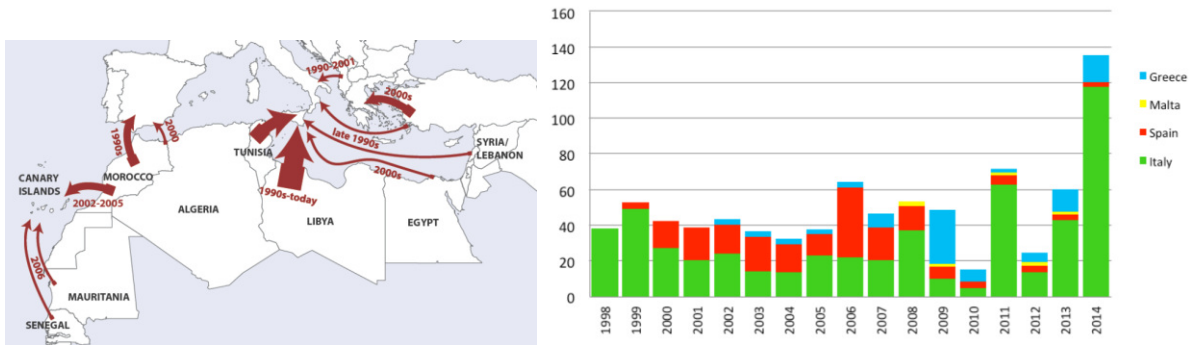


**Figure 1.1:** The disaster Risk Management Cycle as proposed by the UN [1].

In this context, SAR can support several aspects of emergency and disasters operations. For example, in the event of flooding, landslides, earthquakes or oil spills, SAR is an useful tool to enhance situational awareness immediately after a disaster has taken place. By collecting information about what happened, where it happened and what kind of infrastructure and how

# 1. Introduction

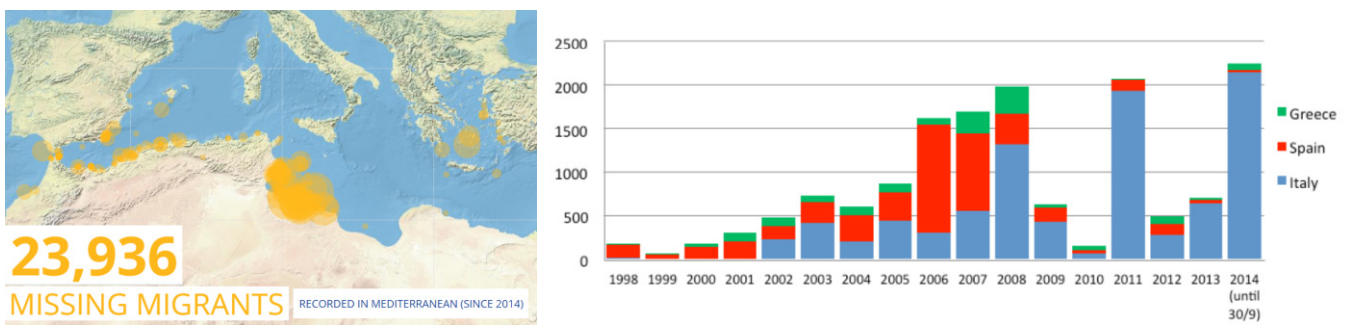
many people have been affected, SAR is capable of supporting disaster response, rehabilitation and recovery. On the other hand, SAR can be used for prevention, mitigation and preparedness for a disaster in the form of early, for example, of warning systems. SAR can therefore enable contributions to several elements of the disaster risk management cycle (Fig. 1.1). The ongoing humanitarian crisis along the southern European maritime borders is a prominent example, where a SAR-based early warning system could be deployed to prevent the loss of human lives at sea.



(a) The main maritime immigrant routes into the EU in the recent decades [2]. (b) Arrival of refugees per country in thousands [2].

**Figure 1.2:** Quantification and location of refugee streams over the last decades.

Most incidents along the European southern maritime border regions happen along the main maritime immigrant routes. The importance of these routes in terms of traffic has been constantly shifting over the last decades as Fig. 1.2a shows. In recent years — and still today — the central Mediterranean routes into the European Union between Tunisia/Libya and Malta/Sicily/The Pelagie Islands (e.g. Lampedusa) have been highly frequented (Fig. 1.2b). That means that refugees and migrants try to use maritime vehicles which are overcrowded and in no sense equipped for open ocean passages for these very long-distance routes of 300 to 450 km.



(a) 2014–2022. Missing Migrants Project from the International Organization for Migration (IOM); [3].

(b) 1998–2014 in thousands [2].

**Figure 1.3:** Missing people at European Southern Borders.

Official statistics (Fig. 1.3) show that the central maritime routes to Italy are the ones used by most of the people seeking refuge and, at the same time, they are the deadliest. Moreover, the exact estimation of this ongoing humanitarian disaster is difficult and we do not know how many people lost their lives or went missing. This is an inherent problem arising from the human trafficking activities of people who enable, facilitate and profit from the stream of migrants at sea.

## 1.1 Civil Search and Rescue at the Southern Maritime Borders

Year	Arrivals	Dead & missing	Previous years	Arrivals *	Dead and missing
2022	26,084	826	2021	123,318	1,977
2021	151,417	3,157	2020	95,774	1,401
2020	99,907	2,326	2019	123,663	1,335
2019	128,663	2,087	2018	141,472	2,270
2018	146,949	2,380	2017	185,139	3,139
2017	187,499	3,140	2016	373,652	5,096
2016	389,976	5,305	2015	1,032,408	3,771
			2014	225,455	3,538

\* Include sea arrivals to Italy, Cyprus, and Malta, and both sea and land arrivals to Greece and Spain (including the Canary Islands). Data are as of 31 December 2021 for all countries.

(a) Source: IOM [4].

(b) Source: UNHCR [5].

**Figure 1.4:** Recorded arrivals and deaths in the Mediterranean 2014–2022.

This difficulty explains the striking differences that can be found in the recordings of independent international bodies such as the International Organization for Migration and the United Nation Refugee Agency (UNHCR) (Fig. 1.4). Search and rescue (SaR) NGOs on the ground warn about skyrocketing numbers of unregistered cases and estimate that the records only list 10% of all casualties.

## 1.1 Civil Search and Rescue at the Southern Maritime Borders

The first incident of a humanitarian vessel rescuing refugees in the Mediterranean Sea happened in 2004 100 nautical miles south of Lampedusa [6]. There, the German vessel Cap Anamur rescued 37 people from a partially deflated dinghy. After bringing them to Sicily, the ship was confiscated and Italy pressed charges of facilitating illegal immigration. After five years, the court acquitted them but this case shows the ability of any border regime to thwart or even turn against any humanitarian intervention from NGOs. It was the first time that rescuing lives resulted in legal prosecution and, thus set a precedent. In 2013, Italy launched the military and humanitarian mission Mare Nostrum as a response to a shipwreck near Lampedusa that caused the death of 366 people. For the first time, a border patrol mission had the specific mandate to rescue people and Mare Nostrum represents the most important step towards the institutional humanitarianization of the EU sea border. One of the reasons stated by NGOs for starting their SaR missions was precisely the termination of Mare Nostrum’s operations in late 2014. The successor mission Triton, launched by Frontex, had no specific SaR mandate, fewer vessels, and a very limited operational area of only 30 nautical miles from the Italian coastlines. Frontex later accused Mare Nostrum of attracting more migrants by patrolling near Libyan waters. On the contrary, the surge in the number of refugees trying to cross the central Mediterranean had already begun in summer 2013 [7].

Thus, large numbers of people have been continuously getting lost or dying at the southern European maritime borders for many years, but the situation attracted extra attention in the year 2014, when the numbers of victims skyrocketed and a civil sea rescue fleet slowly formed. The first actors to form a search and rescue fleet were the European NGOs Sea-Watch (SW) and Migrant Offshore Aid Station (MOAS) — these being the first to start their operations

together with Doctors Without Borders (MSF). The following years, many NGOs follow and setup SaR ships and other assets to send them to the SaR zone near the Libyan coastal waters<sup>1</sup>.

## 1.2 Repoliticization of Migration

Their interventions changed the search and rescue scene in the Central Mediterranean. Regardless of the NGOs political views, their engagement has led to a repoliticization of migration and border policies and rekindled political discourse on the topic of migration. This has created space for disagreement and different point of views beyond the technocratic, expert and security-based ones which were previously allowed to go unchallenged, given the socioeconomic and political context in which migration takes place. Cuttitta [7] discussed in his article whether humanitarian action can be politically neutral, or if it is unavoidably political. Repoliticizing migration and border policies therefore means promoting “the existence of antagonism, conflict, difference and choice. Based on document analysis, fieldwork and press releases by the NGOs the article concludes that MOAS keeps politically neutral, whereas MSF + SW also regard their activities as a political commitment and see their role as that of a watchdog.

This repoliticization pushes back against a trend towards depoliticization which is associated with the marketization of policy-making processes and the rise of technocratic forms of governance [8]. This refers to a tendency of politicians to obscure the political character of negotiation processes and to present policy-making as a neutral, necessary and unimpeachable process. In this way, the possibility of choosing between different political alternatives, as well as that for disagreement and resistance, is limited or denied. A key factor in depoliticization can be humanitarianization, which refers to the increasing deployment of moral sentiments in contemporary politics [9] and to the increasingly organised and internationalised attempt to save the lives, enhance the welfare, and reduce the suffering of the world’s most vulnerable populations [10]. In the context of border management, human rights and migration, the NGOs play an important role in fostering such humanitarianization. With their work, they become political actors and part of alliances, power relations and the systems of negotiations between states and international institutions.

To draw a comprehensive picture, the article describes the legal aspects of SAR missions: shuttling, push backs, the cooperation with national authorities and coast guards, other NGOs and EU authorities and the role of civil ships. The article summarises the situation in the Mediterranean and the developments since 2014 regarding the work of the NGOs, local authorities and EU-missions, their interactions and implications for the political discourse, the rise in criticism of the NGOs and associated accusations of human trafficking/migrant smuggling. Further, it describes the ongoing reconfiguration: First, EU + Italy are strengthening the Libyan Coast Guard to carry out SAR in their own waters which would increase push backs. Second, the media, political and judicial campaign against SAR NGOs seems to aim at undermining their popular support. It was non-governmental SAR per se that were the main obstacle for the envisaged outsourcing of borderwork to the Libyan authorities. This will restore a more restrictive, and yet depoliticised and unquestioned, border regime in the Central Mediterranean and will confront the NGOs with a serious challenge. Therefore, contesting or even resisting the outsourcing of SAR to Libya (by continuing to patrol the area close to Libyan waters and refusing to return the rescued people to Libya) seems to be becoming a political task for SAR NGOs in the changing context of the Central Mediterranean.

---

<sup>1</sup>list of civil search and rescue ships: [https://en.wikipedia.org/wiki/List\\_of\\_ships\\_for\\_the\\_rescue\\_of\\_refugees\\_in\\_the\\_Mediterranean\\_Sea](https://en.wikipedia.org/wiki/List_of_ships_for_the_rescue_of_refugees_in_the_Mediterranean_Sea)



Regardless of their political positions and the degree of criticism they express towards government policies, all NGOs cooperate with the Italian authorities and the respective Maritime Rescue Coordination Center (MRCC). For the central Mediterranean, the MRCC Rome, run by the Italian Coast Guard, is responsible for the coordination of SaR operations. That includes the decisions about which vessel should assist the migrants and which one should bring them to the mainland. The Ministry of the Interior of the respective country has then to indicate in which port people should be disembarked. Libya has never established its MRCC and therefore Italy must assume SaR responsibilities for the central Mediterranean [7].

In 2016 a new situation evolved where the EU started to train the Libyan Coast Guard (LCG) while Italy started, in 2017, to supply them with patrol boats. Since 2016, attacks by the LCG on NGO ships have occurred and soon the European authorities started to attack SaR NGOs as well. The LCG intervened in SaR operations of NGOs, sometimes under the coordination of MRCC Rome and committed forced, illegal pushbacks of refugees to Libya. At the same time, relations between the MRCC Rome and the SaR NGOs began to deteriorate.

### 1.3 'Peripheralisation' of Human Rights

Between the imperative of rescuing migrants in distress at sea and the goals of the European border security one question stands out: What happens when refugees encounter a coast guard patrol vessel? Are the local actors willing and able to respect and implement human rights laws such as the International Convention on Maritime Search and Rescue or the Geneva Refugee Convention? Klepp [11] conceptualises the European regime for migrants in the central Mediterranean as a dynamic and conflict-driven multi-sited arena of negotiation:

When you have a land border, here is country A and therefore the subject of law is country A, and here is country B, there is no limbo in between. At sea it's different. Here you have country A, here you have the high seas and here begins the jurisdiction of country B. But in between, on the high seas, things are a little bit delicate..

(Commander Borg, Armed Forces of Malta, from: [12])

We can observe regionally varying patterns of the implementation of human rights [11]. The decisions and the actions of the coast guard personnel often determine whether a refugee gains access to the European asylum system. And these informal operational methods carried out in the Mediterranean Sea function as a trailblazer of the overall EU refugee policy. The principle of non-refoulement could first be undermined and then abolished in this process.

In 2011, the Guardian published the case of a disabled refugee vessel with 72 people, among them two babies, that received no help. It drifted for 16 days in the central Mediterranean and only three survivors were washed ashore after a storm on the Libyan coast. The vessel was detected by the alerted Italian Coast Guard, was overflowed and seen by several NATO aircrafts, was sighted by several fishing boats and cargo ships and was supplied with water and food by a military helicopter. The Council of European investigated the case and directed the harshest of accusations at NATO, Italy and Libya. This case shows typical and commonplace absence of regulation and control frameworks on how to deal with refugee in distress at the European sea borders [13]. Moreover, many cases are documented (and verified by NGOs such

## 1. Introduction

as Human Rights Watch, the Council of Europe, the UNHCR) in which the border control activities, coordinated by Frontex, infringed basic human and refugee rights<sup>2</sup>.

### 1.4 Motivation

This thesis confronts the ongoing humanitarian crisis and pursues the vision of establishing an early warning system with the goal of supporting civil search and rescue missions in their goal of finding highly vulnerable maritime vehicles used by migrants to cross the Mediterranean Sea. The vehicles which are very often used and are, at the same time, the most vulnerable, are 12 m long five-chamber rubber boats equipped with a 40 HP outboard engine. These boats, fully packed with refugees who try to cross oceans, are in distress from the moment of embarkation and not seaworthy. Due to their small dimensions they are very hard to find.

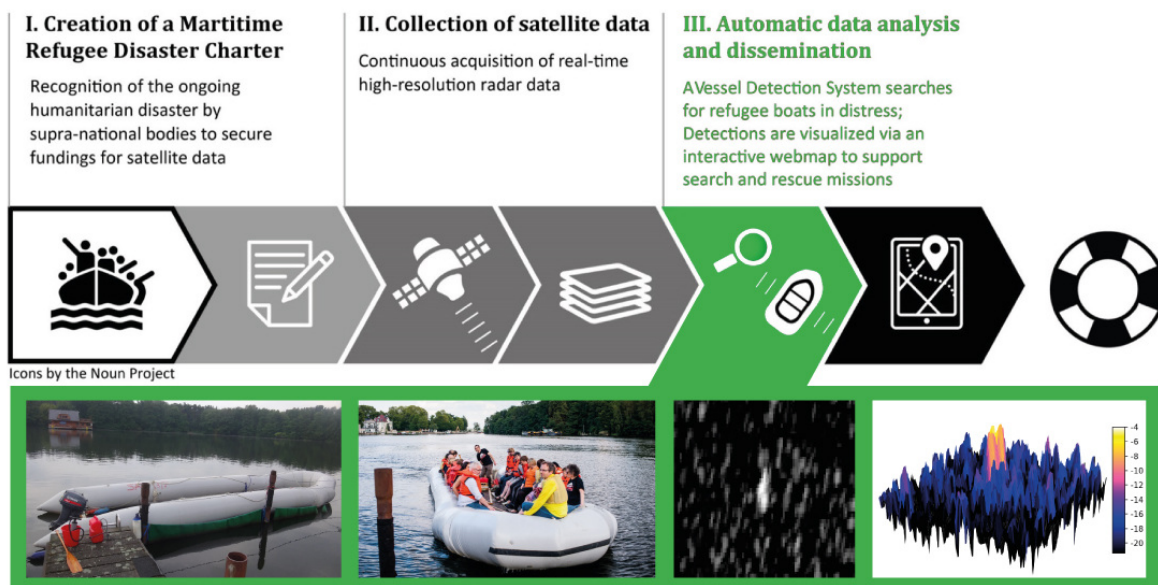


Figure 1.5: The vision for an early warning system.

The early warning system proposed here is fed with a steady stream of SAR images covering the main search and rescue zone in the central Mediterranean. The heart of the automatic data processing chain is semi-automatic detection of the refugee inflatables using this imagery (Fig. 1.5). Geographic Information Systems (GIS) are capable of handling and systematically visualising all available information from large scale disasters [14, 15, 16]. A web-based GIS (Web-GIS) would be the appropriate solution to disseminate the detection results and, at the same time, function as a documentary tool. Such an interactive web application should have a web map service providing a map of the search and rescue zone as the base layer which would show the position, the timestamp and the confidence level (or quality) of the detections. Additionally, this service should function as a revision tool. Experts can double-check and verify the detections before they are finally documented and released to search and rescue operatives on the ground.

<sup>2</sup>see various reports from the Council of Europe: 'Report to the Italian Government on the visit to Italy carried out by the European Committee for the Prevention of Torture and Inhuman or Degrading Treatment or Punishment from 27 to 31 July 2009'

As far as the main maritime migrant routes in the central Mediterranean Sea are concerned, the search and rescue region of interest is about 450 km north to south and about 350 km east to west — just to give a first impression of the immense SAR data requirement such a system would have. But it can be covered, when we consider, for example, the scene width of the Stripmap Mode of 30 km, which is supported by most SAR sensors. Further, the recent development of spaceborne SAR platforms is promising. There are more and more SAR satellites in orbit with a rising number of commercial missions as well. Combining all data from (some of) these SAR satellites promises a reasonably good temporal resolution. In addition, SAR is undisturbed by clouds or rain and does not need illumination from an external source. These all-weather capabilities further increase the temporal resolution and make SAR the perfect tool for time-critical early warning systems and disaster-related applications. When using such a large-scale covering acquisition mode, there is a certain trade-off in terms of the spatial resolution or the polarimetric information depth and, obviously, a highly sophisticated detector that is especially designed for these 12 m rubber inflatables is needed.

## 1.5 Objectives

The objective of this work is an anomaly detection task. To solve that task, the goal was the development of an algorithm that can function as a semi-automatic detector for small, non-metallic rubber inflatables with SAR. The rubber boat in our scenario is the anomaly in the surrounding water surface.

For that, we need to understand the radar pattern of the inflatable, the radar pattern of the water surface and their interactions. To this end extensive analyses of these patterns and of the factors influencing them were carried out. And we need to understand that these patterns are constantly changing; and with them, the SAR image changes. Inspired by the recommendations of [17] the development of a detector according to the following criteria was pursued:

- low probability of missing the small maritime objects
- low probability of false alarms caused by water surface clutter (e.g. waves, spray, etc..) or by other man-made maritime objects which should provide statistical robustness
- highly adaptive to the changing patterns of the vessel, the water surface and the interactions between them

For visualisation and comparison of the true positive rate with the false positive rate of the same detector, the graphical plot called receiver operating characteristic (ROC) curve was used. The concept of ROC curves was originally developed for operators of radar receivers and makes detectors comparable at various threshold settings. Therefore, it is perfectly suitable for visualising the first two items from the list. The last list item reflects the inherent challenges of the research question. We have a rubber inflatable whose radar pattern is highly variable, meaning not constant over time, and depends on a variety of influencing factors. These influencing factors are very diverse, such as for example, the radar sensor settings or the local wind direction. And the same is true for the surrounding water surface. Further, we see subtle interactions between the inflatable and the water surface, which themselves depend on the influencing factors mentioned, and can act as indicators for these factors. In attempting to configure an appropriate detector for this application, these factors need to be understood and the detector should have a high level of adaptability.

For conceptualisation of the research, the recommendations from [18] were followed and adapted on the way to the identification and/or the development of a well-suited detector:

## 1. Introduction

---

- specify a surveillance scenario
- find archived SAR data or collect new SAR data with the target object in the most realistic environment possible
- decide on appropriate radar parameters and geometry
- set up benchmark tests based on authenticated field data
- compare the different detection algorithms

The ongoing humanitarian crisis in the central Mediterranean defined the surveillance scenario. But finding radar satellite data showing real boats filled with people was expected to be very difficult from the start. As it turned out, that there is no feasible way for this research — being part of the civil sector — to get hold of ground truth data. Therefore, the collection of test data that cover a variety of sensor parameters and scene parameters became an objective in itself. The selection of parameters to test should be taken in the context of the detection scenario and the detectors used. There are a number of well-developed algorithms for detection in the maritime domain, but they were designed for large, mostly metallic man-made objects (such as ships and oil rigs), oil spills or icebergs. In this thesis a selection of these detectors for the special case of a very small, non-metallic vehicle are tested and adapted. A broad variety of sensor settings makes the results more meaningful and raises the chance of improved detection capabilities by identifying the most favourable parameters. The test object is very small and was expected, from the beginning, to exhibit a rather weak radar backscattering pattern. A number of other scene parameters can render this signal even weaker. In conclusion, the quality of the test data is crucial and was collected with the goal of the establishment of a comparison matrix for as many of the radar pattern influencing factors as possible.

Working with SAR means having the chance of exploring polarimetric information. SAR polarimetry is a widely used technique for the derivation of physical information about objects on the ground. It is a powerful additional information layer for applications on land, on snow and ice, in the maritime environment and for urban applications. The polarimetric properties of man-made and natural scatterers make it possible to build up a powerful observation space that is sensitive to their shape, their orientation, their movement and their dielectric properties. This approach led to the development of a number of physical models for the identification and separation ('decomposition') of scattering mechanisms occurring inside the same resolution cell. The decomposition of scattering processes in and around the inflatable and their interpretation are an important objective and can be helpful for improving ship detection systems and interpreting their output.

## 1.6 Structure

The next chapter attempts to cover all the important basic concepts of SAR and Polarimetric SAR. Chapter three introduces the more specialised topic of SAR applications in the maritime domain and includes introductions to detection and thresholding and vessel detection systems. Further, a description of a variety of such vessel detection algorithms is provided. Chapter four provides a frame for the scientific work, which we published in three independent papers. Each subsection represents one paper, the description of the respective methods and data used and the results generated, including a discussion and outlook. Chapter five has the overall discussion and a summary and closes with an outlook for future research.

# 2

## SAR and PolSAR

A radio detection and ranging (radar) system transmits/receives an electromagnetic pulse and observes the strength (detection) and the time delay (ranging) of the return signals. This work is concerned with Synthetic Aperture Radar (SAR) which is a special kind of imaging radar. Radar is an active system and transmits its own signal, which is an electromagnetic wave of specific wavelength and polarisation. The backscattered signal, coming from the objects on the ground, is then collected and focused to image the observed scene. In addition to conventional radar, SAR makes use of the movement of the radar platform, together with signal processing to generate high-resolution images. SAR systems can be payloads on drones, airborne or spaceborne platforms, as well as platforms on the ground.

Prior to SAR, imaging radars operated using the real-aperture principle and were known as side-looking aperture radars (SLAR) . Carl Wiley of the Goodyear Aircraft Corporation is generally credited as being the first who used Doppler frequency analysis of coherent<sup>1</sup> radar signals to improve the along-track resolution. This method was known as Doppler beam sharpening, but later became known as SAR. Wiley [20] presents an interesting table with a short description and the authors of seminal developments in the field of SAR such as autofocusing, multilooking, the spotlight acquisition mode or interferometry.

SAR offers very good spatial resolution (depending on radar parameters) and all-weather capabilities. This is because it is mostly unaffected by weather conditions like rain and clouds, it suffers very low attenuation by atmospheric constituents, and it does not rely on the illumination of the sun. These advantages make SAR highly available and therefore especially useful for disaster mitigation and urgent (near) real time monitoring.

Further advantages in comparison to optical remote sensing come from the different way that objects interact with microwaves. For instance, there is sensitivity to the dielectric properties of mediums (influenced by moisture), the surface roughness, the target structure (especially with polarimetry) and the ability to penetrate subsurfaces and canopies.

---

<sup>1</sup>coherent radar systems: here, the term coherent refers to a radar system in which the integration of the emitted pulses is done including the phase information [19]. In non-coherent radar systems, the phase information is not used

However, on the other hand, the interaction between EM waves and the objects is generally complex and requires the use of models. Furthermore, being an active system, it requires a higher complexity of the sensor electronics and a much higher energy consumption compared to optical passive sensors. This limits the number of images which can be acquired per orbit [21, 22].

### 2.1 SAR Missions and Capabilities

The monitoring of large areas, such as the central Mediterranean is challenging and even more difficult when the application needs to be quasi-real time. Over the past decades, spaceborne remote sensing has developed to a mature technology and is now playing an important role in Earth observation due to its capabilities of global coverage, high temporal and spatial resolution, and the advantage of long-term observation missions.

Platforms with SAR sensors like, for example, TerraSAR-X (TSX), TanDEM-X (TDX), RADARSAT-2, COSMO-SkyMed Second Generation (CSG), ALOS-1 and ALOS-2 or SENTINEL-1 (S-1) can provide high-resolution imagery of the ocean surface. The spatial resolutions range between one meter to tens of meters depending on the specific satellite. They are very useful for maritime surveillance and detection of small maritime vehicles while maintaining a large spatial coverage. The combination of different SAR satellites would be capable of reducing the temporal resolution to less than a day. Besides, they deliver wind and wave information for the ocean surface.

### 2.2 SAR Principles

The Electromagnetic (EM) Spectrum is the frequency range of all types of EM waves. It spans from frequencies above  $10^{25}$  hertz to below one hertz, corresponding to wavelengths from a fraction of the size of an atomic nucleus up to thousands of kilometres. It can be divided into ionising radiations having the shortest wavelengths and being capable of transporting the highest energy, visible light and infrared and finally microwaves and radio waves with longer wavelengths and lower frequencies. Figure 2.1 gives a detailed insight into the range of applications of the spectrum in the microwave and radio wave category, which are separated on a base-10 logarithmic scale.

In this order, the frequencies used for radar remote sensing are called Super High Frequencies (between 3 and 30 GHz) and cover a number of different bands (the bottom part of Fig. 2.1). The selected frequency plays a great role in the design of a radar sensor since the wavelength contributes to a great extent to what can be seen by the radar [23, 24]. This is because waves interact more with objects on the ground of about the same size as the wavelength  $\lambda_r$  [25, 23]. Therefore, structures which are of the size or bigger than  $\lambda_r$  have a higher radar return. The most commonly used bands for satellite-based imaging radar are L, S, C and X-band. X-band is used by civil, military and government institutions for a broad number of applications such as radar remote sensing, weather monitoring, air traffic control, maritime vessel traffic control, defence tracking and vehicle speed detection for law enforcement. C-band is primarily used for, apart from radar remote sensing, satellite communications, for full-time satellite TV networks and commonly used in areas that are subject to tropical rainfall, since it is less susceptible to rain fade than for example the Ku-band. The S-band is primarily used for weather radar, surface ship radar, and some communications satellites, especially those

of NASA for communication with the ISS and with Space Shuttles. The L-band supports the well-known Global Positioning System (GPS) as carrier waves and also satellite mobile phones, providing communications at sea, land and air and satellite radio [26].

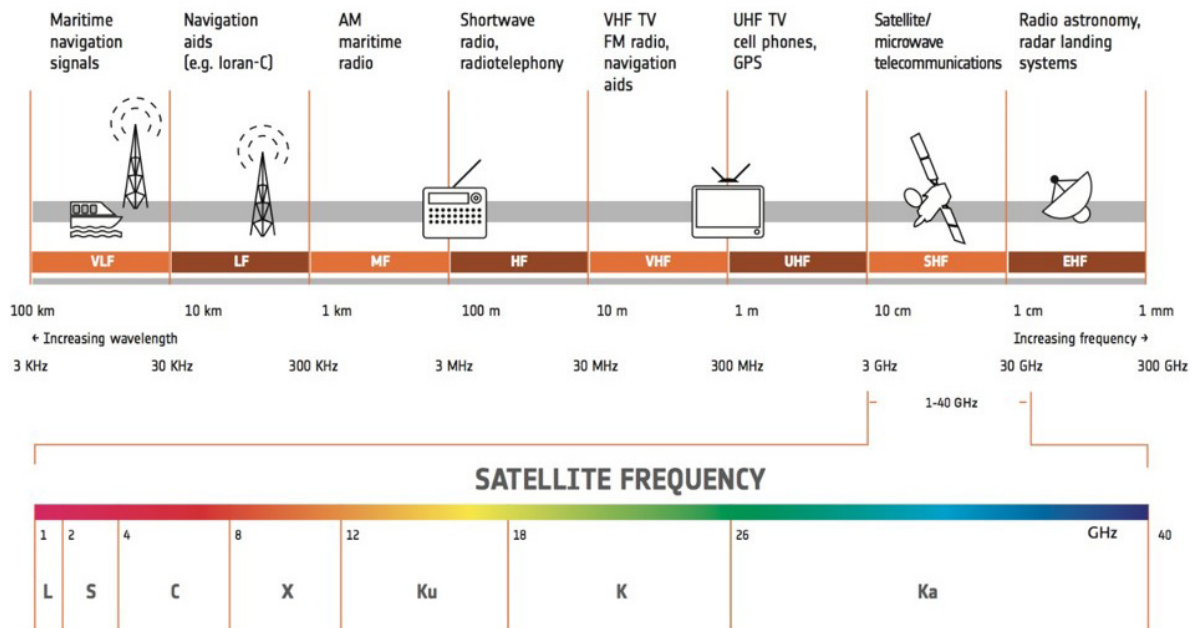


**Figure 2.1:** The electromagnetic spectrum [26].

The SAR sensor itself mainly consists of a signal generator, a radio frequency (RF) transmission and reception component, a signal processor and a communication unit. The microwave signal is generated first and then transmitted by the antenna at the RF unit. The backscattering from the scene on the ground is received by the antenna and then fed into the SAR signal processor where the input is defined raw data. This raw data passes through a number of preprocessing steps which are often (but not always) done in the frequency domain to decrease the computational time. For the compression in range and azimuth direction (see Fig. 2.3), the SAR processor correlates the received signal with the previously emitted pulse, called *chirp*. For a more detailed description of SAR image formation please see chapter 2.2.2.

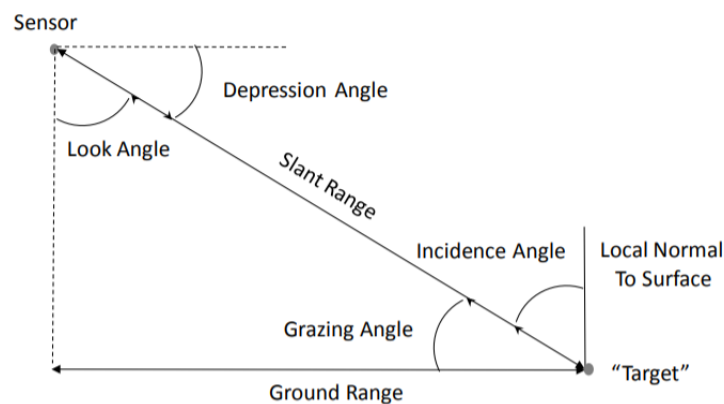


**Figure 2.2:** Common radar imaging angles & terms [27].

SAR sensors are side-looking (Fig. 2.4) which gives them the ability to unambiguously identify the backscattered electromagnetic response. That way, each point in the image plane

## 2. SAR and PolSAR

can be uniquely identified by its time delay (range direction) and by its Doppler shift (azimuth direction). This adds important sensor parameters to all SAR sensors: the look angle, which is defined as the angle between nadir and the wave direction at the sensor, and the incidence angle, which quantifies the deviation of the angle between the wave direction and the surface nadir (Fig. 2.2). The grazing angle is the complementary of the incidence angle. For spaceborne systems, the incidence angle for flat surfaces such as calm waters is always larger than the look angle. The reason for that difference is that the look angle depends on the local surface curvature of the planet. For low-flying airborne SAR on the other hand, the surface curvature can be neglected and the two angles can be assumed to be equal [19]. The local incidence angle varies within a SAR image due to topography and the curvature of the Earth's surface. This variation is much larger for airborne SAR than for spaceborne SAR for a comparable footprint because of the difference in their flight altitudes.

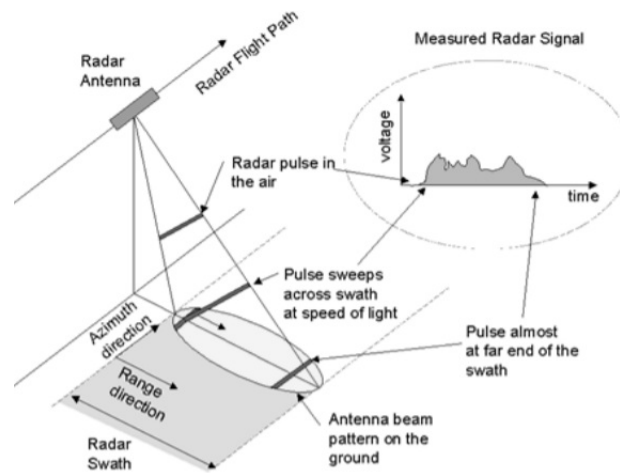


Figure 2.3: SAR imaging geometry [27].

The local, native 2-D coordinate system of each SAR image has a range and an azimuth direction. To locate each pixel in its correct place, both the range information, which is derived from the time needed by the pulse to travel to the ground and back, and the azimuth information, which is derived from the linear displacement of the antenna along the track, are needed. The value of the pixel is a complex number including magnitude and phase of the backscattered signal, sampled along azimuth and range.

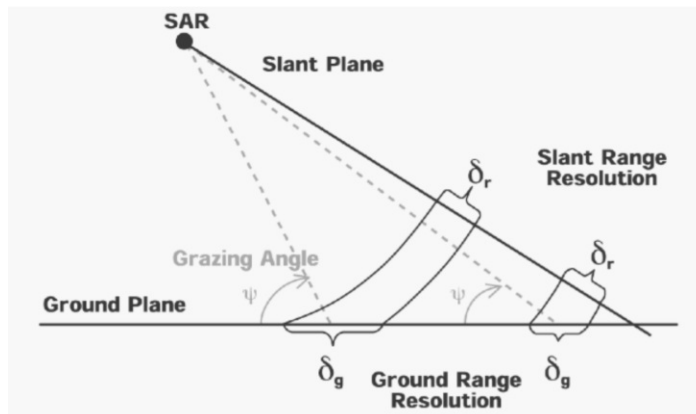


Figure 2.4: SAR projection surfaces. Source: [28].



The data is received by the sensor in analogue form as voltages [29]. An analogue-to-digital converter carries out the task of sampling. These samples are 2-dimensional arrays and are saved within each pixel digitally as complex numbers. In the slant plane, relative<sup>2</sup> distances are measured between the sensor platform and the target object. To generate a geo-referenced radar image product, the data has to be projected on the ground range using a spatial reference system. That transformation requires correction for each data point in respect of the local terrain elevation.

$$\frac{G_r}{S_r} = \frac{1}{\cos \theta} \quad (2.1)$$

Projecting the data from the slant range to the ground range plane is done while making allowance for the incidence angle  $\theta$  (Fig. 2.1, [30]). Since  $\theta$  becomes larger in the far range, the ground range resolution  $G_r$  in the far range is better compared to those in the near range (Fig. 2.4). This does not affect the slant range resolution  $S_r$ .

The coherent sum of the contributions of a resolution cell can be written as:

$$V_{re} + jV_{im} = V = \sum_{i=1}^N V_i e^{j\phi_i} = \sum_{i=1}^N V_i \cos \phi_i + j \sum_{i=1}^N V_i \sin \phi_i \quad (2.2)$$

with  $V_i e^{j\phi_i}$  as the return from the  $i$ -th scatterer within a resolution cell [17]. The complex number consists of the real part  $V_{re}$  and the imaginary part  $jV_{im}$ . On the right side a different notation is shown with the power  $V$  and the phase  $\phi$ .

If the number of independent samples (in our case resolution cells) is big enough, the central limit theorem<sup>3</sup> can be applied. Following this theorem, we can assume a normally distributed real part ( $V_{re} \sim N(\mu, \sigma^2)$ ) and imaginary part ( $V_{im} \sim N(\mu, \sigma^2)$ ) with their corresponding probability density functions (pdf) as:

$$f_{V_{re}}(V_{re}) = \frac{1}{\sqrt{2\pi\sigma^2}} \exp\left(-\frac{V_{re}^2}{2\sigma^2}\right), \quad f_{V_{im}}(V_{im}) = \frac{1}{\sqrt{2\pi\sigma^2}} \exp\left(-\frac{V_{im}^2}{2\sigma^2}\right) \quad (2.3)$$

The real part ('In-phase', here:  $V_{re}$  commonly:  $I$ ) and the imaginary part ('Quadrature', here:  $V_{im}$ , commonly:  $Q$ ) are independent of each other and their means equal zero [29]. The SAR raw signal data is represented as complex numbers and a pixel value  $z$  is given as:

$$z_{m,n} = V_{re} + jV_{im} \quad (2.4)$$

The notation used in Equ. 2.4 is called the rectangular (or Cartesian) form. The same pixel can be described in the polar (or exponential) form using the complex number's amplitude ( $A$ ) and its phase angle ( $\phi$ ):

<sup>2</sup>relative: because SAR does not measure absolute distances but only relative distances to the first pixel in range

<sup>3</sup>the central limit theorem tells us that the summation of many random processes will tend to have a Gaussian distribution, even if the individual processes have other distributions. In other words, when a lot of random phenomena accumulate, the result appears to be approximately Gaussian

$$z_{m,n} = Ae^{j\phi} \quad (2.5)$$

Another notation form, which is commonly used to describe quadrature signals in communication systems, is the trigonometric (or polar) form:

$$z_{m,n} = A(\cos \phi + j \sin \phi) \quad (2.6)$$

with  $A$  as the amplitude of the complex number  $z$  and with  $\phi$  as the phase. This complex number can be used to calculate  $A$  and  $\phi$  from the voltage of the pixel:

$$A = \sqrt{V_{re}^2 + V_{im}^2} \quad \phi = \arctan \frac{V_{im}}{V_{re}} \quad (2.7)$$

The magnitude  $A$  is sometimes called the modulus of the complex number  $z$ . Reversely, the real and the imaginary part can be calculated using the magnitude and the phase angle as:

$$V_{re} = A \cos \phi \quad V_{im} = A \sin \phi \quad (2.8)$$

### 2.2.1 SAR Resolution and Data Preprocessing

For conventional ("real aperture") radar systems (RAR), the spatial resolution in azimuth  $r_{RAR}$  of a RAR antenna is determined by the wavelength of the radar  $\lambda_r$  and the antenna length  $L$ , and by the slant range  $R$  [31]:

$$r_{RAR} = \frac{\lambda_r R}{L} \quad (2.9)$$

Since the wavelength is fixed, the azimuth resolution can only be improved by increasing the antenna length. This is because the longer the antenna, the narrower the antenna beam width and the easier it is for the system to separate targets. However, the desired antenna lengths would be impractical (in the order of km).

A solution to that, which takes advantage of the movement in the azimuth direction to synthesise and artificially create a longer antenna, is SAR. The imaging Synthetic Aperture Radar technique delivers a much better resolution in azimuth  $r_a$  which only depends on the (physical) antenna length. Remarkably, it is no longer a function of the distance between the object and the antenna  $R$  and  $r_a$  is dramatically improved through the synthetic aperture, where a single antenna is moving along the flight line (in azimuth direction). That movement is equivalent to an array of antennas, or one very long antenna, if the received signals are coherently recorded and added. The targets on the ground are assumed to be static during that period.

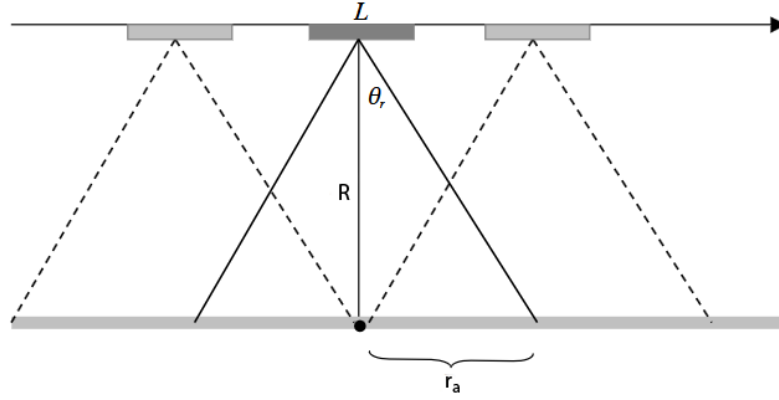


**Figure 2.5:** SAR azimuth resolution (adapted from [26]).

A derivation of the resolution formula can be done by considering that the diffraction resolution can be written as  $\sin \theta_r = \frac{\lambda_r}{L}$  where  $\lambda_r$  is the radar wavelength,  $\theta_r$  is the look angle and  $L_s$  is the synthetic aperture length. The azimuth resolution would then be a function of the nominal slant range  $R$ , the height of the platform  $H_r$ , the physical length of the real radar antenna  $L$  and  $\lambda_r$ :

$$r_a = R * BW_a = R * \sin \theta_r = \frac{R\lambda_r}{L_s} = \frac{\lambda_r H_r}{L \cos \theta_r} \quad (2.10)$$

The latter evolution of the equation was derived due to the fact that  $R$  can be expressed as  $\frac{H_r}{\cos \theta}$ .  $BW_a$  is the antenna beam width which is proportional to the aperture size [32]. The length of the synthetic aperture is a function of the wavelength  $\lambda_r$ , the length of the real antenna  $L$  and the slant range  $R$ :

$$L_s = \frac{2\lambda_r R}{L} \quad (2.11)$$

When forming a synthetic aperture that has a length of  $2r_a$ , the improved azimuth resolution now is:

$$r'_a = \frac{R\lambda_r}{\frac{2R\lambda_r}{L}} = \frac{L}{2} \quad (2.12)$$

That way, the azimuth resolution of such a system is (theoretically) independent of the distance to the target as well as of the wavelength of the sensor.

The resolution in slant range  $r_r$  of a SAR system depends only on the speed of light  $c$  and on the bandwidth  $B$ :

$$r_r = \frac{c\tau}{2} \simeq \frac{c}{2B} \quad (2.13)$$

with  $\tau$  as the pulse length.

## 2. SAR and PolSAR

Scatterers along the range are resolved using a match filter with a transmitted chirp function. The radar system emits continuous pulses of EM waves and, as described above, conventional SAR systems send out waves with linearly increasing frequency (called Linear Frequency-Modulated Waveform: LFM) to improve the (range) resolution of the radar. The frequency change in the LFM is called the bandwidth  $B$ . It corresponds to the difference between the upper and lower cut-off frequencies of the radar receiver and it is the reciprocal of the pulse length  $\tau$ :

$$B = \frac{1}{\tau} \quad (2.14)$$

$B$  is roughly proportional to the amount of information carried by the signal. Since noise exists in all frequencies, a broader bandwidth results in a higher noise level. This lowers the signal to noise ratio (SNR) of the sensor and with it its sensibility. The Doppler effect will affect frequencies and, therefore, the bandwidth itself.

The ground range resolution  $r_g$  varies throughout the image as a function of the incidence angle  $\theta$ . As it is true for  $r_a$ , this is independent of the distance between the object and the sensor:

$$r_g = \frac{c\tau}{2} \frac{1}{\sin \theta} \quad (2.15)$$

For nadir looking, the resolution in range is infinite and improves as the local incidence angle is increased.

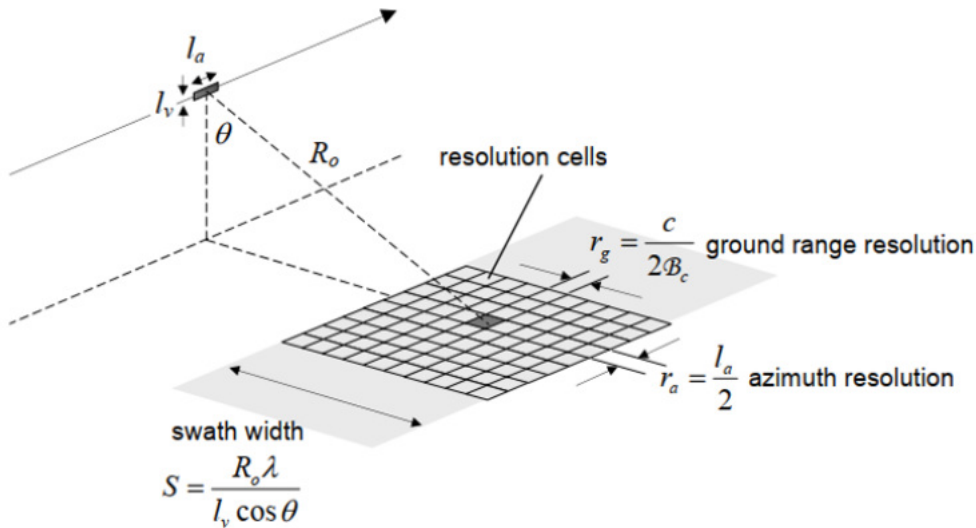


**Figure 2.6:** Schematic of a SAR image divided into resolution cells. From [33].

To sum up, the dimension of the SAR resolution cell is determined by the azimuth resolution and the range resolution — two values which are not the same. Therefore, a resolution cell is generally not squared (Fig. 2.6). A resolution cell is the minimum area that an object on the ground can be resolved or separated in [31]. The study of the aperture or antenna synthesis is beyond the scope of this document. For a detailed description please refer to e.g. [34, 35, 31, 24].

## 2.2.2 SAR Image Focussing

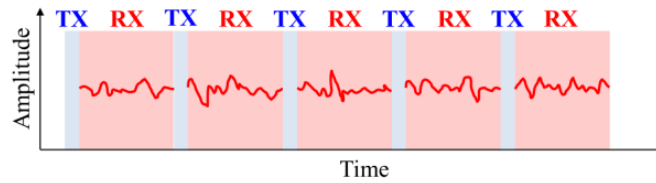


**Figure 2.7:** Sequence of transmission and reception of EM pulses [36].

The emitted pulses can be expressed in voltage as a function of time and can therefore be seen as a one-dimensional signal. Fig. 2.7 illustrates the alternating intervals of transmission ('TX') and reception ('RX').

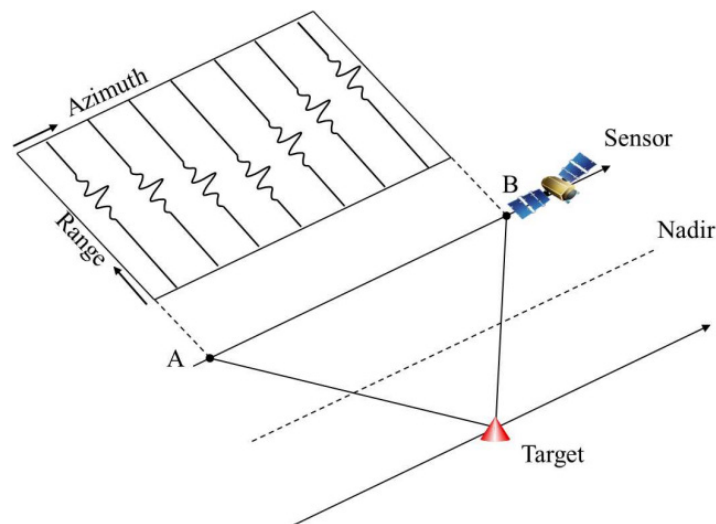


**Figure 2.8:** The time variation of the received signal [36].

SAR processing is a two-dimensional problem where several one-dimensional signals are acquired over time. Fig. 2.8 illustrates a simplified scenario with only one single, coherent scatterer present. Using the example of a point target, it will be illuminated for a period of time, the so-called maximum illumination time  $T_{az}$ :

$$T_{az} = \frac{L_s}{v} \quad (2.16)$$

which is defined by the extension of the antenna footprint in azimuth direction and the platform velocity  $v$  [35]. Therefore, the backscattered signal of a point target exists in different azimuth samples as the platform passes by each corresponding to different azimuth times and each with different range values, since the slant range coordinate  $r$  of any given object changes with the azimuth coordinate  $x$  [35]:

$$r = \sqrt{R^2 + x^2} \quad (2.17)$$

with  $R$  as the distance between the object and the sensor. If this difference exceeds the distance between two range samples, the contribution will migrate to the closest cell [36].

In SAR processing, the energy that disperses over several cells in both image directions, is focused into a single pixel in the final SAR image. Theoretically, SAR image processing could be done independently in range and azimuth direction, if range cell migration (RCM) can be neglected. For modern design SAR sensors with large synthetic apertures, the RCM correction is necessary. For the processing of the raw SAR data, stored as a series of complex numbers (I and Q), there exist a number of techniques, such as the range–Doppler algorithm or the Stolt interpolation (uses the wavefront reconstruction theory) [37]. The former is the most commonly used and accommodates range varying parameters such as the Doppler centroid, the azimuth frequency modulation rate and the RCM [38]. It is based on Doppler frequency shifts, preserves the phase and uses FFTs [35, 34, 39]. The result is a single look complex (SLC) SAR image and can be subdivided into the following main tasks (following [38]):

1. range compression
2. azimuth Fast Fourier Transformation (FFT)
3. RCM correction
4. azimuth compression
5. azimuth Inverse Fast Fourier Transformation (IFFT)

When designing SAR systems, it is often a trade–off between high resolution and broad swath. A higher azimuth resolution can only be acquired by using a large Doppler bandwidth  $B$ . A high pulse repetition frequency (PRF) leads to azimuth ambiguities and timing problems, since all return echoes should ideally be received before the next transmit pulse. Therefore, it narrows the swath and limits the maximum range that can be unambiguously detected and, with it, the coverage of the SAR system:

$$swath\ width = \frac{c}{2\ PRF\ \sin\theta} \quad (2.18)$$

A brief overview of that trade–off looks like the following:

- high azimuth resolution needs large  $B$
- large  $B$  needs high PRF
- a high PRF means a short pulse
- short pulse can carry less energy, reduces the range and narrows the swath
- less energy decreases the SNR

The solution to this conflict of objectives is a method called intra–pulse modulation (or modulation on pulse; MOP). It combines the energetic advantages of very long pulses with the advantages of very short pulses. As a result, a good range resolution can be combined with as much energy as possible to illuminate the scene. It is accomplished by linearly changing the frequency within the pulse as a function of time. The resulting pulse is called chirp [40]. This decouples the bandwidth from the pulse length and a long pulse (i.e. high energy, high signal–to–noise ratio) with a wide bandwidth (i.e. high range resolution) can be constructed.

Normally, the minimum distance of two distinguishable objects is half the pulse length. With a frequency modulated pulse, it is possible to fall below this minimum distance. That is achieved by cross–correlating the backscattered pulse with a reference signal, which is the complex conjugate of the emitted signal.

The range compression and the azimuth compression are done using a match filtering operation [40, 35, 41]. The matched filter adapts itself to the transmitted waveform, and its impulse response equals the complex conjugate of the time-inverted signal itself. To process the correct part of the frequency spectrum, the Doppler centroid of the transmitted pulse is required, which can be estimated by searching for the peak magnitude of the power spectrum. Furthermore, it requires information about the transmitted pulse for range compression and parameters that describe the image geometry for the construction of the matched filter [35]:

$$h(t) = \text{rect} \frac{t}{T} e^{-j\pi K t^2} \quad (2.19)$$

where  $K = \frac{B}{\tau}$  as the linear frequency modulated (FM) chirp rate,  $t$  as the range time and  $T$  is the pulse duration or chirp time. The essence of pulse compression usually involves going to the frequency domain and multiplying the received pulse with the complex conjugate of the transmitted pulse. That means that the filter is used as a correlation. This is equivalent to a convolution in the time domain [35].

### 2.2.3 The Radar Equation

The radar equation describes the interaction of an electromagnetic wave with a given scatterer. It establishes a relation between the power transmitted and that received after interaction with a scatterer.

$$P_r = \frac{P_t G_t}{4\pi R^2} \sigma \frac{A_r}{4\pi R^2} \quad (2.20)$$

where  $P_r$  is the power of the scattered wave which arrives at the sensor. The first term on the right side represents the incidence wave which is emitted by the sensor. It consists of the transmitted power  $P_t$ , the antenna gain in the direction of the target  $G_t$  and the distance between the SAR system and the object  $R$ . It describes a power density as power per unit area. The last term is dimensionless and describes the receiving sensor with the effective aperture of the antenna  $A_r$ . The central term  $\sigma$  in Equ. 2.20 embodies the effects the scattering object has on the balance of power in the radar equation. Its unit is defined by an effective area, characterizing the scatterer [42]. Scattering is a process that, in general, changes the emitted (incident) electric field  $\underline{E}_t$  when impinging on the objects on the surface. This will generally change the amplitude, the phase and the polarisation of the received (scattered) field  $\underline{E}_r$ .

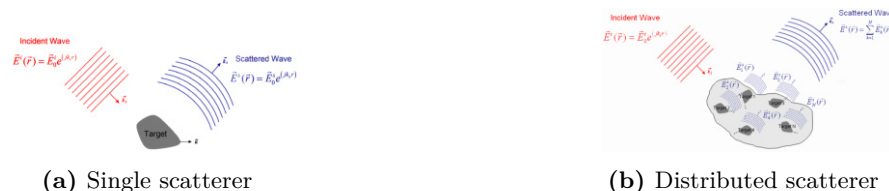


**Figure 2.9:** Target dichotomy.

There are two main typologies of scatterers (or targets) which is often referred to as target dichotomy (Fig. 2.9). When the object completely dominates the return in the SAR resolution cell without the presence of other scatterers of significant magnitude we call it a single or a point scatterer (Fig. 2.9a). The second category of objects are, for example, homogeneous areas without clear boundaries such as rough surfaces, vegetation, ice or snow [42]. They are

called distributed, partial or extended scatterers (Fig. 2.9b). An example for a single scatterer which is distributed would be the ocean surface.

Single scatterers can be characterised by the so-called radar cross section (RCS; denoted by  $\sigma$ ). To make it independent of the size of the resolution cell, the RCS is referenced to an idealised isotropic scatterer (a sphere). The RCS identifies the power coming from a metal sphere of a specific size. That is to say an  $RCS = 1$  will be generated by a metal sphere with a visible area of  $1 \text{ m}^2$ .

The characterisation of a given scatterer by means of  $\sigma$  also depends on the polarisation of the transmitted field  $\underline{E}_t$ . If we denote the polarisation of  $\underline{E}_t$  by  $y$  and the polarisation of  $\underline{E}_r$  by  $x$ , the polarisation dependent RCS of a point target can be written as:

$$\sigma_{xy} = 4\pi R^2 \frac{|\underline{E}_{xy}^r|^2}{|\underline{E}_{xy}^t|^2} = 4\pi |S_{xy}|^2 \quad (2.21)$$

where the Sinclair scattering matrix  $[S]$  represents the complex scattering amplitude of the object and  $4\pi R^2$  is a loss due to the fact that energy spreads in spherical waves. The RCS depends on object parameters (e.g. form, roughness, dielectric properties), as well as system parameters such as frequency, incidence angle and polarisation of the emitted radar wave [43].

The RCS in a single pixel describes the power efficiency of a scattering mechanism of a given object, but is not useful when it comes to distributed targets. Here, each resolution cell contains many scatterers and to estimate their characteristics we average the RCS over the surface or volume where the scatterers extend. In this mathematical approach, in each resolution cell a target is seen as an infinite collection of statistically identical point scatterers [36]. The average RCS per unit of resolution cell is called the differential scattering coefficient sigma nought, expressed as:

$$\sigma^0 = \frac{\langle \sigma \rangle}{A_0} \quad (2.22)$$

It is a dimensionless parameter and represents the statistically averaged (indicated by  $\langle \cdot \rangle$ ) scattered power density (or power return) integrated over, or normalised by, the area of the resolution cell  $A_0$ . The phase can be considered constant throughout  $A_0$ . As Equation 2.22 is valid for imaged surfaces, it can be extended to the case of imaged volumes by replacing  $A_0$  with a volumetric denominator.

$\sigma^0$  is also called normalised radar cross section (denoted by NRCS) and enables the comparison of different SAR systems with different resolutions by removing the area-dependency from the RCS measurement.  $\sigma^0$  represents the usual output of a SAR system [18]. Compared to  $\sigma$ , the range has less impact on  $\sigma^0$ . It is defined with respect to the nominally horizontal plane, and, in general, has significant variations depending on the incidence angle, the wavelength and the polarisation, as well as properties of the scattering surface itself.

There are two more types of radar backscatter conventions which are used to define how to normalise SAR data. When the reference area is in the slant range plane ( $A_\beta$  in Fig. 2.10), it is called radar brightness [44] or  $\beta^0$  and shows the reflectivity normalised to the unit area of the slant range resolution cell [42].



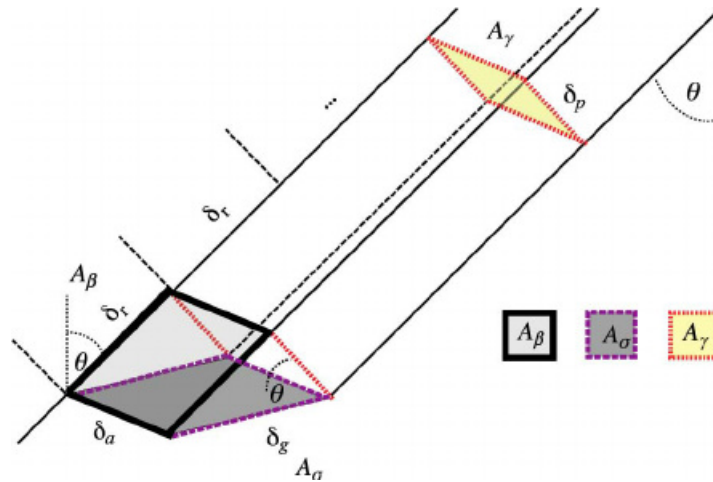


**Figure 2.10:** Normalisation areas for SAR backscatter [45].

It expresses the power ratio between the scattered wave and the emitted wave at ground level [45] and is defined as:

$$\beta^0 = \frac{\beta}{A_\beta} \quad (2.23)$$

and can be calculated using the image pixel values.  $\sigma^0$  represents a terrain-dependent modulation of  $\beta^0$  and can be precisely derived from knowledge about the incidence angle  $\theta$ . In that case, the reference area  $A_\sigma$  is chosen to be the ground area:

$$\sigma^0 = \beta^0 \sin \theta \quad (2.24)$$

The third variant gamma nought ( $\gamma^0$ , [46]) helps to reduce the dependence on the incidence angle for rough surfaces. It expresses the normalised reflectivity in relation to the unit area of the incidence wave front. The reference area  $A_\gamma$  is perpendicular to the local look direction (or the line of sight (LoS) of the sensor). It relates to  $\beta^0$  as:

$$\gamma^0 = \beta^0 \tan \theta \quad (2.25)$$

Whereas  $\beta^0$  is projected on the ellipsoid and suffers modulation caused by the local topography,  $\sigma^0$  and  $\gamma^0$  take into account the terrain information [45]. Therefore, brightness dependencies of the incidence angle are stronger in  $\beta^0$ , reduced in  $\sigma^0$  and further reduced in  $\gamma^0$  [47].  $\beta^0$  can be derived with the SAR product's digital number (DN). For  $\gamma^0$  and  $\sigma^0$ , a model of the earth such as a digital elevation model (DEM) is needed to determine the local incidence angle. They both are geocoded-terrain-corrected (GTC) products having the geometry of the backscatter estimate corrected. Meanwhile, the radiometry of the GTC remains ellipsoid-based [45].

Since  $\underline{E}_r$  contains not only the backscattering from the objects in the scene but also noise, one key factor to measure the quality of the radar image is its SNR. The SNR considers the effect of the thermal noise, which results from the fact that all objects at temperatures higher

than absolute zero emit radiation across the electromagnetic spectrum. The noise component that is within the receiver's bandwidth  $B$  is passed through together with the signal. The thermal noise power is given by:

$$\underline{E}_n = kTB \tag{2.26}$$

where  $k$  is Boltzmann's constant and  $T$  is the total equivalent noise temperature in kelvin. The SNR is then the proportion of the total received energy compared to the energy coming from noise:

$$SNR = \frac{\underline{E}_r}{\underline{E}_n} \tag{2.27}$$

The weakest return that can be detected by a given system must be above the noise level  $\sigma_n$  (which would give an SNR equal to 1). This is called the noise equivalent backscatter cross section [48]. Depending on its reference plane it is called noise equivalent sigma zero (NESZ<sup>4</sup>) or noise equivalent beta nought (NEBN<sup>5</sup>). For TerraSAR-X dual-pol Spotlight and Stripmap modes, the NEBN is roughly between  $-20\text{dB}$  and  $-22\text{dB}$ , depending on the range time [50]. For common land targets this value is rather low and the contribution of thermal noise can therefore often be neglected. On the other hand, on areas with very low reflectivity, such as calm water bodies, the noise floor can dominate the pixel and corrupt the measurement.

### 2.2.4 The Speckle Phenomenon

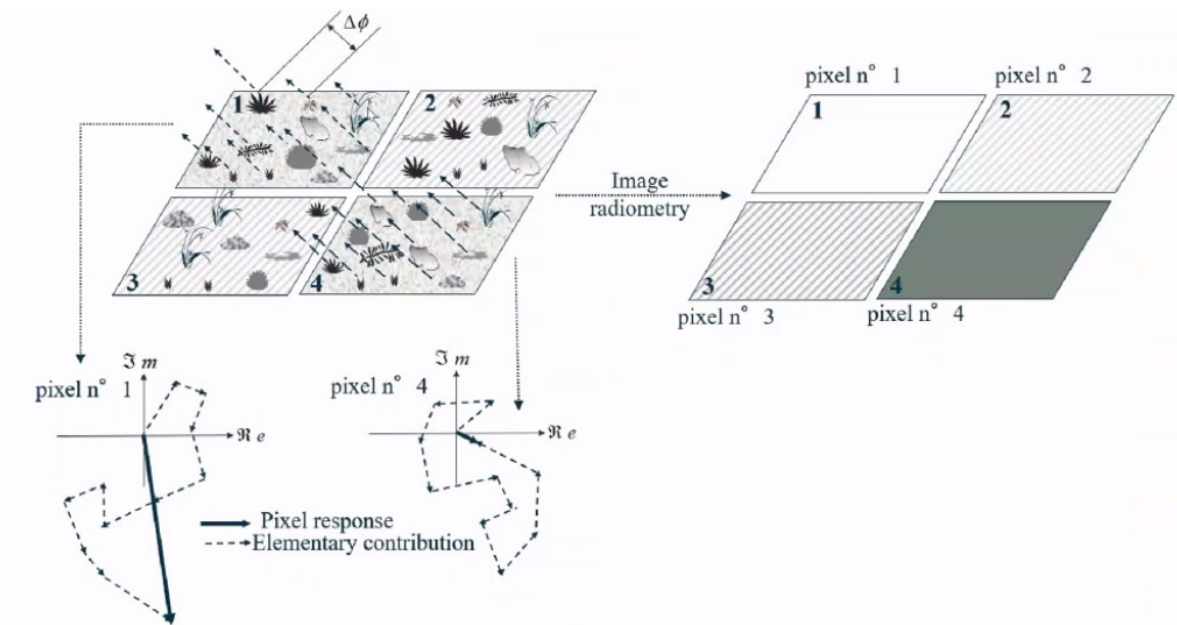


**Figure 2.11:** Origin of speckle [51].

<sup>4</sup>the value of sigma zero, when a resolution cell's response is equal to the system thermal noise floor, is known as the NESZ

<sup>5</sup>NEBZ is a system parameter that is better suited to describe the background noise of the SAR system than NESZ, because it does not depend on the local incidence angle [49]

Visual inspection of a SAR image reveals a brightness variation which looks like noise. This granular appearance is called speckle. Speckle is an inherent property of a SAR image. A SAR pixel is the result of the fact that Maxwell equations are linear and scatterers inside the same resolution cell are summed together in a coherent way [52]. The different contributions (or complex numbers) within one resolution cell are summed up to one single complex number representing the pixel.

These complex numbers interact in different ways. If there is no dominant scatterer, we call it fully developed speckle and the complex numbers for each scatterer will have comparable magnitudes [53]. If the pixel is dominated by constructive interference, the result is a bright pixel (n°1 in Figure 2.11). In the case of destructive interference, the pixel has low values and is therefore darker (pixel n°4 in Fig. 2.11). More specifically, for 'fully developed' speckle, the following assumptions are implied [54]:

- all the scatterers are independent
- the magnitude and the phase of a scatterer are independent
- all the magnitude values are identically distributed
- the phase values are uniformly distributed between  $-\pi$  and  $\pi$

This leads to the following statistical models (from [55]):

- the observed in-phase and quadrature components  $A \cos \phi$  and  $A \sin \phi$  are zero-mean, independent and show identical Gaussian distribution
- the amplitude  $A$  has a Rayleigh distribution
- the observed intensity or power  $I = A^2$  has an exponential distribution (this implies that the standard deviation is equal to its mean)
- the multi-looked intensity is a Gamma distribution

If the spatial resolution is very high, the Gaussian assumption may not be valid since the non-Gaussian speckle regime arises in very high-resolution landscape SAR images. The implementation of non-Gaussian models can deliver more realistic results [36, 56].

For areas in the SAR image with dominant scatterers (for example a corner reflector) the strong backscattering of that scatterer is much higher than that of the other scatterers and, therefore, the final sum of the complex numbers will be approximately equal to the complex number representing the dominant scatterer. Since speckle has a negative impact on many applications, it has to be dealt with and the most common technique is filtering, which is spatial averaging to mitigate the noise-like effects. In radar jargon, this is often referred to as multilooking. There are several ways to produce multilook images. Typically, in a first step, a number of single look complex SAR data are chosen and the intensity is computed (i.e. the phase information is lost). The final step is to incoherently average the intensity values as [57]:

$$I = \sum_{p=1}^N \frac{I_p}{N} \quad (2.28)$$

where  $N$  is the nominal number of looks which can, in this case, be replaced by the equivalent (or effective) number of looks (ENL). The latter describes the number of pixels used to average together SAR measurements and quantifies the amount of independent samples used for averaging. The signal standard deviation  $S_N$  is related to the mean signal power  $\bar{P}$  by:

$$S_N = \frac{1 \bar{P}}{\sqrt{N}} \quad (2.29)$$

The advantage is that the variance of the image intensity  $I$  is reduced which facilitates easier interpretation [58]:

$$\text{Var}\{I\} = \frac{\sigma^2}{N} \quad (2.30)$$

Increasing  $N$  leads to a better radiometric quality, but decreases the spatial resolution of the image by the same factor  $N$ . In the case of an application searching for very small objects, it is advisable to avoid using multilooking too much, to preserve the spatial resolution or to apply averaging in combination with an edge-preserving filter. In case the ENL is unknown, Equ. 2.30 can be used to calculate it.

Additive noise adds itself to  $I$  without being dependent on it. In the case of multiplicative noise, the random term does show a statistical dependency on  $I$ :

$$I = \sigma^2 n \quad (2.31)$$

with  $n$  as a random process with a mean and a variance equal to 1, called speckle noise. If the mean value of  $I$  increases, the variance increases as well. Therefore, this model is known as the multiplicative speckle noise model [42].

Speckle is multiplicative noise and, with speckle filtering, we try to assess the scene reflectivity from  $I$  by reducing the variance of  $I$ . At the same time, the filter tries to leave the radiometry unbiased. This can be done through frequency (or spectral) filtering during SAR processing of certain bands or by applying spatial filtering using moving window kernels. The availability of more than one acquisition enables multi-channel filtering which can be polarisation-based, time-based or frequency-based. Polarimetric speckle filter (e.g. [59]) takes into account all the polarimetric information and it can preserve the polarimetric properties of the image.

A classic example of a filter is the boxcar (or multilook) filter. It performs spatial averaging over a defined time or area using the boxcar function implemented as a rectangular moving window and using convolution. Convolution is an operation between two signals to produce a third signal that represents how one signal (the boxcar 2D kernel) modifies the other signal (the SAR image). It is essentially a low-pass filter, smoothing out noise and short-term fluctuations in data by replacing each pixel value with the average of its neighbouring pixels. The boxcar filter is a Finite Impulse Response (FIR) filter and takes the length of the window as an input parameter [60]. Its impulse response has the disadvantage of blurring the image and of smearing the edges [59, 61]. Finding the right size for the area where the averaging takes place is always a compromise between radiometric and spatial resolution. As a rule of thumb, approximately 50 ENL, which could correspond to an area of 7x7 pixel, is a good starting point for many cases.

The filtering can be improved by applying adaptive techniques. For homogeneous areas, large windows should be applied since it reduces the statistical variation. In heterogeneous areas, speckle filtering should be applied very carefully, since it decreases the spatial resolution and details, such as edges, are smeared. Examples of such filters are Lee's local statistics filter [62]

and the refined Lee filter [63].

Speckle filtering is still an open research topic. The main issues when applying speckle filters are edge sharpness and line and point target contrast preservation and the retention of texture information, polarimetric information and mean values in homogeneous areas.

### 2.2.5 Radar Image Artefacts

Radar images can contain a number of artefacts which are a result of the acquisition geometry and the image formation process. Some of them are similar to what can be seen in optical systems as well, such as blurring due to defocussing or smearing effects due to moving objects in the scene. Other artefacts are very unique to radar systems. Radar was first designed to measure distances and therefore the objects in the imaging radar scene are still arranged depending on their respective distance to the sensor. This is the reason why SAR sensors are side-looking, in contrast to optical systems which are most often oriented close to a nadir view. A radar in nadir looking (e.g. altimeters) has very poor horizontal resolution.

**Ambiguous returns of SAR:** these artefacts are connected to the radar system's parameters. In the case of range ambiguities, these do not occur in current satellite systems but they may occur if the timing of the emitted pulses is not correctly calculated and the end of the previous received signal overlaps with the beginning of the next one. Range ambiguities can be fixed by selecting an appropriate value for the PRF such that the echo coming back to the sensor is completely within an inter-pulse period. Azimuth ambiguities are produced by the fact the chirp is a repeated pulse with an envelope (a *rect*) and therefore the spectrum will have replicas (or ghosts) outside the bandwidth that will overlap in the visible bandwidth. Since they are not centred like the rest of the Doppler they will appear in other places and therefore they will suffer a shift in azimuth. Azimuth ambiguities can be mitigated with the right PRF where lower PRF will push the ambiguity further away and therefore reduce its intensity [19]:

$$PRF \geq 2\left(\frac{B}{2}\right) = \frac{2v}{L} \quad (2.32)$$

with  $B$  as the bandwidth. At least one sample pulse should be emitted every time the sensor moves by half the length of the real antenna  $L$ :

$$B = \frac{2v}{L} \quad (2.33)$$

where  $v$  is the platform's speed.

**Side lobes:** another type of artefact depends on the focusing. After pulse compression, the point targets will be represented by the impulse response, also called spreading function of the SAR system. They are visible as side lobes and can be reduced by suitable weighting of the signal spectra during matched filter compression [27]. This artefact is mainly visible when a very bright object is surrounded by a dark area, for example a very calm water surface around a metal-made ship. However, it is present for each resolution cell and increases the correlation between neighbour pixels.

**Moving objects:** movement of objects is the reason for the train-off-the-track effect. It is a phenomenon whereby moving objects appear shifted from their actual location in the

SAR imagery, depending on their speed and the direction of their movement relative to the LoS. Movement in azimuth (along-track) causes a blurring in azimuth direction whereas an object moving in range (cross-track) direction is displaced in azimuth and also blurred. This is because the velocity vector changes the Doppler centroid of the point, which is therefore displaced [64, 65, 66].

Geometrical Distortions: There are a number of topographic and geometric effects such as foreshortening, radar shadow or layover. Fig. 2.12 illustrates examples of these phenomena.

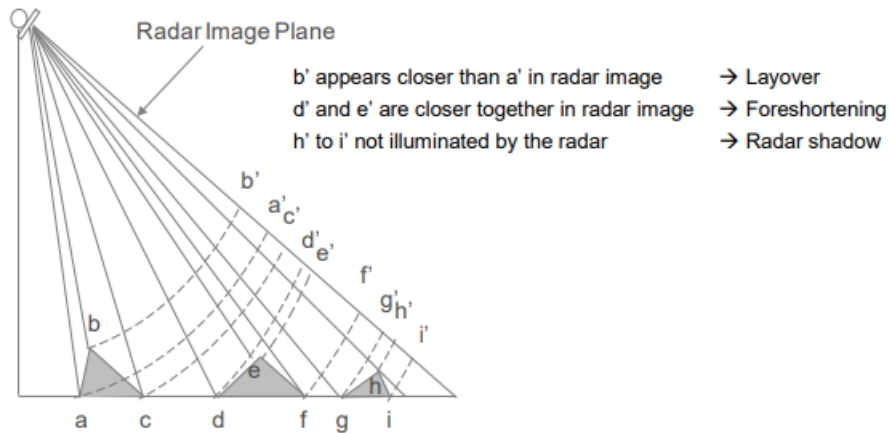


Figure 2.12: SAR geometric distortions (from [19]).

In the maritime domain, the location of the scene is generally flat (beside some coastal regions), therefore geometrical distortions do not generally affect maritime detection.

## 2.3 SAR Polarimetry

polarisation is, by definition, the geometrical orientation of the oscillations of plane <sup>6</sup>, transverse <sup>7</sup> and electromagnetic waves. Wave polarimetry deals with the representation and the understanding of the polarisation state of an electromagnetic wave [42]. The first part of this section focuses on the polarisation of the plane wave propagating in space.

### 2.3.1 Wave Polarimetry

The first comprehensive combination of formulae to mathematically describe how the electromagnetic wave propagates was put together by James Clerk Maxwell in 1864 [67]. With his so-called Maxwell equations (see [68]) he linked the work of Faraday, Ampere and Gauss. Later, Helmholtz used them to derive his propagation equation of a field in the time/space domain. These equations are capable of describing the generation and propagation of electric and magnetic waves and their interaction with matter. With his set of equations, Maxwell described electromagnetism mathematically. It basically states that accelerating charges produce EM waves and the transmitted energy has its source in that moving charge [67]. Electromagnetic waves like microwaves consist of two components: the electric field

<sup>6</sup>plane wave: it has constant phase over any plane that is perpendicular to the direction of propagation

<sup>7</sup>transverse wave: the oscillations of the wave are perpendicular to the direction of propagation

$\underline{E}$  and the magnetic field  $\underline{H}$ . These two are time-varying fields which induce each other. The direction of polarisation is taken to be that of the electric field vector because the most common manifestations of EM radiation is mainly due to the electric field [24].

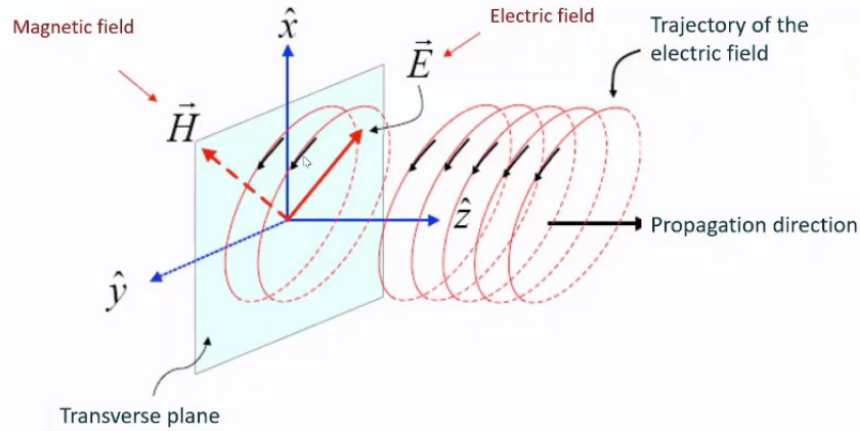


**Figure 2.13:** Coordinate system convention with  $z$  as the propagation direction [69].

Waves radiated by an EM source, such as an antenna, have spherical wavefronts. To a distant observer, however, the wavefront across the observer's aperture appears approximately planar [43]. In plane waves, the two fields are arranged orthogonally in space as two sinusoidal waves, propagating in  $z$  direction (Fig. 2.13). In the most general case ( $z = 0$ ), the electric field phasor  $\underline{E}_z$  of a  $+z$ -propagating plane wave consists of an  $x$ -component  $E_x(z)$  and a  $y$ -component  $E_y(z)$ . They interact and the relative phase difference between the two fields amplitudes  $|E_x|$  (also called  $E_{x0}$ ) and  $|E_y|$  (also called  $E_{y0}$ ) defines the polarisation state (e.g. [43, 42]). These two complex amplitudes each have magnitudes and phases so we need four real numbers to describe the polarisation vector in the  $x$ - $y$  plane. They can be explicitly written as:  $E_x = E_{x0}e^{i\phi_x}$  and  $E_y = E_{y0}e^{i\phi_y}$ . A widely used parameter to represent the polarisation state is the normalised complex polarisation vector  $\underline{p}$  [70]:

$$\underline{p} = \frac{\underline{E}}{|\underline{E}|} \quad (2.34)$$

As long as the polarisation is stationary, this ratio is sufficient to describe the direction of the electric field on a plane (the transverse plane in Fig.2.13) perpendicular to the direction of propagation  $z$ .  $\underline{p}$  is a vector, consisting of two real parameters, which can entirely describe the polarisation of the electromagnetic wave.

The term polarimetry refers to this vector nature of the electromagnetic wave. If there is no phase difference between  $E_x$  and  $E_y$  (when they are 'in phase', with a phase difference  $\delta = 0$ ) or they are 'out of phase' ( $\delta = \pi$ ), we call it a linear polarised wave because when looking in the direction of propagation, the wave draws a line on the transverse reference plane. The majority of the state-of-the-art space-borne SAR makes use of linear polarised waves, which can be classified into horizontally polarised (H) and vertically polarised (V). Each polarisation refers to the orientation of the electric field relative to the reference plane which, in our case, is the (horizontal) earth surface.

The use of  $E_x$  and  $E_y$  assumes that the wave propagates in the  $z$  direction following the EM-wave coordinate system as defined in Fig. 2.13. The choice of parameters depends on the

selected coordinate system. Introducing a more generalised expression, we can use the generic orthogonal unitary vectors  $\underline{u}_x$  and  $\underline{u}_y$  on the plane transverse to the propagation. Then, the electric field can be noted as [69]:

$$\underline{E} = \underline{u}_x E_x + \underline{u}_y E_y = |E_x| e^{j\phi_x} \left( \underline{u}_x + \underline{u}_y \frac{|E_y|}{|E_x|} e^{j(\phi_y - \phi_x)} \right) \quad (2.35)$$

using the amplitudes of the electric field components as scalars ( $|E_x|, |E_y|$ ) and their phases ( $\phi_x, \phi_y$ ).

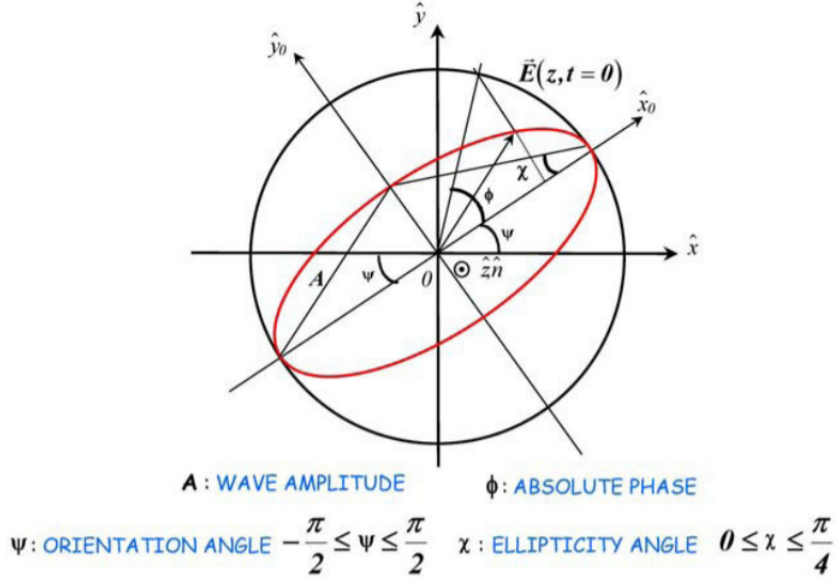


Figure 2.14: The polarisation ellipse [71].

The circular polarised wave can be expressed as two linearly polarised perpendicular waves, with a phase shift of  $90^\circ$  (or a quarter wavelength,  $\frac{\pi}{2}$ ) of equal amplitudes ( $E_{x0}$  equals  $E_{y0}$ ). In this case, the projection on the reference plane becomes a circle shape. According to the direction of the rotation of the circular polarised wave it is called right-handed circular polarisation or left-handed circular polarisation [72]. When  $E_{x0}$  and  $E_{y0}$  are different and the relative phase is nonzero, the polarisation changes in magnitude as it rotates in the reference plane. It thereby describes an ellipse, and this is called elliptical polarisation. In other words: plane waves that are not linearly or circularly polarised are elliptically polarised.

This polarisation ellipse (Fig. 2.14) can be described using a set of geometric ellipse parameters: the polarisation ellipse amplitude  $A$ , the absolute phase  $\phi$ , the orientation angle  $\Psi$  and the ellipticity angle  $\chi$ .  $\Psi$  varies between minus  $90^\circ$  and plus  $90^\circ$  and describes the orientation of the main axes of the ellipse with respect to the  $\hat{x}$  axis. It is defined as:

$$\Psi = \tan^{-1} \left( \frac{|E_y|}{|E_x|} \right) \quad (2.36)$$

When  $E_{x0}$  equals  $E_{y0}$   $\Psi$  can be either plus or minus  $45^\circ$ .  $\chi$  provides us with information about the polarisation handedness: waves with a  $\chi > 0$  rotate anti-clockwise (LHCP), clockwise rotating (RHCP) waves have  $\chi < 0$  [71, 73, 74]. It is defined as:



$$\chi = \tan^{-1}\left(\frac{b}{a}\right) \quad (2.37)$$

with  $a$  and  $b$  as the main axes of the ellipse. Furthermore,  $\chi$  describes the degree of ellipticity, i.e. the shape of the ellipse.

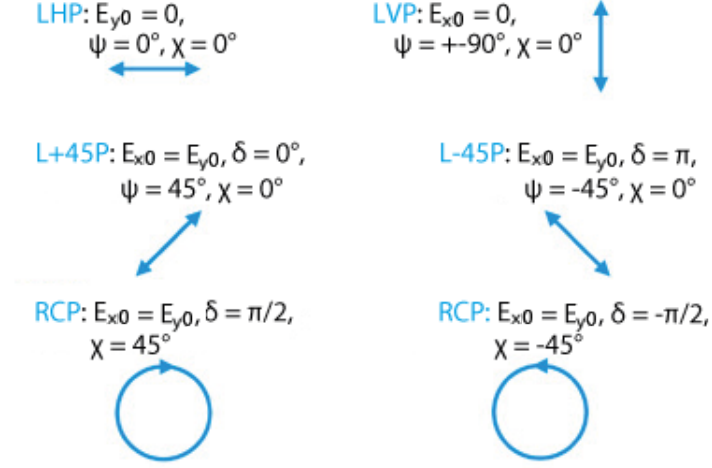


**Figure 2.15:** Examples for different polarisation states: linearly horizontal/vertical polarised waves (LHP/LVP), linear  $\pm 45^\circ$  polarised waves (L+45P/L-45P) and right/left circularly polarised waves (RCP/LCP). (adapted from [43, 75]).

For elliptically polarised waves exist several combinations of amplitude and phase (phase difference  $\delta = \delta_x - \delta_y$ ) that are especially important (Fig. 2.15). This convention to define the rotation direction in the SAR community is arranged exactly opposite to how it is done in optics.  $\chi$  represents the ellipse aperture.  $A$  can be calculated using the major and minor ellipse axis amplitudes or from the amplitudes of the wave in each coordinate [42]:

$$A = \sqrt{E_{x0}^2 + E_{y0}^2} \quad (2.38)$$

Moreover, additional equivalent descriptors such as the Jones vector also exist. To simplify Maxwell's equation, we can switch to the complex domain by using this Jones vector. By definition, a Jones vector is the representation of a plane monochromatic electric field and describes the wave polarisation using the minimum amount of information [76]. It is used for coherent systems and is therefore determined by two complex quantities. These two components are able to describe the two sinusoidal components of the wave: one electric field oscillating in H direction and the second perpendicular one, oscillating in V direction. The Jones vector  $\underline{E}$  shows the information in the direction of propagation as it describes a 2D-plane. Removing the space dependency from  $\underline{E}_z$  by setting  $z$  to 0 results in:

$$\underline{E} = \underline{E}(0) = \begin{bmatrix} E_{x0}e^{j\delta_x} \\ E_{y0}e^{j\delta_y} \end{bmatrix} \quad (2.39)$$

and this denotation is independent of space and time. Here,  $E_x$  and  $E_y$  represent the horizontal and vertical shares of the EM field. Each contains the magnitude ( $E_{x0}$ ) and the phase ( $e^{j\delta_x}$ ).

The components of the Jones vector enables us to reconstruct all the geometrical parameters of the polarisation ellipse. It further enables us to perform transformations between the different polarisation bases. On the contrary, handedness information cannot be included within the Jones vector as the propagation indices has been removed [42, 77].

The wave transmitted by an incoherent source (e.g. not a radar or a laser) will, in general, change its polarisation over time. Also, the medium can change the polarisation of a coherent wave. In this case we talk about a partially polarised plane wave and the state of such a wave can be noted using a 2x2 complex Hermitian positive semi-definite wave covariance matrix  $[J]$ , also called the Jones coherency matrix [77]:

$$\langle [J] \rangle = \langle \underline{E} \cdot \underline{E}^{*T} \rangle = \begin{bmatrix} \langle E_x E_x^* \rangle & \langle E_x E_y^* \rangle \\ \langle E_y E_x^* \rangle & \langle E_y E_y^* \rangle \end{bmatrix} = \begin{bmatrix} \langle J_{xx} \rangle & \langle J_{xy} \rangle \\ \langle J_{xy}^* \rangle & \langle J_{yy} \rangle \end{bmatrix} \quad (2.40)$$

where the superscript  $*T$  indicates the complex conjugate transpose of the matrix and the superscript  $*$  denotes complex conjugation [27]. Between the two extremes of  $\langle J_{xy} \rangle = 0$  (no correlation between  $E_x$  and  $E_y$ , the wave is called unpolarised or completely depolarised) and  $\det([J]) = 0$  (the correlation between  $E_x$  and  $E_y$  is at its maximum, the wave is completely polarised) lies the general case of partial polarisation. This can be expressed by the degree of polarisation [78].

Another representation considers the stokes vector which was used to express the measurement of incoherent systems, which were only able to measure the power of an incoming wave. Stokes derived this matrix when working on the polarisation of visible light and expressed this matrix using the Pauli matrices group:

$$\sigma_0 = \begin{bmatrix} 1 & 0 \\ 0 & 1 \end{bmatrix} \sigma_1 = \begin{bmatrix} 1 & 0 \\ 0 & -1 \end{bmatrix} \sigma_2 = \begin{bmatrix} 0 & 1 \\ 1 & 0 \end{bmatrix} \sigma_3 = \begin{bmatrix} 0 & -j \\ j & 0 \end{bmatrix} \quad (2.41)$$

resulting in the development of the four Stokes parameters  $\{g_0, g_1, g_2, g_3\}$ , introduced in 1852 [79]:

$$\underline{E} \cdot \underline{E}^{*T} = \frac{1}{2} \{g_0 \sigma_0 + g_1 \sigma_1 + g_2 \sigma_2 + g_3 \sigma_3\} = \frac{1}{2} \begin{bmatrix} g_0 + g_1 & g_2 - jg_3 \\ g_2 + jg_3 & g_0 - g_1 \end{bmatrix} \quad (2.42)$$

From a mathematical point of view, they are real and independent of the absolute phase (hence allowing for averaging). For a monochromatic wave, in the rectangular coordinate system the Stokes vector  $\underline{g}_E$  can be developed from the corresponding Jones vector  $\underline{E}$ :

$$\underline{g}_E = \begin{bmatrix} g_0 \\ g_1 \\ g_2 \\ g_3 \end{bmatrix} = \begin{bmatrix} |E_x|^2 + |E_y|^2 \\ |E_x|^2 - |E_y|^2 \\ 2\Re\{E_x E_y^*\} \\ -2\Im\{E_x E_y^*\} \end{bmatrix} \quad (2.43)$$

This Stokes vector is the real representation of the output of the antenna, containing only four real parameters. Each of the four components are connected to a physical interpretation:

- $g_0$ : total power (polarised and unpolarised) of the wave
- $g_1$ : power of the linear polarisation component
- $g_2$ : power of the linear polarisation in the direction of  $45^\circ$  to the reference plane
- $g_3$ : power of circular polarisation

Further, the degree of polarisation (DoP) can be calculated using all four Stokes parameters. Natural sunlight is an example of completely unpolarised light and so it could be represented by  $\underline{g}_E = [g_E, 0, 0, 0]^T$ . In general, however, waves are partially polarised and so it consists of polarised and unpolarised components,  $\underline{g}_E = \underline{g}_{E,pol} + \underline{g}_{E,unpol}$ . The *DoP*, or fraction polarised, is defined as  $\underline{g}_{E,pol}/g_E$  [80]:

$$DoP = \frac{\sqrt{\langle g_1 \rangle^2 + \langle g_2 \rangle^2 + \langle g_3 \rangle^2}}{\langle g_0 \rangle} = \left( 1 - 4 \frac{|J|}{Tr(J)} \right)^{\frac{1}{2}} \quad (2.44)$$

and  $\langle g_0 \rangle^2 \geq \langle g_1 \rangle^2 + \langle g_2 \rangle^2 + \langle g_3 \rangle^2$  is valid. The polarisation ellipse of partially depolarised waves varies over time and the amplitude and phase are random processes in time or in space. The Stokes parameters  $\{g_1, g_2, g_3\}$  can be used as coordinates with the radius  $g_0$  to locate any polarisation on (or inside) a sphere called the Poincaré sphere [81].

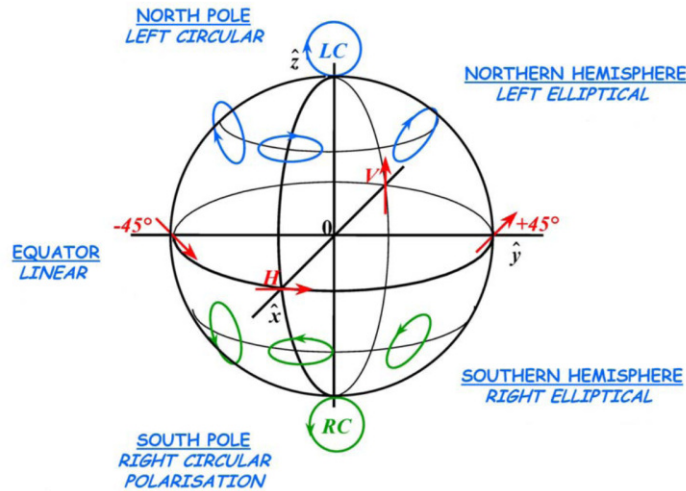


**Figure 2.16:** Poincaré Sphere [71].

This Poincaré sphere was introduced to visualise the polarisation state and its behaviour over time and is a result of a unique transformation from the 2D–complex space of the wave to a 3D–real coordinate space [82]. Each point on the sphere corresponds to a specific polarisation (Fig. 2.16). Any totally polarised wave sits on the surface of the sphere, whereas a wave’s partial polarisation states could be averaged and mapped inside the sphere. Orthogonal polarisation states relate in an antipodal way on this sphere. The orthogonal polarisation of any wave can be calculated by forming the orthogonal Stokes vector and adding a negative sign to the three polarised Stokes vectors  $g_1, g_2, g_3$ . Hence, the orthogonality of the polarisation plots in an antipodal way on the sphere.

## 2.3.2 Scattering Polarimetry

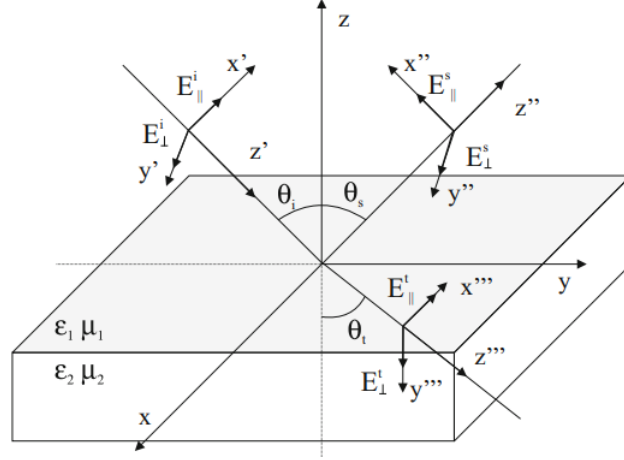


**Figure 2.17:** Scattering on a flat transition between two dielectric, infinite, lossless and homogeneous media in oblique incidence [42].

Scattering polarimetry focuses on the scattering processes taking place due to the scatterer of interest and how they are represented in the received EM wave. The way the wave is scattered depends on the properties of the incidence wave and on the scatterer itself [42]. The received wave can then be used to derive information about the scatterers on the ground. This is done by comparing specific properties of the incidence wave and the backscattered wave, such as the polarisation state. When the antenna transmits and receives linear polarised microwaves, an H polarisation impinging on a target can produce both H and V backscattered polarisation and vice-versa. The incident wave  $\underline{E}^i$  can be decomposed into these two perpendicular components ( $\underline{E}_{||}^i$  and  $\underline{E}_{\perp}^i$  in Fig. 2.17). In this scattering example in Fig. 2.17 one part of the incidence wave is scattered in the same media whereas another part of the energy is transmitted to the second media. It is possible to relate the scattered wave  $\underline{E}^s$  to that of the incident wave by using two Jones vectors:

$$\underline{E}^i = \begin{bmatrix} E_H^i \\ E_V^i \end{bmatrix}, \quad \underline{E}^s = \begin{bmatrix} E_H^s \\ E_V^s \end{bmatrix} \quad (2.45)$$

This relation can be established by means of a 2x2 complex matrix  $[S]$ :

$$\underline{E}^s = \frac{e^{-jk_0 R}}{R} [S] \underline{E}^i \quad (2.46)$$

where  $R$  is the distance between the scatterer and the sensor and  $k_0$  is the wavenumber of the illuminating wave. This wavenumber, also known as the spatial frequency of a wave, is measured in cycles per unit distance (ordinary wavenumber) or in radians per unit distance (angular wavenumber). The angular wavenumber is linked to the angular frequency  $\omega$  via the phase velocity  $v_p$  which equals the speed of light in a vacuum ( $k_0 = \frac{\omega}{v_p}$ ) and is linked to the wavelength by  $k_0 = \frac{2\pi}{\lambda}$  [43]. It is measured by cycles (or radians) per unit distance. The phase factor  $e^{-jk_0 r}$  is dependent on the delay of the wave when travelling from the scatterer to the sensor.

This 2x2 complex matrix represents the basic measurement made by a full-pol SAR system and is called the Sinclair scattering matrix. In the horizontal and vertical polarisation basis (H, V) it can be noted as:

$$[S] = \begin{bmatrix} S_{HH} & S_{HV} \\ S_{VH} & S_{VV} \end{bmatrix} \quad (2.47)$$

where the matrix elements are the complex scattering coefficients (or: complex scattering amplitudes). The  $[S]$ -matrix coefficients depend on the radar frequency, the waveform and the polarisation state of the transmitted wave. Furthermore, it is influenced by a number of characteristics of the scatterers on the ground such as their structure, the conductivity of the objects, their orientation relative to the LoS (pattern angle, roll angle), its environment (clutter, jamming) etc.  $[S]$  therefore offers a complete description of the objects on the ground, while remaining, however, very complex to analyse [83].

For each pixel of the SAR image, there is one  $[S]$ -matrix, holding four phase and four amplitude values. From that we can derive three independent amplitude values (from the polarisation channels HH, VV and HV), following the assumption backed by the reciprocity theorem, which is true for monostatic systems and reciprocal medium, that  $S_{HV}$  and  $S_{VH}$  are equal except for noise. Since the absolute phase term of a single image is a function of the distance between the sensor and the object, it is not considered as a target parameter. But, we can yield two more independent values from the phase differences between the three independent polarisation channels. This step leads us to the relative backscattering matrix, which is derived from the absolute backscattering matrix by separating the absolute phase factor and replacing it with the relative phase terms  $e^{j(\phi_{VH}-\phi_{HH})}$  for the cross-pol channels and  $e^{j(\phi_{VV}-\phi_{HH})}$  for the VV-polarisation. These five independent parameters can now be used to characterise a single, deterministic target by its polarimetric information. Since the  $[S]$ -matrix contains absolute phase values, statistical averaging is not valid.

To make it easier to mathematically handle the information stored in the  $[S]$ -matrix, we can vectorize the matrix by using the trace of its product with a matrix basis  $tr^8$ :

$$\underline{k} = V(S) = \frac{1}{2}tr(S\Omega) \quad (2.48)$$

where  $\Omega$  is a set of 2x2 complex basis matrices, constructed as an orthonormal set under a Hermitian inner product [42]. The interpretation of  $\underline{k}$  depends on the chosen basis  $\Omega$ . The two most commonly used are the Pauli basis and the lexicographic basis. In both cases, the total power of both vectors equals the span of  $[S]$ . The result in the first case is the so-called Pauli scattering vector:

$$\underline{k}_p = \frac{1}{\sqrt{2}} \left[ S_{HH} + S_{VV} \quad S_{HH} - S_{VV} \quad S_{HV} + S_{VH} \quad j(S_{HV} - S_{VH}) \right]^T \quad (2.49)$$

The last component  $j(S_{HV} - S_{VH})$  can provide information about the noise level of the SAR image. Considering reciprocity and the Backscatter Alignment (BSA) convention, we can assume that  $S_{HV}$  equals  $S_{VH}$  and reduce the Pauli basis to:

<sup>8</sup>the trace of a matrix is defined as the sum of the elements of the main diagonal, from upper left to lower right, so to speak

$$\underline{k}_p = \frac{1}{\sqrt{2}} \begin{bmatrix} S_{HH} + S_{VV} & S_{HH} - S_{VV} & S_{HV} + S_{VH} \end{bmatrix}^T \quad (2.50)$$

It has the advantage of having a very close relation to the physical properties of the scatterers.  $S_{HH} + S_{VV}$  ('Pauli1') corresponds to the scattering matrix of an isotropic surface, a sphere, a plate or a trihedral and is generally referred to as single bounce, or odd-bounce scattering.  $S_{HH} - S_{VV}$  ('Pauli2') represents double bounce or even bounce scattering and  $S_{HV} + S_{VH}$  ('Pauli3') is generally connected to 45° tilted bounce and/or volume scattering.

The target vector in the Pauli basis is constructed with the help of Pauli spin matrices which are commonly used in quantum mechanics:

$$\underline{\Omega}_p = \left\{ \sqrt{2} \begin{bmatrix} 1 & 0 \\ 0 & 1 \end{bmatrix}, \sqrt{2} \begin{bmatrix} 1 & 0 \\ 0 & -1 \end{bmatrix}, \sqrt{2} \begin{bmatrix} 0 & 1 \\ 1 & 0 \end{bmatrix}, \sqrt{2} \begin{bmatrix} 0 & -j \\ j & 0 \end{bmatrix} \right\} \quad (2.51)$$

In general, the Pauli basis vector supports the physical interpretation of the scatterers on the ground. An arbitrary 2x2  $[S]$ -matrix may be written in the Pauli basis as:

$$S = \begin{bmatrix} a+b & c-jd \\ c+jd & a-b \end{bmatrix} = a \begin{bmatrix} 1 & 0 \\ 0 & 1 \end{bmatrix} + b \begin{bmatrix} 1 & 0 \\ 0 & -1 \end{bmatrix} + c \begin{bmatrix} 0 & 1 \\ 1 & 0 \end{bmatrix} + d \begin{bmatrix} 0 & -j \\ j & 0 \end{bmatrix} \quad (2.52)$$

with  $a, b, c, d$  being complex elements. Following the decomposition of  $[S]$  in Fig. 2.52 it is possible to identify the four elements of the Pauli basis with the scattering matrices of some of the canonical scatterers presented in Fig. 2.20 below. Therefore, the elements of the target vector  $k$  represent the contribution of the canonical scattering mechanisms and the following interpretation is possible [42]:

- $a$ : single scattering from a sphere or a plane surface
- $b$ : dihedral scattering
- $c$ : dihedral scattering with a relative orientation of  $\pi/4$  rad ( $=45^\circ$ ) relative to the LoS
- $d$ : non-symmetric, helix-type scattering mechanisms, transforming the scattered wave into its orthogonal circular polarisation state

What is described in Fig. 2.52 is the decomposition of the scattering response from an object, i.e. a *target decomposition*. The scattering components of the Pauli basis are orthogonal, which means that they can be separated without ambiguities.

The lexicographic scattering vector straightforwardly lists the four components of the scattering matrix:

$$\underline{\Omega}_l = \left\{ 2 \begin{bmatrix} 1 & 0 \\ 0 & 0 \end{bmatrix}, 2 \begin{bmatrix} 0 & 1 \\ 0 & 0 \end{bmatrix}, 2 \begin{bmatrix} 0 & 0 \\ 1 & 0 \end{bmatrix}, 2 \begin{bmatrix} 0 & 0 \\ 0 & 1 \end{bmatrix} \right\} \quad (2.53)$$

In the most general case explicitly expressed, the scattering vector in the lexicographic basis is noted as:

$$\underline{k}_l = \begin{bmatrix} S_{HH} & S_{HV} & S_{VH} & S_{VV} \end{bmatrix}^T \quad (2.54)$$

with the advantage of the direct relation to the system measurements. The multiplicative factors are necessary to maintain the total scattered power constant, defined as:

$$SPAN(S) = tr(SS^{*T}) = |S_{HH}|^2 + |S_{HV}|^2 + |S_{VH}|^2 + |S_{VV}|^2 \quad (2.55)$$

It is therefore more valuable for system engineers to use it for calibration and radar hardware development tasks. Moreover, the elements are related to special targets: horizontal dipoles, 45° oriented dihedral and vertical dipoles [17].

In the monostatic case and under BSA convention, it can be reduced to:

$$\underline{k}_l = \begin{bmatrix} S_{HH} & \sqrt{2}S_{HV} & S_{VV} \end{bmatrix}^T \quad (2.56)$$

It is possible to mathematically switch between these two vectors, using a unitary transformation that preserves the norm (magnitude) of the vector.

Every SAR image involves multiplicative speckle which is independent from the signal. Apart from adaptive and non-adaptive speckle filtering, spatial averaging can be used for speckle reduction and to enable statistical analysis of the SAR data. There are three polarimetric target descriptors that involve spatial averaging:

- the covariance matrix  $[C]$
- the coherency matrix  $[T]$
- the Kennaugh matrix  $[K]$

In general, objects can be categorized as either single targets or partial targets, following the way they are represented with SAR data [82]. Single (i.e. deterministic or coherent objects) scatterers can be described completely using one single scattering matrix. Partial (i.e. statistical or distributed) targets show spatial differences. An average of many pixels is needed to derive meaningful information about the object's SAR signature [55]. Furthermore, the backscattering of partial targets shows changes of the polarisation state and a change of degree of polarisation. Considering that the polarisation state is a function of time and space, partial targets can be approached as stochastic. A statistical description and many realisations (i.e. pixels) are required, since the single measurements can differ [84, 85].

A point (or single, pure) scatterer has a physical dimension of five. A target that changes its polarimetric behaviour pixel per pixel is called a partial target and can be characterised by a statistical description. The second order statistics, needed for that step, are generally arranged in a covariance matrix  $[C]$ , which is derived from the outer product of the lexicographic vector with its conjugate transpose [78, 74, 82, 86]. Normally, it is a 4x4 matrix, but for the monostatic case under the BSA convention it looks like:

$$[C] = \langle \underline{k}_l \cdot \underline{k}_l^{*T} \rangle = \begin{bmatrix} \langle |S_{HH}|^2 \rangle & \langle \sqrt{2}S_{HH}S_{HV}^* \rangle & \langle S_{HH}S_{VV}^* \rangle \\ \langle \sqrt{2}S_{HV}S_{HH}^* \rangle & \langle |S_{HV}|^2 \rangle & \langle \sqrt{2}S_{HV}S_{VV}^* \rangle \\ \langle S_{VV}S_{HH}^* \rangle & \langle \sqrt{2}S_{VV}S_{HV}^* \rangle & \langle |S_{VV}|^2 \rangle \end{bmatrix} \quad (2.57)$$

## 2. SAR and PolSAR

The result is a Hermitian<sup>9</sup>, positive semi-definite<sup>10</sup> matrix. In the main diagonal we find the values for all the three polarimetric channels' scattering coefficients  $\sigma_{HH}^0$ ,  $\sigma_{VV}^0$  and  $\sigma_{HV}^0$ . If we use the Pauli vector we obtain the so-called coherency matrix  $[T]$ :

$$[C_P] = [T] \quad (2.58)$$

For the monostatic case, the 3x3 Hermitian  $[T]$ -matrix has the following parameterization (representing a segment of the 4x4  $[T]$ -matrix in [87]):

$$[T] = \langle \underline{k}_p \cdot \underline{k}_p^{*T} \rangle = \begin{bmatrix} \langle |S_{HH} + S_{VV}|^2 \rangle & \langle (S_{HH} + S_{VV})(S_{HH} - S_{VV})^* \rangle & \langle 2(S_{HH} + S_{VV})S_{HV}^* \rangle \\ \langle (S_{HH} - S_{VV})(S_{HH} + S_{VV})^* \rangle & \langle |S_{HH} - S_{VV}|^2 \rangle & \langle 2(S_{HH} - S_{VV})S_{HV}^* \rangle \\ \langle 2S_{HV}(S_{HH} + S_{VV})^* \rangle & \langle 2S_{HV}(S_{HH} - S_{VV})^* \rangle & \langle 4|S_{HV}|^2 \rangle \end{bmatrix} \quad (2.59)$$

Each element of the main diagonal is linked to a physical interpretation of the Pauli decomposition. The two matrices  $[T]$  and  $[C]$  share the same eigenvalues and contain the same information about the polarimetric scattering mechanisms. Their elements on the diagonal are real positive. They are regarded as powers and the off-diagonal terms are complex. They contain five independent parameters (monostatic configuration): the three real values at the main diagonal and the three off-diagonal complex terms of the upper triangular part which are two relative phase terms; just as it is the case for the  $[S]$ -matrix they originate from [42].

$[C]$  can be estimated from any basis set. The scattering vector in a generic basis given by  $\underline{k} = [k_1, k_2, k_3^T]$  would result in the following covariance matrix:

$$[C] = \langle \underline{k} \cdot \underline{k}^{*T} \rangle = \begin{bmatrix} \langle |k_1|^2 \rangle & \langle \sqrt{2}k_1k_2^* \rangle & \langle k_1k_3^* \rangle \\ \langle \sqrt{2}k_2k_1^* \rangle & \langle |k_2|^2 \rangle & \langle \sqrt{2}k_2k_3^* \rangle \\ \langle k_3k_1^* \rangle & \langle \sqrt{2}k_3k_2^* \rangle & \langle |k_3|^2 \rangle \end{bmatrix} \quad (2.60)$$

Eqs. 2.57 and 2.59 represent the most general form of the covariance matrix and the coherency matrix. As they are Hermitian, they contain up to nine independent parameters. But for special kinds of targets, the number of parameters can be reduced. For example, for a target that has reflection symmetry in a plane normal to the LoS, the matrices will have the general forms as [88, 89, 90]:

$$[C] = \begin{bmatrix} C_{11} & 0 & C_{13} \\ 0 & C_{22} & 0 \\ C_{31} & 0 & C_{33} \end{bmatrix} \quad [T] = \begin{bmatrix} T_{11} & T_{12} & 0 \\ T_{21} & T_{22} & 0 \\ 0 & 0 & T_{33} \end{bmatrix} \quad (2.61)$$

For this case, with symmetry in the backscattered wave, the cross-pol terms will be totally uncorrelated with the co-pol terms which is not always the case in natural environments [88]. In this case,  $[C]$  and  $[T]$  only have up to five independent parameters. In addition, an object can also show rotation symmetry (or azimuthal symmetry), leaving  $[T]$  with only two independent parameters.

<sup>9</sup>hermitian matrix: is a complex square matrix that is equal to its own conjugate transpose

<sup>10</sup>positive semi-definite matrix: all its quadratic forms ( $x^T C x$ ) are not negative



The elements of the above presented  $[C]$ -matrix and  $[T]$ -matrix have location-specific characteristics. The diagonal elements contain the power information, the off-diagonal ones contain the correlation information between the different channels.

### 2.3.3 Scattering Mechanisms

We can combine different polarimetric channels to acquire a more complete characterisation of the targets on the ground. The backscattered signal comes from the combination of different scattering mechanisms. Most well-known scattering mechanisms are surface (also called single-bounce or odd) scattering, double bounce (or even) scattering and volume (or multiple) scattering. These three mechanisms are assumed to be totally uncorrelated [91]. The contribution of these mechanisms depends on scene-specific parameters, such as geometry and dielectric properties of the objects on the ground. Further, there are sensor-specific parameters; mainly the radar frequency, the antenna orientation and the incidence angle.

The dielectric properties are given by the dielectric constant of the material, often expressed as relative permittivity. The latter is the ratio of the frequency-dependent permittivity of a given material divided by the permittivity of a vacuum  $\epsilon_0$ :

$$\epsilon_r(\omega) = \frac{\epsilon(\omega)}{\epsilon_0} \quad (2.62)$$

The reflectivity of an interface with a known dielectric constant can be calculated using the Fresnel equations [43]. Most natural dry materials have a dielectric constant in the range of three to eight. Polymers like plastics and PVC are between two to four. For water, this factor is one magnitude bigger. Due to this high dielectric constant, the presence of water inside/over objects can result in dramatic variations of their reflectivity. Microwave radiation is able to penetrate dielectric mediums, with penetration depths related to the permittivity of the medium (associated with the density in the case of cluster medium) [92, 25].

For instance, when looking at the interactions between the radar wave and vegetation cover, the important scene parameters would be the density and the orientation of the scatterers (leaves, branches), their dielectricity and their size relative to the radar wavelength. Therefore, if seen as compound materials, their composition and water content define their overall dielectric properties. In the case of vegetation, the HV component, representing the volume scattering mechanism, is expected to be much stronger than for surface scattering or double bounce since the microwaves are scattered from a cloud of randomly oriented, very thin, cylinder-like scatterers within a volume of canopy [91]. In case of a uniform orientation distribution of these cylinder-like scatterers,  $\langle S_{HH}S_{VV}^* \rangle = \langle |S_{HV}|^2 \rangle = \frac{1}{3}$ . This leads to depolarisation, meaning a change of the polarisation basis of the wave.

The link between the cross-polarisation channels (HV and VH) and depolarisation is not unique. The cross-polarisation channels include all scattering and wave propagation processes that change the polarisation of the received wave. For example, double bounce scattering from water surfaces can contribute to the cross-pol channels [93]. These processes can be deterministic or stochastic. Depolarisation is inherently a purely stochastic phenomenon. Although it is stochastic, the signal is not noise and information can be extracted from it. Hence, all depolarising systems cause cross-polarisation, but not vice-versa [73].

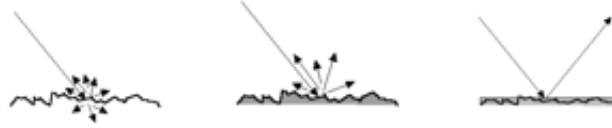


Figure 2.18: Surface scattering mechanisms [52].

Scattering on a surface is dependent on the roughness of the surface and its water content. The roughness governs the scattering pattern with respect to the wavelength. If the roughness (e.g. root mean square of surface undulation) is of similar size to the wavelength (or bigger), more energy is scattered back to the sensor. Very smooth surfaces act as mirrors and almost no energy comes back to the sensor (right depiction in Fig. 2.18). The moisture content of the surface determines its dielectric constant and the ability of the microwave to penetrate and scatter from the medium. In case of a very wet medium, there should be very limited penetration (Fig. 2.18, central and right). In the case of a dry surface (Fig. 2.18, left), the EM can partly penetrate the medium, depending on the structure of the medium and the EM wave's  $\lambda$ .



Figure 2.19: Scattering and surface structure [94].

The effects of the roughness and the surface's dielectricity can look similar in terms of intensity. But the polarisation helps to differentiate between them. For smooth surfaces, the depolarisation and, therefore, the cross-pol channels (HV or VH) equal zero and surface scattering results in strong HH-pol and VV-pol with a higher Fresnel reflectivity for the VV-pol channel (Fig. 2.19, left). In the case of rough surfaces, some depolarisation takes place and the cross-pol channel is greater than zero (Fig. 2.19, right). This phenomenon has a very similar equivalent which occurs on water surfaces, called Bragg scattering (please see the according section 3.1.3 further down).

For scatterers, whose scattering behaviour is anisotropic, the scattering intensity is aspect dependent, it changes with the direction of the EM wave and its polarisation [95]. Examples of this are scattering from cylinders, dipoles or Bragg scattering. Isotropic objects scatter in all directions with the same intensity. The scatterer interacts the same way with all polarisations and this interaction is independent from the direction of the electric field vector. Examples of this are odd bouncing objects such as spheres or surfaces [17]. Volume scattering from multiple scatterers can lead to perfect depolarisation. The amount of anisotropic and isotropic scattering of an object can be statistically analysed and used for discrimination in detection and classification schemes using subapertures (e.g. [96]).

### 2.3.4 Polarimetric Response: Canonical Scattering Mechanisms

Fig. 2.20 lists canonical scatterers with the corresponding diagrams and formulae for the parameter  $c_x$ . The first canonical scatterer described in Fig. 2.20 is a sphere. It produces the same scattering matrix as flat plates (single bounce) and trihedral corner reflectors [97].

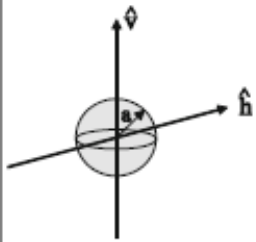
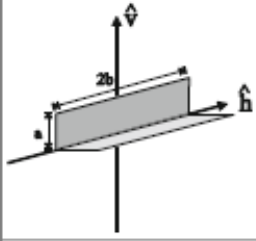
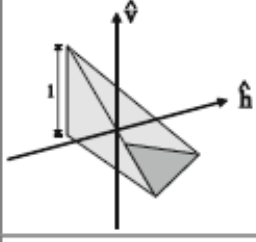
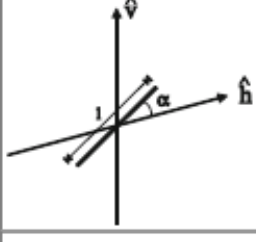
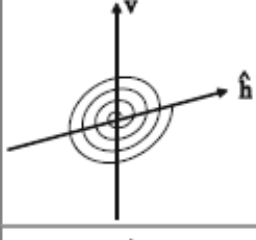
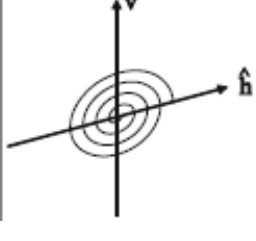
Canonical body	Diagram	Scattering matrix
Sphere		$\frac{a}{2} \begin{bmatrix} 1 & 0 \\ 0 & 1 \end{bmatrix}$
Dihedral corner reflector		$\frac{4ab}{\pi} \begin{bmatrix} 1 & 0 \\ 0 & -1 \end{bmatrix}$
Trihedral corner reflector		$\frac{4l^2}{\sqrt{12}\pi} \begin{bmatrix} 1 & 0 \\ 0 & 1 \end{bmatrix}$
Short thin cylinder		$\frac{4l^2 a^2}{3(\ln(\frac{4}{\pi})-1)} \begin{bmatrix} \cos^2 \alpha & \sin \alpha \cos \alpha \\ \sin \alpha \cos \alpha & \sin^2 \alpha \end{bmatrix}$
Left-handed helix		$\frac{1}{2} \begin{bmatrix} 1 & -j \\ -j & -1 \end{bmatrix}$
Right-handed helix		$\frac{1}{2} \begin{bmatrix} 1 & j \\ j & -1 \end{bmatrix}$

Figure 2.20: Canonical scatterers [42].

Spheres and plates have in common an odd number of reflections ('odd-bounce') and produce the following scattering matrix:

$$[S] = c_1 \begin{bmatrix} 1 & 0 \\ 0 & 1 \end{bmatrix} \tag{2.63}$$

where  $c_1$  is a function of the wavelength and the edge length of the flat plate or the edge length of the trihedral corner reflector or the radius of the sphere. The main diagonal represents the co-pol channels (HH and VV), the off-diagonal hosts the cross-pol channels (HV and VH).

The radar response increases with increasing size of the scattering object and decreases with longer wavelengths [27]. As Equation 2.63 shows, the horizontal and the vertical polarisations are scattered to the same amount and they are in phase. No cross-pol components are generated for the linear polarisation case. Even-bounce scatterers, such as a dihedral corner reflector, have the following scattering matrix:

$$[S] = c_2 \begin{bmatrix} 1 & 0 \\ 0 & -1 \end{bmatrix} \quad (2.64)$$

where  $c_2$  increases with shorter wavelengths and greater length and width of the dihedral. There is no cross-pol component and the equally strong co-pol channels are out of phase. For oriented dihedrals the equation becomes:

$$[S] = c_2 \begin{bmatrix} \cos 2\alpha & \sin 2\alpha \\ \sin 2\alpha & -\cos 2\alpha \end{bmatrix} \quad (2.65)$$

where  $\alpha$  describes the tilt of the corner reflector relative to the LoS of the sensor. Consequently, when the dihedral corner reflector is rotated  $45^\circ$  relative to the horizontal axis, the scattering matrix changes to:

$$[S] = c_2 \begin{bmatrix} 0 & 1 \\ 1 & 0 \end{bmatrix} \quad (2.66)$$

where  $c_2$  has the same attributes as before. Now, the cross-pol channel is dominant and the co-pol channels equal zero [19].

In the case of short, thin, vertical conducting dipoles, the VV-pol channel produces the vast majority of the scattering response. Very little contribution may arise from the orthogonal component, too. In that case, the corresponding scattering matrix is:

$$[S] = c_3 \begin{bmatrix} 0 & 0 \\ 0 & 1 \end{bmatrix} \quad (2.67)$$

where  $c_3$  increases with increasing length of the object and decreases with the object's radius and its lengthening wavelength. The vertical polarised microwaves are scattered by thin objects which are orientated likewise; the same is true for the horizontal case. HH-pol cannot be scattered by this object and therefore HH-pol and the cross-pol channels equal zero. It is the first case where the emitted polarisation is not scattered. This means that there is no coupling to the dipole and no scattered wave [27].

If the dipole is rotated by  $45^\circ$  from the vertical direction, the scattering matrix changes to:

$$[S] = \frac{c_3}{2} \begin{bmatrix} 1 & -1 \\ -1 & 1 \end{bmatrix} \quad (2.68)$$

where  $c_3$  increases with shorter wavelengths and a longer dipole. The maximum in the co-pol response is shifted to  $45^\circ$ . This is an indicator for the link between the orientation of the short cylinder and the polarisation response which is important for the analysis of the scattering of vegetated areas.

More generically, the scattering matrix of the cylinder for every rotation angle  $\alpha$  can be calculated as follows:

$$[S] = \frac{c_3}{2} \begin{bmatrix} \cos^2 \alpha & \sin \alpha \cos \alpha \\ \sin \alpha \cos \alpha & \sin^2 \alpha \end{bmatrix} \quad (2.69)$$

The rotation is performed in an imaginary plane which lies orthogonal to the line of sight of the radar.

Helix-type scattering is anti-symmetric and a kind of scattering that transforms the incidence wave into a circular polarisation state. It creates a left-handed or right-handed linear polarisation in the scattered wave for all incident linear polarisation states. In the case of a left-handed helix, the scattering matrix looks like:

$$[S] = c_4 \begin{bmatrix} 1 & -j \\ -j & -1 \end{bmatrix} \quad (2.70)$$

and the corresponding matrix for the right-handed case is written as:

$$[S] = c_4 \begin{bmatrix} 1 & j \\ j & -1 \end{bmatrix} \quad (2.71)$$

This helix component has, such as  $45^\circ$  oriented dihedrals, no reflection symmetry. It generally appears in complex urban areas but it is rare for a natural distributed scatterer [98]. Reflection symmetry is given when the two co-cross-correlations (HV HH, VH VV) equal zero. The two terms which are related to this property are the  $T_{13}$ ,  $T_{23}$ ,  $T_{31}$  and  $T_{32}$  of the polarimetric coherency matrix [99]. For the  $[C]$ -matrix, the terms  $C_{12}$ ,  $C_{21}$ ,  $C_{23}$  and  $C_{32}$  show the co-cross correlations (see Fig. 2.61 above). Hence, the moduli of these amplitudes is a good indicator to measure reflection symmetry [100].

Following the theoretical model for reflection symmetry developed by Cloude et al. [89, 101], for symmetric objects such as those characterised by Bragg scattering and double bounce scattering [91], the scattering matrix looks like:

$$S = \begin{bmatrix} S_{HH} & 0 \\ 0 & S_{VV} \end{bmatrix} \quad (2.72)$$

Sea and forest areas are typical for reflection symmetry scattering. Artificial structures like vessels and urban areas do have much lower reflection symmetry, dependent on their orientation relative to the LoS [42]. The reflection symmetry metric was defined as the modulus of the correlation between the co-pol and the cross-pol scattering amplitudes [100, 102, 103]:

$$RS = |\langle S_{xx} S_{xy}^* \rangle| \quad (2.73)$$

Consequently, the mean values for  $RS$  are expected to be close to zero. Gao et al. [104] derived a statistical model for the sea clutter to improve the detection of vessels. For metallic ships, consisting of planes, dihedrals, trihedrals, dihedral corner reflectors and thin wires, reflection symmetry is not expected and  $RS$  would then be larger than zero.

### 2.3.5 Polarimetric Correlation Coefficients

For some applications the strength of a SAR system lies in the relation between the polarisation channels of the scattering matrix  $[S]$ . This ratio can be expressed using the co-polarisation ratio  $p$  and the cross-polarisation ratio  $q$ :

$$\begin{aligned} p &= \frac{\langle |S_{HH}|^2 \rangle}{\langle |S_{VV}|^2 \rangle} \\ q &= \frac{\langle |S_{HV}|^2 \rangle}{\langle |S_{VV}|^2 \rangle} \end{aligned} \quad (2.74)$$

Oh et al. [105] implemented the polarisation coefficients as functions of the surface roughness and its dielectric constant.  $p$  is low for smooth surfaces and tends closer to 1 as roughness increases. For areas where volume scattering is dominant, it is about 1 and when dihedral (double bounce) is strong  $p$  it is bigger than 1.  $q$  can discriminate between surface scattering and volume scattering. It is very low for smooth surfaces and increases with the surface roughness. In the case of volume scattering it is relatively high, when dihedral scattering is predominant  $q$  gets low.

Minchew [106] also investigated the connection between the co-pol ratio and the dielectric property of the surface. Migliaccio [107] used the standard deviation of the co-pol phase difference to distinguish between oil spills and biogenic lookalikes. It can be derived from circularly polarised [108] and from linearly polarised data and has been used to characterise rough surfaces [109], to examine the sea surface [110], to study different types of sea ice [111] or for the development of ship detection algorithms (e.g. [112]). In the circular polarisation basis, it seems to be unaffected by the object orientation and was used to distinguish urban areas from their surroundings [113].

The correlation coefficient  $\rho$  is the complex average of the one channel and the conjugate of the second channel, normalised by the square root of the product of the two channels' powers [114]. In the co-pol case it is defined as:

$$\rho = \frac{\langle S_{HH} S_{VV}^* \rangle}{\sqrt{\langle |S_{HH}|^2 \rangle \langle |S_{VV}|^2 \rangle}} \quad (2.75)$$

$\rho$  ( $\in \{-1, 1\}$ ) is being used for the detection of depolarisation and double bounce scattering. Surface scattering is represented by a high amplitude (low depolarisation) and a small difference of the phases. In case of depolarisation due to volume scattering, the amplitude is lower, the phase difference is poorly defined. Double bounce scattering shows a phase difference close to  $180^\circ$ . Pure surface scattering will have a co-pol phase difference of  $0^\circ$  [27]. The co-pol phase difference can be useful to detect, for example, water surfaces [115] as it is characteristic of the number of bounces the electromagnetic wave experiences during scattering. If the magnitude of the correlation coefficient equals one, the signals of the two channels are linearly related. An example for that case would be an ideal trihedral corner reflector. If the magnitude is smaller than one, the two channels are not directly related. It may also mean that one or both channels are partially depolarised and/or noise is present.

A cross-pol phase difference would be defined analogously but is usually random as there is generally little correlation between the phase centres of the co-pol and the cross-pol channels.

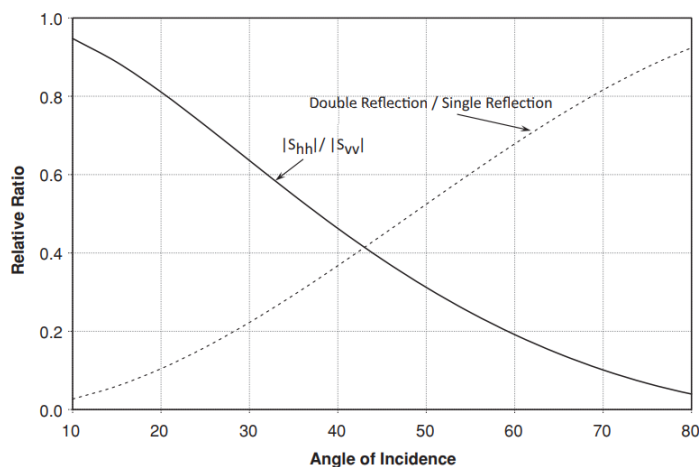


**Figure 2.21:** The expected co-polarisation ratio and double-bounce/single bounce scattering ratio as a function of the incidence angle for fresh water [27]

When it comes to dielectric surfaces like the ocean, the incidence angle needs to be added to the function that describes the co-polarisation ratio [27]. The dielectric constant (real part,  $\epsilon'$ ) of water is around 80 at  $20^\circ\text{C}$  (for salty ocean water it drops to somewhere around 70 [116, 117] and Fig. 2.21 shows the expected co-pol ratio at different incidence angles. At larger angles, the co-pol ratio drops far under 1 despite the fact that the Pauli basis forces the HH-pol and the VV-pol terms to be equal for the single scattering term. The bigger this discrepancy, the bigger the dihedral component (dashed curve), which is needed to explain it. The first-order small perturbation model, which is used to describe the scattering of rough surfaces, only includes single scattering terms [27]. The interpretation of having double bounce scattering at the water surface is a necessary consequence of the basis we chose and the associated assumptions.

### 2.3.6 Polarimetric Decomposition

Polarimetric decompositions allow a physical interpretation of the scattering mechanisms present in the scene. In this frame, the polarimetric covariance matrix  $[C]$ , and the polarimetric coherency matrix  $[T]$  are often used. In the past few decades, many polarimetric decompositions

have been proposed (e.g. [74]). In most cases, the 'cleaning of the data' in the form of speckle filtering is the first processing step and enables initial interpretation of the data.

After that, a polarimetric decomposition, which is a deeper analysis of the objects on the ground, may follow. It enables the development of physical models for the identification and/or separation of scattering mechanisms occurring inside the same resolution cell. Target decomposition theorems for SAR were first formalised by Huynen [118], but have their roots in the work of Chandrasekhar and Elbert [119] who explored the scattering of light by small anisotropic particles. Since then, many approaches were developed with the goal of breaking down the scattering response into coherent speckle noise and contributions from different scattering mechanisms and can be used to extract information about these scattering processes.

They can be grouped into three main categories, depending on the polarimetric descriptors used [87]: first, there are the 'target dichotomy' decompositions which are applied to the Kennaugh Matrix [ $K$ ]. They attempt to extract a single scattering matrix from the averaged Stokes matrix (e.g. decompositions from Huynen [118] and Barnes [120] but afterwards it was viewed sceptically and Cloude doubted the uniqueness<sup>11</sup> of Huynen's theorem [121] and later proved the nonexistence of target dichotomy.

The second group is represented by coherent theorems, which try to decompose the scattering matrix [ $S$ ] into the sum of elementary matrices. Examples of this category are the Krogager decomposition [122] and the Cameron decomposition [123]. Since the absolute phase values do not allow for speckle filtering, these decompositions are prone to problems coming from speckle noise.

Finally, we have the class of decompositions working with eigenvalues and eigenvectors of the coherency matrix [ $T$ ] or the covariance matrix [ $C$ ]. Holm [120], Touzi [124] and Cloude & Pottier [87] are prominent examples. The group of model-based approaches is led by Freeman & Durden [125], Yamaguchi (e.g. [98]) and Singh [126], to name just a few. Van Zyl [27] came up with methods to combine the eigenanalysis with a model-based decomposition approach. It revealed that the three eigenvalues and a set of angles, obtained from the unitary eigenvectors, are connected to physical scattering mechanisms.

The choice of the right decomposition to use depends strongly on the nature of the particular application. For instance, eigenanalysis may be more useful for identification and detection tasks. The reconstruction of a specific scattering mechanism can be easier with a model-based approach, since the [ $C$ ]-matrix and the [ $T$ ]-matrix can be separated and reconstructed for the particular scattering process.

### 2.3.6.1 Coherent Decompositions

Coherent decompositions try to decompose the scattering matrix [ $S$ ] into the sum of elementary matrices. They are suitable not only for detection but for identification as well, since they provide information about the physical structure of scatterers [127]. Further, they facilitate the estimation of the orientation of the scatterer relative to the LoS and give insight into regions of motion [128]. Examples of this category are the Van-Zyl decomposition [115] and the Krogager decomposition [122]. Here, we describe the Cameron decomposition [123, 129] in more detail. It considers reciprocity ( $S_{HV} = S_{VH}$ ) and symmetry of scatterers. A symmetric scatterer has an axis of symmetry in the plane orthogonal to the LoS and its [ $S$ ]-matrix can be diagonalised using a rigid rotation transformation [118].

---

<sup>11</sup>uniqueness of a target decomposition theorem: given a target matrix we must be able to perform the appropriate decomposition e.g. single target plus noise in only one way [121]



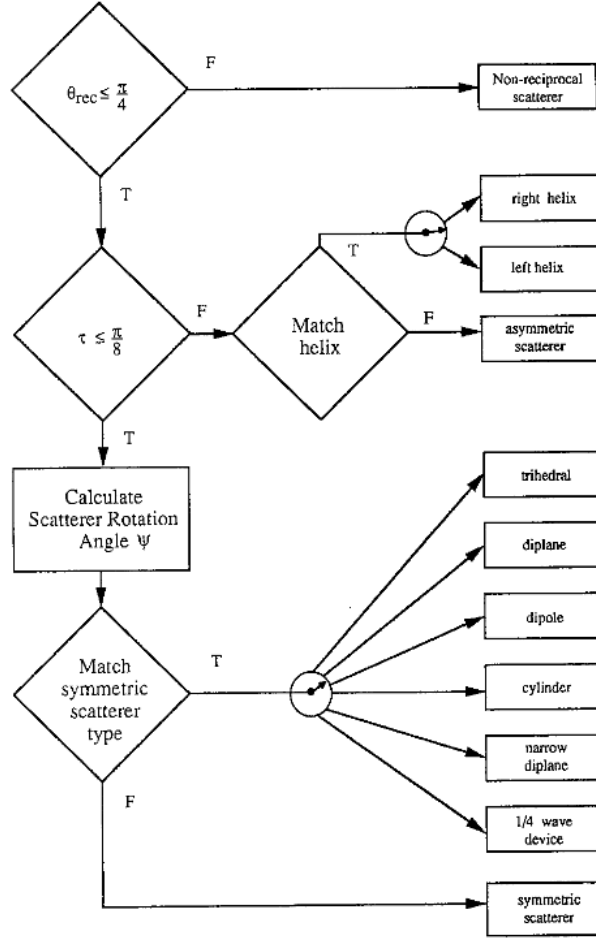


**Figure 2.22:** The scattering matrix classification scheme of the Cameron decomposition [123].

The workflow is first to decompose  $[S]$  into reciprocal and non-reciprocal components. Then the reciprocal scatterers are decomposed into helix scattering, asymmetric scatterers and symmetric scatterers. Finally, the maximal symmetric scattering features are then assigned to one of six elemental scatterers (Fig. 2.22).

Cameron expanded the  $[S]$ -matrix using the Pauli matrices group (see Equ. 2.41) called  $S_a$ ,  $S_b$ ,  $S_c$  and  $S_d$

$$S = \alpha S_a + \beta S_b + \gamma S_c + \delta S_d \quad (2.76)$$

where  $\alpha$ ,  $\beta$ ,  $\gamma$  and  $\delta$  are complex. For reciprocal scatterers ( $\Theta_{rec}$  in Figure 2.22)  $\delta$  equals zero. After the extraction of the maximal symmetric scatterer component of  $\Theta_{rec}$ , a normalised diagonal form of the  $[S]$ -matrix is specified which thus associates a physical scattering mechanism. That is done by rotating  $[S]$ :

$$\Lambda_z = \frac{1}{\sqrt{1+|z|^2}} \begin{bmatrix} 1 \\ 0 \\ 0 \\ z \end{bmatrix} \quad (2.77)$$

## 2. SAR and PolSAR

where  $z$  ( $z \in \mathbb{C}$  and  $|z| \leq 1$ ) determines the scatterer type. The most common ones are listed in Table 2.1.

**Table 2.1:** Cameron's common symmetric elementary scattering types [129].

Scatter Type	normalised Form
Trihedral	$\hat{\Lambda}(1)$
Dihedral	$\hat{\Lambda}(-1)$
Dipole	$\hat{\Lambda}(0)$
Cylinder	$\hat{\Lambda}(\frac{1}{2})$
Narrow Diplane	$\hat{\Lambda}(-\frac{1}{2})$
Quarter Wave Device	$\hat{\Lambda}(i)$

Unlike the original Cameron classification scheme, which identified eleven elementary scatterers, it was found to be feasible for ship detection to reduce them to only five, which are likely to be indicative of large, metallic vessels: dihedral, narrow diplane, cylinder, dipole and quarter wave device. Other studies found that ships are dominated by dihedral, narrow diplane and quarter wave device scatterers [128].

### 2.3.6.2 Eigenanalysis-based Decomposition

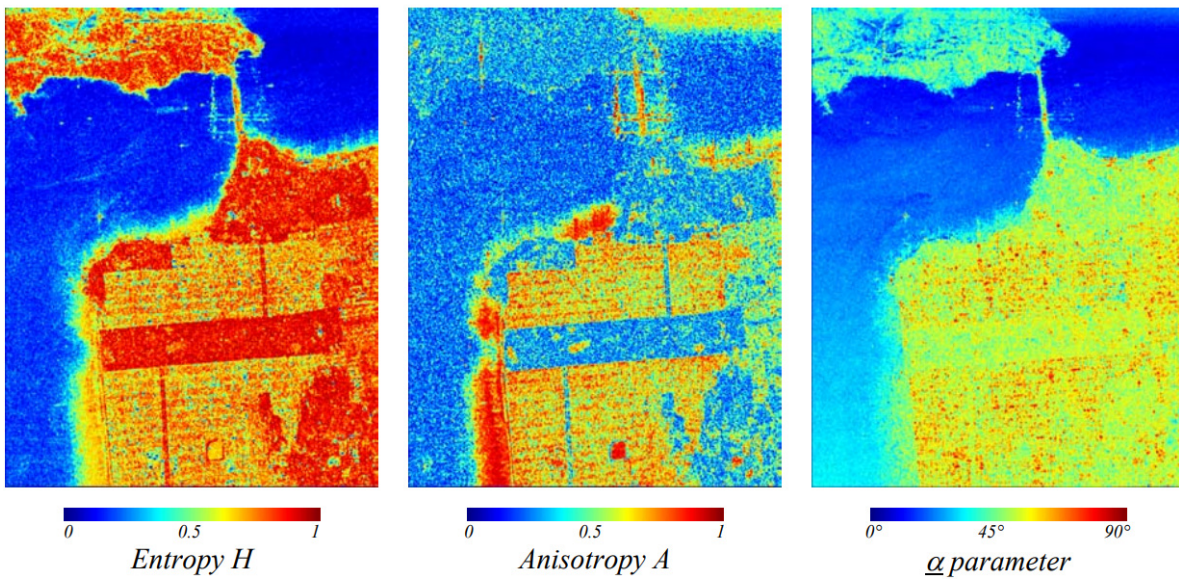


**Figure 2.23:** The roll-invariant parameters  $H$ ,  $A$  and  $\bar{\alpha}$  [130]

It was Cloude [121] who built on the work of Jones [76] on wave polarimetry and introduced the diagonalization of the coherency matrix into the field of target polarimetry. This enabled him to decompose  $[T]$  in terms of its eigenvalues  $\lambda_i$  and eigenvectors  $\underline{e}_i$ :

$$\langle [T] \rangle = \sum_{i=3}^3 \lambda_i \underline{e}_i \underline{e}_i^{*T} \quad (2.78)$$

Since  $[T]$  is semi-definite Hermitian, its eigenvectors are orthogonal and real. Cloude & Pottier [87] introduced the Entropy/Anisotropy/Alpha decomposition (H/A/ $\bar{\alpha}$ ) which considers the existence of three different scattering mechanisms, the three eigenvectors. Fig. 2.23 shows the roll-invariant<sup>12</sup> parameters H, A and the mean alpha angle  $\bar{\alpha}$ . The roll-invariance property of  $\bar{\alpha}$  depends on the polarisation basis and is lost in the case of dual cross-pol data and in the lexicographic basis.

The H/A/ $\bar{\alpha}$  decomposition is based on the analysis of the eigenvectors and the eigenvalues of the local estimate of the coherency matrix  $[T]$ . The three (in the case of quad polarimetry) eigenvectors are an equivalent to the target vector. This allows for the reconstruction of three orthogonal scattering mechanisms. This model is limited to reflection symmetric media [132]. From the eigenvalues ( $\lambda_1$ ,  $\lambda_2$  and  $\lambda_3$ ), we can define the pseudo probabilities of the scattering mechanisms as:

$$P_i = \frac{\lambda_i}{\sum_{k=1}^3 \lambda_k} \quad (2.79)$$

which is the ratio of one eigenvalue divided by the sum of all eigenvalues. Cloude & Pottier [132] then introduced a set of unitary (denoted by the superscript  $\hat{\cdot}$ ) parameters  $\hat{\alpha}$ ,  $\hat{\beta}$ ,  $\hat{\delta}$  and  $\hat{\gamma}$  to describe the three target eigenvectors.  $\hat{\alpha}$  is an indicator of the type of scattering. If the scattering medium does not have reflection symmetry, then there exists a preferred orientation angle  $\hat{\beta}$  which is the physical orientation of the object about the line of sight [133]. With the help of the probability values for each eigenvector, the mean of these angle parameters can be constructed. That way, the target vector  $\underline{k}_0$  of the mean dominant scattering mechanisms can be reconstructed:

$$\underline{k}_0 = \sqrt{\bar{\lambda}} e^{j\phi} \begin{bmatrix} \cos(\bar{\alpha}) \\ \sin(\bar{\alpha}) \cos(\bar{\beta}) e^{j\bar{\delta}} \\ \sin(\bar{\alpha}) \sin(\bar{\beta}) e^{j\bar{\gamma}} \end{bmatrix}^T \quad (2.80)$$

using all the information from  $[T]$ .  $\underline{k}_0$  is a product of the target unitary vector and the target magnitude  $\lambda$ , which is the sum of the averaged eigenvalues. Compared to  $[T]$ , which has a physical dimension of nine, this target vector is only a five-dimensional construct. The eigenvalues and their probabilities are roll-invariant. Of the introduced parameters in this model only  $\hat{\alpha}$  is not roll-invariant, since it depends on the eigenvectors too, and requires that the basis is the Pauli one. It ranges between 0 and  $\frac{\pi}{2}$  and holds characteristic physical properties of the scattering object: an  $\hat{\alpha}$  close to zero means single bounce scattering (rough surface), an  $\hat{\alpha}$  around  $90^\circ$  is associated with double bounce and helix scattering and an  $\hat{\alpha}$  close to  $45^\circ$  corresponds to volume scattering. Fig. 2.24 shows standard scatterers which are associated with different  $\hat{\alpha}$  values. The extremes are reached for isotropic objects.  $\hat{\alpha}$  angles of about  $\frac{\pi}{4}$  show high anisotropic behaviour which means that the scattering property of the object observed is not identical in all directions or throughout the area the object occupies. An example for this are dipoles. Here, a rotation around the LoS can be considered which concentrates all the power in one linear co-polarisation throughout the movement (i.e. in all directions).

<sup>12</sup>variables which do not change if the target changes its orientation angle (which is measured by rotation about the LoS) are called roll-invariant target parameters. The invariant target variables are still dependent on the target aspect (which is the LoS direction) [131]

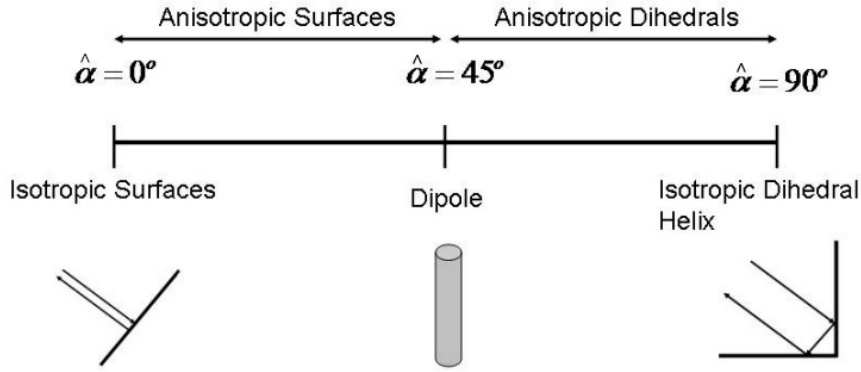


**Figure 2.24:** interpretation of the alpha angle [17]

The physical meaning of  $\hat{\beta}$  reveal information about the orientation of pure targets relative to the LoS (e.g. [74, 73]). The one of the phase angles for the second and third components  $\hat{\delta}$  and  $\hat{\gamma}$  can be used to define the scatterer orientation angle [74].

When the second and the third eigenvectors are not very low, averaged information is required to represent the partial scatterer. For the full-pol case,  $\bar{\alpha}$  is the weighted average of all three  $\hat{\alpha}$  angles, using their probabilities:

$$\bar{\alpha} = \sum_{k=1}^3 P_k \hat{\alpha}_k \quad (2.81)$$

Next, they introduced another parameter which covers the degree of randomness of the eigenvectors. For that, the concept of the entropy  $H$  in the Von Neumann sense (not to be confused with Shannon Entropy which is the degree of randomness of information, [87]) was adopted as a logarithmic sum of eigenvalues probabilities:

$$H = - \sum_{i=1}^3 P_i \log_3(P_i) \quad (2.82)$$

with the probabilities  $P_i$  of the eigenvalues.  $H = 0$  would mean the first eigenvalue has all the target's energy and the other two are zero ( $\lambda_1 = SPAN$ ,  $\lambda_2 = \lambda_3 = 0$ ). This means that there is only one very dominant scattering mechanism and indicates a pure target. For  $H = 1$ , the eigenvalues are randomly distributed and share the energy of the target vector in equal parts ( $\lambda_1 = \lambda_2 = \lambda_3 = SPAN/3$ ), representing three orthogonal, independent scattering mechanisms showing a randomly polarised or fully unpolarised target.

Another descriptor is called anisotropy  $A$ . Generally speaking, in physics the concept of anisotropy allows materials to change specific properties in different directions. In the Cloude-Pottier decomposition, anisotropy provides information about the relation between the second and the third eigenvalues:

$$A = \frac{\lambda_2 - \lambda_3}{\lambda_2 + \lambda_3} \quad (2.83)$$



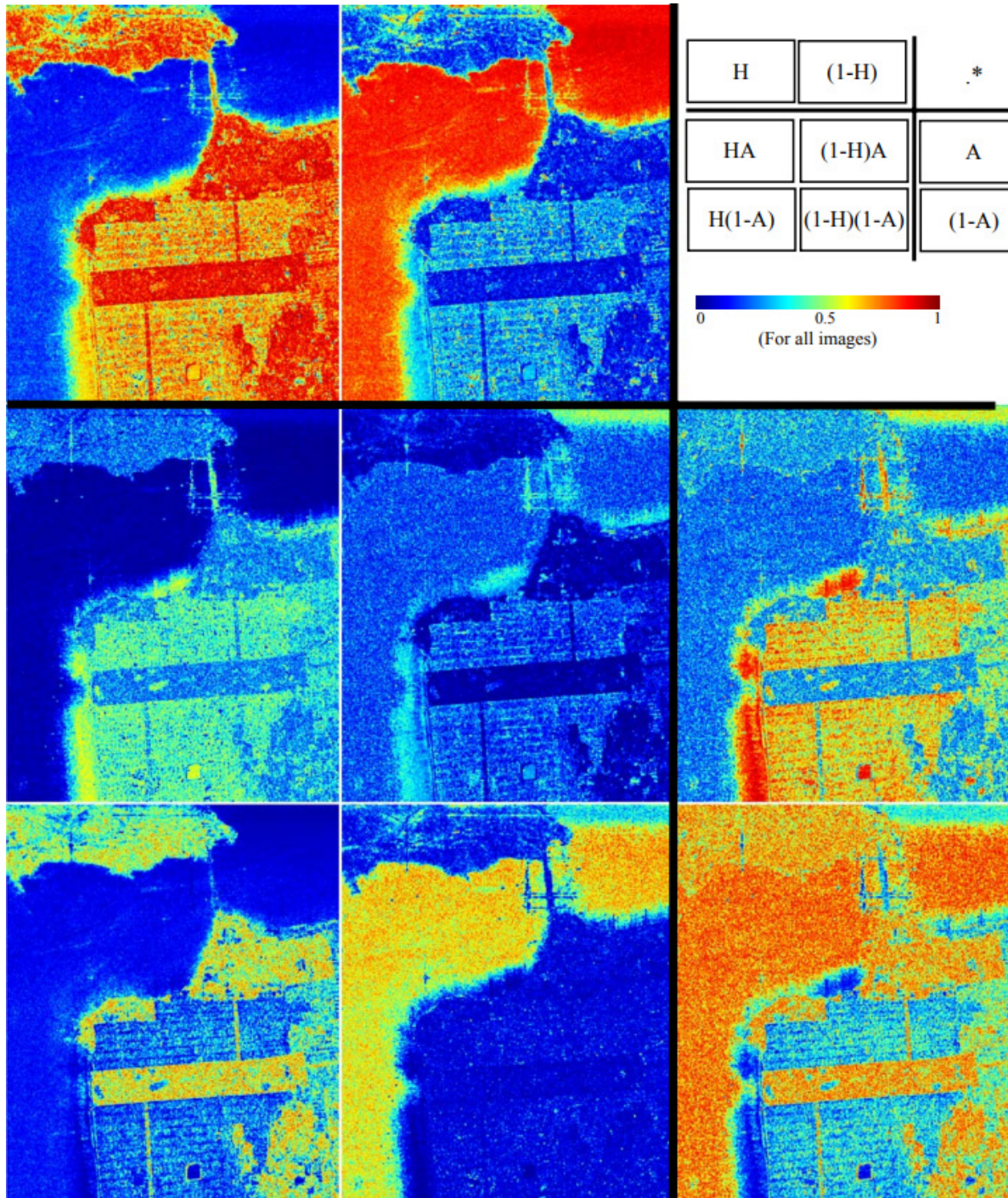


**Figure 2.25:** Different combinations of entropy and anisotropy [130].

For surfaces where  $\lambda_2$  equals  $\lambda_3$ ,  $A$  becomes 0. For surfaces with intermediate  $H$ , a high anisotropy indicates the presence of only one strong secondary scattering process, while a low anisotropy indicates the appearance of two equally strong scattering processes. It can be seen as a complementary indicator which can be helpful especially when it becomes more and more difficult to discriminate between scattering mechanisms, especially when  $H$  is high. For example,  $H = 0.9$  may correspond to two different scattering processes:  $\lambda_1 = 1, \lambda_2 = \lambda_3 = 0.4$  or  $\lambda_1 = \lambda_2 = 1, \lambda_3 = 0.3$ . To distinguish between them, it was necessary to introduce  $A$ . On the other hand,  $A$  alone is very hard to interpret and, in that case, for a consistent explanation,  $H$  is needed additionally [132]. At least four combinations of  $A$  and  $H$  parameters can be defined to interpret the observed target [134] and Fig. 2.25 delivers a set of images for a visual

## 2. SAR and PolSAR

comparison. The examination of different combinations of  $H$  and  $A$  lead to the following interpretations [74]:

- $(1 - H)(1 - A)$  indicates one dominant scattering mechanism that lowers the entropy and the anisotropy, because the second and the third eigenvalue is very low or zero
- $H(1 - A)$  can identify scenarios with three independent scattering mechanisms, since all the eigenvalues are quite similar. This parameter can be very useful for forest detection where volume scattering is very strong
- $HA$  is high when there are two dominant, and similarly strong, single scattering mechanisms and it can be used to identify urban areas with strong single bounce (on roofs) and strong double bounce (on the side of the buildings and the road) scattering. The third eigenvalue tends to zero
- $(1 - H)A$  reveals that there are two single targets, but one of them is much stronger than the other one.  $H$  is low because there is one dominant scatterer and  $A$  is high since the second and the third eigenvalues are close to zero. The coastal areas of the oceans with the waves in the surf area are one example where this parameter is high: there is strong single bounce from the top of the waves plus some minor double bounce contributions from the wave walls

The  $H/A/\bar{\alpha}$  approach was developed for quad-pol data, but is possible for dual-pol data as well. In the dual-pol case, the physical interpretation has to be used with caution, since a part of the polarimetric information is missing. Whereas the DoP and  $A$  use the same eigenvalues, in the full pol case  $A$  is calculated using the two weakest eigenvalues (see Formula 2.83) but the DoP is calculated using the two strongest ones [73]:

$$DoP = \frac{\lambda_1 - \lambda_2}{\lambda_1 + \lambda_2} \quad (2.84)$$

Accordingly, for a completely polarised wave, the anisotropy equals 1 (the second eigenvalue and the entropy equals zero) [121, 135]. A method for an unsupervised classification of quad-polarimetric SAR data by only using  $H$  and  $\bar{\alpha}$ , is called the  $H-\bar{\alpha}$  classification scheme. The latter proposes to project these two parameters onto the  $H-\bar{\alpha}$  plane (Fig. 2.26). Here,  $\bar{\alpha}$  provides information about the type of dominant scattering mechanism and  $H$  indicates the number of strong, independent scattering mechanisms.

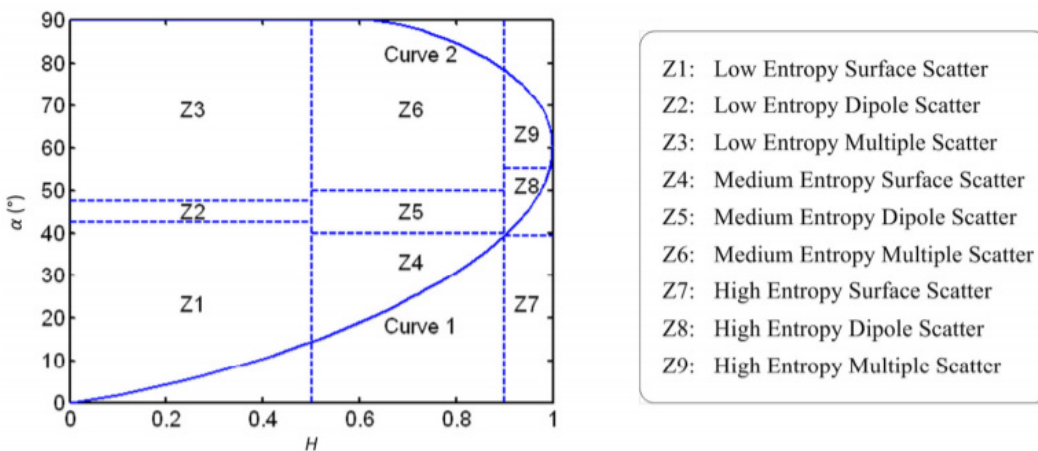


**Figure 2.26:** The  $H/\alpha$  plane and subsections connected to physical properties for the full-pol scenario [136].



This plane is divided into different segments, each corresponding to different physical meanings.  $Z1$  is associated with Bragg scattering and single bounce surface scattering,  $Z2$  is volume scattering from isotropic dipoles,  $Z3$  is for dihedral scatterers often from urban areas, in  $Z4$  we can identify surface roughness propagation effects (e.g. vegetation),  $Z5$  identifies scattering from vegetation,  $Z6$  is characterised by double bounce scattering from forests,  $Z7$  has a high degree of randomness,  $Z8$  is caused by a cloud of anisotropic needles (e.g. vegetation) and finally  $Z9$  is attributed to a completely depolarised event as it can be thermal noise [74].

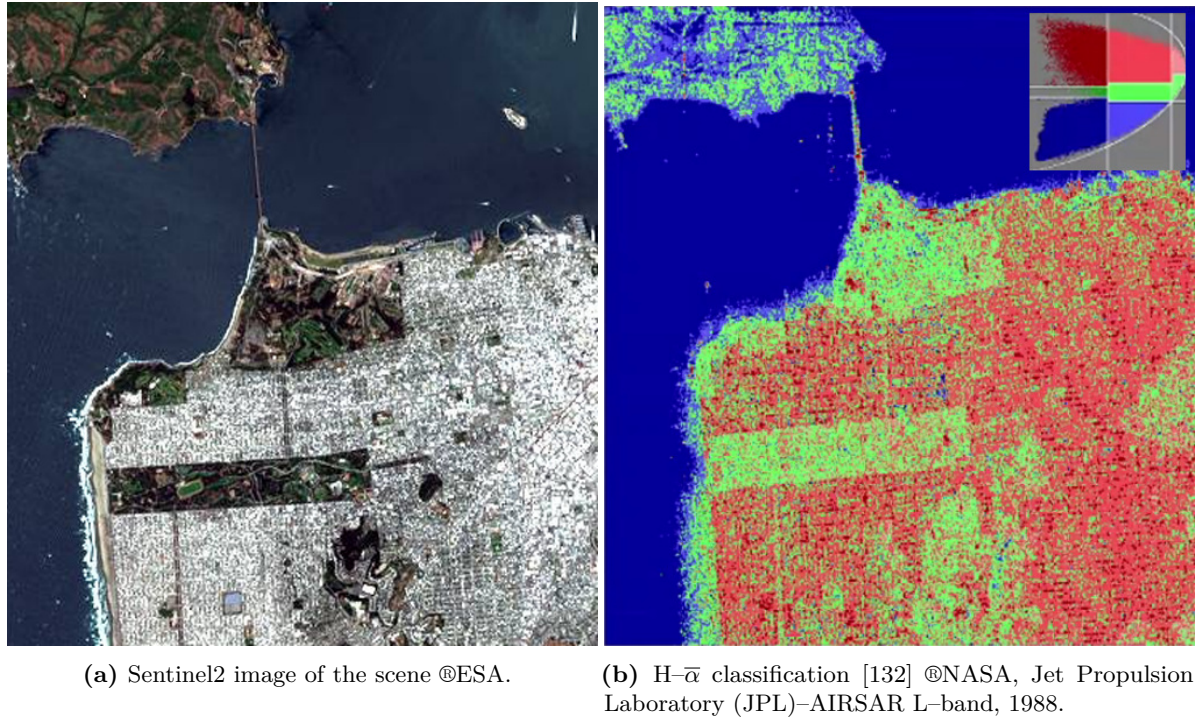


**Figure 2.27:** Comparison between a Sentinel2 scene and the  $H-\bar{\alpha}$  classification.

Figure 2.27b shows the first example of this classification approach, applied to the area of San Francisco. This reconstruction of the scattering mechanisms on the ground using the eigen-based information of the  $[T]$ -matrix was done without any a priori ground knowledge. Much research was done to further improve this concept (e.g. [137, 134, 133, 138]). Fang and Wen [139] later tried to add the intensity as another information layer to this concept, called the  $H-\bar{\alpha}$ -SPAN classification. They divided each of the existing nine categories into three different parts, according to the level of intensity ('low', 'medium' and 'high'), resulting in 27 categories. Another problem was the location of the boundaries between the different areas on the  $H-\bar{\alpha}$  plane, which are placed with a certain degree of arbitrariness. Nonetheless, it emphasises the geometrical segmentation of physical scattering processes. To solve this problem, the Cloude-Pottier scheme is combined with a Wishart classifier [140]. It uses the complex Wishart distribution and can broadly be applied since it is independent of the number of looks and of the polarisation basis. More recently, it was combined with machine learning techniques [141]. To follow a k-mean classification procedure, cluster centres are used for each of the defined areas on the  $H-\bar{\alpha}$  plane. Figure 2.28a shows an exemplary result after four iterations. Each colour represents one of the eight segments on the  $H-\bar{\alpha}$  plane which have a physical representation. In an improving next step, the anisotropy was added, producing an improved classification in 16 different categories (Figure 2.28b). A further improvement of the unsupervised PolSAR classification was then proposed by Lee et. al [142] with the idea to better preserve existing scattering mechanisms and to link the segmentation better to physics.



(a)  $H-\bar{\alpha}$  Wishart classification (four iterations).      (b)  $H-A-\bar{\alpha}$  Wishart classification (four iterations).

**Figure 2.28:** Comparison between the  $H-A-\bar{\alpha}$  Wishart classification and the  $H-\bar{\alpha}$  Wishart classification [74].

After applying the Freeman & Durden decomposition, the pixels are then grouped into three categories, according to the main scattering mechanisms. The classification is performed separately in these three categories before the three resulting clusters are finally merged.

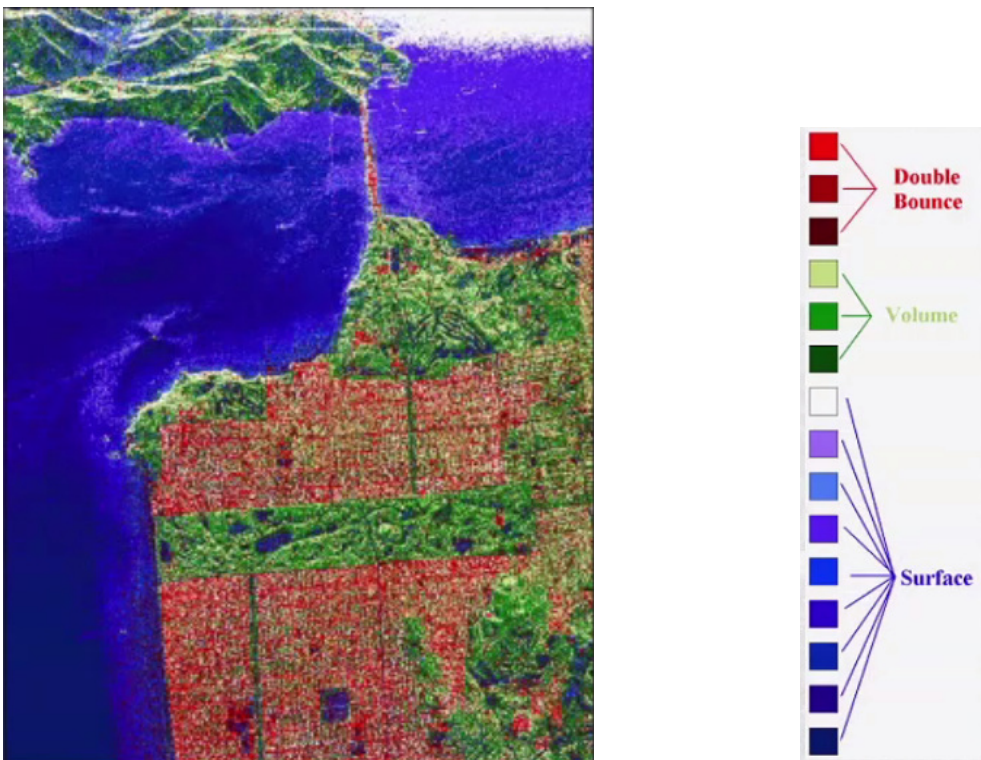


**Figure 2.29:** Freeman Wishart Classification [142].



The number of categories can be chosen depending on the predominance of a specific scattering mechanism, as it is the case for surface scattering in Fig. 2.29.

### 2.3.6.3 Model-Based Decompositions

The model-based decompositions use physical models to characterise the scattering mechanisms. Following that, each pixel consists of contributions of different proportion from the postulated scattering mechanisms. Freeman and Durden [125, 91] developed that idea first and their Freeman–Durden decomposition assumes that target scattering can be expressed as the sum of three scattering mechanisms [73]:

$$\langle [T] \rangle = f_S \langle [T_S] \rangle + f_D \langle [T_D] \rangle + f_V \langle [T_V] \rangle \quad (2.85)$$

The components are called single scattering [ $T_S$ ], double scattering [ $T_D$ ] and volume scattering [ $T_V$ ]. The associated coherency matrices for single scattering can be represented by the Fresnel coefficients ( $R$ ) for H and V of the scattering matrix [ $S$ ]:

$$[S_S] = \begin{bmatrix} R_H & 0 \\ 0 & R_V \end{bmatrix} \Rightarrow \underline{k}_S = \begin{bmatrix} R_H + R_V \\ R_H - R_V \\ 0 \end{bmatrix} \quad (2.86)$$

This considers the contributions from the HH channel and from the VV channel. There is no depolarisation and therefore the off-diagonal elements are zero as well as the last element of the target vector  $\underline{k}_S$ . This assumption holds when the first component models are not tilted and for slightly rough first-order Bragg surfaces. Using  $\underline{k}_S$ , the corresponding coherency matrix of that single scattering mechanism can be constructed as:

$$\langle [T_S] \rangle = f_S \begin{bmatrix} |\beta + 1|^2 & (\beta + 1)(\beta - 1)^* & 0 \\ (\beta + 1)(\beta - 1)^* & |\beta - 1|^2 & 0 \\ 0 & 0 & 0 \end{bmatrix} \quad f_S = |R_V^2| \quad \beta = \frac{R_H}{R_V} \quad (2.87)$$

where  $f_S$  represents the power contribution of the single bounce scattering and  $\beta$  is the ratio between the Fresnel coefficients. For double bounce, the contributions from the ground ( $R_G$ ) and from the trunks of trees or from a building ( $R_T$ ) have to be taken into account for HH and VV channels and there is no depolarisation. Accordingly, the [ $T$ ]-matrix for double bounce scattering can be written in the form of:

$$\langle [T_D] \rangle = f_D \begin{bmatrix} |\alpha - 1|^2 & (\alpha - 1)(\alpha + 1)^* & 0 \\ (\alpha - 1)(\alpha + 1)^* & |\alpha + 1|^2 & 0 \\ 0 & 0 & 0 \end{bmatrix} \quad f_D = |R_{GV}R_{TV}| \quad \alpha = \frac{R_{GH}R_{TH}}{R_{GV}R_{TV}} \quad (2.88)$$

introducing  $f_D$  as the proportion factor of the double bounce scattering and  $\alpha$  which is the ratio between the corresponding Fresnel coefficients. The third model, corresponding to volume scattering, considers the source scattering objects on the ground as randomly oriented, very

thin cylinder-like scatterers. In fact, this coherency matrix attempts to model the scattering coming from a cloud of randomly oriented dipoles. To do that, the scattering matrix of an oriented dipole is calculated by multiplying the  $[S]$ -matrix of a horizontal dipole with a rotation matrix:

$$[S_\theta] = [U_2(\theta)]^T [S] [U_2(\theta)] \quad (2.89)$$

Then, the average overall possible rotation is taken by the integration over zero to  $2\pi$ , multiplied by the distribution of the orientation  $P(\theta) = \frac{1}{2\pi}$ :

$$\langle [T_V] \rangle = \langle [T_\theta] \rangle = \sum_0^{2\pi} [T_V] P(\theta) d(\theta) \quad (2.90)$$

Using that, we can define the theoretical corresponding coherency matrix:

$$\langle [T_V] \rangle = \frac{f_V}{3} \begin{bmatrix} 4 & 0 & 0 \\ 0 & 2 & 0 \\ 0 & 0 & 2 \end{bmatrix} \quad (2.91)$$

The sum of these three coherency matrices (see Equ. 2.85) should explain the total scattering scenario. Bringing it all together, five unknown real coefficients face four observed equations:

$$\begin{aligned} T_{11} &= f_S |\beta + 1|^2 + f_D |\alpha - 1|^2 + \frac{4f_V}{3} \\ T_{12} &= f_S (\beta + 1)(\beta - 1)^* + f_D (\alpha - 1)(\alpha + 1)^* \\ T_{22} &= f_S |\beta - 1|^2 + f_D |\alpha + 1|^2 + \frac{2f_V}{3} \\ T_{33} &= \frac{2f_V}{3} \end{aligned} \quad (2.92)$$

To make the system of equations solvable, one unknown, either  $\alpha$  or  $\beta$  is set equal to 1 [125], according to the result of:

$$\Re(\langle S_{XX} S_{YY}^* \rangle - \frac{f_V}{3}) \quad (2.93)$$

If it is positive,  $\alpha$  is set to 1; if it is negative,  $\beta$  is set to one. Then, the reconstruction of all five unknowns is possible:

$$\begin{aligned} SPAN &= \langle T_{11} \rangle + \langle T_{22} \rangle + \langle T_{33} \rangle = f_S (1 + \beta^2) + f_D (1 + |\alpha|^2) + \frac{2f_V}{3} \\ f_S (1 + \beta^2) &\Rightarrow \text{single (odd) bounce scattering} \\ f_D (1 + |\alpha|^2) &\Rightarrow \text{double bounce scattering} \\ \frac{2f_V}{3} &\Rightarrow \text{volume scattering} \end{aligned} \quad (2.94)$$

where the proportions of the power of the share of the three different scattering mechanisms are estimated. Using them, we can reconstruct the equivalent coherency matrices and the equivalent covariance matrices of the single scattering mechanisms.



(a) Eigenanalysis Decomposition.

(b) Freeman/Durden Decomposition.

**Figure 2.30:** Comparison of Eigenanalysis decomposition and Freeman/Durden Decomposition. Single bounce in blue, double bounce in red and volume in green [74].

The visual examination of the results shows that, compared to the eigenanalysis, (Fig. 2.30a), this model overestimates volume scattering (Fig. 2.30b). Further, this model is only valid for areas where reflection symmetry is given [27].

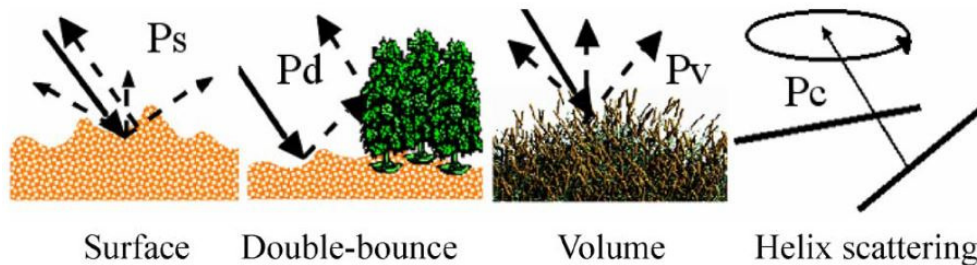


**Figure 2.31:** Illustration of the Yamaguchi four-components power decomposition scattering model [143].

Yamaguchi et. al. [98, 144, 145] presented the four-components scattering model (Fig. 2.31). It extends the model by Freeman & Durden by introducing a fourth component called the helix scattering:

$$\langle [T] \rangle = f_S \langle [T_S] \rangle + f_D \langle [T_D] \rangle + f_V \langle [T_V] \rangle + f_H \langle [T_H] \rangle \quad (2.95)$$

This helix scattering term is useful to describe artificial objects with a high correlation between the co-polarisation and the cross-polarisation channels. Its  $[S]$  and  $[T]$  matrices are defined as:

$$[S]_{\pm Helix} = \frac{1}{2} \begin{bmatrix} 1 & \pm j \\ \pm j & -1 \end{bmatrix} \quad (2.96)$$

$$\langle [T]_{Helix} \rangle = \frac{1}{2} \left\langle \begin{bmatrix} 0 & 0 & 0 \\ 0 & 1 & \pm j \\ 0 & \pm j & 1 \end{bmatrix} \right\rangle \quad (2.97)$$

This new parameter helps to mitigate the over-estimation of the volume scattering (compare Equ. 2.97 and Fig. 2.30b). It describes anti-symmetric, helix-type scattering mechanisms that transform the incidence wave into its orthogonal circular polarisation state [42]. Yamaguchi et. al continued his research and developed augmented variants of their first model. Singh et al. presented additional modelling approaches [146, 147, 148]. Based on these results, research continued and models including decompositions with four, five and six components were developed [149, 150, 151].

Still, it is an unresolved issue whether this kind of decomposition can handle oriented scatterers. For example urban areas with blocks aligned in regular patterns of  $45^\circ$  relative to the sensor's LoS are interpreted as vegetation/forests (the light green triangle in the centre of the right-hand edge of Fig. 2.32a and Fig. 2.32b).



(a) Singh Decomposition.

(b) Yamaguchi Decomposition.

**Figure 2.32:** Comparison between Singh decomposition and Yamaguchi decomposition. Single bounce in blue, double bounce in red and volume in green [74].

This subsection gave an overview of different ways to work on target decomposition with polarimetric quad-pol (or full-pol) data and the physical interpretation that can be derived. In the next section we present the work with dual-pol polarimetric SAR data, addressing the challenges, possibilities and shortcomings.

### 2.3.7 The Dual-Pol Case

SAR sensors are, in general, capable of different acquisition modes. In terms of the polarisation-wise information depth, there are quad (or full)-polarisation, dual-pol and single-pol modes. In contrast to the quad-polarisation mode, where a radar system coherently transmits and receives two polarisations, in dual-pol mode it would transmit either one polarisation (cross-pol modes: HV HH or VH VV) or two polarisations (co-pol mode: HH VV) during one acquisition while receiving the backscattering of two orthogonal polarisation components of the scattered EM-wave. If the sensor receives these two polarisations coherently, this corresponds to the measurement of the full state of polarisation of the scattered signal for a fixed illumination [152]. We can describe the data acquired by that dual-pol system using Jones vectors.

Single-pol and dual-pol modes miss a part of the polarimetric information, but can be advantageous in terms of costs, data rate and coverage when compared to the full-pol mode. Several methods developed in the field of wave polarimetry for the full-pol case can be adapted to dual-pol data. But when it comes to the physical interpretation of the results, the dual-pol case has some limitations since it is only possible to reconstruct a section of the  $[S]$ -matrix: either the first column (for cross-pol HV HH), the second column (for cross-pol VH VV) or the main diagonal (for co-pol HH VV).

As mentioned, the output of a dual-pol system can be described by the complex Jones vector  $\underline{E}$ :

$$\underline{E}_S = \begin{bmatrix} S_{xx} \\ S_{yx} \end{bmatrix} \quad (2.98)$$

In the complex domain, the Jones vector presents two amplitudes and one phase value (the latter is the relative phase calculated between the two elements of the vector). When approaching the wave through the polarisation ellipse, the three necessary parameters are the amplitude  $A$ , the orientation angle  $\phi$  and the ellipticity angle  $\chi$ .

The 2x2 covariance matrix is derived similarly to the 3x3 full-pol covariance  $[C]$ -matrix. Depending on whether the transmitted wave is H or V polarised, for dual cross-pol modes  $[C]$  looks like [152]:

$$\langle [C_H] \rangle = \langle \underline{E} \cdot \underline{E}^{*T} \rangle = \begin{bmatrix} \langle S_{HH} S_{HH}^* \rangle & \langle S_{HH} S_{HV}^* \rangle \\ \langle S_{HV} S_{HH}^* \rangle & \langle S_{HV} S_{HV}^* \rangle \end{bmatrix} \quad \langle [C_V] \rangle = \langle \underline{E} \cdot \underline{E}^{*T} \rangle = \begin{bmatrix} \langle S_{VV} S_{VV}^* \rangle & \langle S_{VV} S_{VH}^* \rangle \\ \langle S_{VH} S_{VV}^* \rangle & \langle S_{VH} S_{VH}^* \rangle \end{bmatrix} \quad (2.99)$$

In the case of coherent transmission and reception of both orthogonal polarisation states (dual co-pol), the covariance matrix looks like:

$$\langle [C_{H,V}] \rangle = \langle \underline{E} \cdot \underline{E}^{*T} \rangle = \begin{bmatrix} \langle S_{HH} S_{HH}^* \rangle & \langle S_{HH} S_{VV}^* \rangle \\ \langle S_{VV} S_{HH}^* \rangle & \langle S_{VV} S_{VV}^* \rangle \end{bmatrix} \quad (2.100)$$

Using the Pauli matrices group, the four real independent Stokes parameters can be derived for the dual-pol case:



$$\langle \underline{E} \cdot \underline{E}^{*T} \rangle = \frac{1}{2} \begin{bmatrix} g_0 + g_1 & g_2 - jg_3 \\ g_2 + jg_3 & g_0 - g_1 \end{bmatrix} \quad (2.101)$$

and with them the Stokes vector and the eigenvectors can be constructed (see Formula 2.43 further up). The wave entropy ( $H_w$ ) and the wave anisotropy ( $A_w$ ) for the dual-pol case are:

$$A_w = \frac{\lambda_1 - \lambda_2}{\lambda_1 + \lambda_2} \quad H_w = - \sum_{i=1}^2 P_i \log_2 P_i \quad \text{with} \quad P_i = \frac{\lambda_i}{\lambda_1 + \lambda_2} \quad (2.102)$$

An unambiguous physical interpretation of dual-pol data is impossible since one polarimetric channel is missing. The number of scattering mechanisms cannot be unambiguously identified. Therefore, in the dual cross pol-case,  $H_w$  provides only information about the degree of randomness of the polarisation of the scattered wave.  $H_w$  and  $A_w$  range from 0 to 1. Since the eigenvalues are invariant under any unitary similarity transformation of the polarisation basis,  $H_w$  and  $A_w$  are base-invariant as well.

The Shannon Entropy  $SE$  can be calculated for the dual-pol case by adapting it to the 2x2  $[C]$ -matrix. It was described by Morio et al. [153] and Réfrégier and Morio [154] as a sum of three parts which relates to the intensity ( $SE_I$ ), to the degree (or the change) of polarisation ( $SE_P$ ) and to the intrinsic degrees of coherence ( $SE_\mu$ ). In the dual-pol case, only the first two components are there:

$$SE = \log(\pi^2 e^2 |C|) = SE_I + SE_P \quad (2.103)$$

In the full polarimetric scenario, the anisotropy is constructed using the two smallest eigenvalues while the entropy consists of all three eigenvalues. Therefore, the anisotropy provides complementary information and improves the physical interpretation of the entropy. In the dual-pol case, on the other hand, this is no longer true and  $H_w$  and  $A_w$  provide the same information since they are constructed using the same two eigenvalues.  $A_w$  is equivalent to the DoP.

Still, dual pol enables us to characterise scattering mechanisms. In dual cross-pol mode, the 2x2 coherency matrices for depolarisation by random surface and volume scatterers, volume scattering from a random cloud of anisotropic particles Bragg scattering from smooth surfaces can be expressed [152, 155]. In the dual co-pol case (HH VV), the 2x2 coherency  $[T]$ -matrix can be formed which allows for the identification of surface scattering, dipole scattering and dihedral scattering [136]:

$$\langle [T_{H,V}] \rangle = \langle \underline{E} \cdot \underline{E}^{*T} \rangle = \begin{bmatrix} \langle |S_{HH} + S_{VV}|^2 \rangle & \langle (S_{HH} + S_{VV})(S_{HH} - S_{VV})^* \rangle \\ \langle (S_{HH} - S_{VV})(S_{HH} + S_{VV})^* \rangle & \langle |S_{HH} - S_{VV}|^2 \rangle \end{bmatrix} \quad (2.104)$$

In [42] the authors discuss the performance of a broad spectrum of different SAR applications and methods to be used with single-pol and dual-pol data in comparison to quad-pol data. It turns out, that there are a number of examples where the dual-pol mode does not have a very large loss of performance, although it is always worse than quad-pol. For example, for forest

classification applications, Papathanassiou et. al recommend the use of dual co-pol covariance matrices (Equ. 2.100) but warn against performance loss and ambiguities compared to the full-pol case. In an approach to cropland classification, Lopez-Sanchez et al. [156] found that for crop classification with multi-temporal airborne SAR, the dual cross-pol data in C-band delivers results of similar quality to the full-pol data. Migliaccio et al. [107] describe dual co-pol data as potentially capable of deriving maritime parameters such as sea ice type, snow and ice thickness and surface roughness features. Tests for the identification of metallic objects with a variety of detection algorithms show that the results achieved with dual-pol data are comparable in some situations.

### 2.3.7.1 Polarimetric Decomposition for the Dual-Pol Case

Over the last decades, most attention was paid to developing decomposition methods for full-pol data (e.g. [157, 74, 158, 27]) and on the utilisation of compact polarimetry (e.g. [159, 160, 161, 162]). Nevertheless, well-established concepts for the decomposition of dual-pol data have also been designed (e.g. [152, 163, 164]). Dual-pol data has the advantages of a better spatial resolution compared to full-pol data (given the same coverage) and has a higher target to noise ratio.

Whereas platforms such as Radarsat-2, S-1 or ALOS-2 provide only dual cross-pol data (HV HH or VH VV channels), other systems like TSX, TDX or CSG are capable of acquiring dual co-pol data (HH VV). This implies phase-coherency and allows for the investigation of the polarimetric phase relation between the two channels which is an important discriminator between surface (odd bounce) and double bounce (even bounce) scattering [157, 27].

Examples of studies and application development in this field include the eigen-based Entropy/Alpha decomposition for dual polarimetric data [152], a new decomposition technique combining the model-based and the eigen-based approach [164], investigations of the usage of the dual co-pol (and the dual cross-pol) mode for land cover characterisation (e.g. [165, 166]), investigations into the phase relation of HH and VV (e.g. [156, 167]) and marine detection (e.g. [112, 168, 103, 169]).

#### Eigenanalysis-based Decomposition for the Dual-Pol Case

When dual-pol data the two eigenvectors and the two real eigenvalues  $\lambda_1 > \lambda_2$  can be derived and the mean Jones vector can be reconstructed using the averaged parameters:

$$\underline{E}_0 = \sqrt{\bar{\alpha}} \begin{bmatrix} \cos \alpha \\ \sin \alpha e^{j\delta} \end{bmatrix} \quad (2.105)$$

Assessed against currently available information, a meaningful interpretation of the  $\delta$  parameter has not yet been found [74]. According to Cloude & Pottier, for Bragg surfaces  $\delta$  is constant with the angle of incident and close to  $\pi$  [87].

The physical interpretation of the  $\bar{\alpha}$  parameter, constructed from dual cross-pol data and therefore using only two eigenvalues, allows only for statements regarding the degree of polarisation. Conclusions regard the occurrence of specific types of scattering mechanisms, as is possible in the full-pol case, cannot be made. With dual co-pol data, canonical scattering mechanism can be distinguished (Fig. 2.33).

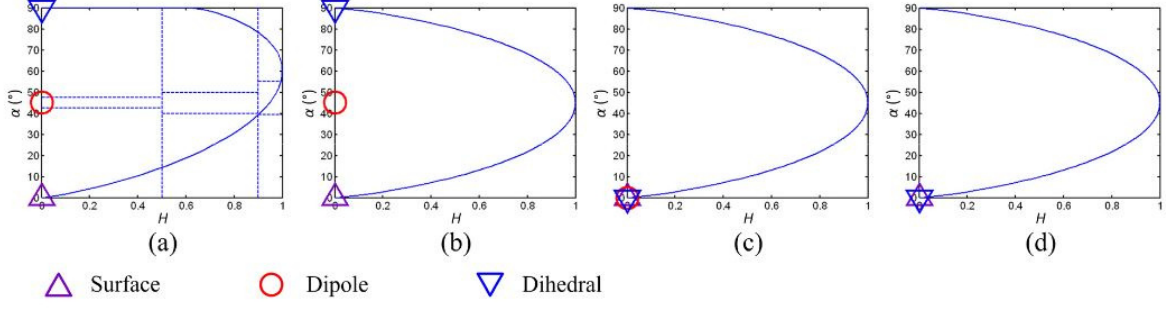


**Figure 2.33:** Three canonical scatterers in the  $H-\bar{\alpha}$  planes with: (a) quad-polarisation, (b) dual co-pol (HH VV); (c) dual cross-pol (HV HH); (d) dual cross-pol (VH VV) [136].

The analysis of the entropy- $\alpha$  plane for dual-pol channel combination involves unresolved problems regarding the physical interpretation since the third eigenvalue is missing. Furthermore, the distribution of scatterers in the  $H-\alpha$  planes of the dual cross-pol channel combinations (HV HH and VH VV) is quite different from that in full-pol mode (Fig. 2.34).

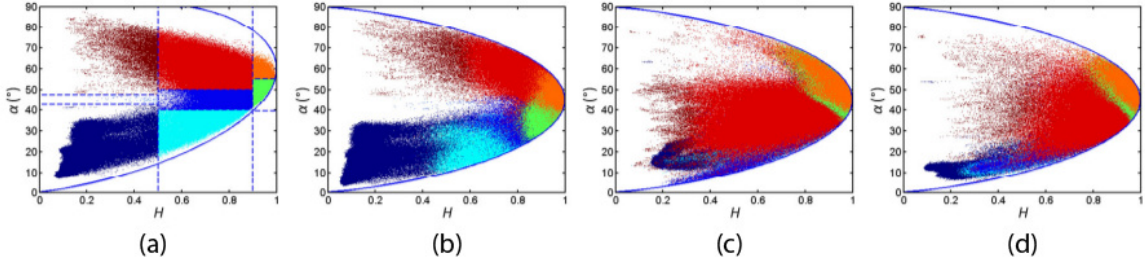


**Figure 2.34:** Scattering plot of the  $H-\bar{\alpha}$  planes with: (a) quad-polarisation, (b) dual co-pol (HH VV); (c) dual cross-pol (HV HH); (d) dual cross-pol (VH VV) [136].

The identification of Z3 (low entropy multiple; dark red), Z4 (medium entropy surface; cyan), Z5 (medium entropy dipole; blue) and Z8 (high entropy dipole; green) is the biggest problem in cross-polarised modes (for the  $Z$ -zones mentioned please see Fig. 2.26 in chapter 2.3.6.2). Meanwhile, dual co-pol data is seen as a suitable alternative to full-polarisation SAR in certain cases; in particular for the discrimination of scattering from an isotropic surface, horizontal dipole and isotropic dihedral [136].

### Model-based Decomposition for the Dual-Pol Case

In the full-pol case, the three-component decomposition works with the  $3 \times 3$  coherency matrix and, after the unitary transformation, with the  $3 \times 3$  covariance matrix as well. In the dual-pol case, the covariance matrix is a  $2 \times 2$  matrix which is only a subsection of the  $3 \times 3$  covariance matrix. Which part of the  $3 \times 3$   $[C]$ -matrix is represented, depends on the polarimetric channel combination. This implies that the well-established full-pol model-based decomposition approach cannot be applied to the dual-pol case without taking into account the loss of a part of the information. For the dual cross-pol variant (HV HH or VH VV), the changes of the models for the scattering mechanisms are the following:

$$\text{single bounce} : \langle [C_{3S}] \rangle = f_S \begin{bmatrix} \beta^2 & 0 & \beta \\ 0 & 0 & 0 \\ \beta & 0 & 1 \end{bmatrix} \Rightarrow \langle [C_{2S}] \rangle = f_S \begin{bmatrix} \beta^2 & 0 \\ 0 & 0 \end{bmatrix} \quad (2.106)$$



$$\text{double bounce} : \langle [C_{3D}] \rangle = f_D \begin{bmatrix} \alpha^2 & 0 & -\alpha \\ 0 & 0 & 0 \\ -\alpha & 0 & 1 \end{bmatrix} \Rightarrow \langle [C_{2D}] \rangle = f_D \begin{bmatrix} \alpha^2 & 0 \\ 0 & 0 \end{bmatrix} \quad (2.107)$$

$$\text{volume scattering} : \langle [C_{3V}] \rangle = f_V \begin{bmatrix} 1 & 0 & \frac{1}{3} \\ 0 & \frac{2}{3} & 0 \\ \frac{1}{3} & 0 & 1 \end{bmatrix} \Rightarrow \langle [C_{2V}] \rangle = f_V \begin{bmatrix} 1 & 0 \\ 0 & \frac{1}{3} \end{bmatrix} \quad (2.108)$$

For the dual co-pol (or twin-pol) mode (HH VV) the models for the scattering mechanisms can be defined as:

$$\text{single bounce} : \langle [C_{3S}] \rangle \Rightarrow \langle [C_{2S}] \rangle = f_S \begin{bmatrix} \beta^2 & \beta \\ \beta & 1 \end{bmatrix} \quad (2.109)$$

$$\text{double bounce} : \langle [C_{3D}] \rangle \Rightarrow \langle [C_{2D}] \rangle = f_D \begin{bmatrix} \alpha^2 & -\alpha \\ -\alpha & 1 \end{bmatrix} \quad (2.110)$$

$$\text{volume scattering} : \langle [C_{3V}] \rangle \Rightarrow \langle [C_{2V}] \rangle = f_V \begin{bmatrix} 1 & \frac{1}{3} \\ \frac{1}{3} & 1 \end{bmatrix} \quad (2.111)$$

The scattering vectors and coherency matrices for an isotropic surface, a horizontal dipole, and an isotropic dihedral for HH VV mode are:

$$\langle [T_S] \rangle = \begin{bmatrix} 2 & 0 \\ 0 & 0 \end{bmatrix}, \quad \langle [T_D] \rangle = \frac{1}{2} \begin{bmatrix} 1 & 1 \\ 1 & 1 \end{bmatrix}, \quad \langle [T_V] \rangle = \begin{bmatrix} 0 & 0 \\ 0 & 2 \end{bmatrix}, \quad (2.112)$$

$$k_S = [\sqrt{2}, 0]^T, \quad k_D = \left[ \frac{\sqrt{2}}{2}, \frac{\sqrt{2}}{2} \right]^T, \quad k_V = [0, \sqrt{2}]^T \quad (2.113)$$

The scattering vectors for the three canonical scatterers are identical in HV HH mode:

$$k = [1, 0]^T \quad (2.114)$$

And in VH VV mode, they are:

$$k_S = [1, 0]^T, \quad k_D = [0, 0]^T, \quad k_V = [-1, 0]^T \quad (2.115)$$

Collecting all the independent parameters for the three scattering mechanisms following the five-parameter decomposition model, the covariance matrix for the full-pol mode features five parameters, the dual cross-pol mode shows only two observables and the dual co-pol mode provides three observables. It goes without saying that it is not possible to reconstruct all five parameters with the two, nor the three observables of the dual-pol cases.

## 2.4 Complex SAR Image Spectral Analysis

Similar to polarimetry and interferometry, sublook (in literature, it is also called subaperture) approaches add another dimension of information. And this can help to solve the detection problem. The foundation of this technique is to extract sublook images from a SAR image and to analyse their cross correlation. Gierull [170] describes it as an active research field with several variants. The main detectors use one of the following processing:

- magnitude of the normalised complex cross correlation called sublook coherence
- magnitude of the complex cross correlation called Hermitian Inner Product

A sublook can be extracted as a sub-band of the SLC in the frequency domain. Hence, it has only a portion of the available system bandwidth, a lower resolution and a different central frequency [54, 171]. Theoretically, more than two sublooks can be created. A partial overlap of the sublook bandwidths is possible. Brekke et al. [172] investigated a continuum of sublook extraction strategies. They proposed a partial overlap to enhance the contrast. The first detector was proposed by Arnaud that connected this to the along-track interferometric coherence between the front and the rear sublook of a SLC SAR image [173]. This concept was then adapted for ship detection with polarimetric data [54, 96].

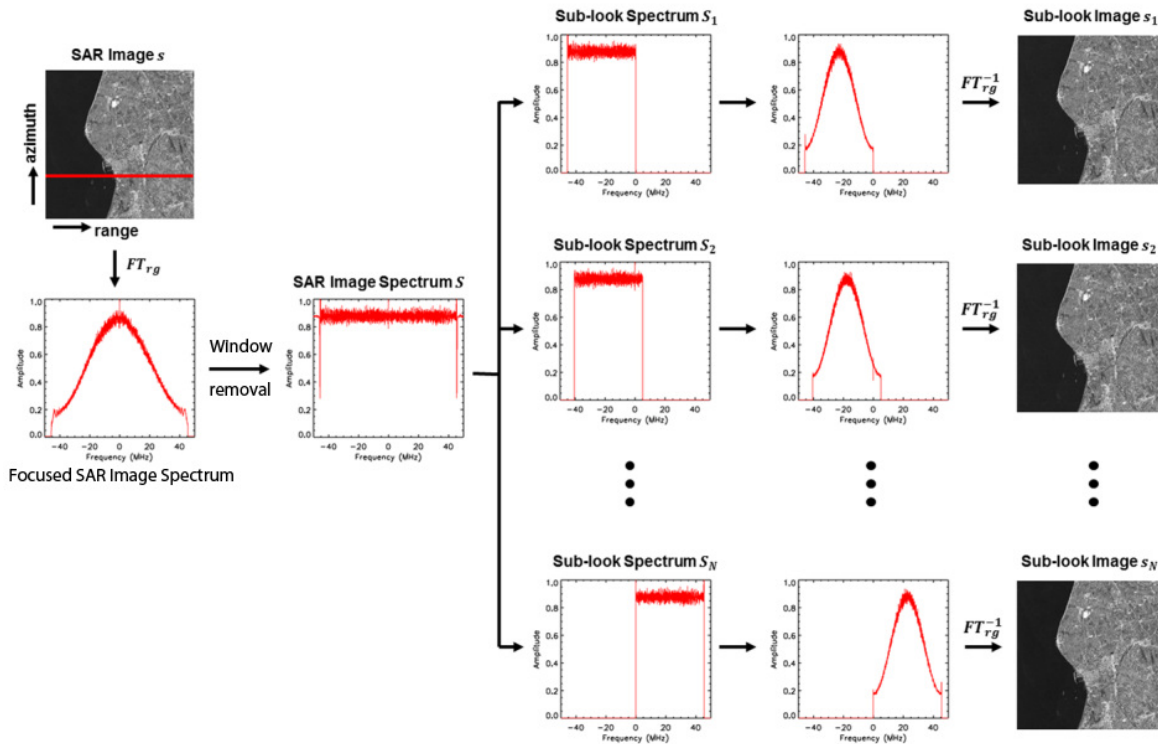


**Figure 2.35:** The sublook generation process in range direction, based on [171] and [36].

The sublook cross-correlation magnitude (SCM) has been proposed to improve the contrast between small ships and the ocean surface clutter using intensity images [174]. It takes advantage of the fact that small waves, which are responsible for most radar return from the water surface (see section 3.1.3), decorrelate faster than maritime artificial objects, including boats and ships. Water surfaces decorrelate in less than 0.05 seconds at C-band [175]. In contrast, the local sublook complex correlation of an ideal point scatterer will be strong because the phase contribution of the target object is slow varying throughout the subimages.

Therefore, the object should remain coherent over the acquisition of the sublooks, even if the scatterer has not a strong contrast with the sea clutter in the intensity image [54]. For more on detection with sublook images please see chapter 3.4.1.2.

The creation of the sublook images (Fig. 2.35) can be done in azimuth and in range direction. Sublook extraction in range enables the testing of the frequency stability of the target object, since the radar response of an ideal point scatterer is unaffected by minor frequency changes [36, 171, 35]. In the azimuth (or Doppler) direction, the sublooks show the objects on the ground under different viewing angles (i.e. looking rearward or forward). According to the viewing direction, the sublooks can be called front-look and rear-look [54]. With azimuth sublooking, the objects on the ground can be analysed for the stability of their radar response under different viewing angles. A perfect point scatterer is isotropic and static corner reflectors stay coherent to a high extent whereas anisotropic structures may show a varying radar response when illuminated from different positions. In the case of moving objects, zero Doppler will be located in a different position which displaces them along the azimuth (the well-known azimuth shift or train-off-the-track effects) [171, 96]. Pitching (i.e. up/down rotation of a vessel about its transverse or port-starboard axis) of maritime vehicles leads to displacement, deviating from the azimuth direction and a skewed representation of the vessel in the SAR image [176]. Further, the focusing will not be successful, leading to smearing effects and increasing the false negative rate for coherent detectors [171].

The right choice seems problematic. Azimuth band splitting is generally considered to be preferable since it better preserves the spatial resolution and the object details [172]. Other literature recommends sublook generation in range direction to preserve the higher spatial resolution of the SAR geometry in range. In this case, additional preprocessing or post processing is suggested to remove azimuth ambiguities and artefacts [177]. For the detection of constant scatterers, such as non-moving maritime vehicles, sublooking in range is seen as the standard choice [36]. For this research, we prioritised the spatial resolution due to the small size of the object to detect and limited ourselves to the range variant.

Ideally, sublooks are derived by filtering raw SAR data (Level 0) before focusing. But raw data is often not available due to the data policies of most space agencies and satellite operators. Standard image preprocessing workflows can be considered to preserve all the information in the frequency domain. The only exception is the windowing operation which reduces unwanted sidelobes. Therefore, sublook images can be directly derived from focused SAR data by [36]:

- conversion of the SAR image to the frequency domain by application of a Fourier transformation in range ( $FT_{rg}$ )
- removal of the range window
- selection of a portion of the bandwidth of the image by multiplying the spectrum by a rectangular weighting function (frequency domain)
- reapplication of a range window for each sublook
- conversion of the sublooks back to the time domain by application of an inverse Fourier transformation in range ( $FT_{rg}^{-1}$ )

This process does not require any information on the sensor used to acquire the SAR data.

## 2.5 Polarimetric Interferometric SAR

SAR interferometry (InSAR; [178]) coherently combines images from acquisitions, separated by a baseline. The baseline should not exceed a certain critical amount, where the spectra of the two acquisitions do not overlap anymore. In such a case, coherency is lost, the two images cannot be matched and interferometric analyses cannot be applied. The interferogram is constructed by using the phase difference of the two images.

A fundamental interferometric measurement is the complex interferometric coherence. This is the normalised interferometric cross correlation and it is a complex number including the interferometric phase. The magnitude, often just referred to as coherence, is a very prominent observable for InSAR. [178]. When time is included as a factor ('multidimensional SAR imagery'), the coherence is an important tool to track changes. Multitemporal SAR data is not generally a stationary, but a stochastic process which reflects the complexity of the environment. Furthermore, InSAR phase data contains information about the topography of the earth's surface and is very useful for the generation of DEMs of the terrain.

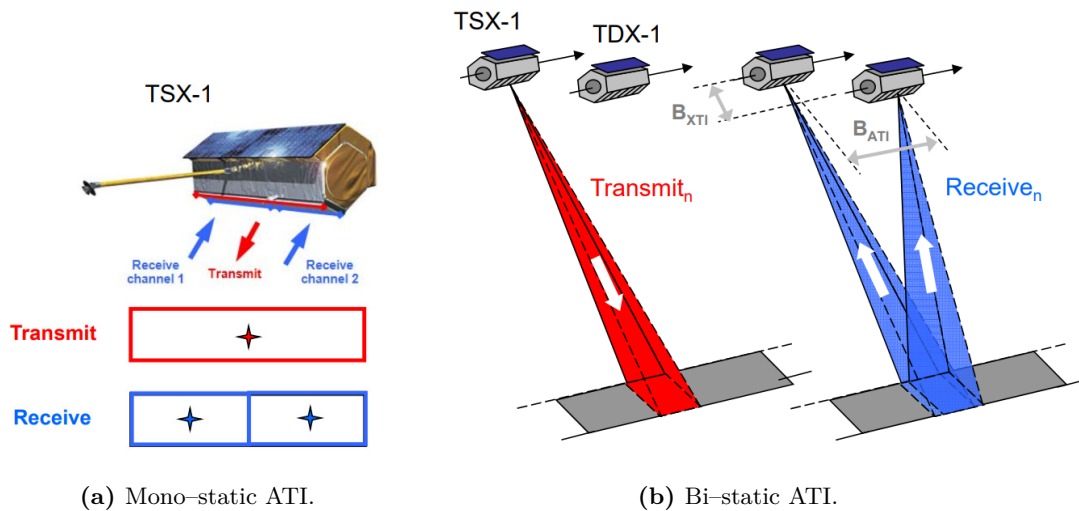


**Figure 2.36:** Along Track Interferometry (ATI) acquisition modes [179].

Two different interferometric modi operandi are used, depending on the sensor constellation setup: along-track interferometry (ATI) and across-track interferometry (XTI). In the case of ATI, the spatial baseline is parallel to the flight direction of the sensor. It generally involves a time displacement between the acquisitions even when a tandem constellation is used. ATI enables an estimation of the velocity of objects on the ground. TanDEM-X can perform a mono-static and a bi-static ATI.

The mono-static setup (Fig. 2.36a) only needs one sensor which divides its antenna 'electrically' into two smaller, independent antennas for reception. In the TSX's Dual Receive Antenna (DRA) mode, the baseline is only 1.2 meters, which decreases its sensitivity to ground motion. Further, the use of aperture switching reduces the effective PRF of the receiving channel.

In the bi-static case (Fig. 2.36b), the ATI baseline  $B_{ATI}$  can vary and 50 meters is often selected, making the mode highly sensitive even to motions that deviate from the LoS. The different flight paths of the two satellites TSX and TDX lead to a across track baseline  $B_{XTI}$  and phase contributions from motion and topography. It is possible to single out the phase

contribution from motion (ATI), but only in areas with constant elevation and under small  $B_{XTI}$  [179], using this formula:

$$\phi_{ATI} = \frac{4\pi B_{ATI}}{\lambda v_s} v_g \sin \Theta \quad (2.116)$$

where  $v_s$  is the velocity of the sensor and  $v_g$  is the velocity of the ground motion. Examples of ATI applications are the measurement of vehicle movement (e.g. [180, 181, 182]) or the measurement of surface currents (e.g. [183, 184]).

XTI requires a lateral separation of the antennas. It uses the phase information to extract location in the vertical direction, producing a DEM. Another application is the mapping of changes in the form of terrain displacement after an earthquake or due a lowering of the ground water table.

Polarimetric Interferometric SAR (PolInSAR) combines polarimetry with interferometry. This combination is able to mitigate some limitations of both methods. The extraction of biophysical and geophysical information is possible by interpretation of the interferogram phase, which changes depending on the polarisation used. For example, adding the interferometric information to the polarimetric classification scheme can help in distinguishing oriented objects in vegetated areas [185, 186].

The PolInSAR feature vector is constructed by combining the target scattering vectors in the Pauli basis of the  $[S]$ -matrices of the two acquisitions  $\underline{k}_1$  and  $\underline{k}_2$ :

$$\underline{k} = \begin{bmatrix} \underline{k}_1 \\ \underline{k}_2 \end{bmatrix} \quad (2.117)$$

The difference between the two acquisitions is the use of either a spatial and/or a temporal baseline. To process this feature vector, the absolute phase values have to be taken out by constructing the 6x6 equivalent coherency matrix:

$$\langle [T_6] \rangle = \langle \underline{k} \cdot \underline{k}^{T*} \rangle = \begin{bmatrix} \langle \underline{k}_1 \cdot \underline{k}_1^{T*} \rangle & \langle \underline{k}_1 \cdot \underline{k}_2^{T*} \rangle \\ \langle \underline{k}_2 \cdot \underline{k}_1^{T*} \rangle & \langle \underline{k}_2 \cdot \underline{k}_2^{T*} \rangle \end{bmatrix} = \begin{bmatrix} \langle [T_1] \rangle & \langle [\Omega_{12}] \rangle \\ \langle [\Omega_{21}]^{T*} \rangle & \langle [T_2] \rangle \end{bmatrix} \quad (2.118)$$

where  $\langle [T_1] \rangle$  and  $\langle [T_2] \rangle$  are Hermitian polarimetric 3x3  $[T]$ -matrices, containing the polarimetric information of the two acquisitions. On the off-diagonal terms, there are non-Hermitian polarimetric 3x3 matrices with complex polarimetric and interferometric cross correlations. The degree of coherency (or the complex polarimetric interferometric coherence) for the two acquisitions is defined as [187]:

$$\gamma = |\gamma| e^{i\Phi} = \gamma(\omega_1, \omega_2) = \frac{\langle I_1 I_2^* \rangle}{\sqrt{\langle I_1 I_1^* \rangle \langle I_2 I_2^* \rangle}} = \frac{\omega_1^* [\Omega_{12}] \omega_2}{\sqrt{\omega_1^* [T_{11}^*] \omega_1 \omega_2^* [T_{22}^*] \omega_2}} \quad (2.119)$$

with  $I_i$  as the two PolSAR images and  $\omega_i$  as the normalised projection vectors. The latter are complex unitary and they can be given physical meaning for interpreting scattering processes.

## 2. SAR and PolSAR

---

The argument of the complex number  $\gamma$  represents the interferometric phase and  $|\gamma|$  is the cross-correlation coefficient.

The modulus of the coherence is the correlation of the signals at the two ends of the baseline; the phase is mainly influenced by the topography. The PolInSAR coherence is affected by decorrelation and a simple model is the following [188]:

$$|\gamma| = \gamma_{temp}\gamma_{vol}\gamma_{base}\gamma_{dc}\gamma_{system} \quad (2.120)$$

as the product of contributions from temporal decorrelation, volume decorrelation, baseline decorrelation, Doppler centroid decorrelation and system imperfections (e.g. thermal noise, coregistration errors, interpolation errors etc.).

When it comes to modelling the phase, the main elements of the phase of the complex coherence are the topography, the flat earth phase, propagation conditions in the ionosphere and in the atmosphere, changes in the scattering behaviour, displacement or deformation of the scatterer and phase noise:

$$\phi = \phi_{topo} + \phi_{flat} + \Delta\phi_{prop} + \Delta\phi_{scat} + \Delta\phi_{\delta R} + \phi_{noise} \quad (2.121)$$

# 3

## Object Detection in the Maritime Domain with SAR

This chapter is dedicated to the challenges of detecting waterborne objects and associated technical aspects. The ocean surface is a heterogeneous, permanently moving surface, winds generate swell and waves. Literature describes many different kinds of waves and together they define the sea state. The latter has a great impact on the SAR image. The heterogeneity of the sea surface makes it harder to tackle detection problems, producing false alarms and missed detections.

Metallic structures, such as oil rigs or ships, normally generate a backscatter signal stronger than the background sea. Non-metallic objects are harder to see, especially when they are small in size. The early development of intensity-based techniques was later extended by research in polarimetry, which provided a number of new approaches to solve more complex detection tasks. Additionally, the movement of an object can be used for interferometric detection. Finally, indirect identification methods try to use anomalies to find ships and boats, such as the vessel's bow waves and areas where its slipstream calms the water surface. This chapter discusses the radar patterns of different ocean features, detection fundamentals and thresholding schemes and it concludes with a description of well known (vessel) detectors.

### 3.1 Microwave Scattering of the Sea Surface

To improve the understanding of the radar return from the ocean surface and to find appropriate models to describe it, from the 1960s on several publications derived a relationship between clutter physics, oceanography and marine hydrodynamics (e.g. [189, 190, 191, 192, 193]). Some more recent examples of publications in the field of sea surface clutter modelling are [194, 104, 195, 196, 197, 198]. The ocean surface is shaped by a number of different influencing factors, with the wind as the most prominent one, and is often modelled as a combination of successive waveforms of different wavelength and amplitudes (e.g. the Bragg model) [24]. Leaving out sensor parameters, the radar return of an unpolluted ocean surface is shaped by the dielectric constant of the two mediums air and water, the roughness of the water surface,

its salinity (sea water contains about 3.2% salt but much less close to sea ice or rivers) and the interactions between the water waves at different scales and the currents [199, 24]. The dielectric constant, or complex permittivity, consists of a real part and an imaginary part:

$$\epsilon_c = \epsilon' - i\epsilon'' \quad (3.1)$$

$\epsilon'$  often refers to the dielectric constant which is an indicator of how much electrical energy a medium can store.  $\epsilon''$  is the loss factor and quantifies the electromagnetic loss of a medium. Both are important factors in calculating the penetration depth  $\delta'_p$  for a given medium at a specific temperature [200]:

$$\delta'_p \approx \delta_p \cos \theta \quad (3.2)$$

with  $\theta$  as the incidence angle and  $\delta_p$  for materials with  $\epsilon'/\epsilon'' < 0.1$  is [52]:

$$\delta_p = \left( 2\pi \frac{\lambda_r \sqrt{\epsilon'}}{2\pi\epsilon''} \right) \quad (3.3)$$

with  $\lambda_r$  as the radar wavelength. Formula 3.3 is usable for most natural material except water. For frequencies typically used for most SAR sensors (1 to 10 GHz), salty ocean water at 20°C has a high  $\epsilon' \approx 70$  and an  $\epsilon''$  of around 40 [201]. For the central Mediterranean ( $\approx 38\%$  salt content; [202]) the penetration depth would be less than 0.1cm for X-band ( $\approx 9GHz$ ) and 0.2 – 0.3 cm for C-band (4 to 8 GHz) [43, 52, 203, 204]. Higher penetration depths lead to an attenuation of the EM-wave and this decreases the backscatter intensity. Further, it can produce volume scattering. In the microwave spectral region, sea water is highly absorptive and therefore not transparent for microwaves. This is because of its high electrolytic conductivity due to dissolved salt ions. The refractive index  $n$  for sea water is in the region of 9.4. Following the formula

$$n = \sqrt{\epsilon_r} \quad (3.4)$$

the relative permittivity  $\epsilon_r(\omega)$  of seawater is about 90.  $\epsilon_r(\omega)$  is a function of the complex dielectric permittivity  $\epsilon_c(\omega)$  (Formula 3.1 and the vacuum permittivity  $\epsilon_0$ ):

$$\epsilon_r(\omega) = \frac{\epsilon_c(\omega)}{\epsilon_0} \quad (3.5)$$

with  $\omega$  as the angular frequency which is the rate of change of the phase of a sinusoidal waveform.

While for land clutter the scatterers are assumed to be stationary (which is sometime not fulfilled, e.g. vegetation moved by wind), the scatterers in sea clutter are in constant motion. Due to its continuously changing, it is hard to predict and to model backscattering in detail without real-time in-situ weather data. Moreover, depending on the local weather, strong scattering phenomena like swells, wave features (including breaking waves) and spray do occur regularly, but rather unpredictably. These features are capable of increasing the false alarm



rate, especially when the target objects are small, weak scatterers with low target to clutter ratios. Conversely, by averaging on larger areas, it is possible to filter out those features. For instance, the derivation of wind parameters from SAR imagery has been thoroughly studied (see chapter 3.2). The mean cross section of the sea clutter depends on many variables. The main influencing factors are:

- winds speed and wind direction relative to the LoS
- extreme weather scenarios (e.g. heavy rain, hail)
- frequency of the radar
- polarisation of the radar
- spatial resolution of the radar
- the incidence angle of the radar

A comprehensive list of objects and processes (such as ocean currents and eddies, ocean bottom topography, sea ice, oil rigs, seaweed, shoals, oil spills, breaking waves, etc..) can be found at [18]. Many of them can cause false alarms and hinder automatic ship detection. The influencing factors in the list above can be divided into sensor-specific and scene-specific factors and are described in the following subsections.

### 3.1.1 Sensor-Specific Parameters

The incidence angle is of great importance for the backscattering of the water surface (Formula 3.8). Basically, the clutter decreases with increasing incidence angles and Fig. 3.1 gives an example of this relation for a wind direction of  $270^\circ$  relative to the LoS.

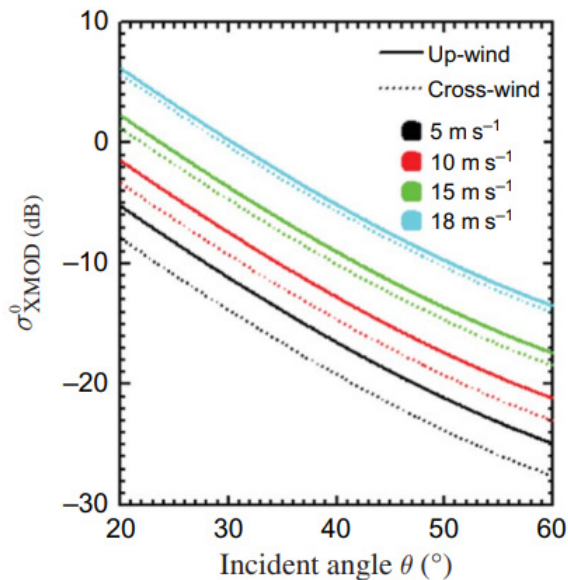


**Figure 3.1:** NRCS values simulated by XMOD for various incidence angles and wind directions for VV-pol [205].

In the lower range of incidence angles ( $<20^\circ$ ) the Bragg scattering can produce a very strong scattering regime [18]. A similar relation with the radar backscatter exists for the radar frequency: an increase in frequency means a decrease of Bragg scattering. At wavelength in the dimension of decimetres (e.g. P-band), there is no Bragg scattering at all. The geometric resolution of the SAR might be of importance when swells have a frequency

smaller than the resolution cell. The swell waves produce a broadening of the spectrum due to their spatial variation within each cell and have to be treated statistically. When the long swell waves are longer than the resolution cell, their influence might be assumed to be constant over all cells [206].

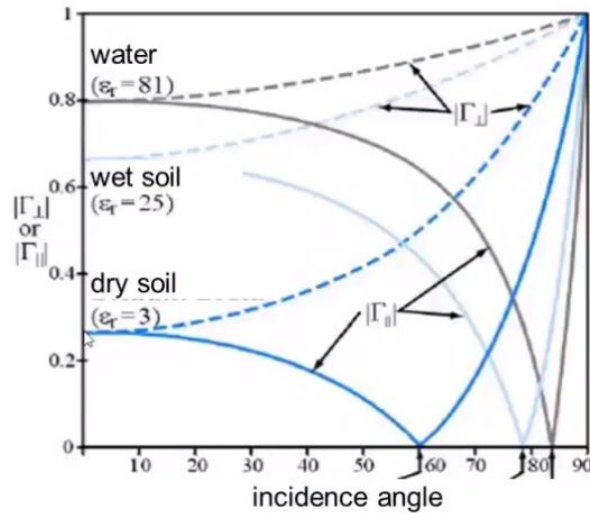


**Figure 3.2:** Backscattering coefficients for water, wet soil and dry soil at different polarisation states ( $\Gamma_{\perp} = \text{VV-pol}$ ,  $\Gamma_{\parallel} = \text{HH-pol}$ ) and incidence angles.

The polarisation is another important factor for backscattering intensity of the water surface. According to Fresnel’s law, ocean reflectivity is usually larger for VV-pol than for HH-pol (Fig. 3.2). This is true for almost all incidence angles and for most frequency bands (X-band [205]; C-band [207]; Ka-band and Ku-band [208] and Fig. 2.21 further up) and the difference increases with increasing incidence angle. At very small incidence angles, the difference between the polarisation channels diminishes. For L-band radar at incidence angles smaller than  $45^{\circ}$  in calm wind situations in the range of 5 – 10 km/h, the clutter will be lower for HH-pol compared to VV-pol [29].

#### 3.1.2 Scene-Specific Parameters

The radar backscatter behaviour of the ocean surface is shaped by its roughness which is produced by different kinds of waves. These waves can be classified based on the stimulation that generated them. First, there are wind waves raised by the wind in the immediate neighbourhood of the place of observation at the time of observation. Second, there are swells in the form of waves with very long wavelengths of up to several 100 meters and generated by non-local winds. Surface water waves, which are created by local winds, can be classified into two main types, depending on the dominant restoring force [209]:

- capillary waves: they form the fine structure of the water surface and the surface tension is the restoring force
- gravity waves: all waves that are somewhat larger and contribute to the visible surface elevation where the restoring force is gravity. Models to mathematically describe them have existed for a long time (e.g. [210])

To describe the sea state and the roughness of the oceans, the World Meteorological Organization (WMO) uses the Douglas Sea Scale. In its original version, it distinguished

between the local wind waves and swells and developed descriptive terms for them. The relation between the sea state and the local wind is described in the Beaufort scale, which is based on empirical measures and observations. The following list describes local and non-local sea state influence parameters which are connected to the wind:

- non-local wind speed: The non-local wind speed creates swells which are independent of the waves created by local winds and superimpose a slow oscillation. By doing so, swells modulate the Bragg scattering, producing a pattern in the SAR image. It is possible to have either a significant sea state or large swells and not have the other i.e. they are mutually independent
- local wind speed: The local wind speed strongly influences the water surface backscattering. For example, in the case of C-band SAR, with wavelengths between four to eight centimetres, wind in the order of two to three meters per second typically generates small waves of a size comparable to the radar wavelength. Increasing wind speed generates rougher water surfaces and, in most cases, increases the backscattering intensity (Fig. 3.1). The rougher water surface can lead to bigger waves with wavelengths much bigger than the radar wavelength and therefore less Bragg. This decrease of Bragg scattering decreases the backscattering amplitude. But increasing wind speed does not completely rule out the prevailing presence of the smaller waves that create Bragg scattering. The relationship between local wind speed  $u_s$  and the radar cross section of the water surface for a given incidence angle can be estimated using a first order power law function [211]:

$$\sigma^0 \sim |u_s|^\gamma \quad (3.6)$$

with  $\gamma$  as a function of the radar wavelength and other sensor specific parameters such as the polarisation and the incidence angle. Equ. 3.6 shows, that the radar cross section of the ocean surface is generally expected to increase with the wind speed

- local wind direction: the local wind direction is the main factor for the direction of the waves in the SAR scene. The largest backscattering can be found for upwind (wind blowing towards the radar look direction) and downwind (wind blowing away from the sensor). The smallest are for (nearly) cross wind directions (wind blowing across the radar look direction).

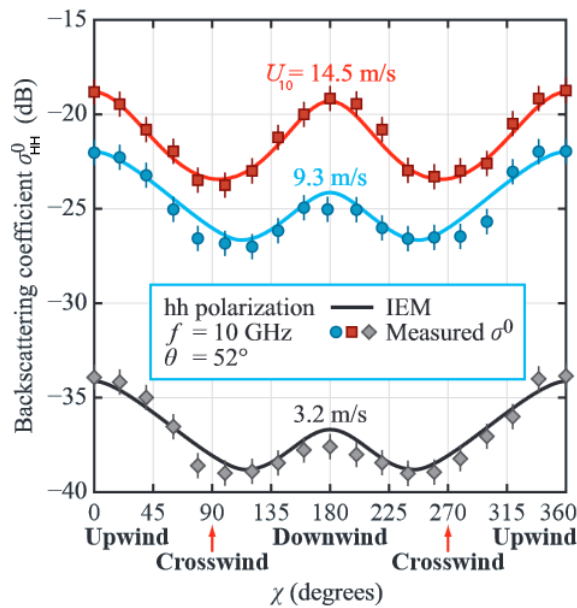


**Figure 3.3:** The relationship between the relative direction of the radar LoS and the wind vector (angle  $\chi$ ) [43]. The example shows model data and measurements for HH-pol in X-band.

This can be explained by the fact that Bragg waves move in the direction of the wind (see Fig. 3.3). So, in case of upwind and downwind, the water waves expose more surface facets which are oriented perpendicularly to the LoS. That increases the magnitude. The ocean backscattering magnitude is further related to the wind speed  $U_{10}$  and its pattern is influenced by the SAR frequency, polarisation and incidence angle [24]. The small capillary waves, like most waves) are asymmetrical and skewed and steeper on the leeward side (or downwind side), thus changing the local incidence angle. That is the reason for a slightly bigger  $\sigma^0$  for upwind compared to downwind [212]. The surface asymmetry of wind-driven ocean waves leads to a directional dependence for the radar backscatter [43, 24].

In general, the radar return from the ocean increases with increasing wind speed regardless of the direction of the wind [207]. That is especially true for winds between 3 and 25  $ms^{-1}$  and this range is covered by well-known models such as the XMOD (for X-band). If the wind slows down to under 2 – 3  $ms^{-1}$ , the capillary waves break down and the water surface appears black in SAR images, just like a smooth, flat surface [213]. For winds stronger than 25  $ms^{-1}$ , it is assumed that the backscattering intensity decreases slightly [214]. These figures vary with the sensor wavelength

The radar return of the ocean surface is influenced by the natural phenomena listed above. Conversely, these phenomena can be derived from the SAR image. For example wind speed, wind direction and properties of ocean surface phenomena can be estimated (see section 3.2). When wind starts blowing, first fluctuations of the atmospheric pressure induce capillary waves. Increasing wind velocity increases gravity forces, contributes to wave motion and creates gravity waves [215]. Detailed calculations of the sea surface scattering field are possible using the Stratton–Chu equations [216, 217]. The calculations were the first proof of a direct relationship between the scattering from the water surface and the sea surface roughness.

For X-band, the strongest clutter return is received from water waves with wavelengths in the range of 1.5 – 2.1 cm. Capillary waves are quite similar in the dimension to X-band radar and are therefore capable of producing strong radar return. They have a dominant role in Bragg scattering at medium grazing angles ( $35^\circ$ ) and low to moderate wind speeds [215, 206]. The influence of the gravity waves has to be considered due to the fact that their underlying movement modifies the local incidence angle and the amplitude [189, 206].

In addition to tilt modulation, Crisp [18] lists two additional mechanisms to describe how gravity waves interfere with the small waves which are relevant for Bragg scattering. One is called hydrodynamic modulation which results in a non-uniform distribution of small capillary waves due to surface currents. The amplitude of the capillary waves is bigger at wave crests and attenuated at wave troughs [218]. This phenomenon is in phase with the gravity waves. The second category is summarised under the concept of motion effects. This concept aims at covering all predictable motion of the water surface particles due to wave movement. Depending on the direction of the movement relative to the LoS, such motion can lead to azimuth displacement ('off-the-track effect') and smearing effects. The motion of the main scatterers (the capillary waves;  $v_{cw}$ ) gives them a certain velocity which is the sum of the velocity of underlying ocean currents  $v_{cur}$ , plus the phase velocity of the capillary waves  $c_p$ , plus the orbital velocity  $vv_{orb}$ :

$$v_{cw}(x) = v_{cur} + c_p + v_{orb}(x) \quad (3.7)$$

$v_{cur}$  is usually assumed to be constant,  $v_{orb}$  is derived from the fact that water particles move in closed orbital paths [215]. That movement is visible in the Doppler spectrum of the radar

return. If the scatterers in the scene and the platform are assumed to be stationary, the normalised power is only received at 0 Hz. In the case of sea clutter, echoes from scatterers with different velocity vectors are received. The Doppler centroid is not at 0 Hz and the clutter power is spread over different Doppler frequencies [206].

The scattering behaviour of the background sea surface can be a combination of different scattering processes in accordance to the water surface behaviour. Their occurrence and intensity depends to a great extent on the local weather conditions (nearby or remote winds that generate swells are neglected in the following list):

- no local wind: according to the law of reflection, microwaves are reflected away with an angle equal to the incidence angle of the sensor ('specular reflection'). This is the case for very calm, totally flat-water surfaces in windless environments. Since there is no return to the radar sensor, the water surface appears black in the SAR image or the noise level will be the dominant process

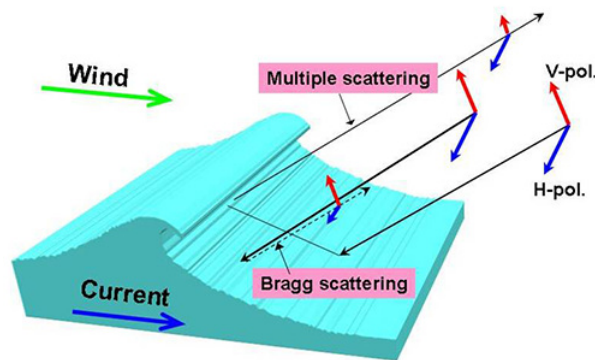


**Figure 3.4:** Scattering mechanisms for breaking surface gravity waves [219].

- low to moderate wind speed (about  $<8 \text{ ms}^{-1}$ ): here, Bragg scattering occurs and describes the scattering mechanisms at incidence angles between  $25^\circ$  and  $70^\circ$  [220, 221]. Its strength depends on parameters such as the local wind speed and wind direction, the precipitation, the radar incidence angle, the radar wavelength and its polarisation. For more on Bragg scattering, please see the next section below
- higher winds<sup>1</sup> (about  $>8 \text{ ms}^{-1}$ ): A third contribution was identified as incoherent scattering, generated by surface disturbances such as breaking waves (Fig. 3.4). This concept helps explain strong HH-pol and cross-pol backscatter contributions coming from the water surface (e.g. [222, 223, 224])
- rain generates ring waves which can decrease or increase the normalised radar cross section (NRCS). The impact level depends on the wind speed, the rain intensity, on the radar system wavelength, the incidence angle and the polarisation used (Fig. 3.5). There are four main physical processes found in the literature that contribute to the radar signature of water surfaces during rain [225]:
  - scattering at the ring waves and wave damping due to turbulence caused by rain drops
  - scattering at splash products, i.e., at craters, stalks, crowns, and rain drops bouncing upwards
  - increase of the sea surface roughness due to falling winds often associated with rain cells
  - volume scattering of the radar pulse by raindrops (hydrometeors) in the atmosphere

<sup>1</sup>which corresponds to a 5 on the Beaufort scale: 'Moderate waves, taking more pronounced long form. Many white horses (white caps) are formed (chance of some spray)'

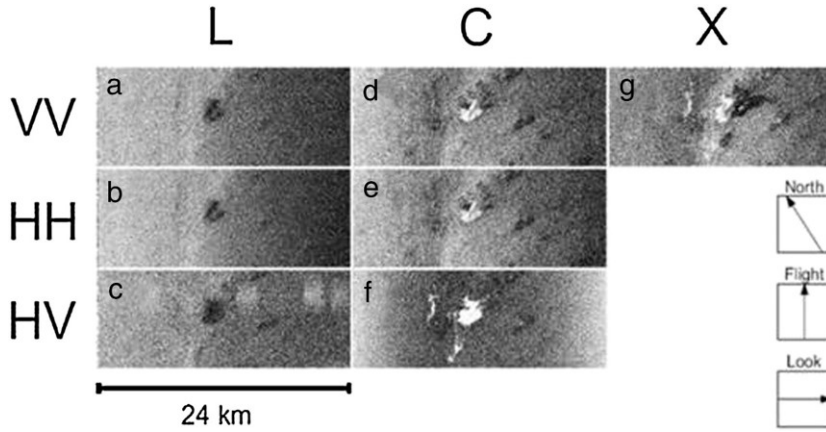


Figure 3.5: Impact of rain on the ocean surface [226].

With C-Band, the first three phenomena increase the NRCS, the latter attenuates the backscattered signal. Further, the NRCS is decreased by attenuation of the Bragg wave pattern due to turbulence generated by raindrops and winds. Influencing factors for these changes of the NRCS are, amongst other unknown processes, the rain rate, the rain drop distribution, the history of the rain event and the local ambient wind speed [226].

The data from the two acquisition campaigns is free from heavy rainfall and the rather calm lake environment rules out breaking waves. That means the specular surface scattering and the Bragg scattering (especially at low incidence angles) are the dominant mechanisms. If both are very low, noise might become the main contributor.

### 3.1.3 Bragg Scattering

The most popular model for scattering processes taking place on a water surface at incidence angles above  $20^\circ$  is the Bragg scattering. It describes a linear relationship between the surface roughness of the ocean and the resonance frequency of EM waves (Fig. 3.6). The name originates from the Bragg brothers [227] who, in 1913, observed an increase of the backscattering of EM waves from crystals with grid structures of size comparable to the wavelength of the EM waves. This principle could be transferred to wave structures of water surfaces [189].

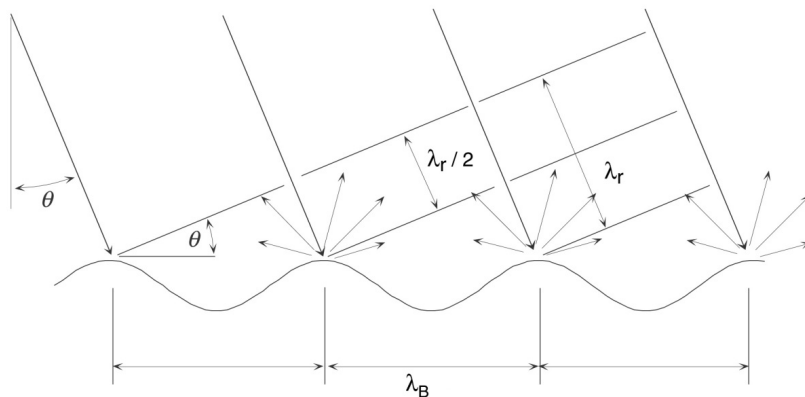


Figure 3.6: Illustration of Bragg scattering [199].

The two-scale continuous Bragg scattering model is built on the composite surface theory which decomposes a rough ocean surface into small-scale and large-scale components. Small scale features (e.g. capillary waves) are highly irregular and are therefore expected to have a short auto-correlation. Their size is in the range of widely used frequency in SAR (such as X-band) and are highly relevant to Bragg scattering. Wind builds these waves and they are directly linked to the speed and the direction of the local winds [228]. Bragg scattering varies with the size, wavelength and direction of the capillary waves.

Large scale features (e.g. gravity waves, swells) have small curvature radii so that they can be seen as planar compared to the short waves. This distinction between these two scales depends on the wavelength of the sensor and the incidence angle. [229]. Bragg resonance is only received from water waves whose wavelength is comparable to the wavelength of the radar:

$$\lambda_B = \frac{\lambda_r}{2 \sin \theta} \quad (3.8)$$

with  $\lambda_B$  as the short, Bragg resonant wavelength of the water wave,  $\lambda_r$  as the carrier wavelength of the SAR and  $\theta$  as the local incidence angle. Formula 3.8 assumes that the ocean waves are travelling in the LoS of the radar. As the local incidence angle changes from small at the front face of a big water wave to a larger value at the back face of the same water wave, the Bragg resonant wavelength changes accordingly. Thus, the radar return on the front side of the water wave, facing the sensor, is at a maximum and the back side of the water wave shows less backscattering [52]. For common SAR frequencies and medium incidence angles (35°), the Bragg wavelength would be between 0.8 cm and about 20 cm. As mentioned above, the movement of the water surface particles can be described in terms of a Doppler shift  $f_D$ :

$$f_D = \frac{2V}{\lambda_r} \pm f_B \quad (3.9)$$

which is induced by a movement in the direction of the LoS ( $V$ ) and the intrinsic frequency of the Bragg resonant short wave ( $f_B$ ; [206]). The two signs depict Bragg waves travelling towards or away from the radar sensor. The theory behind the Bragg scattering concept explains the influence of the polarisation and it is commonly known that the phenomenon is stronger in VV-pol than in HH-pol [17]. It approximates the intensity and the Doppler bandwidths of the radar return from the sea surface for incidence angles in the range of 20° to 60° for VV-pol and for 20° to 70° for HH-pol [220].

The Bragg scattering model fits well with low sea states [18]. However, questions about its limitations and accuracy in field conditions have been raised and the existence of other, equally important scattering mechanisms, cannot be ruled out [206].

## 3.2 Wind Field Estimation with SAR

Much work has been done in order to relate the NRCS to the near surface wind vector over the ocean with suitable Geophysical Model Functions (GMFs). There are a number of models for C-band and VV-polarisation of which the first largely used one was the CMOD2 [230]:

$$\sigma^0 = B_0[1 + B_1 \cos(\phi_N) + B_2 \cos(2\phi_N)] \quad (3.10)$$

with  $B_0$ ,  $B_1$  and  $B_2$  as coefficients which depend on the radar incidence angle, the wind speed  $U_{10}$  (= wind speed 10m above ground in  $ms^{-1}$ ) and the wind direction  $\phi_N$ . It bases on the CMOD1, developed by [231]. Further research resulted in successors such as the CMOD4  $\sigma^0$ -to-wind transfer function [232]. On this basis, more GMFs have been developed since, such as the CMOD5 [233] which is intended for use in high winds and storms or the CMOD7 [234] which improves the predecessor models for close to zero winds.

These models were originally designed for the European Remote Sensing (ERS) Advanced SCATterometer (ASCAT) and later adapted for a C-band SAR (both sensors are located on the ERS). They were derived using transfer functions for the original GMF [235], sea surface wind field data and/or in situ buoy measurements. The three antennas on the ASCAT are capable of unambiguously measuring the wind speed and its direction but the SAR has only one antenna. Therefore, when using the model with SAR data, one has to add additional measurements to unambiguously retrieve the wind direction. Earlier, these measurements came from external sensors but today, the wind direction can be derived from the same SAR image [214]. To estimate the wind speed, the SAR image with the NRCS values, the incidence angle and the wind direction have to be fed to invert the CMOD model. To extract the wind direction, wind driven phenomena in the marine atmospheric boundary layer such as the Langmuir circulation or circular rotating winds (boundary layer rolls) are helpful, since they produce drafting effects at the water surface. For the extraction of the wind direction different techniques are applicable, such as using the Doppler information (e.g. [236, 237]), a wavelet transform approach [238] or a Frequency domain approach using the Fast Fourier Transformation (FFT) [239].

Since the CMOD functions were originally developed for VV-pol, polarisation ratio (PR) models are used to convert the SAR data from  $\sigma_{HH}^0$  to  $\sigma_{VV}^0$  to then apply the CMOD functions (e.g. [240, 241]). PR is defined as the ratio between HH-pol and VV-pol intensity values:

$$PR = \frac{\sigma_{VV}^0}{\sigma_{HH}^0} \quad (3.11)$$

which is then used in a hybrid model with the C-band model function:

$$\sigma_{HH}^0 = \frac{CMOD(U_{10}, \theta, \phi_N)}{PR} \quad (3.12)$$

An L-band GMF to retrieve sea surface wind from ALOS/PALSAR was developed for HH-pol by [242]. Vachon and Dobson [243] developed a model to extract wind speed from  $\sigma^0$  values for C-band and HH-pol. Ren et al. [205] developed a model called XMOD (or XMOD1) to retrieve wind speed at a height of 10m with X-band for VV-pol. It uses a linear GMF and adapts existing PR models that consider the influence of the incidence angle. Shao et al. [244] proposes an exponential variant of the PR model, called X-PR, to retrieve sea surface wind speed from X-band HH-pol data. Later, the successor called XMOD2 was augmented using a nonlinear geophysical model function [245]. That enabled the model to take into account the influence of the horizontal wind direction (upwind and downwind) on the backscattering from the sea surface. Thompson et al. [246] constructed X-band GMFs for both, HH-pol and



VV-pol, by interpolating the — at that time — more accurately tested C-band and Ku-band GMFs.

Another interesting feature to extract from ocean SAR imagery is the orientation angle of the waves. More precisely, the azimuth slope angle and the range slope angle can be derived with sub-degree accuracy [108, 247, 248]. This concept was later expanded to estimate ocean wave slope spectra [249, 110]. The shift in the orientation angle in the polarisation signature can be measured and used to determine the ocean surface tilt in azimuth. This relationship can be simplified to [249]:

$$\tan \omega \approx (\sin \phi) \tan \theta \quad (3.13)$$

where  $\tan \omega$  is the azimuth slope,  $\phi$  is the incidence angle and  $\theta$  is the shift in the orientation angle. To measure the ocean slopes in range direction, an FFT of a parameter alpha ( $\alpha$ ) from the Cloude–Pottier decomposition [132] may be used, which can then be converted to a range wave slope spectrum [249].

### 3.3 Detection Fundamentals

The problem of solving the detection task is a decision-making problem and is subject to modern detection theory [250].

For ship detection in SAR images this becomes a binary hypothesis testing problem, in which it has to be established whether the SAR image contains only noise and backscatter from the water surface or if there is also backscatter from a vessel, producing some kind of anomaly. When we try to deduce specific properties of the detected vessel such as its dimensions or its dielectric property, it becomes a pattern recognition or classification problem [251].

The ways to solve both problems have in common that they rely on data that contains noise which is inherently random so that a statistical approach is necessary. The modelling of the sea surface radar return allows to modify the threshold to keep constant probabilities of false alarms — assumptions that can be upheld across the whole SAR scene, even when the local statistics vary.

#### 3.3.1 Statistical Modelling of the Ocean Clutter

The backscatter is generally stronger when the objects are of the same dimension as or bigger than the wavelength [25, 92]. The resolution cell in the X-band and C-band SAR imagery used in this work is about two orders of magnitude bigger than the wavelength. Therefore, each resolution cell represents the sum of a large number of scatterers. They are coherently summed together depending on the phase (the direction in the complex plane) so that the total power of the resolution cell is smaller than the sum of the power contributions. Given the case where there is no dominant scatterer, the problem of information extraction has to be solved with a statistical approach [55, 92].

For the statistical description of the thermal noise a Gaussian (Normal) distribution can be used. It is random and typically characterised by white noise  $\psi$  where all frequencies are

equally likely (like in white light where all colours are equally likely). This means that the power spectral density is uniform. White noise is regarded as uncorrelated, random variables with zero mean  $\mu$  and a constant variance  $\sigma$ .

For the statistical description of speckle noise, a classical Rayleigh model can be used. The real and imaginary parts of the complex field are independent, zero mean, identically distributed Gaussian random variables [53]. Then, the real and the imaginary parts have the following joint probability density function  $p$  (PDF) [252]:

$$p(X_{re}, X_{im}) = \frac{1}{2\pi\sigma^2} \exp\left(-\frac{X_{re}^2 + X_{im}^2}{2\sigma^2}\right) \quad (3.14)$$

The term  $2\pi\sigma^2$  is used to normalise the PDF so that the total probability equals 1 [24]. Here, the phase angle is uniformly distributed between 0 and 360° and the amplitude  $A$  lies anywhere between zero and (theoretically) infinity. Converting this expression into polar coordinates, the amplitude ( $A = \sqrt{X_{re}^2 + X_{im}^2}$ ) has a Rayleigh probability distribution:

$$p(A) = \frac{A}{\sigma^2} \exp\left(-\frac{A^2}{2\sigma^2}\right) \quad (3.15)$$

In accordance with the central limit theorem, this statistical model is suitable for speckle noise, as long as it represents a large number of identically distributed random variables, i.e. through multilooking where a large number of samples have been averaged [253, 18]. The Gaussian model is applicable and sometimes used for ocean surface clutter as well.

In the field of SAR, the power, or intensity  $I$  is more interesting since that is the quantity that directly relates to the definition of the NRCS through the radar equation.  $I$  is  $A^2$  and its PDF has the form of:

$$p(I) = \frac{2}{\sigma^2} \exp\left(-\frac{I}{2\sigma^2}\right) \quad (3.16)$$

It is a negative exponential distribution with  $\mu$  and  $\sigma$  are proportional. Therefore,  $\sigma$  is the value needed to estimate the underlying RCS. To reduce the uncertainty of single samples, applying a smoothing filter by spatially averaging pixels inside a small window of the image can help — but only under the assumption that the averaged pixels are of the same target. A different approach is called Multi-look, where independent measurements during the measurement process itself are taken. They are called 'looks' and are generated by splitting up the azimuth beam into sub-beams or sub-apertures. [24]. The difference to spatial averaging is, that the looks are independent samples of the same resolution cell, whereas averaging takes samples of different (adjacent) resolution cells. As the number of looks increases, the mean stays the same but the variance decreases and so the estimate of the average becomes increasingly better.

For single look images (no averaging has been applied) with low wave clutter occurrence, an exponential distribution function [253] or the negative exponential distribution [18] is more appropriate to model the intensity. To model the backscattering of the ocean surface after averaging, a gamma distribution (with fixed order parameters) or a multilook intensity

K-distribution are good choices [207, 18]. For the gamma model, the false alarm rate depends on the variance normalised by the mean.

For the detection of small objects in extremely heterogeneous clutter, the Alpha-stable distribution model was introduced which is capable of describing impulsive and skewed behaviour of the background statistics [254]. Other examples for sea clutter models are the non-centred chi-2 Gamma [255] or the NG-distribution [256].

Totir [257] discusses a phenomenological model for sea clutter where the clutter is described as the product of a Gaussian speckle process with rapid variation and a second component which covers the slower movements of the water surface. The statistical model which provides the best fit is the K-compound distribution which is the product of a Rayleigh distribution for capillary waves and a Gamma distribution for large gravity waves and swells. That way, the K-compound distribution attempts to represent the concept of a dual nature of two superimposed sea surface scattered electromagnetic fields. It proves useful to describe the local statistics of sea clutter for very high incidence angles.

There are different ways to approach the estimation of parameters used in the mathematical modelling of the clutter PDF. Eldhuset [258] introduced an algorithm that compares the local means from the cells under test (CUT) with the mean and the standard deviation of the local background statistics to take variations of the local mean into account. Just like the modelling schemes, this approach tries to find maritime objects by comparing local values with the values of the adjacent local background. In this thesis, the most common of the choices, where the average over all pixels in a moving window is calculated, is used.

### 3.3.2 Thresholding Schemes for (Semi-) Automatic Detection

One challenge in a detection task is to choose the right balance between the true positive rate and the false positive rate, in other words: to set the optimal threshold value. In SAR images, the presence of multiplicative noise with unknown and varying power can result in many false alarms and many missed detections in different regions of the same image. For maritime applications, the heterogeneous sea clutter increases the problem.

The detection performance depends upon the degree of difference between the PDF the background clutter and the PDF of the target object. As the separation between the PDFs increases, the signal to clutter ratio (SCR) increases [250]. We can define the SCR or target to clutter ratio (TCR) as:

$$TCR = \frac{P_{target}}{P_{clutter}} = 10 \log \frac{P_{target}}{P_{clutter}} dB \quad (3.17)$$

Following modern detection theory, there are three probabilities of particular relevance in estimating the detector capabilities [250]:

- probability of detection ( $P_D$ ): this is the probability in a case when the target object is present and the detector detects it. Such cases are also called true positive
- probability of missed detection ( $P_M$ ): this is the probability in a case when the target object is present and the detector misses the detection. Such cases are also called false negative

### 3. Object Detection in the Maritime Domain with SAR

- probability of false alarm ( $P_F$ ): it is the probability in a case when the target object is not present, but the detector has a positive response. Such cases are also called false positive

The detection performance depends on the selected threshold and, in detection theory, several approaches have been designed to find the optimal threshold. Their main goal is to minimise  $P_F$  while at the same time maximise  $P_D$ . Examples are the Neyman–Pearson theorem or Bayesian techniques [250].

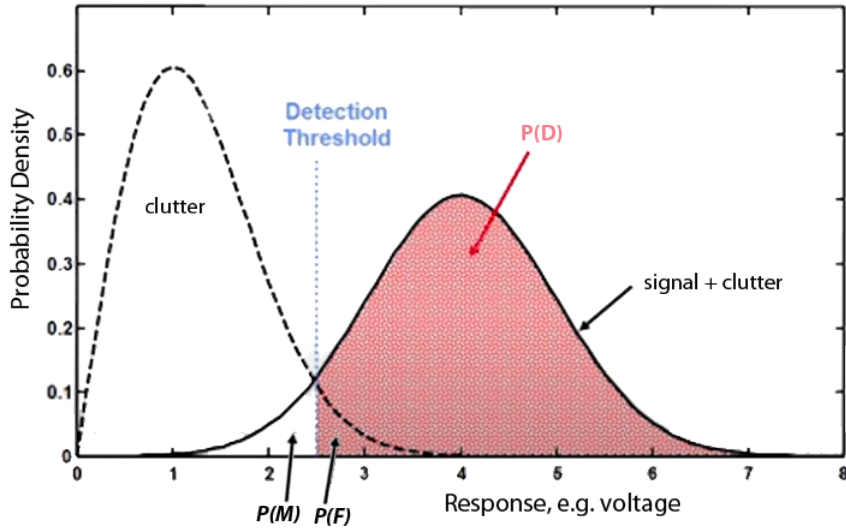


**Figure 3.7:** The detection problem (adapted from MIT Lincoln Laboratory, 2001).

Fig. 3.7 shows the PDFs of clutter (left) and of clutter including signal of the target object (right). In this example, the most probable value for clutter is close to one and the most likely value for the PDF of the target is around four; the average TCR is 15dB (which results in a power ratio of about 31.5).

The area under the clutter PDF and over the target PDF from zero to the threshold covers all true negatives. The area under the clutter’s PDF curve from the detection threshold till infinity is  $P_F$ . The area under the target PDF from the threshold till infinity is  $P_D$ . If the TCR increases, the PDF curve with the target signal moves away from the clutter–only PDF curve. With the result that their overlap area decreases and  $P_D$  increases. In the case of a fixed threshold,  $P_F$  remains the same. The threshold value has to be chosen to minimise  $P_F$  and maximise  $P_D$ .

A sophisticated approach which is effective when adjacent regions in the SAR scene show quite different median clutter values, is adaptive thresholding. It can use clutter–only floor samples to estimate the local clutter floor in the general area around the target object. This is a form of Constant False Alarm Rate (CFAR; [259], where the thresholding is no longer absolute but defined in an adaptive manner. The CFAR returns a detection if the value of the test cell (CUT) exceeds the clutter estimate by a certain amount (defined by the threshold):

$$\frac{\text{test cell}}{\text{clutter floor estimate}} > \text{threshold} \quad (3.18)$$

If the clutter floor increases, the threshold increases as well. This mechanism keeps the false alarm rate at a constant level.

There are many more different CFAR thresholding schemes. One very prominent example is the Cell-Averaging CFAR (CA-CFAR) which is based around a local moving average. A local window calculates the average (or arithmetic mean) of the local background around the CUT. Nearby objects can raise the threshold and suppress a successful detection. Therefore, adjacent cells are not considered but excluded by guard cells (in the case of an application in 1D space) or a guarding window (2D case). For more about CFAR please see section 3.4.1.1.

### 3.3.3 The Detection Problem

Ship monitoring with SAR is subject to some constraints. The limited resolution, the coherent speckle noise with grainy appearance, land masking and image distortions due to the dynamic environment are some of the reasons why it has mainly been restricted to ship detection of medium and large ships. But the new generation of SAR sensors, such as TerraSAR-X or Cosmo-Skymed, offer increased resolution and better polarimetric and revisiting time capabilities. They are changing this situation and increase the chances of detecting small and less reflective vessels [260]. Nevertheless, it is a hard task when the dimensions and the shape of the signature of the vessel are unknown. Moreover, oceanic SAR imagery is affected by different kinds of disturbances, such as speckle or marine discontinuity effects due to wind, currents and rain. In detecting small maritime objects, the intensity characteristics of the image might not be sufficient [261].

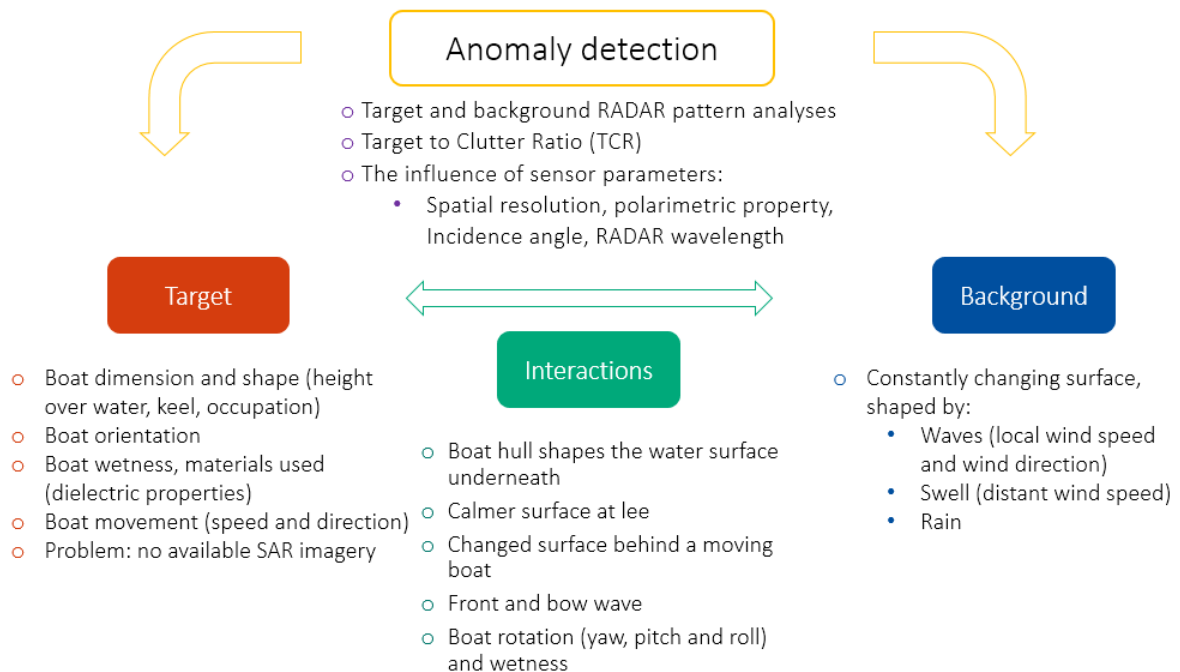


**Figure 3.8:** The detection problem.

Apart from the difficulties in understanding and estimating the polarimetric radar backscattering from the ocean surface, neither are the radar pattern of the rubber inflatable and its polarimetry constant over all situations. It depends on factors such as its orientation relative to the LoS, its movement, whether its surface is wet or dry and not least by the

number of passengers on board (Fig. 3.8). As already mentioned, there are no freely available SAR datasets from such boats, therefore it was not possible in this research to use actual observations to investigate their radar backscattering.

The continuously moving water surface and the moving boat do interact and affect each other's backscattering in a number of ways (Fig. 3.8). These interactions can be useful because new anomalies arise from them, which can, in turn, be exploited by detection algorithms. For example, the small patch of relatively flat-water surface at the lee side of the vessel can be used to improve the effectiveness of surface detection algorithms. On the other hand, the constant variability of the object and the background makes the choice of the right detector difficult. One way to deal with this situation is to find detectors which exploit a specific property of the vessel which stays relatively constant and maintains a high TCR. Another way could be to combine more than one detector to diversify the range of detection mechanisms.

## 3.4 Automatic Vessel Detection

The detection, identification and monitoring of ships and their activities in the open oceans have a wide range of applications including support for search and rescue missions and for monitoring of illegal activities such as push-backs to unsafe ports. Shore-based electromagnetic sensors such as HF radar are capable of covering these tasks close to the shore or other bases (e.g. offshore wind farms). SAR provides remotely sensed data with a good spatial and temporal resolution to cover vast oceanic areas. The main challenge in ship detection is to find small vessels in high sea states.

The first experiment on ship detection with microwaves took place in 1904. The German inventor Christian Hülsmeier was able to detect ships on the river Rhine with his 'telemobiloscope'. It was further developed before and during the second world war when it got its name which refers to its main applications 'radio detection and ranging'. The next milestone was the development of SAR in 1951 and imaging radar systems which use the backscattered wave to create an image. The first civilian satellite-based SAR was launched in 1979 under the name Seasat and was, like ERS-1 and Radarsat-1, a single-pol SAR. With the launch of Envisat ASAR in 2002, dual-pol imagery became available and PolSAR algorithms were introduced to civil vessel detection [262]. Most of the currently available SAR systems are capable of acquiring quad-pol data which has proven very useful for maritime object detection.

### 3.4.1 Vessel Detection Schemes

The main feature of an artificial maritime object is the brightness of its backscattering intensity. The first vessel detection systems (VDS) tried to make use of exactly that property and we call them intensity-based or radiometric-based detectors. The simplest way to search for bright objects is to define a global threshold [127]. Adaptive thresholding algorithms decrease the false positive rate by considering the local variations of the sea surface clutter.

More recently, new methods evolved, using at least one of the characteristic polarimetric properties of the vessel. Studies show that the TCR varies according to the polarimetric channel and the incidence angle [128]. Another approach is to rely on the information kept in the spectrum of a single look complex (SLC) SAR image, called sublook detectors. This section examines a broad variety of detection algorithms, covering all three categories:

- intensity-based detectors
- polarimetric detectors
- sublook correlation techniques/sub aperture analysis detectors

The detectors were implemented with a moving window and an adaptive thresholding methodology.

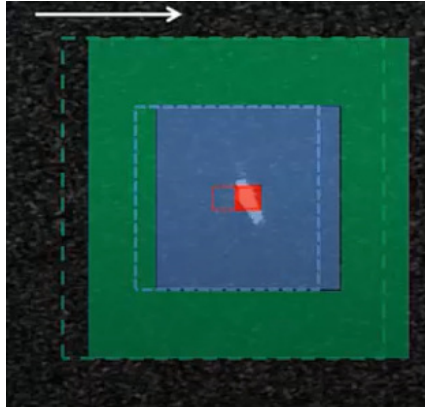


**Figure 3.9:** Moving Window approach.

A moving window approach consists of a small target window, a bigger guard window and an even bigger background window (Fig. 3.9). The target window (red) contains the pixel(s) being tested and should be the size of the smallest target object in order to prevent loss of resolution through averaging. The guard window (blue) prevents contamination of the background values by any pixels of the target that could extend outside the test window. It should be big enough to cover the largest objects assumed to appear in the SAR image. Finally, the background window (green) represents the local background. When choosing the dimensions of this background window, the local waves and swells, which shape the spatial variation of the water surface, should be taken into consideration. If it is large enough to extend over several sea swells wavelengths, it can provide a good estimation of the overall mean clutter level. The shorter the cell-averaging block size the more fine-grained can be the response of the detector to local variations of the water surface clutter [263].

Apart from the VDSs presented in the following subsections, there is a variety of other detectors which we came across in literature but did not investigate closely. Thus, they are not described here in detail but should, at least, be mentioned:

- the SPAN detector [264]
- the Van Zyl method [115], used as ship detector in [128]
- the optimum detector [265]
- the Generalized Likelihood Ratio Test (GLRT) [266]
- the generalized-K (GK) Filter [267]
- a detector using the anisotropy [268]
- a detector using the Cameron decomposition and the symmetry property (e.g. [128])
- a detector based on the wavelet theory using sub-band information [261]

#### 3.4.1.1 Constant False Alarm Rate Detectors

Objects with a backscatter signal stronger than the surrounding water surface appear as a bright spot in the SAR image. Following this assumption, several intensity-based (or

### 3. Object Detection in the Maritime Domain with SAR

---

radiometric-based) detection techniques have been developed. One of their great advantages is that only single-polarisation SAR data is necessary [127].

A threshold is determined based on the calculated background statistics in order to achieve a constant false alarm rate (CFAR). In this way, it is ensured that the threshold value is high above the clutter level in different regions in the image. It therefore relies on the locally calculated backscattering of the clutter. This calculation can follow a number of different CFAR thresholding schemes.

A common approach is to choose a parametric distribution to model the clutter. With this choice, the associated PDF  $f(x)$  of the background clutter is specified. The probability of false alarm (PFA) for the threshold  $T$  is defined as:

$$PFA = 1 - \sum_{-\infty}^T f(x)dx = \sum_T^{\infty} f(x)dx \quad (3.19)$$

where  $x$  ranges through the possible pixel values. The equation (3.19) for  $T$  can be solved by trial and error since cumulative distribution functions are monotone increasing [269] or by evaluating the equivalent detection test numerically [18]

$$\sum_{x_o}^{\infty} f(x)dx < PFA \iff target \quad (3.20)$$

where  $x_o$  is the value of the CUT. Using a Gaussian distribution model is often applicable since the central limit theorem states that the average of a large number of identically (gamma) distributed random variables tends to have a Gaussian distribution. It is not the best model but a simple way to design a two parameter CFAR detector:

$$x_o > \mu_c + \sigma_c t \iff target \quad (3.21)$$

where  $x_o$  is the CUT,  $\mu_c$  and  $\sigma_c$  are the statistical descriptors of the local ocean clutter (calculated from the background window) and  $t$  is the detector design parameter which controls the PFA (and the false alarm rate).

$$PFA = \frac{1}{2} - \frac{1}{2} erf\left(\frac{t}{\sqrt{2}}\right) \quad (3.22)$$

In practice,  $t$  is fixed and has to be chosen according to the desired PFA. This can be acquired by solving Equation 3.22 numerically. Using, instead of the Gaussian distribution, a gamma model or a negative exponential model, the detector will look like this:

$$x_o > \mu_c t \iff target \quad (3.23)$$

and is called a cell averaging CFAR (CA-CFAR). Like before  $t$  is fixed and determines the PFA and  $\mu_c$  is calculated with pixel values from the background window. Considering imagery



with a constant normalised variance ( $\sigma_{normalised} = \frac{\sigma}{\mu^2}$ ),  $\sigma_{normalised}$  is proportional to  $\mu$  and the two-parameter CFAR effectively becomes a CA-CFAR with a different design parameter  $t$ .

When searching for bigger objects, a variation of the CA-CFAR, where the CUT is expanded to a group of cells, seems useful. They form the target window, over which the mean value is calculated and compared with the threshold accordingly:

$$\mu_o > \mu_{ct} \iff target \tag{3.24}$$

Even with the guarding techniques described here, in the case of special circumstances such as sharp changes of the clutter or interference boundaries, the detection approach can lead to excessive false alarm rates. In this case, the cell averaging greatest-of Mean Level CFAR (CAGO-CFAR) can be applied, where both sides of the sliding window are analysed separately. The threshold value is then determined by using the larger clutter estimate of these two mean values. That helps in reducing false alarms but still suppresses detection and produces false negatives. Moreover, nearby objects still raise the threshold.

### 3.4.1.2 Sublook Correlation Techniques

The sublook or sub-aperture technique performs a spectral analysis of SAR data by extracting the spectrum and analysing portions of it, here defined as the sub-spectrum. The image that is obtained by executing the anti-transformation of a sub-spectrum is called a sublook or sub-image. To increase the efficiency, an FFT (fast Fourier transform) is used to transform into the frequency domain.

Sublook approaches were revealed to be beneficial to detect point-like coherent targets [171]. An advantage of that method is that objects do not necessarily need to have a high radar backscattering in order to be detectable [270] which is very helpful for this case of small vessels. They can be also be implemented for iceberg detection [271].

The sub-images can be generated in range and in azimuth direction. A perfect point scatterer and corner reflector remains coherent under small changes of the frequency. In azimuth, objects are tested when observed at different angles in the azimuth footprint where point targets would be isotropic and corner reflectors would stay coherent. Moving targets may smear out and lose coherency which may cause the detector to miss them [171].

It is still an active field of research and several variants of sublook correlation techniques are known, such as the sample cross magnitude correlation [170], the phase variance approach [272] or an approach that uses the generalised likelihood ratio test approach (GLRTA; [273, 36]).

The sublook correlation detector (herein called SubCorr; [171, 172, 54, 274, 36]) uses the cross-correlation between the two sublooks:

$$\rho = |\langle X_1 X_2^* \rangle| \tag{3.25}$$

with  $0 \leq \rho \leq 1$ ,  $X_n$  as the two sublooks and  $*$  as the complex conjugate operator.  $\langle \rangle$  indicates spatial averaging (e.g. a boxcar filter). The sub-images can overlap in parts of the spectral domain to detect vessels which are not robustly stable [171].

The sublook entropy detector [214, 36, 171] compares the inter-look entropy values and has a similar principle to the polarimetric entropy detector as described in section 3.4.1.3.

The sub-aperture or sublook coherence [171, 54, 173, 214, 275, 270] evaluates the phase similarities between two sublooks and is defined as:

$$\gamma = \frac{|\langle X_1 X_2^* \rangle|}{\sqrt{\langle X_1 X_1^* \rangle \langle X_2 X_2^* \rangle}} \quad (3.26)$$

which is the normalised cross-correlation of the sub-images.

#### 3.4.1.3 Polarimetric Entropy Detector

The polarimetric entropy detector (PolEntropy) uses the scattering entropy. There are two different concepts of such entropy ( $H$ ): the Shannon Entropy (SE), which was introduced to PolSAR theory by Refregier et al. [154] and the entropy in the Von Neumann sense which refers to the degree of randomness of the scattering. For the latter, which is used in this research,  $H = 0$  indicates a single dominant scattering mechanism of an isotropic object. Fully depolarising objects have a  $H = 1$  where all three basic scattering mechanisms are equally strong [276]. It can be calculated using the eigenvalues  $\lambda_i$  of the averaged  $[T]$ -matrix as [132]:

$$H = -\sum_{i=1}^n P_i \log_n P_i \quad (3.27)$$

where  $0 \leq H \leq 1$  and  $n = 3$  for quad-pol backscatter problems and  $n = 2$  for dual-pol data  $P_i$  are given by:

$$P_i = \frac{\lambda_i}{\sum_{j=1}^N \lambda_j} \quad (3.28)$$

where  $\lambda_1 \geq \lambda_2 \geq \lambda_N \geq 0$ . The PolEntropy uses the contrast between the entropy of the clutter  $H_{sea}$  and the entropy of the target  $H_t$ :

$$\Lambda_H = \frac{H_T}{H_{sea}} > T \quad (3.29)$$

with  $T$  as the threshold. It was first successfully tested to be used for ship detection in [277] and for the detection of sea ice in [276].

The entropy of water surfaces shows a very interesting behaviour. On calm water surfaces, the backscattered energy is so low that it drops below the sensor noise level. Since noise is statistically random, the entropy in that case becomes very high.

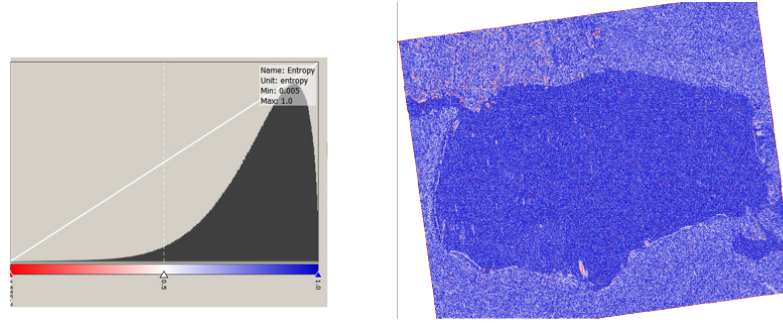


**Figure 3.10:** The entropy (from red = 0 to blue = 1) of the calm water surface of the small lake test-bed of the first data acquisition campaign (©DLR 2017).

Figure 3.10 visualises an example of high entropy levels, triggered by noise. At that stage, the entropy of the lake is higher than that of the vessel. With increasing wind and waves, the entropy of the water surface drop below the entropy of the vessel.

Multilook (sublook average) processing is required to obtain unbiased entropy values. Over-averaging degrades the spatial resolution. The degree of averaging (number of looks) influences the calculation of the entropy. The same is true for the anisotropy and the mean alpha. There is a bias at when the ENL is too low and the entropy seems lower, whereas the anisotropy and the mean alpha angle appear higher. Averaging can remove this bias [278, 279]. Therefore, the right choice for the level of averaging is very important.

#### 3.4.1.4 Polarimetric Match Filter

The Polarimetric Match Filter (PMF; [280, 264]) is a linear polarimetric detector that processes the polarimetric channels to maximises the TCR. This method has its origin in the context of pattern recognition and linear discriminant analysis [281]. It aims to find the set of linear weighting coefficients which provide the highest TCR. This TCR is given by

$$\Lambda_{PMF} = \underset{\underline{h}}{\text{Argmax}} \left[ \frac{\underline{h}^* |C_t| \underline{h}}{\underline{h}^* |C_{sea}| \underline{h}} \right] > T \quad (3.30)$$

with  $\underline{h} \in \mathbb{C}^3$ ,  $C_t$  and  $C_{sea}$  as the covariances of the target and the sea surface and T as the threshold. The optimal weight vector  $\underline{h}^*$  is the solution of the generalised eigenvalue problem

$$\underline{h}^* |C_t| = \lambda^* \underline{h}^* |C_{sea}| \quad (3.31)$$

where  $\underline{h}^*$  is the eigenvector with the highest eigenvalue  $\lambda^*$  and  $*$  is a conjugate transpose. The optimisation maximises the contrast between target and clutter selecting the best scattering mechanism to be used for the following detection [282].

#### 3.4.1.5 Polarimetric Whitening Filter

The Polarimetric Whitening Filter (PWF, [264, 283]) is designed to reduce the speckle variation. Its performance depends on the quality of the clutter estimation. The general form can be given as:

$$y = \underline{X}^* A \underline{X} \quad (3.32)$$

where the weighting  $[A]$ -matrix is assumed to be Hermitian symmetric and positive (semi-)definite and  $\underline{X}$  is the polarimetric scattering vector. The optimal weighting matrix is the one that results in an image with the minimum standard deviation-to-mean ratio. Therefore,  $A^*$  is a whitening filter using polarimetric vectors. The detector image with the minimum variation in its speckle is constructed as:

$$\underline{X}^* \Sigma_c^{-1} \underline{X} > T \quad (3.33)$$

with  $\Sigma_c^{-1}$  as the clutter covariance matrix,  $\underline{X}$  representing the scattering vector and  $T$  as the threshold.

The PWF underwent further development and was extended to be used with multilooked data [284, 285].

#### 3.4.1.6 Optimal Polarimetric Detector

The Optimal Polarimetric Detector (OPD) uses the likelihood ratio test in conjunction with complex Gaussian statistics. It was introduced by Novak et al. [264] under the assumption, that the PDFs for both the target and the clutter come from a Gaussian process and the TCR is known. The detector provides the best possible detection performance under these assumptions and is sometimes considered the gold standard against which other detectors can be compared.

The likelihood ratio has been shown to be a quadratic algorithm:

$$\underline{X}^* \Sigma_c^{-1} \underline{X} - (\underline{X} - \underline{\bar{X}}_t)^* (\Sigma_t + \Sigma_c)^{-1} (\underline{X} - \underline{\bar{X}}_t) > T \quad (3.34)$$

with  $\underline{X}$  as the radar return in the form of a polarimetric feature vector,  $\underline{X}_t$  as the target scattering vector,  $\Sigma_t$  and  $\Sigma_c$  representing the  $[C]$ -matrices of the target and the clutter and  $T$  as a detection threshold.

The decision was made not to use the OPD in this work because we do not know the exact scattering matrix of the rubber inflatable.

### 3.4.1.7 Polarimetric Symmetry Detector

The Polarimetric Symmetry Detector (here called PolSym) was introduced by [100] as a ship detector. It exploits the difference between the symmetry properties of the sea surface and those of metallic ships. Polarimetric reflection symmetry means there is no correlation between the co-pol and the cross-pol channels [286] and it can be defined using the elements of the  $[C]$ -matrix:

$$C_{12} = C_{21} = C_{32} = C_{23} = 0 \quad (3.35)$$

For most of naturally distributed objects, experiments have shown that the cross-correlation between the co-pol and the cross-pol scattering is close to zero. This is called reflection symmetry [88]:

$$\langle S_{HH}S_{HV}^* \rangle = \langle S_{VV}S_{VH}^* \rangle \approx 0 \quad (3.36)$$

In other words, the correlation coefficient between the co-pol and the cross-pol elements of the corresponding covariance matrix have to be zero [88]:

$$\sigma_{HHHV} = \sigma_{HVHH} = \sigma_{VVVH} = \sigma_{VHVV} = \sigma_{HHVH} = \sigma_{VHHH} = \sigma_{VVHV} = \sigma_{HVVV} = 0 \quad (3.37)$$

The reflection symmetry metric  $r$  is described as the modulus of the correlation between co-pol and cross-pol intensities [100, 102, 103]:

$$r = |\langle S_{xx}S_{xy}^* \rangle| \quad (3.38)$$

where  $x, y \in H, V$  leads to a  $[C]$ -matrix of the following form (see section 2.3.2):

$$\langle [C] \rangle = \begin{bmatrix} \langle S_{HH}S_{HH}^* \rangle & 0 & \langle S_{HH}S_{VV}^* \rangle \\ 0 & \langle S_{HV}S_{HV}^* \rangle & 0 \\ \langle S_{VV}S_{HH}^* \rangle & 0 & \langle S_{VV}S_{VV}^* \rangle \end{bmatrix} \quad (3.39)$$

In natural environments, such as the water surface of the open ocean which is constantly moving, reflection symmetry is generally satisfied but not always the case. Symmetry on the ocean surface depends on the local wind speed and its direction. Very calm water surfaces have reflection symmetry. Water waves show reflection symmetry too, but only if the azimuthal direction coincides with the local wind direction [88].

Artificial objects on the water surface, such as ships, show a different degree of reflection symmetry and  $C_{12} = 0$ ; it is often disrupted by complex structures where  $C_{12} > 0$  [104]. For detection purposes, this difference can be used to distinguish these objects from the water surface [100]. To obtain a binary detection mask for dual-pol HH HV data, the decision rule would be:

$$X = |\langle S_{HH}S_{HV}^* \rangle| > T \quad (3.40)$$

with  $T$  as the threshold.

#### 3.4.1.8 Geometrical Perturbation Polarimetric Notch Filter

The Geometrical Perturbation Polarimetric Notch Filter (GP-PNF; in this work called: PNF; [287, 17, 69, 288]) assumes the sea surface without a target to be homogeneous and it searches for coherency between the original and the perturbed target. The geometrical perturbation is performed by slightly changing the value of the Huynen parameters representing the target of interest [17]. This is preferred due to their close links with phenomenological properties of the target [118]. Alternatively, the  $\alpha$  model or any other parameterization based on a continuous function can be used [73, 132]. The concept of the polarimetric perturbation analysis is inverted and the PNF suppresses the radar return from the selected target [289]. That way, the detector makes use of the polarisation fork of the target.

To model partial targets, a stochastic approach is needed, in which second-order statistics in the form of the  $[C]$ -matrix are used. The detector itself is not based on a statistical technique but rather a physical approach based on the sensitivity of the polarimetric complex coherence to changes in polarisation [287]. It considers the full range of polarimetric information from the  $[C]$ -matrix and assumes a homogeneous scattering behaviour of the surrounding sea surface [290, 289]. The detector is finalised by setting a threshold on the coherence amplitude.

The formal expression of the detector for dual-pol data is:

$$\gamma_{dn} = \frac{1}{\sqrt{1 + \frac{RedR}{t_d^{*T} t_d - |t_d^{*T} t_{dsea}|^2}}} > T \quad (3.41)$$

with  $RedR$  as a reduction ratio which is set, based on the minimum intensity of the target to be detected. It also avoids numerical errors when computing the detection mask.  $t_{dsea}$  is the dual-pol normalised partial feature vector for the sea surface and  $t_d$  is the dual-pol normalised partial feature vector for the target (a six-dimensional complex vector obtained by stacking the independent elements of the covariance matrix).

This method was first proposed by [291]. Later, versions that work with dual-pol data [292] and single-pol along-track interferometry data [289] were presented. It is more of a general detector and can be used for all kinds of ocean targets, for example icebergs [293].

#### 3.4.1.9 Intensity Dual-polarisation Ratio Anomaly Detector

Originally, the Dual-polarisation Ratio Anomaly Detector (DPolRAD) was designed for detecting icebergs. It follows the expectation that icebergs will generate either more volume scattering or more multiple scattering than the water surface [112]. To enable successful detection, the algorithm explores the intensity ratio between the coherent cross-pol and co-pol channels of one dual-pol acquisition:

$$\Lambda = \frac{\langle |cross - pol|^2 \rangle_{test} - \langle |cross - pol|^2 \rangle_{train}}{\langle |co - pol|^2 \rangle_{test}} > T_\Lambda \quad (3.42)$$

That way, the detector identifies an increase in depolarisation with a smaller test window and a bigger training window. The two windows are spatially averaged and  $T_\Lambda$  is a chosen threshold.

The Intensity Dual-polarisation Ratio Anomaly Detector (iDPolRAD) is the DPolRAD augmented by multiplying with the cross-pol channel:

$$I = \frac{\langle |cross - pol|^2 \rangle_{test} - \langle |cross - pol|^2 \rangle_{train}}{\langle |co - pol|^2 \rangle_{test}} * \langle |cross - pol|^2 \rangle = \Lambda * \langle |cross - pol|^2 \rangle > T_\Lambda \quad (3.43)$$

Homogeneous clutter let  $\Lambda \rightarrow 0$ . If volume and multiple scattering is reduced in the test window  $\Lambda$  becomes a negative figure and if an object like a vessel enters the test window  $\Lambda \rightarrow \infty$  [294].

#### 3.4.1.10 Maritime Moving Target Indication

The indication of ground moving target (GMTI) or marine moving targets (MMTI) is a problem that can be solved with interferometric approaches. Most GMTI methods try to filter the clutter contribution from the signal by using the fact that it is non-moving. An example for that approach is space-time adaptive processing (STAP; [295]). Along track interferometry (ATI; [296]) tries to discriminate non-moving from moving contributions by estimating a velocity-dependent attribute. Distributed compressed sensing (DCS) can estimate target velocity parallel and perpendicular to the azimuth direction [297].

Ships often move and therefore detection approaches such as coherent time-frequency analysis are susceptible to distortions due to the fact that the focusing process is designed for scenes with static or slow-moving objects; the assumptions about the phase behaviour of a non-moving point scatterer signal are no longer valid for moving objects. The LoS projection of the velocity produces an along track displacement of the moving object (de-location), coarsened resolution, decreasing amplitude and vanishing of the target image, if the Doppler frequencies fall outside the processed Doppler band. This effect is also called off-the-track-effect or boat-off-the-wake effect.

The amount of the displacement due to an object's slant-range velocity can be estimated as [298, 299]:

$$\Delta X = -\frac{Rv}{V} \quad (3.44)$$

where  $R$  is the range,  $v$  is the slant-range velocity of the moving object and  $V$  is the SAR system velocity.

### 3. Object Detection in the Maritime Domain with SAR

---

Any along-track velocity component leads to a defocussing of the moving object in the form of a smearing effect and an amplitude reduction [296]. Large radial velocities induce Doppler frequencies larger than half the PRF and increase the azimuth displacement [300].

Once detection is successful, additional information about the moving object, such as velocity and direction can finally be extracted by exploiting these effects. For instance, along track velocity may be estimated from sub-aperture processing, while line of sight velocity is derived from ship-wake displacement [299, 301].



# 4

## The InflateSAR Campaign

This chapter comprises the scientific work of this thesis, including two data collection campaigns. It developed in five main steps represent a continuous process and build upon one another:

1. the first data acquisition campaign from March till September 2017. It mainly yielded single-pol and dual-pol data from TSX of an empty rubber inflatable on a lake.
2. the first section (4.3) use the data from the first campaign to:
  - find out whether/under which circumstances a detection of the target is possible with SAR
  - understand the radar backscattering pattern of the inflatable, including first polarimetric analyses
  - identify the most suitable methods (detectors) and data (sensor parameters such as the spatial resolution) to solve the detection problem
3. the second section (4.4) builds on the results of section 4.3 using the same test data and has the following goals:
  - to test a variety of VDSs with the inflatable
  - to identify the main influencing parameters and quantify their impact on the detection capabilities of the VDSs being trialled
4. the second data acquisition campaign from March till August 2022: after shedding some light on the SAR potential for detecting an empty refugee inflatable on a lake, a second data acquisition campaign was planned with the aim of finding out how to detect a full vessel under different weather situations on the open ocean. For that, a rubber inflatable was placed on a lake and prepared so that it appears fully occupied with 80 people in SAR imagery.
5. the third section (4.5) uses data from that campaign and wants to:
  - analyse the polarimetric scattering behaviour of the inflatable using a variety of polarimetric decompositions
  - create test data that emulates the real situation of a fully occupied vessel on the open ocean
  - test different VDSs with the inflatable, including new detection algorithms and different detector fusion approaches
  - estimate the influence of the sea state on the detection capabilities of the different VDSs.

## 4. The InflateSAR Campaign

---

- find the best-suited detection approaches for high sea states and different sensor parameters (polarisation, incidence angle, spatial resolution) and scene parameters (vessel orientation)

Accordingly, this chapter is put together mainly from existing content which was previously published in the three journal papers within MDPI Remote Sensing [302, 303, 304].

### 4.1 The Test Object

The vessel that is to be detected is a 0.8 m high, 3.5 m wide and 12 m long rubber inflatable. It is a non-metallic (apart from the outboard engine), small, heterogeneous scatterer. The main body is an inflated chamber with a diameter of 80cm, subdivided into five sub-chambers. It consists of ca. 1mm thick PVC. The floor of the boat is, in most cases, put together of wooden particle boards, screwed together to maintain a minimum amount of stability.

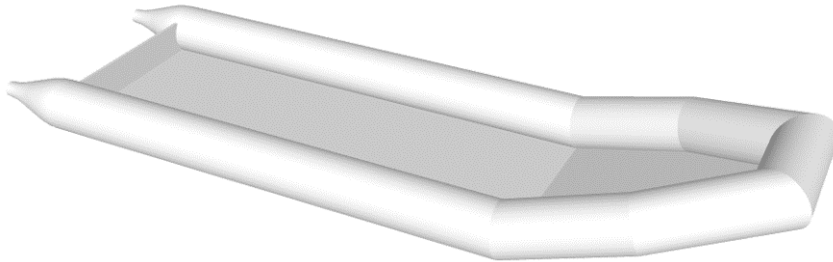


**Figure 4.1:** 3D model of the test object, the rubber inflatable [305].

Due to the absence of available data from a fully occupied inflatable, there is no certainty about the scattering mechanisms in play at and around the inflatable yet. In theory, the dry vessel should be more or less invisible for microwaves.

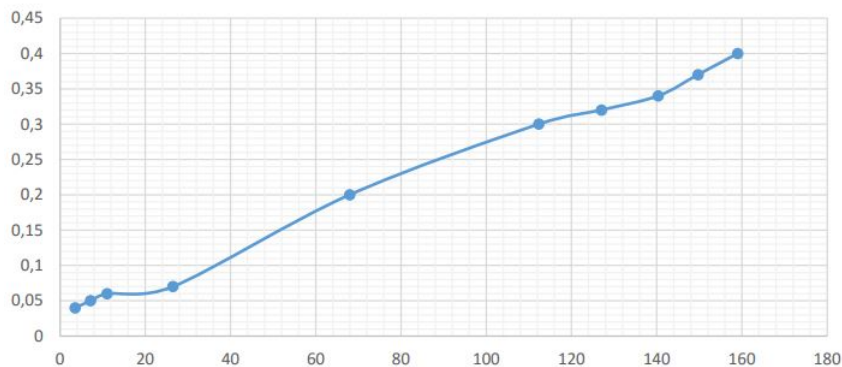


**Figure 4.2:** Draught of the rubber inflatable (y-axis, in meters) with different numbers of passengers (x-axis) [305].

Its strong floating capabilities and its flat hull reduce its draught to a minimum — even when fully occupied with 160 passengers the inflatable draws only about 40 cm (Figure 4.2).

## 4.2 Spaceborne SAR Data: Overview

For the first data campaign and the first and second published papers, single-pol and dual-pol X-band SAR data from TSX, provided by the German Aerospace Center (DLR), were acquired. TSX (launched in 2007) and its twin TDX (launched in 2009) operate from a height of 514km on a sun-synchronous orbit with a ground speed of about  $7\text{km s}^{-1}$  (15 orbits per day). They use a carrier wavelength of  $\approx 31\text{mm}$  and a frequency of 9.65GHz [49]. The repeat cycle is 11 days, but the same region can be imaged at different incidence angles every two to three days, depending on the scene latitude. Typical TSX incidence angles range between  $20^\circ$  and  $55^\circ$  [306]. The Noise Equivalent Sigma Zero (NESZ) for single-pol and dual-pol Stripmap imagery is  $-19\text{dB}$  [49].

Additionally, the freely available C-band data from the two SAR Sentinels (1a and 1b) from the European Space Agency (ESA) were used. The two satellites use the same orbit, phased  $180^\circ$  apart, providing a revisit time of six days at the equator [307]. However, it showed that they offer insufficient spatial resolution for this application. More information about and key parameters of the Sentinels can be found at [308].

For the second data campaign and the third publication, mainly dual-pol TSX data was collected and used for detector testing and benchmarking. In addition, the collection of a small number of quad-pol X-band data from Cosmo-Skymed Second Generation (CSG; provided by the Agenzia Spaziale Italiana, ASI) was possible. The CSG consists of two SAR satellites, launched in 2019 and 2022 and their repeat cycle is 16 days [309]. It is the successor to the COSMO-SkyMed first generation constellation which consists of four satellites, launched between 2007 and 2010. They are still operational and can image an area of interest several times a day. The quad-pol data was well-suited to analyse the scattering behaviour of the vessel and its surroundings using polarimetric decompositions.

Finally, a few very high-resolution VV-pol X-band data from ICEYE were collected, a Finland-based global company, and used it to learn about the scattering intensities of different parts of the vessel. ICEYE operates the world's first small SAR satellite constellation. Its fleet consists of 20+ satellites (as of 2022) with 10+ more planned for the near future. ICEYE offers sub-day revisit-times and near-real time processing [310, 311].

## 4.3 Evaluating SAR Identification Capabilities of Distressed Refugee Boats

In this section the outcomes and analysis of the first InflateSAR campaign are described. SAR data were collected over the Müggelsee in Berlin where an original refugee inflatable was deployed in. SAR acquisitions include the TanDEM-X (TDX) and TerraSAR-X missions from the German Aerospace Center (DLR) with the High-Resolution Spotlight (HS) and Stripmap (SM) modes and the European Space Agency's (ESA) Sentinel-1 (S1) with Interferometric Wide Swath mode (IW). Multispectral data from Sentinel-2 were collected as well, but were not used here. Then follows the data processing and data quality analysis, including an evaluation of sea clutter and its implications for ship detection. The results give a comprehensive picture of the inflatable's backscattering with these two sensors and its behaviour under different scene and sensor settings. Finally, there follows an investigation of the usability of such SAR data for mitigation of the ongoing humanitarian crisis on the open sea with a special focus on the central Mediterranean Sea, where rubber boats like ours are frequently in distress.

The section's findings are the basis for further developments of a vessel detection system

specially tailored for inflatable boats. Its main parts are also available as a journal paper in Remote Sensing [302].

### 4.3.1 Introduction to Ship Detection

Ship detection, classification and monitoring have become some of the first operational services to be provided by civilian space-borne synthetic aperture radar satellites [312, 313, 314]. It has been observed that usually, the main feature of maritime vehicles in SAR images is a bright backscatter. In most cases, this can be explained by the presence of several metallic structures and corners [171]. Unfortunately, rubber boats do not have metallic features at all, except the small outboard engine.

The detection of ships and other maritime objects with SAR has a long research history (e.g. [264, 127, 265, 128, 268, 315, 316, 100]). Semi-automatic detection and classification of large, metal-made maritime vessels has been a popular research topic in recent decades. State-of-the-art, high-resolution SAR data and methods from polarimetry (e.g. [317, 177, 103]), sublook analysis (e.g. [318, 319]), along-track interferometry (ATI; e.g. [320, 321, 299]), Displaced Phase Center Antenna (DPCA; e.g. [321, 322]) or moving target indication (MTI; e.g. [323, 180, 182]) were tested with success in a broad variety of projects and applications. A number of recent international, high-level research projects, such as SAGRES [324], Space Shepherd [325] and NEREIDS [326] included the objective of automatically detecting small, non-metallic maritime objects. SAGRES especially deserves attention, since a seven meter long rubber boat was successfully identified with SAR imagery from RADARSAT-2, leading to the rescue of 38 migrants in distress.

It has been observed that the backscatter from ships is generally dominated by the double reflection occurring between the vertical walls or structures of the ship and the sea surface (e.g. [327, 266]). Polarimetric decompositions can be used to identify such scattering mechanisms, although double reflections do not always appear as the Pauli double bounce. Polarimetry can also be used to indicate surface conditions, such as roughness, shape, orientation and material properties [328]. Speed and heading of the vessel relative to the sensor's line of sight (LoS) are used in ATI for detection (as in [329]). Phenomena on the water surface, such as wakes of a moving ship, can be visible under certain conditions (for example [330]).

Geophysical processes generally have a high special variability and they produce variations in ocean backscatter, even within small areas. Under some conditions (e.g. very high winds), the water backscattering can be extraordinarily bright, covering less bright vessels. Especially small waves in the dimension of the radar beam's wavelength generate a spatially periodic structure or a rough water surface which dominates the mean backscatter intensity. This phenomenon appears stronger for frequencies higher than 5 GHz (C-band) and at incidence angles smaller than  $25^\circ$  [171], and the Bragg model was proven to be a reliable scattering model [31]. A sound understanding of ocean clutter and its statistical characteristics forms the basis of designing high-performance detection algorithms.

Sensor-related parameters which influence the backscattering over the sea are geometric and radiometric resolution, surface roughness, polarisation, incidence angle and frequency [331, 332, 73, 333, 334, 335]. Generally, a calm water surface will scatter away the electromagnetic radiation (surface scattering) and it will appear relatively dark. Metallic vessels call for a number of different scattering mechanisms; their radar signal is generally stronger and appears as a bright spot in SAR intensity images. For this reason, many vessel detection systems (VDS) aim at the identification of small, strong scatterers over a clutter background [127, 253,

342, 207, 287, 343, 344, 345, 346, 262, 336, 337, 338, 339, 340, 260, 341]. In this context, the contrast between the backscatter of the sea surface and the target (target to clutter ratio, TCR) is a crucial factor when using intensity-based detectors [347]. It was established that the TCR should at least be larger than 10 dB to enable reliable identification [348].

A common way to apply thresholds on intensity images uses statistical tests on the clutter intensity trained with local information. This method keeps the probability of false alarms constant across the entire image and is called the constant false alarm rate (CFAR) [349]. To adapt to changing levels of brightness, several local estimators can be used. The cell averaging CFAR (CA-CFAR) uses the mean pixel values for the clutter and the region of interest (ROI) window after a guard window has been used to reject contamination from the object under analysis [350, 351, 352, 353, 354]. Other detectors try to implement speckle noise reduction [355], using the Gabor wavelet correlator [356] or the tensor robust principle component analysis 'tensor RPCA' [317].

Much work has been done on modelling and simulations, and when polarimetric data are available, decomposition techniques can contribute to the effectiveness of vessel detection systems, as described in [357, 257, 358, 197, 359]. Other approaches consider different statistical methods (e.g. the probability distribution function) [312, 358].

Apart from the exploration of differences in intensity values, there are sublook detectors (as in [318, 171, 174, 319]), polarimetric detectors [315, 277, 265, 169]) and approaches that exploit the phase coherence instead of the intensity [173].

The polarisation and the incidence angle have been proven to be important factors in defining the detection capabilities. Studies aimed at detecting large metallic vessels revealed that HH polarisation is in comparison to VV polarisation less sensitive to waves and water roughness, has less clutter and has a better TCR [312]. A stronger radar return of the water surface at high sea states has been reported under higher incidence angles in [207]. The combination of HH polarisation with high incidence angles reduces water surface backscatter and enhances the detectability of (big, metal-made) ships. The contrast between boat and clutter in the HH polarisation channel is weaker with medium and low incidence angles [360]. The cross-polarised channels (HV, VH) provide a better TCR with moderate and low incidence angles [361, 277]. They also allow for more accurate calculation of ship size in the case of big metallic vessels. In principle, the cross channels exhibit a lower ocean backscatter and they are much less affected by the presence of bright sea features than co-polarised data. It can be observed that the ships' backscattering is weaker compared to co-polarised channels, but the TCR is higher, especially for low angles. The combination of both co- and cross-polarisation, is beneficial and offers higher potential for the detection and classification of vessels [348, 362].

With the rapid evolution in processing power, the pattern recognition community also added an important contribution to ship detection. However, many of the traditional methods, such as region selections, scale-invariant feature transform (SIFT), support vector machine (SVM) and histogram of oriented gradients (HOG), are typically associated with high computing costs. With deep learning, the time performance increases because it uses GPU acceleration.

The region-based convolutional neural network (RCNN; [363]) and the sliding window were followed by Fast-RCNN [364] and Faster-RCNN [365, 366]. Improvements and reduced complexity were achieved by using the softmax function instead of SVMs by using multi-resolution convolutional features and by dividing the large detection area into region of interest (ROI) images. Ref. [367] used this approach for the detection of ships.

## 4. The InflateSAR Campaign

---

Ref. [368] presented a grid-CNN (G-CNN), which is a combination of a backbone-CNN (B-CNN) and a detection-CNN (D-CNN) to further improve and speed up automatic ship detection. Other approaches, such as YOLO [369] and YOLOv2, attempt to embrace the whole image during the training and testing period [370]. Ref. [371] used a deep neural network (DNN) for SAR image classification with the sliced Wasserstein distance (SWD) to provide a better solution to the optimisation problem<sup>1</sup>.

### 4.3.2 A Scattering Model of an Inflatable Refugee Boat

The inflatable vessel used in the InflateSAR experiment is 12 by 3.5 m in size (Figure 4.3). The volumes rise about half a meter over the water surface. Inflatable of this kind are not ready to cross any bigger water body and they cannot withstand high seas. Therefore, they can be declared as in a state of distress from the moment of disembarkation. The construction materials used were rubber (mainly PVC) and wooden floor plates as stabilising inlays. Excluding the outboard engine and small rings and bits, there are no metallic components. The small size of the engine and the absence of other large metallic parts results in a small radar cross section. This was expected to impede detection efforts.



**Figure 4.3:** The inflatable rubber boat.

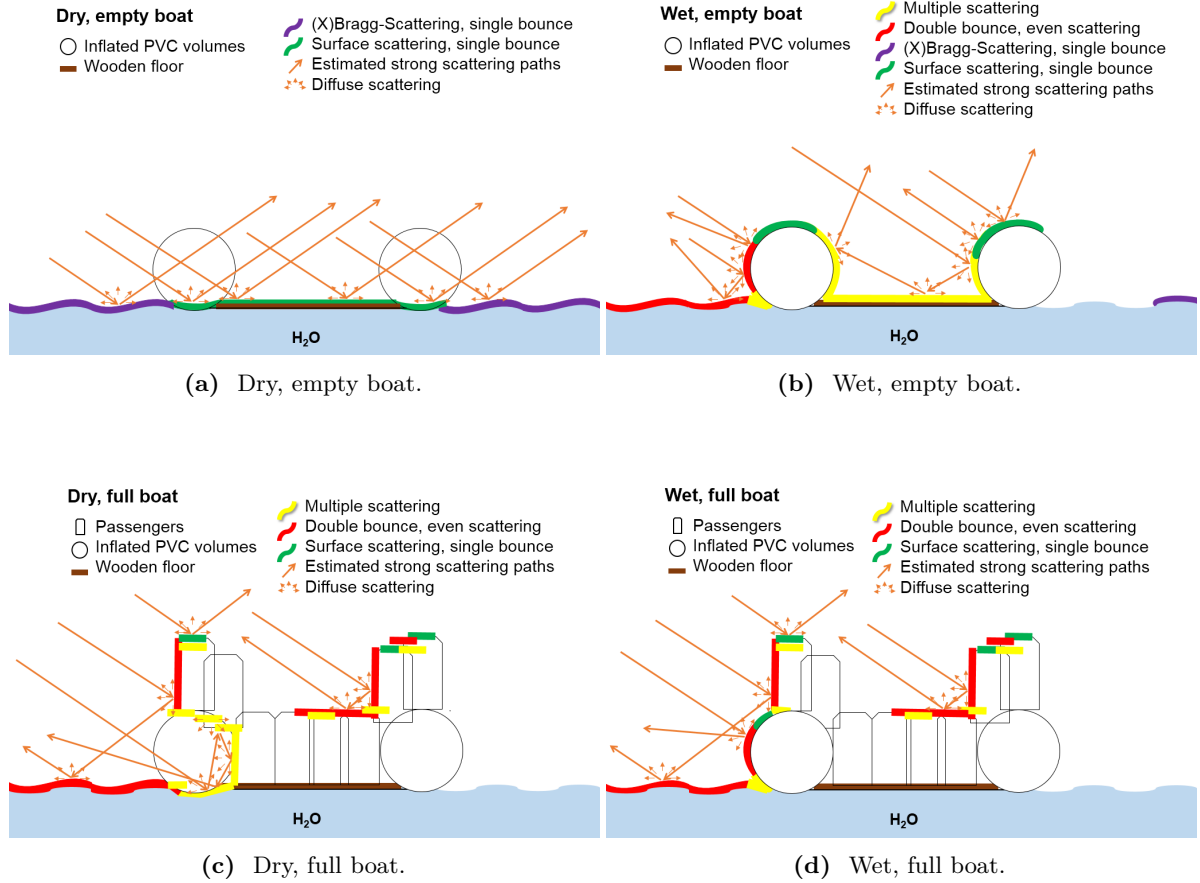
When microwaves impinge on a surface, the energy backscattered depends on many physical factors. A very prominent one is the dielectric constant  $\epsilon'$ .  $\epsilon'$  is an intrinsic characteristic of the material and varies due to a number of factors, such as the material's moisture, temperature and salinity. It can be used for the identification of specific materials, for example, metals [74]. Plastic exhibits a low dielectric constant, which makes the material relatively transparent to the radiation in C and X bands. However, the situation changes if the plastic is covered by a thin layer of water (even just a few millimetres, brought about by dew or spray). This is because the dielectric constant of water is very high in C and X bands.

Figure 4.4 should give an idea about the appearance of the different scattering mechanisms expected on the rubber inflatable. They are shown in an example scenario of low sea state, under an incidence angle of  $57^\circ$  with the boat broadside facing the sensor's LoS at  $90^\circ$ . The model shows how in theory the dominant mechanisms change depending on wetness and the presence or absence of passengers. Refraction of the electromagnetic wave is expected when passing through media of different refraction indices  $n$  at TerraSAR-X's carrier frequency (9.65 GHz), such as air ( $n \approx 1$ ), polyurethane ( $n \approx 1.6$ ) and the wooden floor ( $n \approx 1.5$ ). The resulting changes of direction before and after the optical thicker mediums are expected to level each other out. Layover shadows prevail at the faces and objects facing away from the sensor. Possible complementary phenomena, such as constructive reflection, destructive

---

<sup>1</sup>the previous four paragraphs are also available in our publication: [304]

reflection, frustrated total internal reflection and the phase jump of  $\frac{\lambda}{2}$  as a function of the incidence angle  $\phi$  should be mentioned here but are not addressed in Figure 4.4. The same is true for the polarisation, which also affects the scattered wave.



**Figure 4.4:** Expected dominant scattering mechanisms at and around the inflatable depending on wetness and superstructure with X-band, an incidence angle of approx. 45°, the boat being oriented 90° to the LoS and a water wave height of about 4cm (Bragg waves).

Another important factor is the object's and the water surface's roughness. X-band TerraSAR-X (TSX) and C-band S1 radar sensors have very limited penetration in liquid water. Since satellite SAR is side-looking, a flat and calm water surface is particularly smooth and scatters very little energy back to the sensor, which is why it appears black in SAR images; the energy is reflected away in the specular direction, as for a mirror. In most of the cases, water surfaces have waves (e.g. capillary and gravity, swells, etc.). Waves and spray induce surface roughness which produces complex scattering interactions, such as Bragg scattering [372]. The sea state is subject to wind speed and wind direction and always is the combination of wind waves from local winds and swell generated by distant weather systems.

Apart from the scene characteristics, sensor parameters such as wavelength, polarisation, incidence angle and radiometric and geometric resolution largely affect the pixel backscattering. These in return influence the capability to detect vessels. In conclusion, a better understanding of scattering mechanisms for water and object connected to scene conditions and system parameters is essential for this undertaking. This is not only for evaluating the detection capabilities, but also for inverse modelling approaches and the design of future data acquisition campaigns.

## 4. The InflateSAR Campaign

In terms of polarimetric richness, we can separate data into single, dual and quad (or full) polarisation data which respectively include one, two or four polarisation channels. Quad-pol data yields better results compared to single-pol or dual-pol data due to its increased information including more independent images, but it suffers from the trade-off a decreased spatial resolution, a smaller swath width or a higher noise level [74, 24, 292]. Advanced methods based on quad-pol data and polarimetric decomposition methods can be applied. They enable the identification of scattering mechanisms such as surface, volume and double-bounce scattering. The exploration based on different combinations of those add a viable layer of information to ship detection approaches (e.g. [373, 327, 169, 264]).

### 4.3.3 Data

#### 4.3.3.1 Data Collection Campaign

In this work a unique SAR dataset with the ground-truth of a refugee inflatable was acquired. Data are from the DLR mission Tandem-X and from ESA’s Sentinel-1 (S1). The five-month data collection campaign was implemented in 2017 at the Müggelsee, a lake near Berlin. In this experiment the backscattering from the inflatable with the minimum disturbance possible from the surrounding water surface’s clutter was investigated. A lake was selected due to the reduced presence of large waves and absence of breaking waves, spray and sea foam. The backscattering from a small lake was expected to be very low and the radar backscattering produced by the inflatable was meant to be easier to delimit. Further, it made it possible to identify more easily the polarimetric scattering mechanisms occurring at the vessel and to gain a deeper understanding of their influences on the vessel’s radar cross section and the inflatable’s detectability. Ground measurements were accomplished using a standard GPS receiver with an average accuracy of about five meters.

The acquisition campaign was designed to cover a broad variety of the main sensor settings which are polarisation, resolution and incidence angle. It resulted in 53 TSX, five TDX (here, they are called: *movingR*) and eight S1 SAR images, collected during 45 data gathering sessions (Table 4.1). In this section, ‘low angles’ cover incidence angles between 20° and 36°, whereas the category of ‘high angles’ represents those between 37° and 53°. The nominal spatial resolution varies depending on incidence angle and polarisation. The pixel shape and size underwent reconfiguration due to preprocessing, including geocoding with the primary goal to maintain the spatial resolution. Most HS mode data has around one meter pixel size, for SM mode values vary between one to two meters, and S1 data reaches about 8.5 m. Some polarisation channels, such as full polarised data, were not available. Therefore, in this section the research has been limited to co-polarised single (HH, VV) and co/cross-dual polarised (HH VV, HH HV, VH VV) channel combinations.

**Table 4.1:** SAR data collection according to acquisition mode, polarisation and incidence angles (low angles ‘L’, high angles ‘H’).

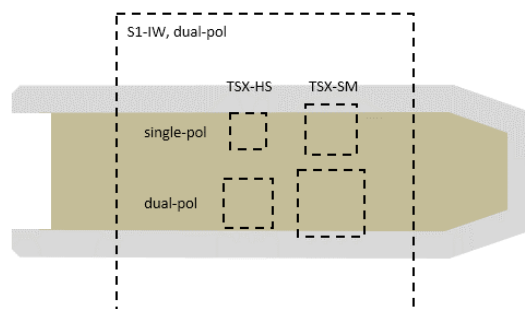
Mission	Acquisition Mode	Single pol HH	Single pol VV	Dual cross-pol	Dual co-pol
TerraSAR-X (TSX)	High-Res. Spotlight (HS)	1L, 7H	1L, 4H	n.a.	2L, 12H
	Stripmap (SM)	1L, 4H	1L, 2H	1L, 5H	3L, 9H
TanDEM-X (TDX)	High-Res Spotlight (HS)	1L, 2H	n.a.	n.a.	0L, 2H
Sentinel-1 (S1)	Interferometric Wide Swath (IW)	n.a.	n.a.	2L, 6H	n.a.



Table 4.2 lists the average pixel size for different acquisition modes in square meters, for which Figure 4.5 provides a visual overview. The image to the right illustrates the size ratios between the various data's pixels and the boat. HS mode and SM mode are assumed to have satisfactory spatial resolution for a successful identification. In S1's IW mode the pixel area is about two times the vessel's area, hampering detection efforts. Therefore, it is very likely that S1 data do not reach the minimum resolution needed for a successful identification of the vessel and more S1 data would be necessary to finally prove this.

**Table 4.2:** Pixel size in  $m^2$  of available acquisition modes after resampling.

	TSX-HS	TSX-SM	S1-IW
Single-pol	0.79	1.52	-
Dual-pol	1.45	2.57	71.74



**Figure 4.5:** Comparison of the vessel's size and the available data's pixel sizes.

During the campaign, different combinations of the inflatable's superstructure (full/empty boat), movement and orientation relative to the sensor's LoS by six setups called 'experiments' (Table 4.3), were covered. It was the goal of these experiments to examine the impacts of selected scene settings on the boat's radar backscattering pattern and its detectability. The main ideas behind the experiments' designs are:

- the superstructures of said open-top inflatables are shaped by the cargo, in this case the passengers. A boat fully loaded with people (*full*; Fig. 4.6) is expected to change scattering mechanisms (e.g. modelled as adding volume scattering and multiple reflections). To investigate these influences, four data takes had 30 passengers occupying the vessel



**Figure 4.6:** The inflatable with 30 volunteers.

## 4. The InflateSAR Campaign

- to test the influence of the inflatable’s orientation compared to the radar wave’s path, the vessel faced different parts toward the sensor: prow or stern side orthogonally (*parallel*), the broadside orthogonally (*orthogonal*) or the broadside at an angle of  $45^\circ$  (*inclined*). This should add to an analysis of the backscattering behaviour of specific parts of the boat, such as the outboard engine, double bounce caused by its passengers and double bounce and volume scattering at the broadside or at the prow of the boat. In principle, electromagnetic waves, impinging on the vessel at  $45^\circ$ , are expected to be scattered away, whereas orthogonal or parallel vessel orientation should lead to a situation wherein the backscattering should be higher
- two of the experiments include a moving inflatable at its highest possible speed ( $\sim 10$  km/h), where *movingAZ* has a boat moving in azimuth and *movingR* relates to movement in ground range. Movement is expected to provide the possibility of detecting the position and orientation of its wakes. However, movement involves smearing effects and azimuth displacement which may impede the detection

**Table 4.3:** Data collection: available datasets per experiment type.

Experiment	Movement	Orientation	Superstructure	# Images	
				TSX	S1
orthogonal	static	$90^\circ$	empty	27	8
inclined	static	$45^\circ$	empty	10	0
parallel	static	$0^\circ$	empty	4	0
full	static	$90^\circ$	$\approx 30$ passengers	4	0
movingAZ	moving	$90^\circ$	empty	8	0
movingR	moving	$0^\circ$	empty	5	0

Apart from the described sensor and scene settings, the morphology of the data is subject to a number of additional scene settings which are not controllable. Amongst them are the inflatable’s surface humidity and the wind situation. The latter was quite stable throughout most acquisitions (Table 4.4a). In the great majority the wind speed is below  $5 \text{ ms}^{-1}$  and the prevailing winds were westerly, deviating no more than  $30^\circ$  from the LoS (Table 4.4b).

**Table 4.4:** Wind speed and wind direction during the data collection.

(a) Wind speed ( $\text{ms}^{-1}$ ).					(b) Wind direction (in degrees relative to the LoS).			
	<2.5	2.5–5	5–7.5	7.5–10		<30°	31–60°	61–90°
# TSX datasets	24	21	6	2	# TSX datasets	27	20	6
# S1 datasets	6	0	2	0	# S1 datasets	4	2	2

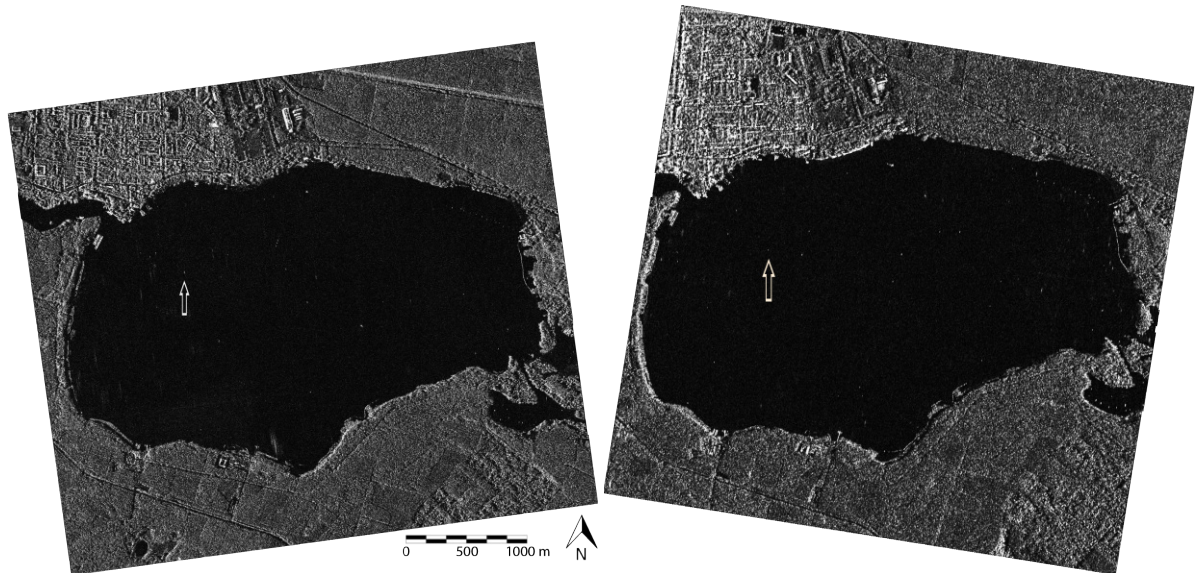
The vessel’s surface moisture was recorded during each acquisition, since especially in the morning, chances were good that the volumes of the inflatable were covered by water drops due to rain or dew. In about 60% of attempts the boat could be identified when it was dry compared to 40% in case of wet conditions. The influence of the boat’s moisture on the detection capabilities or its radar backscatter behaviour could not be proven statistically, though. For that, a much more comprehensive data basis would be necessary here.

### 4.3.3.2 First Inspection of the Backscattering of Inflatable Boats

The preliminary processing includes radiometric calibration, geometric calibration and georeferencing. Preprocessing steps are slightly different for each satellite platform. For

instance, S1 data require additional processing steps, such as applications of an orbit file, removal of thermal noise and debursting. This was done using the Sentinel Application Platform (SNAP) in combination with the Sentinel-1 Toolbox from the European Space Agency.

After the preprocessing, the image pixels represent the normalised radar cross section expressed as scattering coefficient or Sigma Nought ( $\sigma^0$ ). Speckle filtering or multilooking was tested, but due to the very small size of the boat they reduced the maximum backscattering and decreased its TCR. Therefore, no additional multilooking was applied to preserve the full spatial resolution of the data at the expense of speckle reduction. Figure 4.7 shows a part of two of such scenes after preprocessing and projecting into the geodetic reference system WGS84. The corresponding snippets further down are Figure 4.8g for Figures 4.7a and 4.9g for Figure 4.7b. The lake can be clearly recognised as the dark area with relatively low radar response and bright dots representing buoys and maritime vehicles; amongst them there is the inflatable at the tip of the white arrow. Most of the surroundings are forest with a residential area in the north-east. Figure 4.7b was taken on a descending orbit with the sensor viewing from the east receiving strong backscatter from the first treeline on the lake’s western shores. The ascending orbit of Figure 4.7a brightens up the treeline on the eastern shore.



(a) VV polarisation, ascending orbit, dual-pol TerraSAR-X Spotlight scene (©DLR 2017). (b) HH polarisation, descending orbit, dual-pol TerraSAR-X Stripmap scene (©DLR 2017).

**Figure 4.7:** Subsets of two examples of dual-pol TerraSAR-X Stripmap scenes showing the lake Müggelsee and its surroundings.

The water surface clutter and the inflatable’s radar signal were statistically analysed in a consistent way and its backscatter behaviour was classified throughout the different datasets. The main purpose was to assess the detection capabilities under different sensors and scene settings. To identify the vessel and to define its extent, pixels with noticeably higher intensity values compared to the water surface clutter were used. All further analyses were computed based on this intensity-based definition of the vessel.

The galleries in Figures 4.8–4.10 show the intensity ( $\sigma^0$  in dB) of the vessel’s radar pattern of all positive identifications after preprocessing. The 100 by 100 m sized cut-outs centre the boat and are grouped by acquisition mode. The colour ramps use each individual image’s mean value as the minimum (dark) and the maximum value for strong radar response. The

#### 4. The InflateSAR Campaign

subtexts indicate the polarisation plus one important scene or sensor parameter. Images with no further description were acquired under a 'standard' set of parameters: high incidence angle; stationary; empty boat oriented orthogonally to the LoS. That is also true for Figures 4.11–4.13 below which comes up with the 3D-representations of the same data of  $\sigma^0$  values in dB-scale. Here, each colour scale covers the full range of values. They illustrate that the vessel's radar signatures differ a lot in terms of size and contrast between the images. That challenges any attempt at developing automatic identification techniques.

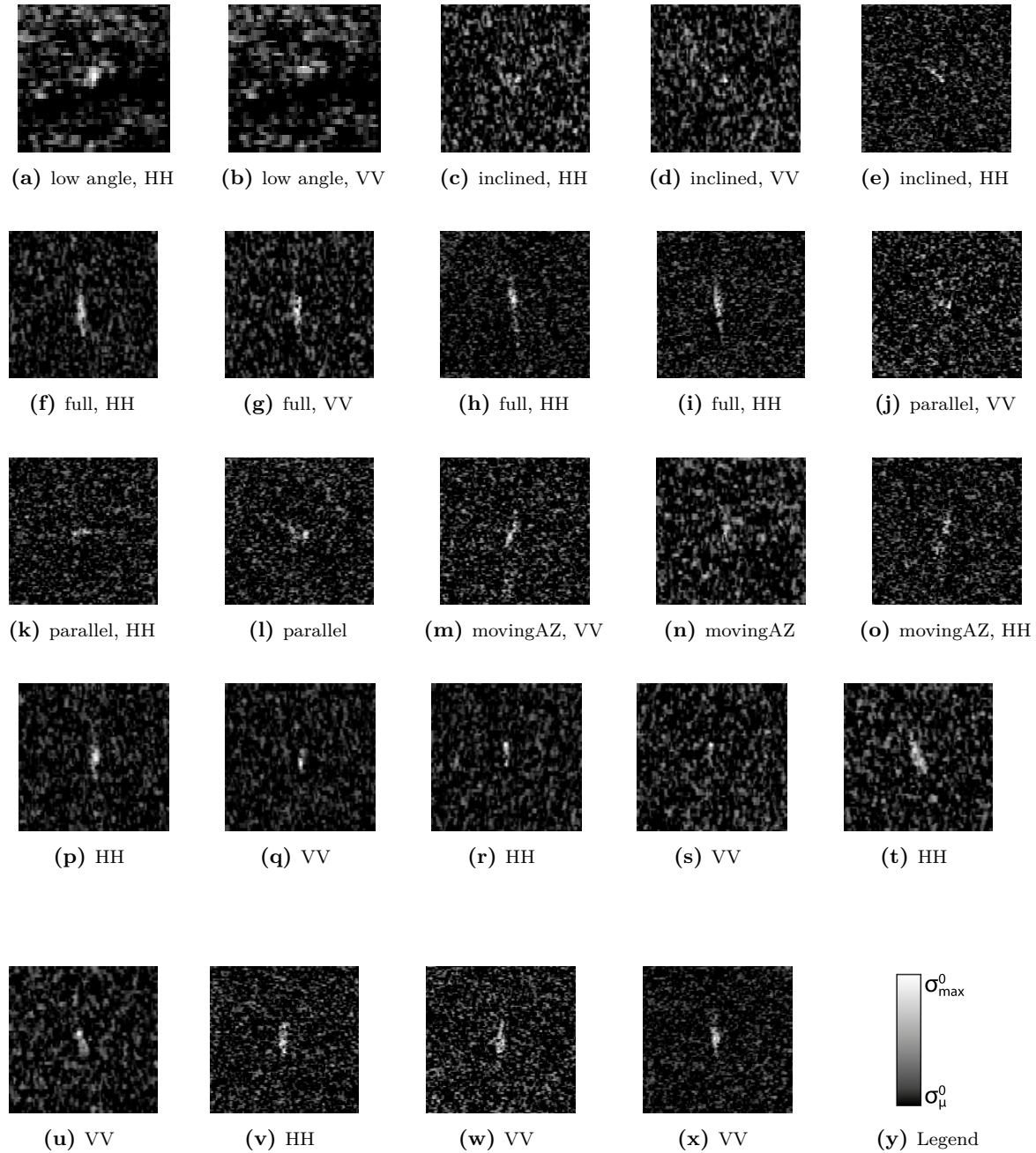


**Figure 4.8:** The vessel's radar footprint in TSX-HS mode (©DLR, 2017) with indications for polarisation and special scene or sensor settings.

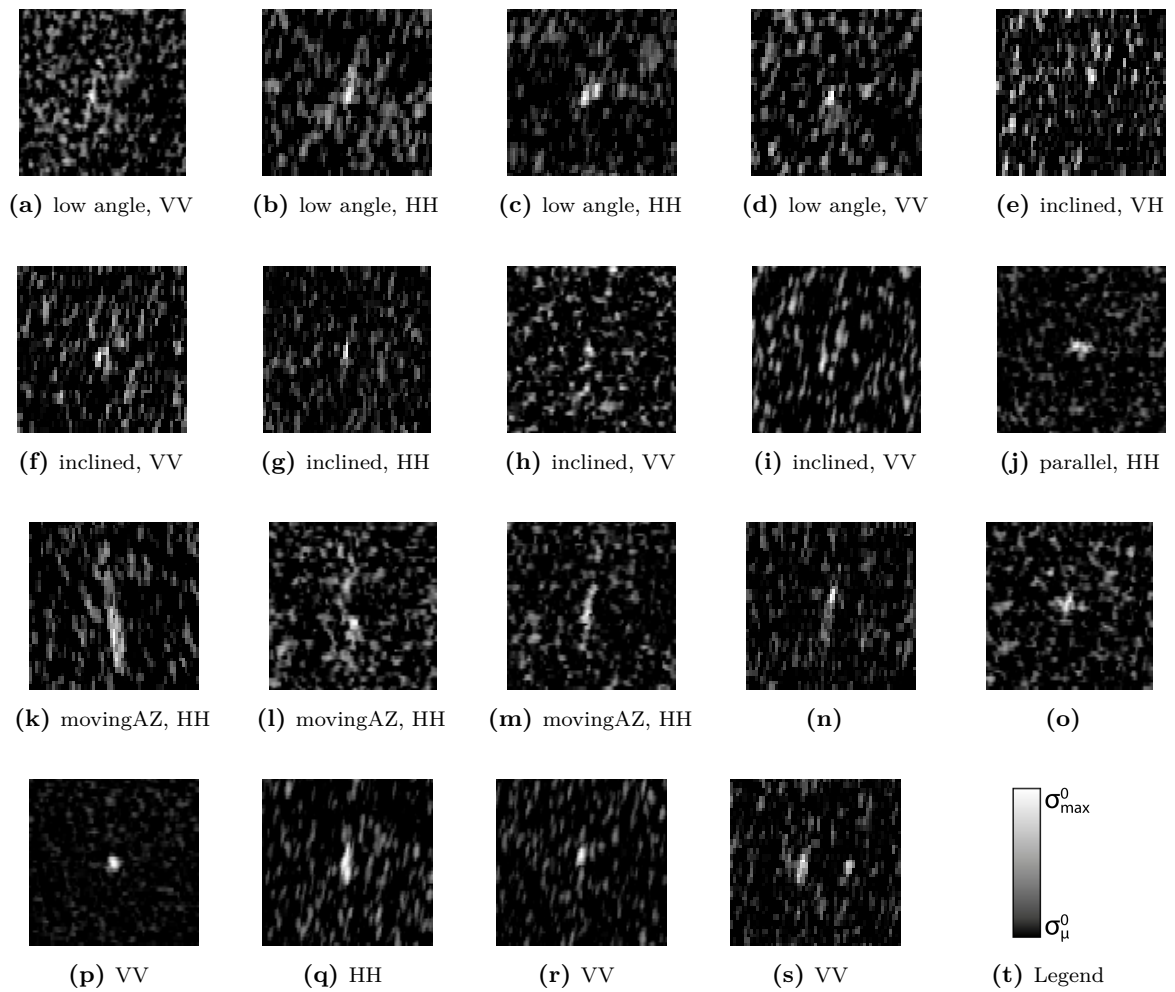


**Figure 4.9:** The vessel's radar footprint in TSX-SM mode (©DLR, 2017) with indications for polarisation and special scene or sensor settings.

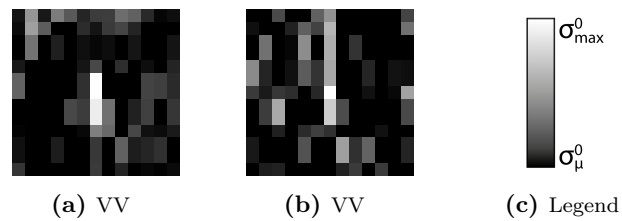
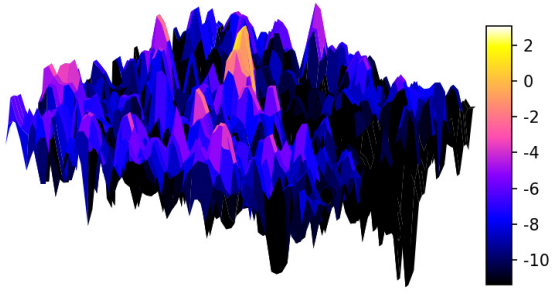
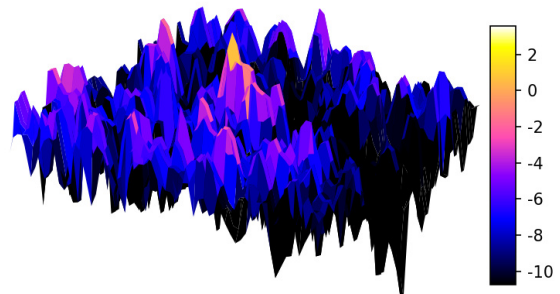


**Figure 4.10:** The vessel's radar footprint in S1 Interferometric Wide (IW) swath mode (©ESA, 2017).

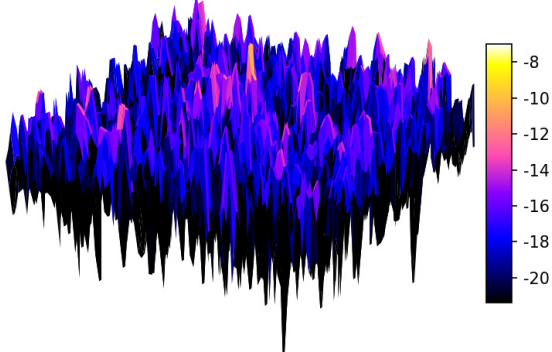




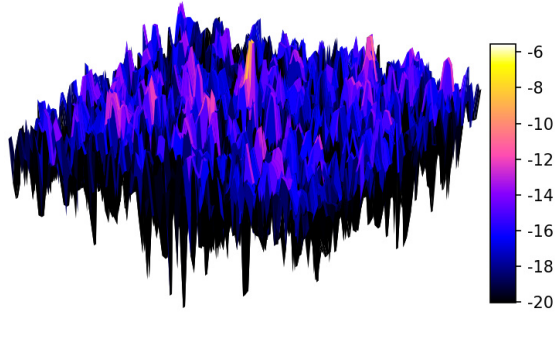
(a) low angle



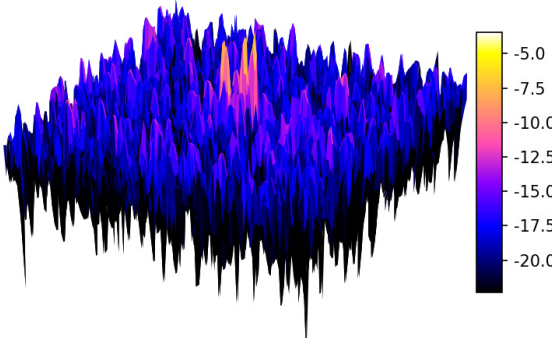
(b) low angle



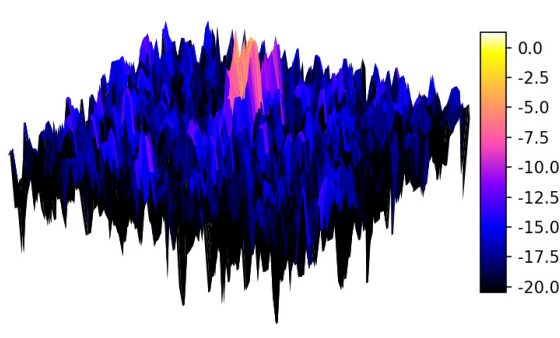
(c) inclined



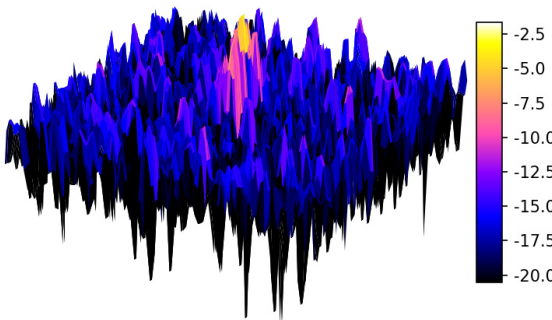
(d) inclined



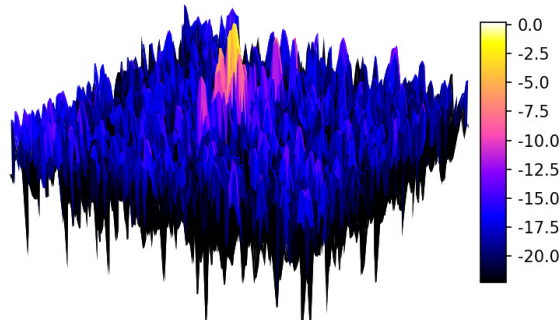
(e) inclined



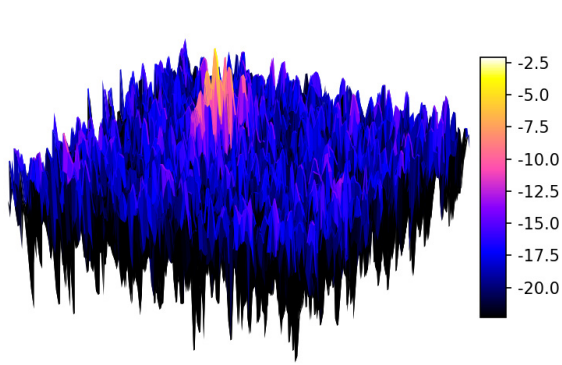
(f) full



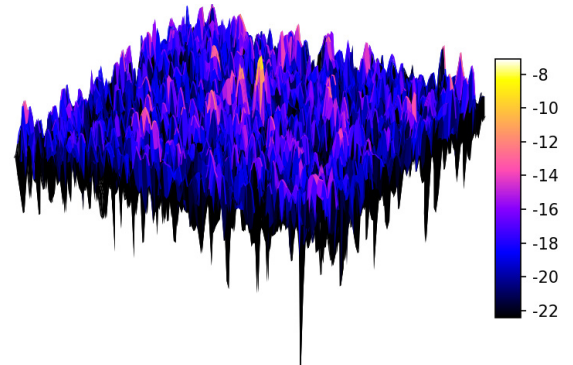
(g) full



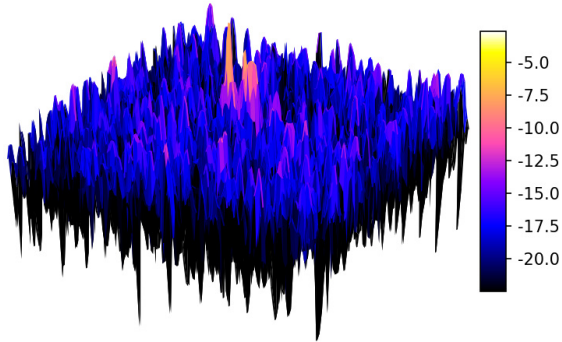
(h) full



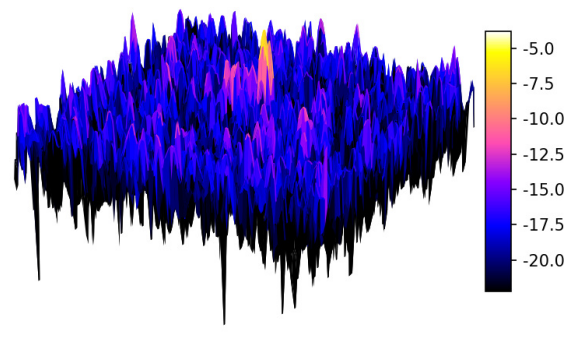
(i) full



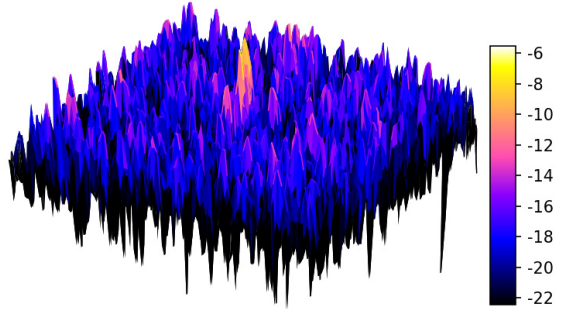
(j) parallel



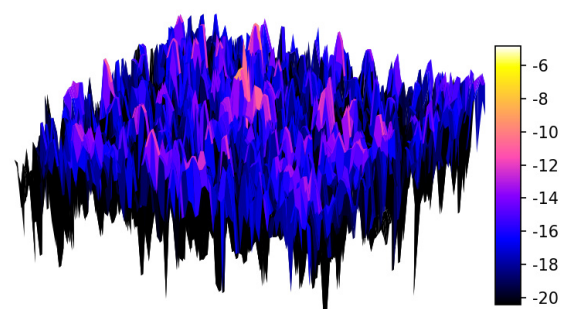
(k) parallel



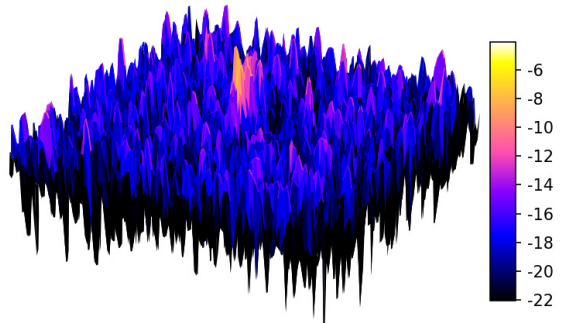
(l) parallel



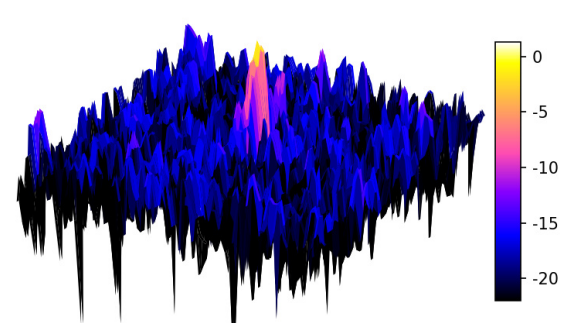
(m) movingAZ



(n) movingAZ



(o) movingAZ



(p)

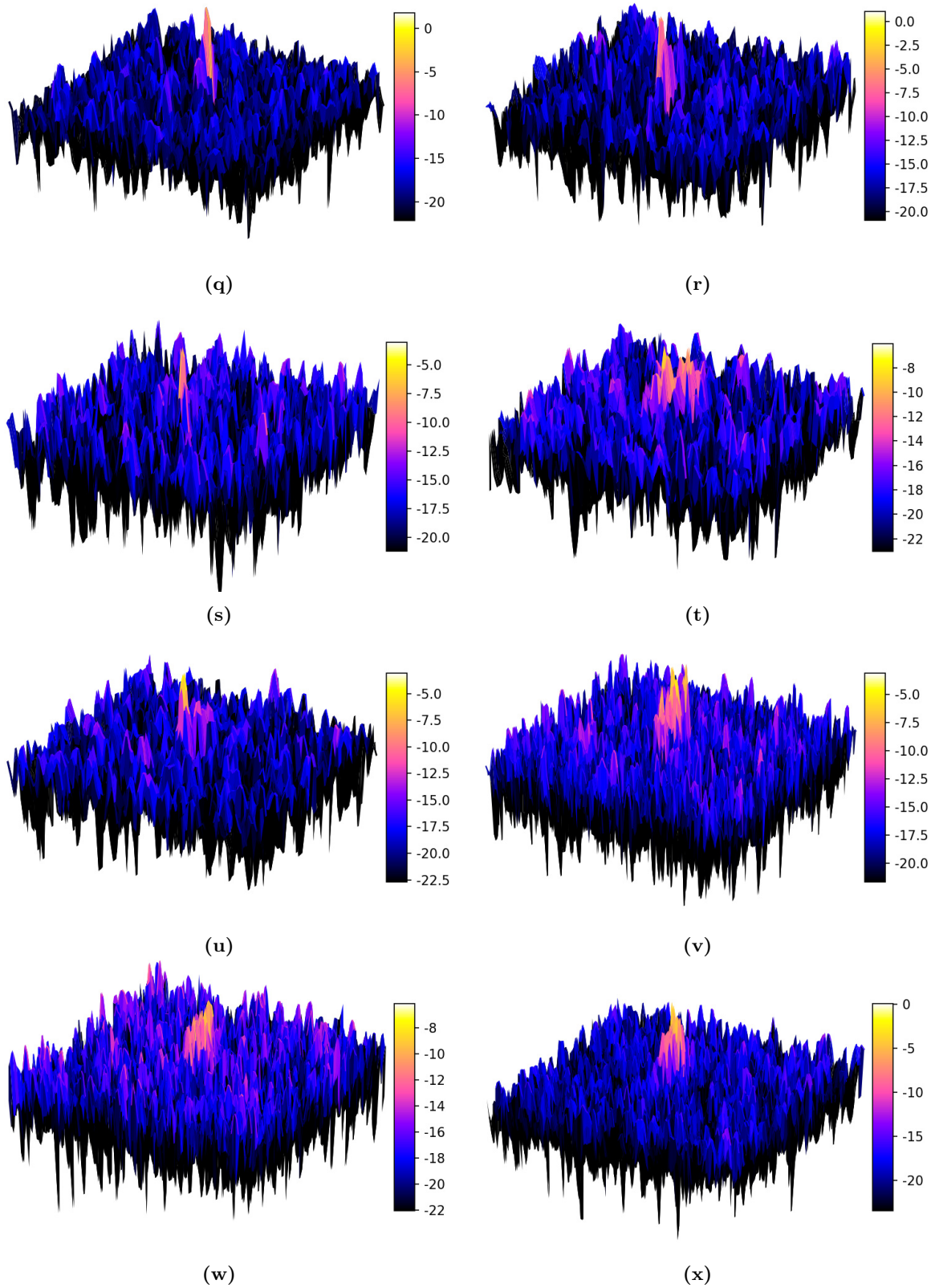
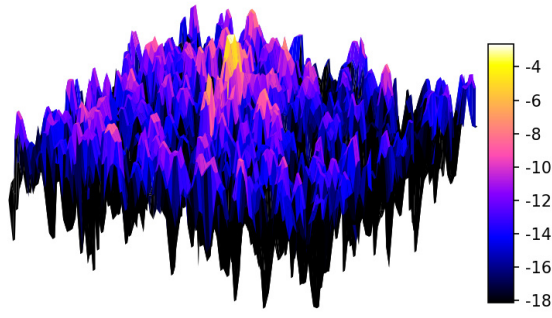
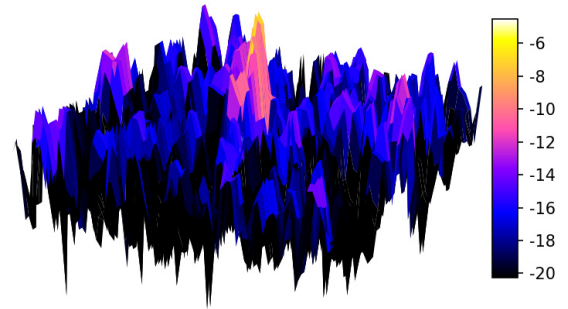


**Figure 4.11:** 3D representations of the vessel's radar footprint in TSX-HS mode (©DLR, 2017) with indications for polarisation and special scene or sensor settings.

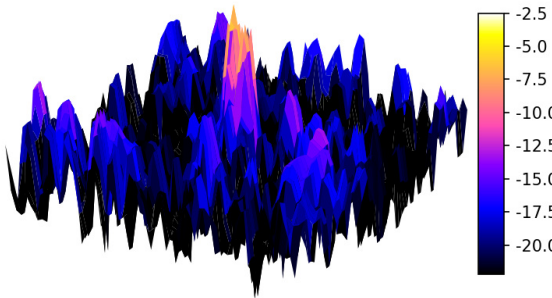




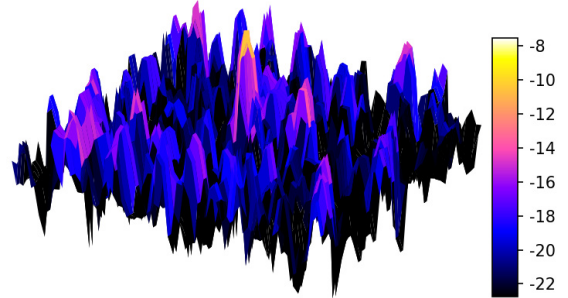
(a) low angle



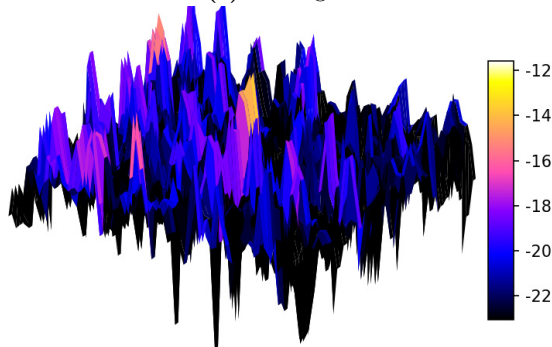
(b) low angle



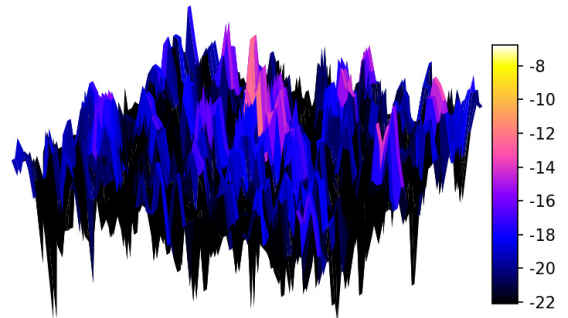
(c) low angle



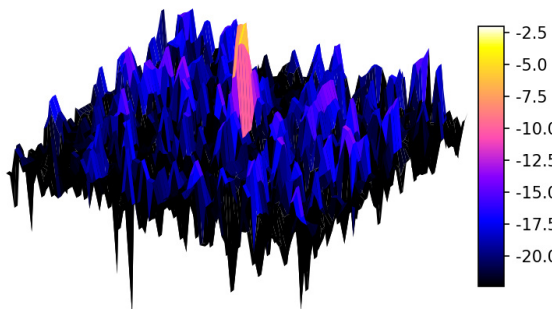
(d) low angle



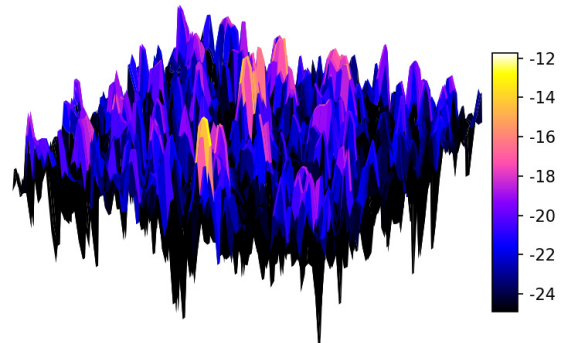
(e) inclined



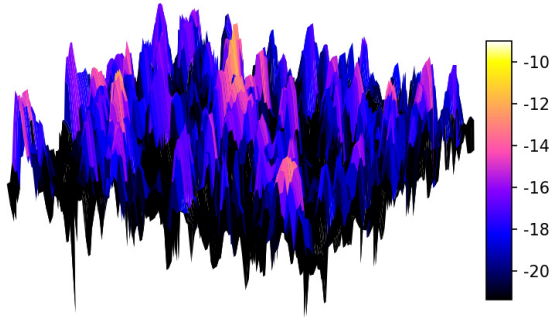
(f) inclined



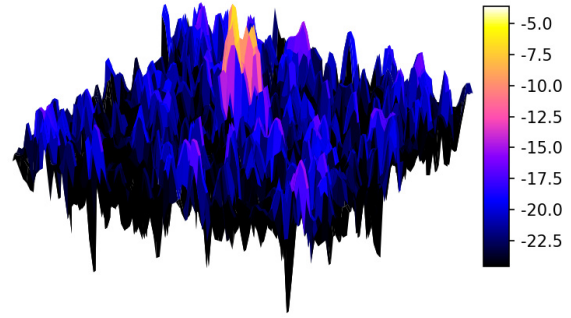
(g) inclined



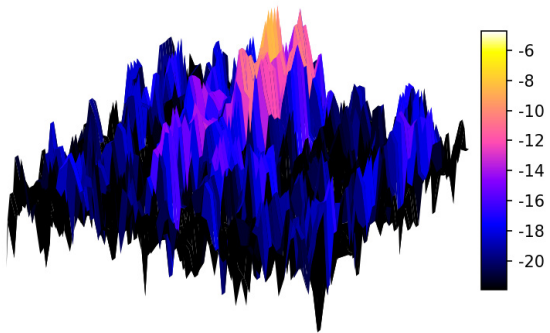
(h) inclined



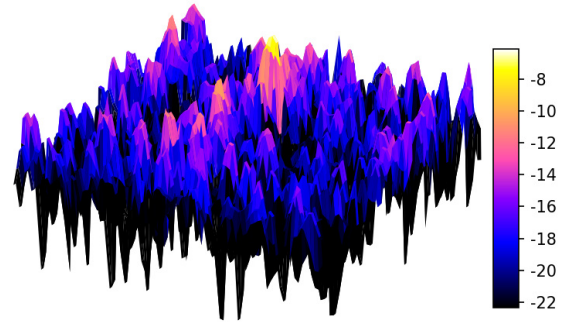
(i) inclined



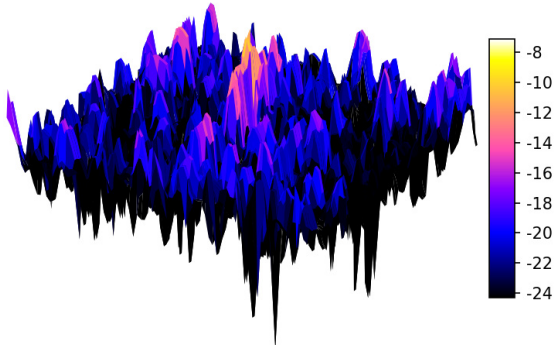
(j) parallel



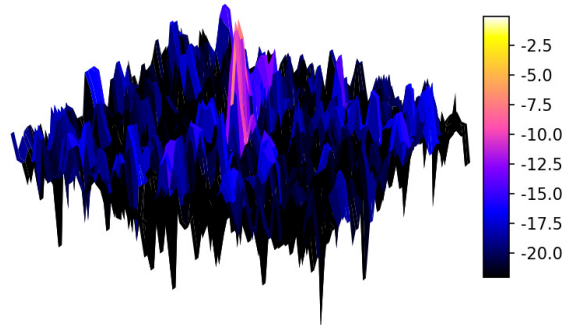
(k) movingAZ



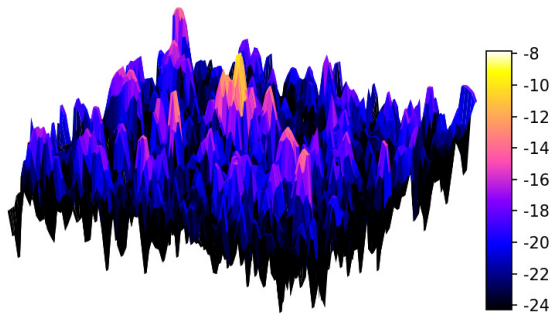
(l) movingAZ



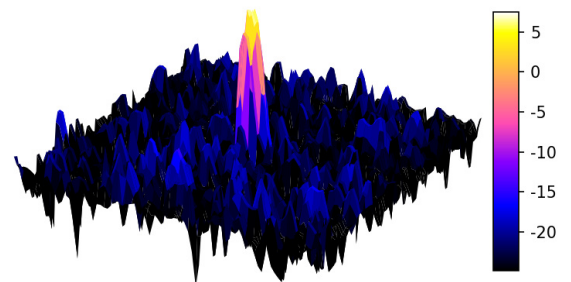
(m) movingAZ



(n)



(o)



(p)

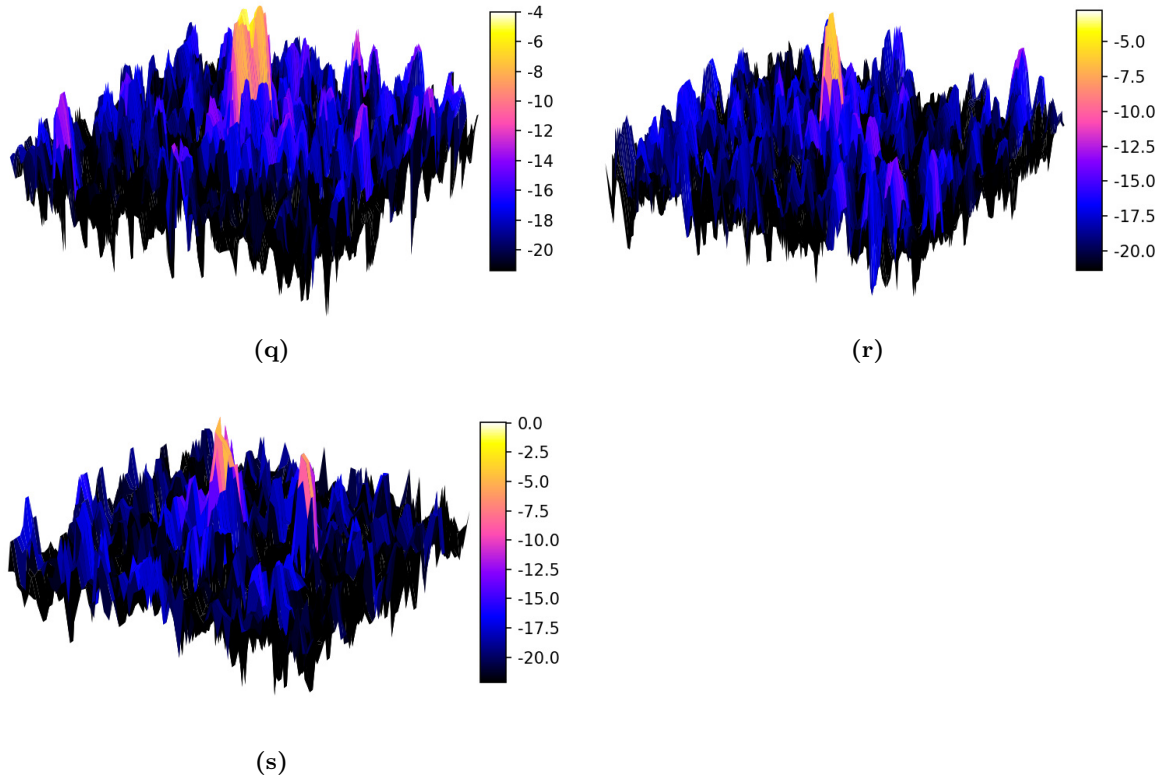


**Figure 4.12:** 3D representations of the vessel’s radar footprint in TSX–SM mode (©DLR, 2017) with indications for polarisation and special scene or sensor settings.

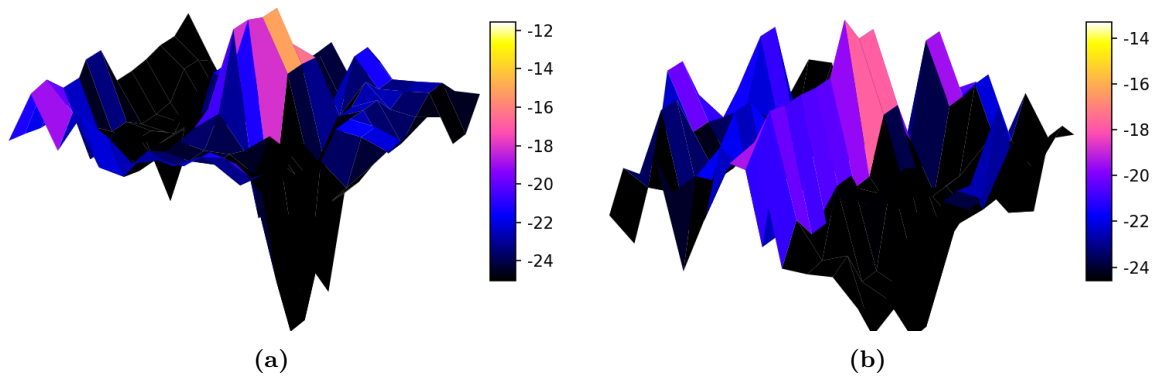


**Figure 4.13:** 3D representations of the vessel’s radar footprint in S1 Interferometric Wide (IW) swath mode (©ESA, 2017).

#### 4.3.4 Methods

##### 4.3.4.1 Water Surface Clutter

Although the main purpose of this work was the analysis of backscattering from inflatable vessels, in this section the analysis of the clutter is shown to understand its impact on the vessel identification. In detection theory, the radar backscattering from the water surface is referred to as clutter. In X–band, the water clutter can be very strong, leading to false alarms at all incidence angles [103]. Water clutter depends on wind speed and direction. As already

#### 4. The InflateSAR Campaign

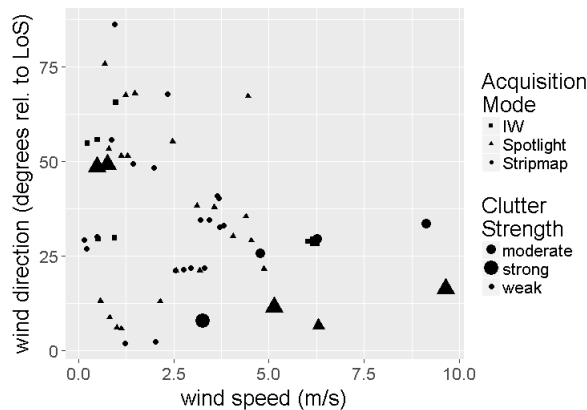
stated above, a small lake was selected as the test site so that the water clutter was less strong. Nevertheless, due to wind conditions, five datasets have strong clutter and an additional five show moderate clutter. The definition of the clutter level was found according to the degree of inhomogeneity of the whole lake surface's radar response. The dispersion is a suitable value to measure, since it combines the influences of the clutter's standard variation ( $\sigma_{clutter}$ ) and the clutter's mean values ( $\mu_{clutter}$ ).

$$Dispersion_{clutter} = \frac{\sigma_{clutter} \times \sigma_{clutter}}{\mu_{clutter}} \quad (4.1)$$

The higher the  $\sigma_{clutter}$  normalised by  $\mu_{clutter}$ , the less homogeneous the water is in the radar image. Here, images with a dispersion value smaller than two are classified as having weak clutter levels, greater than two are moderately cluttered and those with a dispersion greater than three are defined as strongly cluttered. This convention corresponds well to the results of the visual image interpretation.

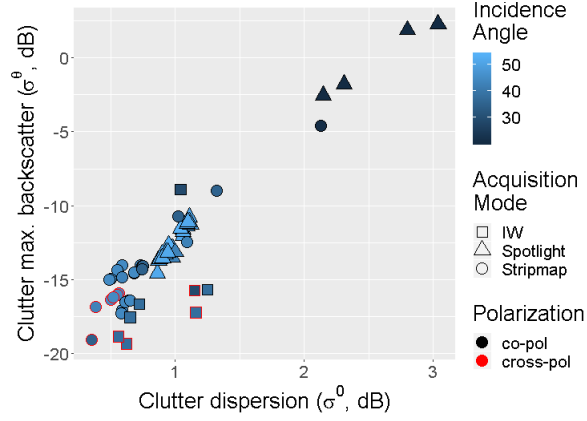
Wind speed and wind direction do trigger higher levels of water surface clutter that can be modelled using Bragg scattering [374, 375]. Thanks to the friendly support of the Leibnitz Institute of Freshwater Ecology and Inland Fisheries (IGB), in-situ weather data from the nearby observation station 'Georg Mothes' at 52°26'46.3"N 13°38'60.0"E were available for each acquisition.

Figure 4.14 compares wind speed and wind direction (the absolute difference to the sensor's LoS in degrees) with the water surface's clutter strength and acquisition mode. Eight out of the ten acquisitions showing 'moderate' or 'strong' clutter were collected when the wind direction was less than 30° with respect to LoS. This produces waves moving mostly parallel to the LoS, which could contribute to a stronger clutter response. Higher wind speed especially increases the chance of moderate or strong clutter throughout the collected datasets.



**Figure 4.14:** Wind speed (©IGB Berlin): impact on ocean clutter.

Figure 4.15 examines the radar response of the 250 × 250 m sections of the surrounding water area with the boat in the centre. Low maxima and low dispersion values benefit a higher TCR and better identification capabilities (bottom left areas). Datasets, finding themselves in the upper right corner, are labelled as biased by strong clutter.



**Figure 4.15:** The water surface’s maximum backscatter and dispersion and its relation to different sensor parameters.

This label was considered for some of the following analyses. Cross-polarised data deliver low dispersion values (low heterogeneity) from the water surface and at the same time a very low maximum  $\sigma^0$ . Low incidence angles are more affected by strong clutter and have high clutter dispersion. Data acquired with a high incidence angle have lower water surface clutter and seem more promising for better identification capabilities. The water surface in S1 data reach on average lower mean and maximum  $\sigma^0$  by about 5 dB compared to TSX data. Images which are marked as affected by strong clutter are characterised by higher mean values (TSX: +7 dB, S1: +5 dB) and a higher clutter maximum (+10 dB). In view of designing an automatic ship detector, it could be appropriate to adopt multilooking and to apply different processing methodologies when the clutter is particularly strong.

#### 4.3.4.2 Identification Scheme

This work was focused on analysing the backscattering behaviour of inflatable vessels. The following methodology is heavily supervised and it is not proposed as an operational technique. It is used here for the mere purpose of identifying the vessel pixel for the statistical analysis. The inflatable identification approach uses intensity values and therefore follows the principles of a simple intensity-based detector with adaptive thresholding. The TCR is defined as the difference (in dB) between the vessel’s maximum backscatter and  $\mu_{clutter}$  where  $\mu_{clutter}$  is a representative of the clutter intensity in dB for the lake’s backscattering in each acquisition:

$$TCR = maximum_{vessel} - \mu_{clutter} \quad (4.2)$$

To apply adaptive thresholding to this visual identification scheme, the boat’s maximum intensity value is compared with the respective scene’s clutter dispersion by using the clutter’s mean and standard deviation. Visual identifications are labelled reliable if:

$$maximum_{vessel} > \mu_{clutter} + 3 \times \sigma_{clutter} \quad (4.3)$$

The selection of factor 3 in Equation 4.3 is a crucial decision which influences all further results. According to literature, a TCR of at least 10 dB is acknowledged as being reasonable for reliable detection and identification with automatic vessel detection systems [376]. Since all



## 4. The InflateSAR Campaign

$\sigma_{clutter}$  in the data are between 3.2 and 5.9, using three times  $\sigma_{clutter}$  will lead to thresholding similarly to the one suggested.

Additionally, an automatic blob detection algorithm was implemented using Python and OpenCV. The blob detector had limited success due to different clutter levels throughout the data. This shows the importance of adaptive thresholds, even in such a homogeneous test bed as in this case. Please note that these algorithms were supervised and were used only for providing a good delineation of the vessel for the analysis of its backscattering. In the future, more work needs to be carried out for finding an automatic detection methodology.

The used classification scheme enabled the analysis of the inflatable radar backscatter. Figure 4.16 illustrates two very different scenarios in false colours where dark blue pixels represent intensities smaller than  $\mu_{clutter}$ . All other colours have values bigger than  $\mu_{clutter}$  with a class width of the standard deviation  $\sigma_{clutter}$ . The inflatable in Figure 4.16a has a comparatively low TCR since most of the pixels representing the vessel show intensity values similar to some parts of the quite heterogeneous surrounding sea clutter. In Figure 4.16b the boat has a clearly higher intensity than the water surface, making this case more favourable for vessel identification. Moreover, the surroundings are of favourably low dispersion. Wind speed and direction relative to the line of sight are influencing the water surface’s radar response. In big water bodies the swell adds to the local sea state. Very calm water leads to low or null surface scattering. In general, bigger waves produce stronger radar backscattering. There are different wind conditions observable throughout the dataset. Since this was a lake, trees were also sheltering some water areas with some wind directions. This explains the variability of water clutter.

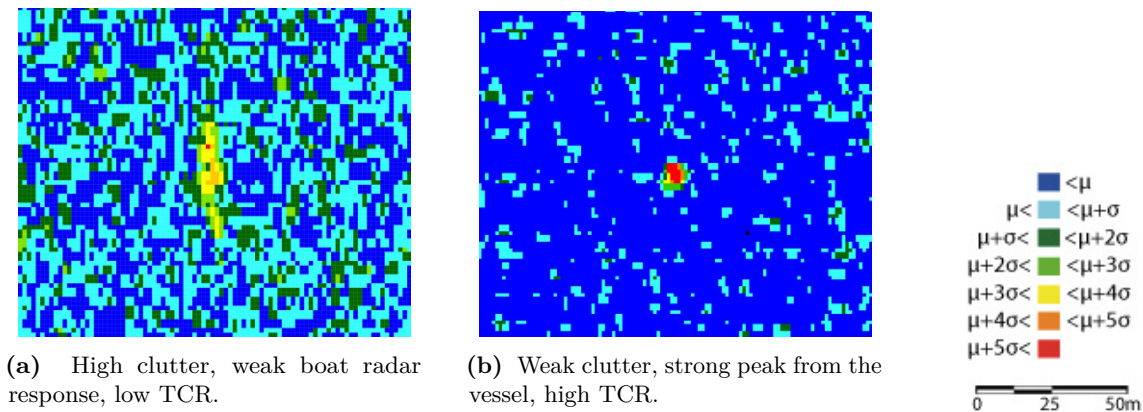


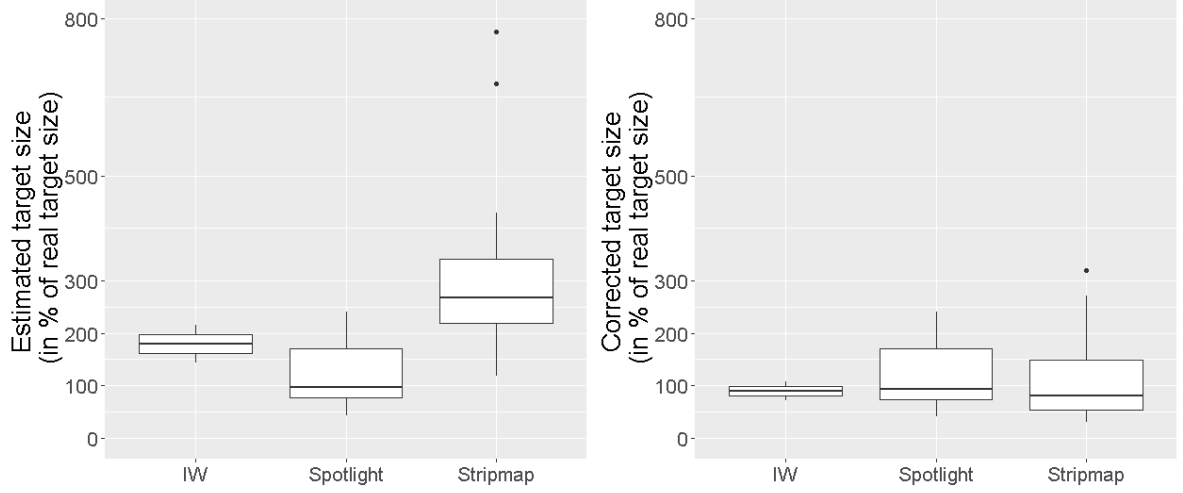
**Figure 4.16:** Examples of the vessel’s radar footprint in TSX–HS mode (©DLR, 2017).

### 4.3.4.3 Estimation of the Inflatable’s Size

When assessing the capability to successfully identify an object, both the maximum TCR and the detected size can be used, because larger objects are easier to detect than smaller ones. Moreover, exact estimation of the detected inflatable’s size enables the discrimination it from other marine objects. This is especially true for the open sea far off the coast, where marine vehicles of such small dimensions are rather unlikely, since the great majority of marine traffic consists of much larger vessels ( $>100$  m in length and at least several meters of freeboard).

The boat size is estimated by multiplying the number of pixels assigned to the vessel category by the pixel area. Figure 4.17 shows the results in a box and whisker plot with the lower and upper hinges corresponding to the first and third quartiles and the whiskers

extending from the hinges to the largest value no further than 1.5 times the inter-quartile range. TSX's HS mode delivers quite good results with an average of 93% of the real boat size (Figure 4.17a). However, with the spatial resolution going down, the results deteriorate and the comparatively coarse spatial resolutions of TSX's SM mode and S1's IW mode are not suitable for that simple approach.



(a) Boat size estimations without a resizing factor. (b) Boat size estimations with the resizing factor  $k$ .

**Figure 4.17:** Introducing a resizing factor ( $k$ ) to improve the estimation of the boat size.

In order to produce more accurate estimations of the vessel silhouette, adjust the edges can be adjusted by using what is sometimes called spatial hysteresis. This exploits vicinity conditions [377]. Here, a scheme that splits boat's radar signature into two groups is used. The first group are high intensity pixels (intensity  $> \mu + 3*\sigma$ ) and they are assigned to the category  $area_{vessel}$ ; the second group are the adjacent, lower-valued pixels ( $\mu + 3*\sigma > intensity > \mu + 2*\sigma$ ), associated with the category  $area_{ambit}$  (Equation 4.4a). This gives the opportunity to apply the now introduced resizing factor  $k$  to parts of the estimation formulae. For the TSX SM mode data,  $k$  is set to 10 and for S1 data to  $k = 2$  and applied it for SM mode data to  $area_{ambit}$  (Equation 4.4b) and for IW mode to both,  $area_{vessel}$  and  $area_{ambit}$  (Equation 4.4c):

$$size_{vessel}^{HS} = area_{vessel}^{HS} + area_{ambit}^{HS} \quad (4.4a)$$

$$size_{vessel}^{SM} = area_{vessel}^{SM} + \frac{area_{ambit}^{SM}}{k^{SM}} \quad (4.4b)$$

$$size_{vessel}^{IW} = \frac{area_{vessel}^{IW} + area_{ambit}^{IW}}{k^{IW}} \quad (4.4c)$$

The results of that correction of the initial size estimations are plotted in Figure 4.17b. It can be seen that the corrected estimations are much more accurate, but since the values for  $k$  deviate from the data, they need to undergo testing and assessment with alternative data.

4.3.5 Results

4.3.5.1 Analysis of the Inflatable’s Backscattering

Before delving into the analysis of the backscattering with regard to sensors and scene parameters, a table summarises the capability of seeing the inflatable in the SAR image. This visibility test is at the base of all the other analyses and provides an overview that could inform possible future data acquisitions.

Table 4.5 shows the probability of identification in this data collection. The figures in brackets indicate the number of datasets available and the number of which suffer from stronger clutter. The overall rates of true positive identifications reached 72% for TSX and 25% for S1. Some of the sensor parameters (row-wise) turned out to have impacts on the detection probability: cross-polarised data clearly cause difficulties identifying the inflatable boat with the lowest sensor-bound rate of only 17%. That shows that the boat does not depolarise the wave and it is likely that single or horizontal double bounce scattering mechanisms may be in place.

**Table 4.5:** Identification rate according to scene and sensor parameters: positive identification in % (datasets available, which suffer from increased clutter).

		Experiment						Sum
		Orthogonal	Inclined	Parallel	Full	MovingAZ	MovingR	(only TSX)
polarisation	HH	83 (12;4)	75 (4;0)	100 (3;1)	100 (3;0)	100 (5;1)	0 (4;1)	77 (31;7)
	VV	83 (12;3)	100 (4;1)	100 (1;0)	100 (1;0)	50 (2;0)	0 (1;0)	81 (21;4)
	HV/VH	0 (3;0)	50 (2;0)	-	-	0 (1;0)	-	17 (6;0)
Incidence	high	88 (17;0)	80 (10;1)	100 (4;1)	100 (4;0)	75 (8;1)	0 (4;0)	79 (47;3)
Angle	low	50 (10;7)	-	-	-	-	0 (1;1)	45 (11;8)
Platform/	TSX-HS	77 (13;4)	100 (3;1)	100 (3;1)	100 (4;0)	75 (4;0)	0 (5;1)	72 (32;7)
Acquisition	TSX-SM	71 (14;3)	71 (7;0)	100 (1;0)	-	75 (4;1)	-	73 (26;4)
Mode	S1-IW	25 (8;1)	-	-	-	-	-	25 (8;1)
Sum (only TSX)		74 (27;7)	80 (10;1)	100 (4;1)	100 (4;0)	75 (8;1)	0 (5;1)	72 (58;11)

It seems that low incidence angles are more likely to be affected by strong clutter, which decreases the TCR and the chance of identification compared to high angles. Eight out of eleven low-angle images have strong clutter, reducing the identification rate to only 45%. On the contrast, low incidence angles with moderate clutter signature are highly suitable for identifying the inflatable with a rate of 100%. The rather flat superstructure of the vessel and its small height do not expose much area to the incoming radiation. This leaves double bounce scattering at the broadside of the vessel not adding to the radar response as strongly as is usually expected in ship detection. That could hamper the identification capability for all cases, but especially for higher incidence angles. To prove that assumption, more data of that category without strong clutter is needed.

TSX’s HS and SM modes show much higher identification rates than S1’s IW mode, since IW mode’s spatial resolution is much lower. As a consequence, the energy of the vessel’s radar backscattering is spread over a larger area, reducing its normalised cross section. This reduces the TCR and makes the identification of the boat impossible for most cases.

The scene parameters are listed as columns and do add some influences in this context as well. If only images with moderate clutter are looked at, the category *orthogonal* would reach 100%. That setup, when the stationary boat is oriented at 90° to the LoS, delivers the best results, as expected. This is because the boat faces the radar, exposing the biggest side at a 90° orientation, and it is expected to produce more single and double reflections. High detection



rates are achieved as well for stationary vessels oriented in a parallel way (*parallel*) to the LoS and for stationary vessels carrying 30 passengers (*full*; oriented at  $90^\circ$ ). The *parallel* case also supports the occurrence of single and double bounce mechanisms at the front where the bow rises from the water and at the counter stern. A full boat rises about twice as high from the water's surface due to the passengers sitting on top of the inflatable volumes, triggering stronger multiple reflections.

Reduced identification capabilities are observed if the stationary vessel is orientated  $45^\circ$  to the LoS (*inclined*), since the faces are oriented in a way that would reflect the energy away from the sensor. Having an inflatable moving in azimuth direction (*movingAZ*) at a maximum speed of about 10 km/h produces a smearing effect and reduces the TCR. A decrease of the chance of identification is expected. *MovingR* represents interferometric TDX-acquisitions with an inflatable moving in range which brings about azimuth displacement. The misplacement is not expected to have a large impact due to the moderate velocity and the quasi-real time nature of the detection. However, defocusing could impede identification. Since interferometric techniques have not been applied up to now, a secure identification with *MovingR*-TDX-data was not possible.

Summing up, the main reasons for an unsuccessful identification seem to be a combination of at least two of the following factors: an inclined or a moving vessel, cross-polarisation, a low incidence angle and a coarse spatial resolution. When removing the *movingR* experiments from the statistics, co-polarised data and high incidence angle data reach the best identification rate of about 86%.

#### 4.3.5.2 Assessment of Acquisition Parameters

Figure 4.18 shows the quality of all 44 positive identifications using the indicators TCR (intensity values in terms of  $\mu$ ) and corrected vessel size estimation (section 4.3.4.3 introduced the resizing factor  $k$  applied). The most favourable results have high TCRs while being located near the 100% line. The data were divided into five experiments representing different scene settings (boat orientation, superstructure/cargo and movement).

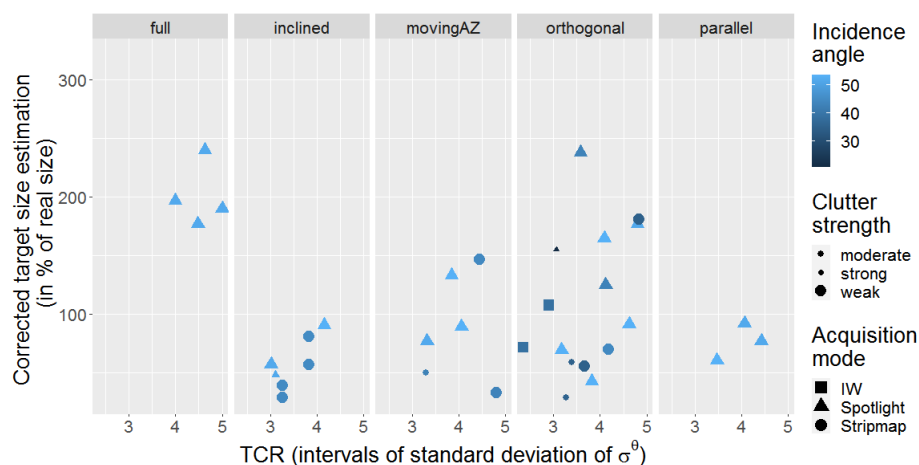


**Figure 4.18:** Impacts of scene and sensor settings on the quality of identification.

To take a closer look at differences in the quality of identification between horizontal and vertical polarisation, dual co-polarised datasets (HH VV) are used. This allows a fair comparison of polarisation channels because all other sensors and scene parameters are equal

#### 4. The InflateSAR Campaign

for each pair of acquisitions. Figure 4.19a lists representations of dual-pol datasets along the x-axis, where seven out of eight cases show larger over-estimations of the boat size with the horizontal polarisation channel. The TCRs (Figure 4.19b) are of comparable quality for HH and VV. Therefore, there is no ground to give a clear preference for either of the two polarisation channels. For completeness, Figure 4.19a shows dual-pol datasets where only one image allowed for a successful identification too.

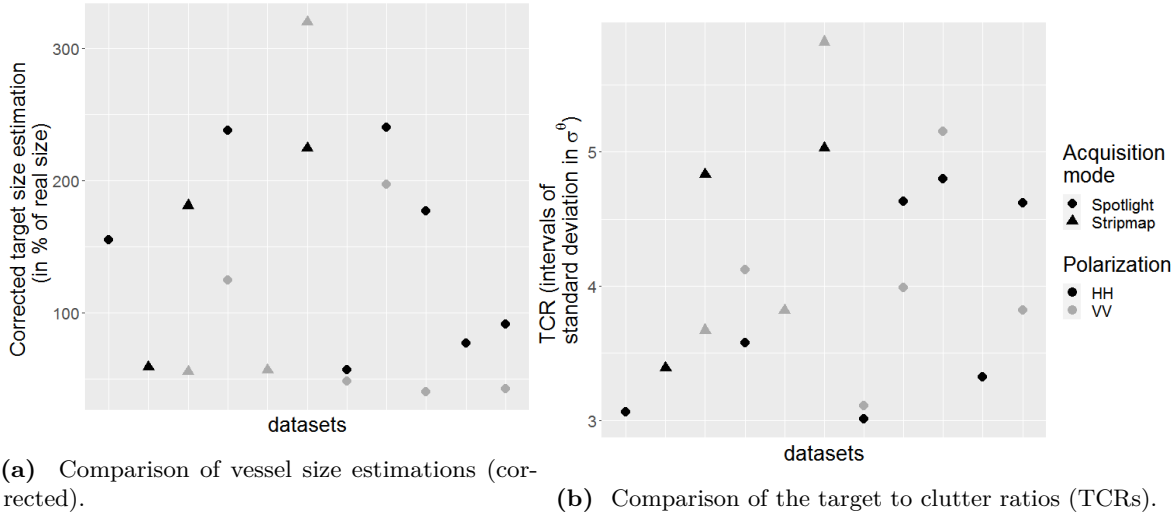


**Figure 4.19:** Using dual-pol acquisitions to compare the quality of identification between HH and VV polarisation. The incidence angle increases from left to right.

#### 4.3.5.3 Analysis of Clutter Effects

Beside the scene and the sensor settings, the vessel identification throughout the experiments is subject to a number of uncontrollable influencing factors, such as clutter. In general, a higher water surface response decreases the TCR. The clutter is defined using the intensity  $\sigma^0$  values up to the 'maximum clutter' level of the median  $\mu$  plus three times the standard deviation  $\sigma$ . Intensities above that threshold are assumed as coming from other objects than the water's surface. Strong clutter is attempted to explain with a high  $\mu$  (strong water surface response) and a high  $\sigma$  (high inhomogeneity).

Figure 4.20 searches for impacts of the sensor and scene settings on the TCR before the background of a statistical analysis of the surrounding water surface's clutter. Figure 4.20a,b show the sensor settings, whereas Figure 4.20c,d focus on the scene settings. In Figure 4.20b,d the standard deviation of the  $\sigma^0$ -values is applied to the x-axis, and for Figure 4.20a,c the maximum clutter thresholds were used. Unsuccessful identifications are represented with TCRs of zero. The background colour illustrates the idea that chances of a reliable vessel identification can be estimated with TCRs relative to the surrounding water surface's clutter behaviour — here near or greater than  $\mu$  plus three times  $\sigma$ , a condition represented by the green area. True positive identifications within the white-reddish area should be flagged with a lower reliability.

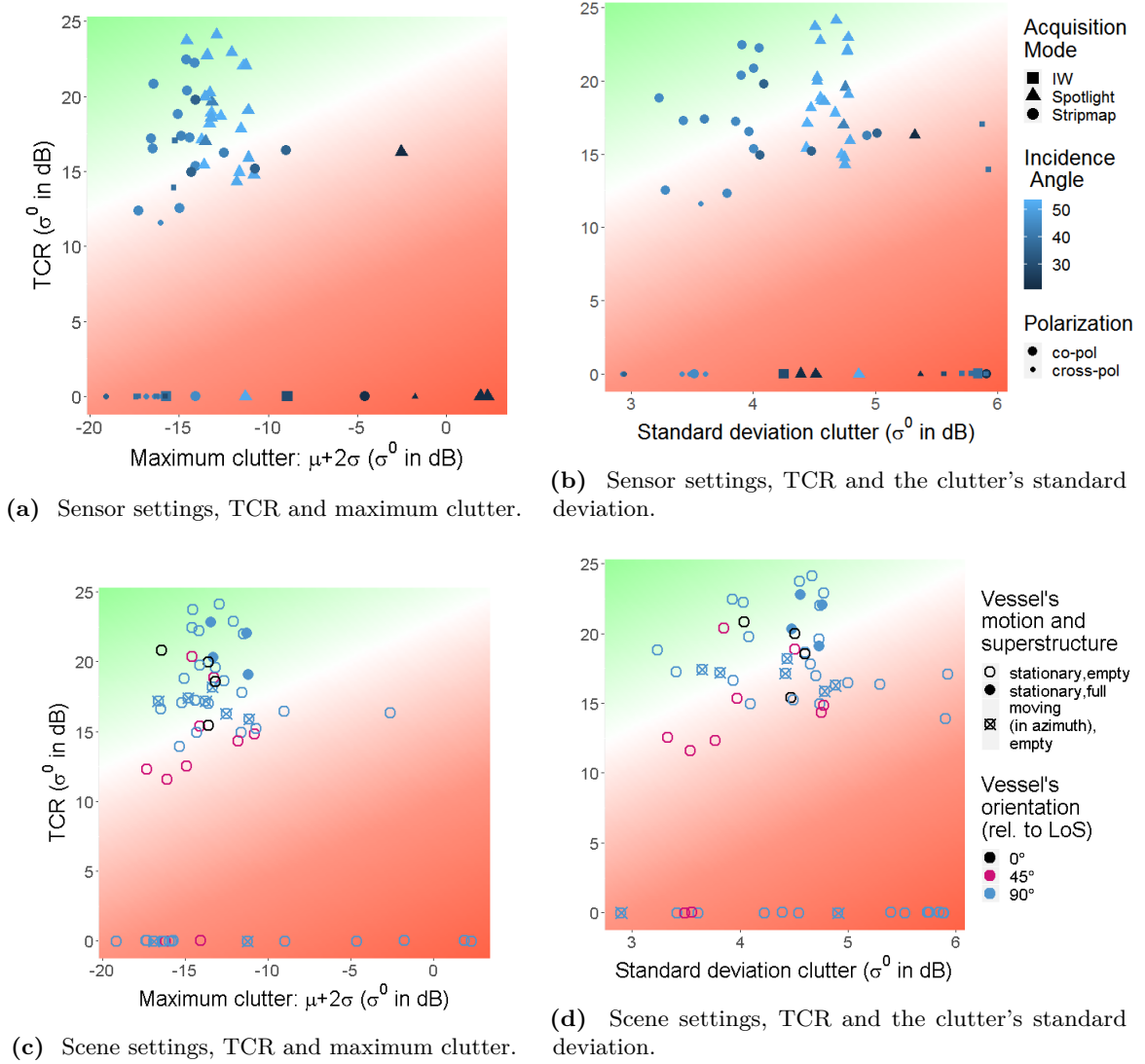


**Figure 4.20:** Influences of selected scene settings and sensor settings on the TCR with respect to the water surface's clutter behaviour.

The figures show that SM mode tends to have slightly lower values for maximum clutter and standard deviation compared to HS mode, which is favourable for vessel identification. Clutter from the S1 mission stands out with higher  $\sigma_s$ , lower  $\mu_s$  and lower TCRs. The figures support the above statement that cross-polarisation and low incidence angles decrease identification capabilities. Further, a vessel full of people is more visible in the data, whereas having the boat oriented at 45° to the LoS or moving in azimuth decreases the TCR.

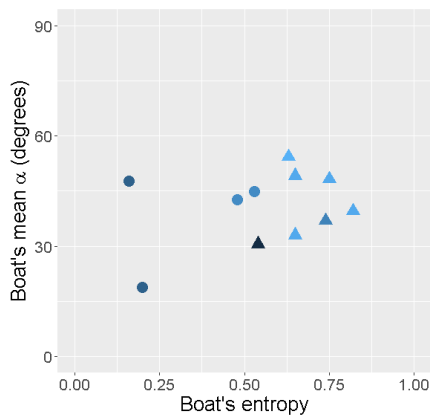
#### 4.3.5.4 Polarimetric Analysis

The availability of dual-pol HH VV images enabled a polarimetric analysis using the Cloude Pottier decomposition. The polarimetric interpretation of the entropy-alpha ( $H-\bar{\alpha}$ ) space could be done, since with HH VV polarisation, the coordinate system can be changed to the Pauli one and the eigenvectors can be interpreted as in the quad-pol decomposition. The comparison between the vessel and the water's surface shows clear differences regarding the polarimetric behaviour: the results for the boat (Figures 4.21a, 4.21c) reveal a preference for dipole and cylinder scattering, with entropy that can be relatively low. This is quite uncommon

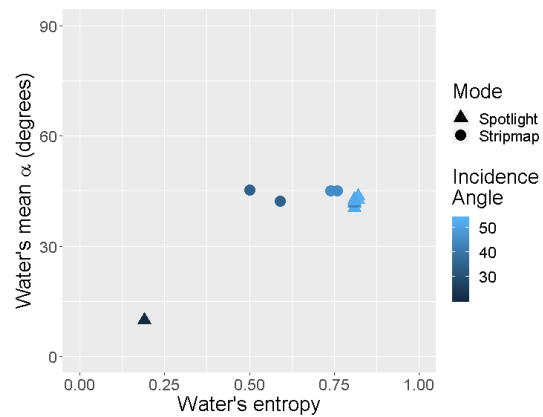
#### 4. The InflateSAR Campaign

for ordinary ship identification, where the entropy is generally high. This is due to the limited size and number of structures over this inflatable vessel. The water surface (Figures 4.21b, 4.21d) presents relatively high values of entropy with an  $\bar{\alpha}$  that sits around  $50^\circ$ . This is a sign that the clutter backscattering is close to the noise floor.

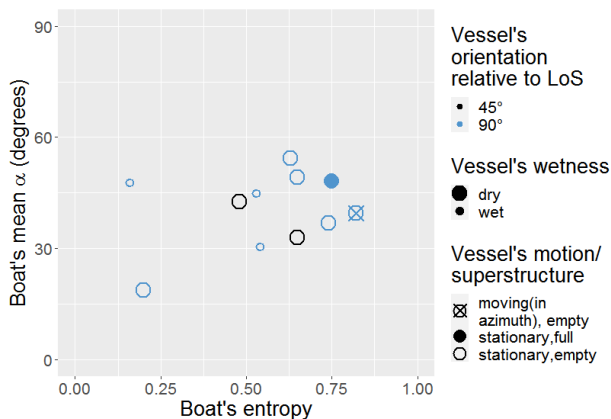
Figures 4.21c, 4.21d show the scene settings. It can be observed that a vessel being full or moving in azimuth has higher entropy. For this data, the characteristics of dominant scattering mechanisms depend on vessel orientation and superstructure. The weather conditions at the moment of acquisition were recorded as well. In Figure 4.21c wet indicates drops of water or a thin water layer on the surface of the inflatable's volumes, either from rain or dew. Apart from the tendency that wet inflatables have rather low entropy, there is no explicit connection between the boat's polarimetric parameters and its wetness. A clear pattern of the influence of the wind conditions could not be observed. Adding the sensor settings to Figure 4.21a, 4.21b might lead to the assumption that a low incidence angle sometimes drastically reduces both the water's and the boat's entropy and the mean alpha angle. For completeness, Figures 4.22a – 4.22d show the  $H-\bar{\alpha}$  space for cross-polarisation data. A physical interpretation here is not straightforward, nevertheless the decomposition can be used as a signal processing tool to show that the backscatter behaviour of the boat and the water are different.



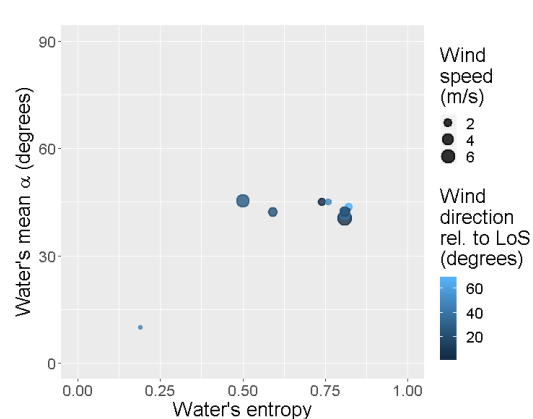
(a) The boat's polarimetric behaviour with selected sensor settings.



(b) The water's polarimetric behaviour with selected sensor settings.

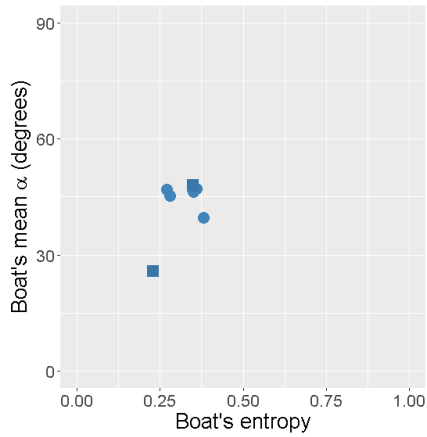


(c) The boat's polarimetric behaviour with selected scene settings.

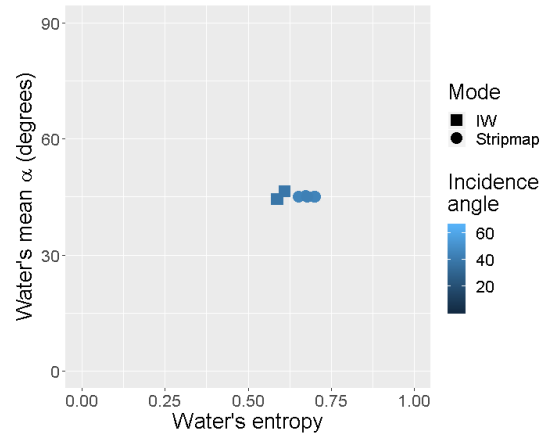


(d) The water's polarimetric behaviour with selected scene settings.

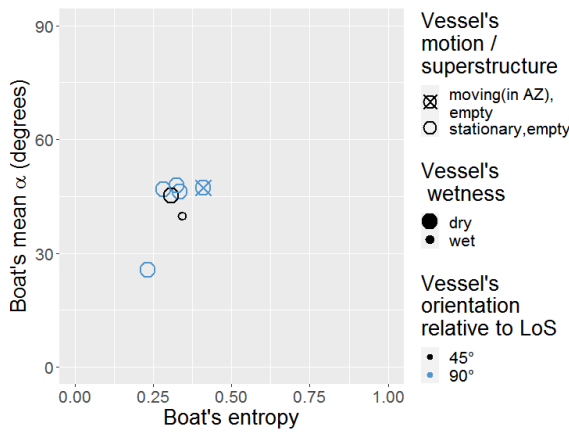
**Figure 4.21:** A comparison of the inflatable's and the water surface's entropy and mean alpha  $\bar{\alpha}$  with sensor settings and scene settings for co-polarised data.



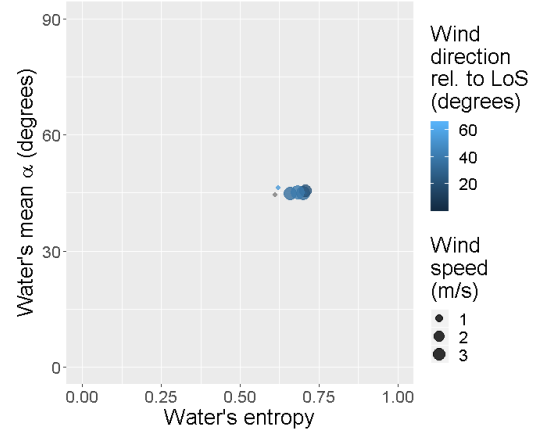
(a) The boat's polarimetric behaviour with selected sensor settings.



(b) The water's polarimetric behaviour with selected sensor settings.



(c) The boat's polarimetric behaviour with selected scene settings.

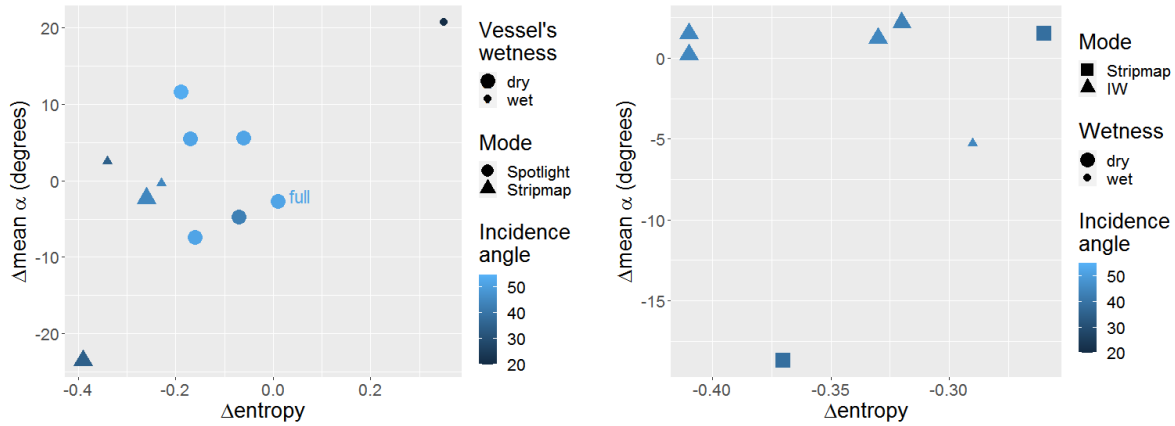


(d) The water's polarimetric behaviour with selected scene settings.

**Figure 4.22:** A comparison of the inflatable's and the water surface's entropy and mean alpha  $\bar{\alpha}$  with sensor settings and scene settings for cross-polarisation data.

Figure 4.23 now compares the previous results and embraces the vessel's particular behaviour in the  $H-\bar{\alpha}$ -space compared with the surrounding water surface. Additionally, selected sensor and scene settings were added to the plot to leave more room for interpretation. Co-pol (Figure 4.23a) and cross-polarisation (Figure 4.23b) scenarios show that the entropy can be used to discriminate between the two entities, as the vessel has lower values in all acquisitions, except for one case, in Figure 4.23a. The limited amount of data does not support a sound assessment, but the very low incidence angle and the vessel being wet could have made a difference.  $\bar{\alpha}$  does not seem to be useful at all to differentiate the boat from the water body, since divergences do not show a uniform trend. The one available dataset with a full boat in Figure 4.23a got a label to especially emphasise on the most realistic scenario. The  $H-\bar{\alpha}$ -spaces change with increasing wave heights; these results relate to rather calm sea states.

#### 4. The InflateSAR Campaign



(a)  $\bar{\alpha}$  and entropy: the water's subtracted from the vessel's for co-polarised data.

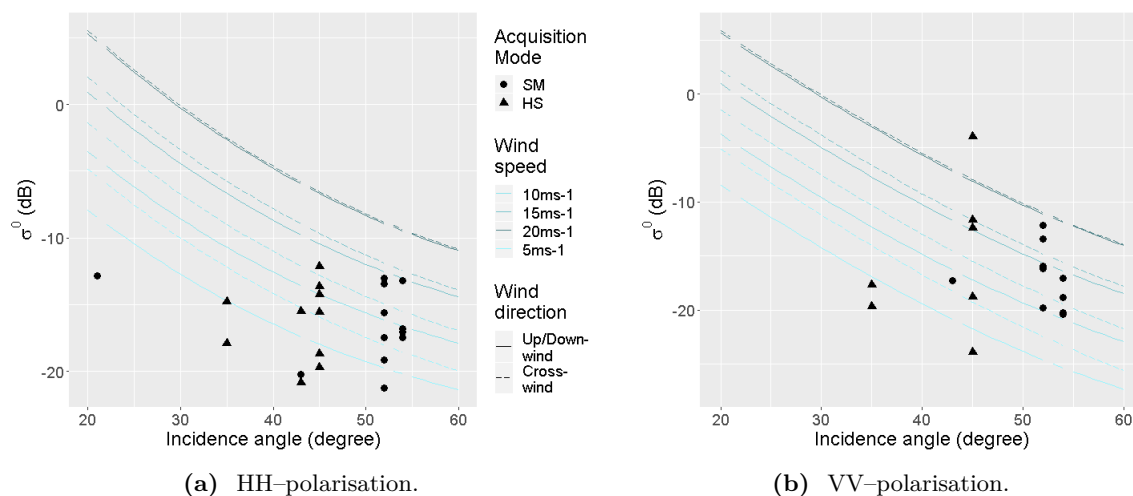
(b)  $\bar{\alpha}$  and entropy: the water's subtracted from the vessel's for cross-polarisation data.

**Figure 4.23:** Distinguishing the vessel and the water surface in the  $H-\bar{\alpha}$ -space of co-polarised and cross-polarisation data.

#### 4.3.5.5 Emulating the Detectability at Higher Sea States

Once again, the collected data originates from a lake. The findings related to water scattering can only be translated to the real situation in which the refugee vessels are in the open ocean at relatively calm sea states. To estimate the robustness of the identification capabilities, the weather and wave conditions of such an environment has to be addressed. It can be assumed that there are stronger winds and rougher sea states most of the time.

Therefore, this research tries to bridge the gap with open ocean data and provide an estimation of feasibility for intensity-based identification methods in stronger wind conditions. To do this, the XMOD1 geophysical model function from [205] is applied to estimate  $\sigma^0$  from  $U_{10}$  wind speed for different wind directions relative to the LoS (cross-wind, up/down-wind) and for a range of incidence angles ( $20^\circ - 60^\circ$ ). Wind speed estimations span the Beaufort scale from 4 (moderate breeze) to 8 (fresh gale) covering a wide range of frequently occurring scenarios of winds in the central Mediterranean capable of bringing severe problems to small refugee vessels.



(a) HH-polarisation.

(b) VV-polarisation.

**Figure 4.24:** The vessel's maximum  $\sigma^0$  (point-like symbols) for HH-pol and VV-pol compared to the water surface's radar return estimations according to different wind scenarios (lines).

Figure 4.24b shows the results for VV-polarisation of an X-band radar sensor. To transfer these results to HH-polarisation (Figure 4.24a), the polarisation ratio model from [240] is used. The dots represent three times the respective image's standard deviation subtracted from the maximum radar response from all successfully identified vessels to ensure a decent TCR. The lines represent the estimated intensities of the water surface's radar response according to different wind scenarios. All phenomena are drawn with respect to incidence angle and polarisation.

#### 4.3.6 Section Resume

Looking at the high identification rates of the inflatable, we have to bear in mind that the data came from a test site which was designed to ease intensity-based identification. On the other hand, most of the dataset shows an empty boat and the analyses revealed that a fully occupied boat has a stronger radar return (and therefore a better TCR). In a maritime context, the results can only be transferred to a very calm, open ocean with low wind (less than 5 m/s) and no swell. Nevertheless, the findings about the backscattering behaviour of small inflatable vessels do represent a basis for further fruitful research in this field. The experiments to test the influences of different scene settings and the polarimetric modes revealed valuable information for further research.

The preliminary hypothesis of expecting the 'wetness' of the boat's volumes to have influence on both its detectability and its polarimetric signature could not be proven at this stage.

SAR data from different platforms and acquisition modes have been examined to evaluate the effects of resolution. It is known that for the current satellites, the higher the spatial resolution, the smaller the areas that can be monitored per unit of time. In addition to this, adding polarimetric channels decreases the image's spatial footprint. It turned out that dual-pol Spotlight mode data are well usable to identify the special object, whereas Sentinel-1's Interferometric Wide Swath mode seems not to meet the requirements. However, the use of more sophisticated detection algorithms may make the use of Sentinel-1 feasible in the future.

It is vital to collect more data using different resolutions (e.g. RadarSAT-2) and with different sea states in the open ocean. Test data or simulations of a fully occupied inflatable would be very valuable to further converge towards the realistic scenario. For that, the following sections will aim at the comparisons and testing of different detectors, and the development of specially tailored detectors. For validation it is crucial to acquire more test data from the open ocean or to alternatively bridge the gap with a data simulation approach.

This section presents an analysis of the very first effective SAR data collection of a refugee inflatable. It proves that using TerraSAR-X, the inflatable boats can be detected with high certainty, despite their low dielectric constant and small size. This was true for the relatively calm weather conditions (mostly less than 5 m/s) and water state prevailing at the test site. Simulations to get a preview how this goal can be achieved in the maritime environment revealed the following:

- higher incidence angles increase the detectability, since the sea has a lower backscattering, whereas the inflatable backscattering intensity remains relatively stable
- wind speed greater than  $10 \text{ ms}^{-1}$  dramatically reduces the detectability for most cases. That is true for both HH and VV polarisations

- above  $15 \text{ ms}^{-1}$ , in almost all cases the TCRs get too low to ensure a reliable intensity-based identification

Unsuccessful vessel identification is in most cases caused by strong clutter. Moreover, specific sensor and scene settings influence the quality of identification to a great extent, such as the vessel's movement and its orientation compared to the radar path. It was observed that:

- a full vessel has comparatively larger footprint estimations of around 200% and strong target to clutter ratios (TCRs) between four and five times the standard deviation of  $\sigma^0$ . This category can be seen as a reference group, since it represents the most realistic situation
- movement in azimuth triggers a smaller TCR due to the well-known smearing effect. The consequence is a reduced identification capability. Size estimations are well around the 100% mark
- throughout the experiments *inclined* and *parallel*, the size of the vessel was underestimated and the TCRs had a tendency to be very low
- the experiments with a stationary vessel orthogonally oriented (*orthogonal*) led to a quite variable identification quality with boat size estimations mainly between 50% and 150% of the real size and acceptable TCRs, mostly concentrated in between three and four times of the respective image's standard deviation
- the acquisition mode played a role with Sentinel-1's Interferometric Wide Swath mode characterised by very low TCRs. TerraSAR-X's Stripmap and Spotlight modes show similar quality of identification throughout. However, this is driven by a combination of many influencing factors and conclusions cannot be drawn without collecting more data
- the incidence angle does not seem to play a role, but meaningful conclusions cannot be drawn considering the limited availability of low incidence angle data not affected by stronger clutter. However, it clearly is prone to the occurrence of increased clutter, which lowers the TCR due to a stronger radar response from the water's surface. Chances for automatic identifications for those cases are expected to be lower
- the majority of corrected boat size estimations are between 50% and 150% of the real vessel size

In terms of polarisation, co-polarised data allow for better object identification than cross-polarised data. Low incidence angles tend to be more susceptible to strong clutter, decreasing the TCR and the quality of identification. The spatial resolution of TerraSAR-X's Stripmap and Spotlight modes seems sufficient, whereas Sentinel-1's Interferometric Wide Swath mode provides very low identification rates.

Most of these findings relate to intensity-based identification and detection schemes which may not be applicable to higher sea states in the open ocean. The polarimetric analysis shows that neither the vessel's superstructure nor its orientation seem to influence its bearing in the entropy- $\bar{\alpha}$ -space much. More importantly, it was found that a clear distinction between the vessel and the water surface is possible, which invites the development of polarimetric-based detectors. The findings show that SAR can be used for a satellite-based surveillance infrastructure to (semi-)automatically identify small rubber inflatables, such as the test vessel in a test bed like a small lake.

### 4.4 Testing SAR Vessel Detection Systems for Refugee Rubber Inflatables

To save precious time, some degree of automation in the detection process is very helpful when it comes to the processing of large amounts of data. For disaster mitigation applications, a



semi-automatic approach where a human-based verification follows a code-based detection increases the results' reliability. To pave the way to a semi-automatic detection workflow and infrastructure especially tailored for refugee inflatables, an array of automatic vessel detection systems (VDS) were tested and benchmarked. Different detection methodologies were brought together with a wide range from intensity-based detection to polarimetric approaches and a sublook detector. The main parts of this section are also available as a journal paper within Remote Sensing [303].

One of the most prominent intensity-based detectors is the Cell Averaging-Constant False Alarm Rate (CA-CFAR) detector, which searches for intensity anomalies with stronger backscattering than the surroundings. The main object's properties that impact the intensity values of a SAR image are the following: surface roughness, the dielectric constant of the material, and the presence of corners (or large-scale roughness). The CA-CFAR is highly usable for ship detection since ships are expected to have a relatively large backscattering compared to the background sea clutter [127]. CA-CFAR adaptively changes the threshold to fix the probability of false alarms throughout the dataset [378]. Polarimetric SAR (PolSAR) has been demonstrated to be very useful to identify objects by decomposing their radar return [379]. In this section, the Polarimetric Match Filter (PMF; [264]), the Intensity Dual-pol Ratio Anomaly Detector (iDPolRAD; [112]), the Geometrical Perturbation Polarimetric Notch Filter (PNF; [380]), a reflection symmetry detector (referred to as PolSym; [381]) and the polarimetric entropy detector (here called PolEntropy; [268]) were tested. Finally, spectral analysis was shown to be useful for ship detection. [173, 174, 171, 172] developed detection techniques which exploit diversity in frequency and are called sublook detectors. The sublook cross-correlation detector (abbreviated with SubCorr) was used in this work.

#### 4.4.1 Vessel Detection Systems: Developments, Approaches and Methods

SAR is still the leading technology for maritime monitoring. Furthermore, it is especially valuable for disaster monitoring, response and mitigation because of its all-day and all-weather capabilities [378, 127]. Furthermore, SAR is the preferred sensor for ship detection from space because the achievable resolutions match ship sizes and it can cover comparatively wide areas. Consequently, there is a great number of research and literature on SAR ship detection. The challenges for a successful detection of maritime vehicles on the open ocean with SAR imagery have remained the same since its beginnings: small, moving vessels made from non-conductive materials are hard to detect. Ship classification and identification is even more difficult. Rough sea conditions and local winds can produce false alarms which are hard to remove. Furthermore, SAR imagery is subject to intrinsic noise (speckle) and a coherent coverage of large areas with a reasonable spatio-temporal resolution have not been realised so far with only the few dozen SAR satellites that exist now.

Comparable research on the detection of small, non-metallic maritime vehicles with SAR is scarce. Marino et al. show that small fishing boats made of fibreglass are hard to detect without ultra-high-resolution SAR imagery [292, 177]. Other research revealed that the Radar Cross Section (RCS) of non-metallic vessels (e.g. wooden) is much smaller than comparably-sized metal made ones and a reliable detection with SAR is hard to provide [128, 382]. Gao and Shi used Along Track Interferometry (ATI) SAR data to successfully detect small vessels [168]. Recently, deep learning algorithms for small ship detection emerged with the drawback of high computational cost and the need for training data support [383]. Liu et al. [384] developed and tested a new polarimetric detector for small ships most recently. This algorithm was constructed using the differences between depolarisation power and total power, as well as the difference between double-bounce scattering and surface scattering.

Single channel (single-pol) ship detectors exploit the fact that the radar cross section of maritime vehicles is in general higher than the one from the sea [258, 261, 338]. This assumption limits the detection to maritime vehicles with a high TCR. One of the first detecting techniques was a simple moving window adaptive thresholding to guarantee constant false alarm rates [385, 18]. For the modelling of high-resolution sea clutter backscattering a compound distribution model, such as the compound K-distribution, is well suited [386]. This is because the backscattering of the sea fluctuates quite rapidly due to waves and other phenomena [387]. Ref. [388] proposed CFAR to be used with various distributions of background statistics. H. Greidanus et al. developed the Search for Unidentified Maritime Objects (SUMO) algorithm which is a pixel-based CFAR detector for multilook radar images [389]. New CFAR developments consider object-based approaches [390] and a CFAR without any sliding window for multitarget situations based on variational Bayesian inference for very complex backgrounds [391].

The development of multichannel SAR (dual and quad-pol modes) enabled more sophisticated methods which explore and combine more than one feature, such as SAR polarimetry (PolSAR; [73]). An advantage of PolSAR techniques is that they are less affected by heterogeneity of sea surface [389]. A first approach to exploit polarimetric information is statistical. Additionally, it opens a spectrum of ways to decompose the polarimetric channels' information into different combinations of backscattering mechanisms (e.g. [74, 73, 392]) occurring at the vessel and the surrounding water surface and to use them as distinctive feature [393, 394, 362, 395]. The list below mentions several popular PolSAR concepts:

- model-based approaches such as the Generalized Likelihood Ratio Test (GLRT; such as in [396]) were successfully tested. Both can better handle rough sea states than the CFAR through improved false alarms rejection [294]. Liu et al. [265] proposed the GLRT methodology where the statistics for the sea are considered normal distributed and the covariance matrix of the target is unknown
- the Generalized Optimization of Polarimetric Contrast Enhancement (GOPCE; [397]) tries to identify the highest contrast through measuring the similarity in the scattering behaviour of an arbitrary target with a plane and a dihedral target
- the polarimetric reflection symmetry detector relies on the concept that surfaces have reflection symmetry and therefore a very low magnitude of the C12 element of the covariance matrix (complex inner product between the co- and the cross-polarised channels). On the other hand, it can be assumed that complex scatterers such as ships are likely to not own particular symmetric properties [381, 169, 100]
- the Geometrical Perturbation Polarimetric Notch Filter (PNF) was proposed by [380] and further improved [398]. It is based on the idea of isolating the full-polarimetric return coming from the sea and detecting anomalies with different polarimetric signatures depending on orientation, material and structure of the vessel. The PNF approach focuses on targets lying in the complement orthogonal subspace of the sea vector. It was later picked up by [168] who tested it with ATI-SAR data
- the Polarimetric Match Filter (PMF), developed by [264], was picked up several times since (e.g. [397]). It intends to enhance the contrast between the covariance matrices of the clutter and the vessel over different scattering mechanisms. The algorithm returns the scattering mechanism that optimises the diversity providing the highest contrast possible. In that very same publication Novak further describes the Polarimetric Whitening Filter (PWF) which uses the trace to minimise the speckle which will facilitate detection and the Optimal Polarimetric Detector (OPD)
- ref. [292] derived the entropy detector from the Cloude-Pottier decomposition [87] to quantify the possible dominance of one scattering mechanism over the others in small fishing boats at low incidence angles. In [268] the polarimetric entropy detector was as well used for ship detection at low incident angles

Sublook detectors follow a different methodological way which is based on the spectral analysis of single-look SAR data to extract the spectrum and analyse portions (sublooks or sub-apertures) of it. This enables the detection of vessels which are correlated between looks before the background of an uncorrelated sea surface [174, 171]. Through the attenuation of that uncorrelated radar returns the water surface's clutter can be reduced while preserving the vessels' signals, leading to a higher TCR. This method is combined with a variety of approaches, each named after the distinctive feature it uses: the sublook entropy detector [214], the sublook coherence detector [214], the sublook cross-correlation detector [172, 274], sublook algorithms exploring variances of the phase [318, 399] and sublook detectors based on the GLRT [36]. In this way it is possible to enhance the TCR with the drawback of reduced spatial resolution according to the number of sublooks employed [54]. Finally, the discrete Wavelet Transform (WT) takes advantage of differences in the statistical behaviour of the vessel and the water surface clutter. It increases the TCR by noise reduction through the addition of the mean and detected edges in different directions [261].

Assuming that the object is visible at all, typical problems of radar images must be dealt with, such as azimuth displacement ('train-off-the-track effect') triggered by object movement in range direction and explained by the Doppler effect. Dual channel maritime moving target indication (MMTI) techniques have been developed to improve the detection of moving objects and even using their movement as an identification feature [296]. Among them are the classical approaches Displaced Phase Center Antenna (DPCA; [300, 400]) and ATI-Along-Track Interferometry [401], as well as promising adaptive techniques such as extended DPCA (EDPCA; [322]) and Imaging Space-Time Adaptive Processing (ISTAP; [402]). Ref. [168] combined ATI with notch filtering and later [321] introduced Oceanic DPCA (ODPCA), an extension of DPCA where the statistics of the open ocean's water surface in ATI-SAR data are taken into account for modelling. [320] designed a new ATI detector based on the complex interferometric dissimilarities in dual-channel data. Another well-known problem are azimuth ambiguity patterns which are image artefacts appearing as weaker repetitions ('ghosts') of a strong discrete scatterer shifted at a fixed distance in azimuth [403]. They can be caused by bright objects on land near the coast as well and much research was done to tackle this problem (e.g. [393, 404, 405]). Ref. [389] proposes to label them as recurrent false alarms if repeat-pass images are available.

Furthermore, moving maritime vehicles can be detected in an indirect way via the turbulent wakes and kelvin wakes they produce when in motion [406, 258]. That approach is often used in combination with maritime moving target indication (MMTI) techniques. [407] investigated the influence of different environmental conditions such as sea state or local wind, ship properties such as ship speed or ship heading, and image acquisition parameters such as incidence angle or satellite heading on the probability of detection with SAR. New approaches are radon transform for wake component detection [408], the generalized minimax concave (GMC)-based method [409] and enhancement of detection using Cauchy distribution [410].

With increasing computational power and growing data resources available, ship detectors have been developed in the pattern recognition community. However, many of the traditional methods such as region selections, e.g. scale-invariant feature transform (SIFT), and histogram of oriented gradients (HOG), and classifiers, e.g. support vector machine (SVM) have a high computational cost. With deep learning, time performance increased since it directly taps GPU power [370]. Different approaches using convolutional neural networks (CNN) (e.g. [383]) began to evolve rapidly and we see different deep learning models for object detection: the region proposal classification (R-CNN; [363]) and the sliding window. R-CNN was followed by fast R-CNN [364] and faster R-CNN [365, 366], reducing complexity and increasing performance by directly using the softmax function instead of SVMs and introducing Region of Interest (ROI) polling. Other approaches such as YOLO [369] and YOLOv2 try to embrace the whole image during the training and testing period [370]. Ref. [411, 412] proposed the integration

## 4. The InflateSAR Campaign

of contextual-based CNNs with deep architecture and the pixel-based multilayer perceptron (MLP) with shallow structures suitable for high-resolution satellite imagery.

With the aim of identifying reliable and robust detection algorithms for refugee rubber inflatables, a selection of intensity-based, polarimetric and sublook VDSs were evaluated for that particular vessel. Genetic algorithms, neural networks or deep learning algorithms could not be used due to the limited amount of training data. Nor were wake detection or MMTI techniques applied because the vessel was mostly stationary.

### 4.4.2 Data and Methods

The data collection covers a broad variety of combinations of different scene settings and sensor settings in comparably calm wind and water surface conditions of a small lake near Berlin. The test inflatable used in the campaign is an original refugee rubber boat, recovered from the central Mediterranean Sea (see [302]). Data from the first data collection campaign of the special target (Figure 4.25), which is made of thin inflated rubber tubes which are parted into five chambers, was used. The wooden parts form the floor and the transom where the outboard engine is attached to. Its roof is flat, it has no bilge or under water body and even when fully occupied has virtually no draught.

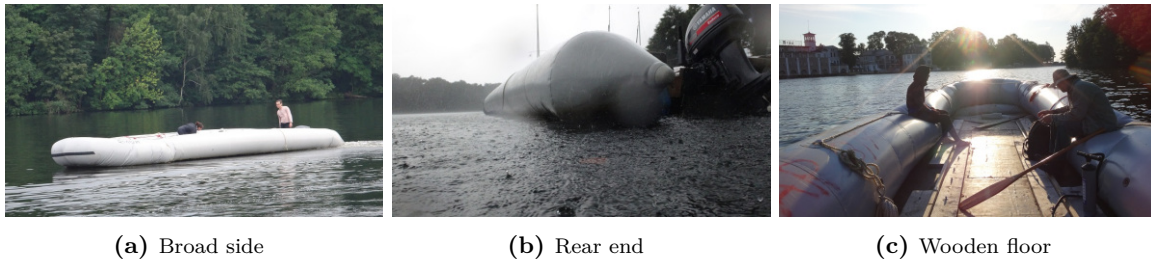


**Figure 4.25:** The vessel on its way to the test-bed lake.

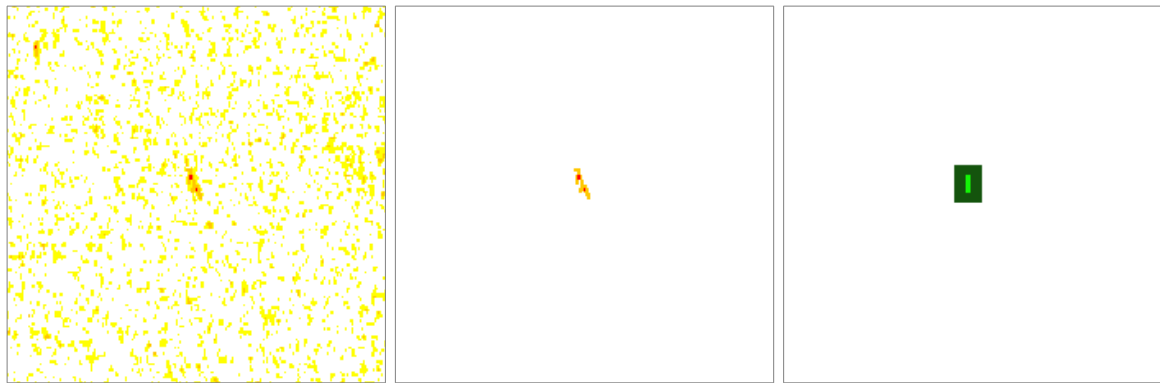
The majority of this work focuses on single-pol and dual-pol data from the TerraSAR-X mission operated by the German Aerospace Center (DLR) with High-Resolution Spotlight (HS) and Stripmap (SM) modes (Table 4.6). Cross-pol data was only available in SM dual-pol mode. Quad-pol observations were not accessible at all so the adaptation of the detection algorithms was necessary accordingly. In addition, testing on a small collection of four dual-pol VH VV datasets from S1's Interferometric Wide Swath (IW) mode, acquired during the campaign, was done.

**Table 4.6:** Available data according to acquisition mode and polarisation.

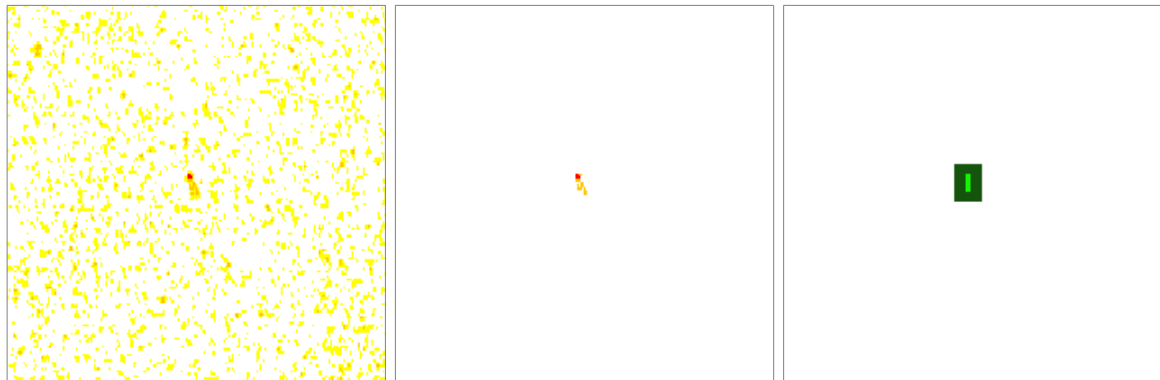
TSX-HS	Images from...		TSX-SM	Images from...	
	Single-pol	Dual-pol		Single-pol	Dual-pol
Co-pol	13	14	Co-pol	8	12
Cross-pol	0	0	Cross-pol	0	6

The binary classification scheme of Receiver Operator Characteristics (ROC) curves was used to visualise and compare the performance of the detectors. In order to quantify and compare the results from the ROC curves, the area under the curve (AUC) was estimated. The ROC curve is created by plotting the true positive rate (TPR) against the false positive rate (FPR) at various threshold settings. The detector under test's finding for each threshold

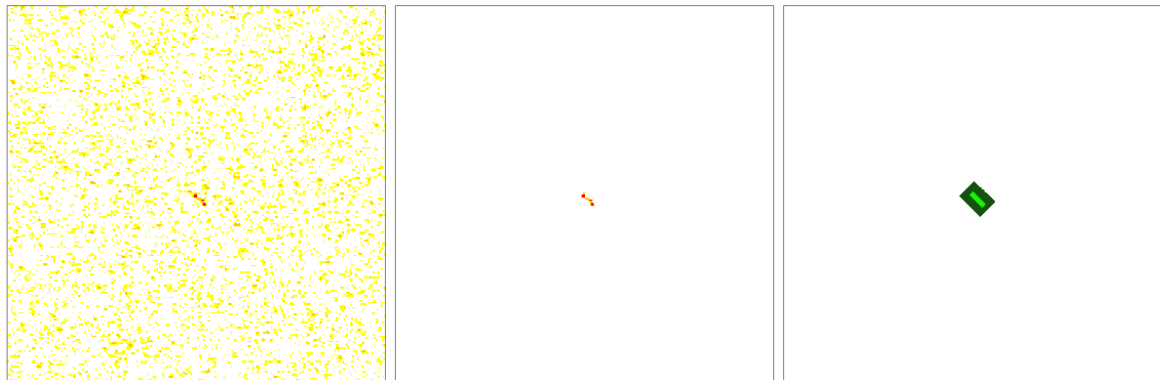
is validated against the sea truth mask. To perform pixel-based and object-based validation two different way of counting true positive pixels were used and two different sea truth masks for each of the SAR datasets were established. Figure 4.26 shows a series of example sea-truth masks for both the pixel-based and the object-based approach. With the pixel-based masks each pixel within a small distance to the boat's real position is selected whose intensity is higher than the mean value plus two times the standard deviation of the local clutter. Every pixel is then evaluated separately. With the object-based approach, on the other hand, all pixels within a rectangle of about  $12 \times 3.5$  m plus an optional buffer zone of about 10 m to compensate for GPS inaccuracies are set to *true*. In the object-based validation, the ship is called detected if at least one of its pixels are detected. The object-based approach is closer to a result interesting to an operator because it assess the detection capability of the boat as a whole, while the pixel-based method is more important to assess the capability to delineate the size of the boat.



(a) HH-pol, mode: HS

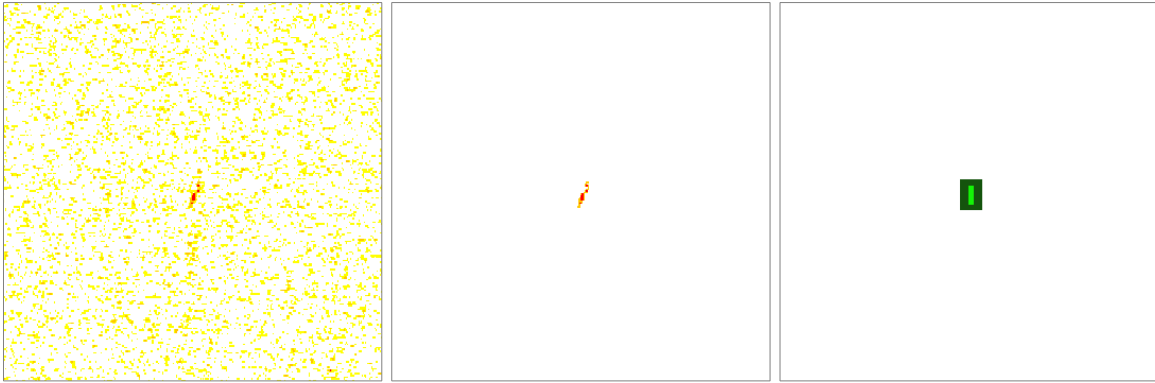


(b) VV-pol, mode: HS

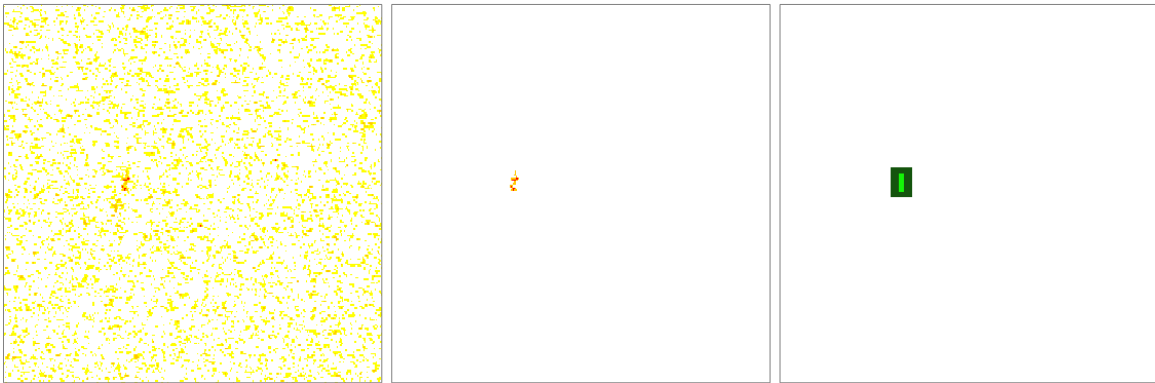


(c) HH-pol, mode: HS, vessel inclined

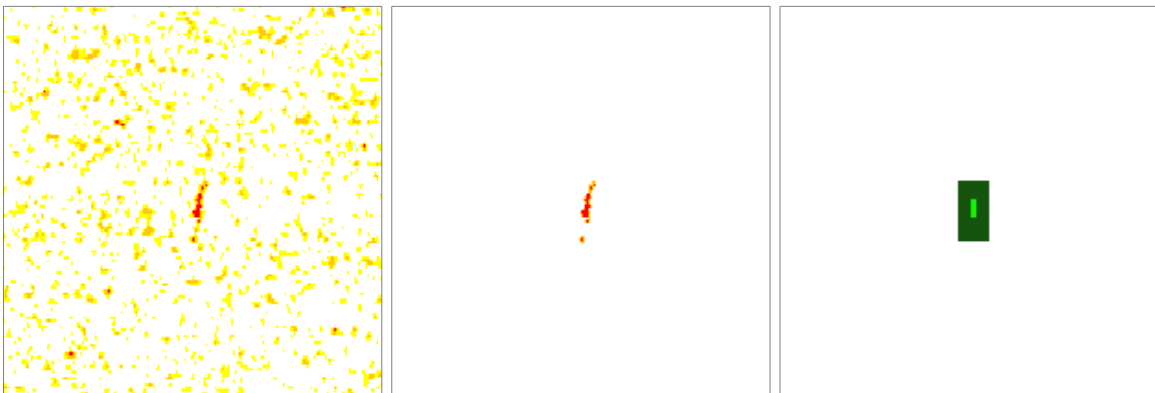
#### 4. The InflateSAR Campaign



(d) VV-pol, mode: HS, vessel moving in azimuth



(e) HH-pol, mode: HS, vessel moving in azimuth



(f) HH-pol, mode: SM, vessel moving in azimuth

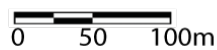
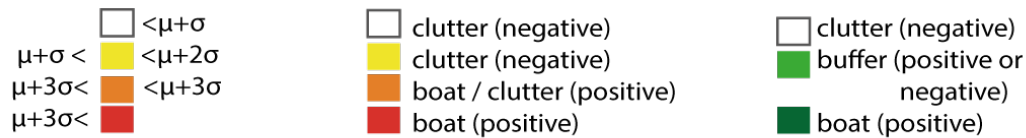


**Figure 4.26:** Example images of sea truth masks. Left column: TSX SAR images (©DLR 2017) coloured according to each image's statistics; centre column: pixel-based sea truth mask; right column: object-based sea truth mask.

If the boat left no identifiable trace in a single-pol image (three cases), the sea truth mask for pixel-based detection is left empty. For the object-based approach, the boat is placed according to the GPS coordinates recording during the acquisition.

Nine different vessel detection algorithms were selected to test the detection capabilities of SAR data for small rubber inflatables. The range of detection techniques include an intensity-based approach, a sublook detector and six polarimetric detectors (Table 4.7). For each VDS, two boxcar filters are applied to the training window (some of them using a guard window if this increases the performance) and the smaller test window (in some cases just one cell) to implement a moving average filter.

**Table 4.7:** VDSs under test, applicable polarimetric channels and total number of samples (n) per detector.

Detector	Category	Single co-pol	Dual co-pol	Dual cross-pol	N (HS,SM)	Fixed Parameters: RR (dimensionless), all others in m
Cell Averaging Constant False Alarm Rate (CA-CFAR)	intensity based	✓	✓	✓	27,26	training window size: 36 guard window size: 24 CUT: 1 cell
Sublook Correlation (SubCorr)	sublook	✓	✓	✓	27,26	training window size: 12 CUT: 1 cell
Polarimetric Notch Filter (PNF)	polarimetric		✓	✓	7,9	training window size: 96 CUT 1 cell RR: 0.02
Polarimetric Entropy (PolEntropy)	polarimetric		✓	✓	7,9	training window size: 7 CUT: 1 cell
Polarimetric Match Filter (PMF)	polarimetric		✓	✓	7,9	training window size: 120 guard window size: 24 CUT window size: 24
Polarimetric Whitening Filter (PWF)	polarimetric		✓	✓	7,9	training window size: 120 guard window size: 24 CUT window size: 24
Polarimetric Symmetry (PolSym)	polarimetric			✓	0,6	training window size: 5 guard window size: 2 CUT: 1 cell
Cross-pol Intensity Dual-pol Ratio Anomaly "volume" Detector (Cross-iDPolRAD)	polarimetric			✓	0,6	training window size: 36 guard window size: 12 CUT: 1 cell
Co-pol Surface Intensity Depolarisation Ratio Anomaly Detector (Co-SiDPolRAD)	polarimetric			✓	0,6	training window size: 36 guard window size: 12 CUT: 1 cell

All VDS algorithms under test are taken from literature except the Co-SiDPolRAD (Formula 4.5) which is an adaption of the volume detection algorithm iDPolRAD. The iDPolRAD algorithm (Formula 4.6) was originally developed for the detection of small icebergs based on their polarisation ratio which is different compared to the surrounding sea or sea ice background. For the sake of clarity, the iDPolRAD is called Cross-iDPolRAD. They can be written as

$$I = \frac{\langle |co-pol|^2 \rangle_{test} - \langle |co-pol|^2 \rangle_{train}}{\langle |cross-pol|^2 \rangle_{train}} * \langle |co-pol|^2 \rangle_{test} \quad (4.5)$$

#### 4. The InflateSAR Campaign

$$I = \frac{\langle |cross-pol|^2 \rangle_{test} - \langle |cross-pol|^2 \rangle_{train}}{\langle |co-pol|^2 \rangle_{train}} * \langle |cross-pol|^2 \rangle_{test} \quad (4.6)$$

where  $\langle \rangle_{test}$  and  $\langle \rangle_{train}$  are the spatial averages (or the value of the cell under test if just one single cell is tested) of the test and the training windows.

Both, the Co-SiDPolRAD and the Cross-iDPolRAD explore the intensity rate between cross-polarisation and co-polarisation channels and both consist of two parts: the first (to the left of the multiplication sign) works as a 'normaliser' to enhance the contrast and reduce false alarms and it can be defined as the 'filtering' component; the second (to the right of the multiplication sign) impacts the probability of detection and represents the 'filtered image' component. The result is a detection map which can be evaluated against an array of thresholds to confront each true positive rate with its counterpart false positive rate. Where the Cross-iDPolRAD is capable of reducing false alarms from clutter that is not a homogeneous surface, its detection capability is limited for inflatables, since these are not very visible in HV. The Co-SiDPolRAD is tailored to detect anomalies of surface scattering, which is suspected to be a prominent scattering mechanism of the inflatable [302].

To improve the iDPolRAD's performance for the special vessel the original detector is combined with the new surface scattering version. The result are algorithms that take the occurrence of both volume and surface scattering mechanisms at or around the inflatable into account and use them for successful detection. Figure 4.27 shows two different ways to pixel-wise integrate the two detectors: one that sums the two detector maps Figure 4.27a and the other with the combination of positive and negative detections via a logical operator Figure 4.27b.

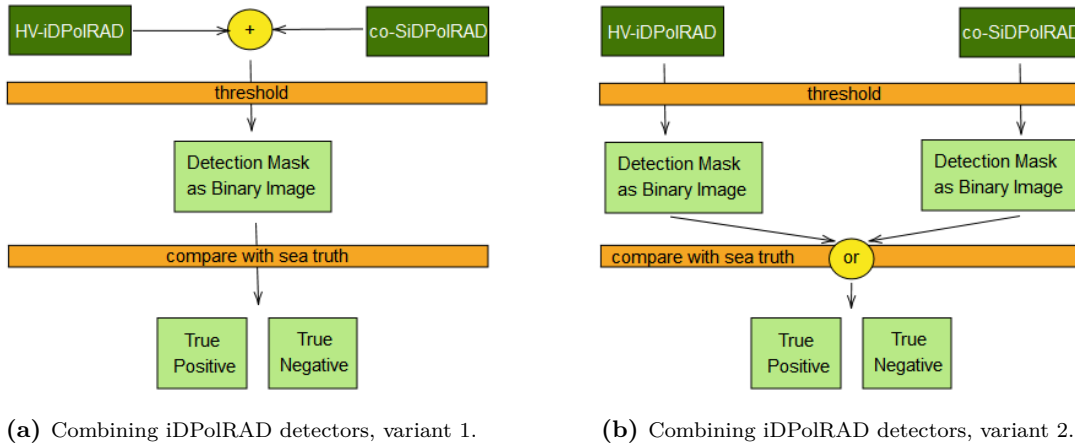


**Figure 4.27:** New combinations of the polarimetric detectors Cross-iDPolRAD (volume detector) and Co-SiDPolRAD (surface detector).

While the entropy/alpha approach was originally designed for quad-pol data, it can also be applied to the simpler case of dual-polarisation [152]. With dual-pol data the scattering matrix  $[S]$  cannot be reconstructed completely. Only a column of  $[S]$  can be derived which is then used to construct a  $2 \times 2$  coherency matrix  $[T]$  to estimate the depolarisation and to use it for the PolEntropy detector. For the inflatable rubber boats on the lake, it looks for low entropy values.

Sublook detectors use the interlook cross-correlation property that fully developed speckle is uncorrelated while deterministic targets are correlated. Therefore, ships show a higher degree



of correlation than the sea surface [174]. This can be done by using Fast Fourier Transform, split the azimuth or range spectrum in two, apply an inverse Fast Fourier Transform and correlate the resulting images. [171] has shown that both deliver similar results, only that the azimuth resolution is lower. Therefore, this is limited to the range variant to gain better results in terms of spatial resolution. Other than the original SubCorr detector described by Schneider [214] here the non-normalised correlation coefficient (or coherence operator) is used. This operator is given by the product of the first sublook image and the complex conjugate of the second sublook image.

All tested algorithms use an adaptive training. Adaptive training is designed to obtain the statistics of the clutter using local windows. The clutter is obtained from a ring in a sliding (or moving) window ('boxcar') with the pixel(s) (or cell(s)) under test (CUT) in the centre surrounded by a guard ring. This guard ring excludes pixels of an extended target from the background ring around it and hence avoid contamination of the clutter statistics.

### 4.4.3 Results

#### 4.4.3.1 Preliminary Analysis of Detectors

The following series of images in Figures 4.28 and 4.30 provide a first visual overview of the detectors' outputs. These outputs are needed to create the detection maps by filtering them with a given threshold (or array of thresholds) using three exemplary dual cross-pol datasets from TSX's SM mode. All detection maps are visualised using dimensionless colour maps of detector-specific ranges. The sea truth masks in the respective sub-figures 'l' shows the co-pol portion in blue and the share coming from the cross-pol channel in green. Subfigures 'm' and 'n' show original SAR data from  $\sigma_{min}^0$  (black) to  $\sigma_{max}^0$  (white).

The three example datasets used represent different sets of sensor settings (incidence angle: 'low'  $< 35^\circ <$  'high') and scene settings (the boat's orientation relative to the line of sight (LoS) and its movement). Figure 4.28 has the boat non-moving in  $45^\circ$  inclined whereas in Figure 4.29 the boat moves in azimuth and in Figure 4.30 we see the non-moving inflatable oriented orthogonally to the LoS. The direct comparisons provide an overview how different the algorithms perform and the impact of each detector's settings regarding the sizes of the training window and the test window. Even small features on the rather calm test-bed's water surface can produce scattering artefacts which, in turn, reduce the TCR. This is especially true for low incidence angles (Figure 4.30) and cross-polarisation channels (e.g. Figure 4.28a compared to Figure 4.28b, 4.28c compared to Figure 4.28d).

There are several reasons that could explain the differences in the detection masks and the detection performance. For instance, the PWF and the PMF produce a bigger detected area (a 'blob'). Possibly this is the case because they are based on optimisations (bigger CUT window size used compared to the other detectors, see Table 4.7) that maximise the detection performance in this problem. In the case of the PolEntropy the low return from the lake produces more false alarms. The PolSym is not designed to deal with this type of targets, while the PNF seems to not optimising the target direction when the clutter is less polarised. The SubCorr detector is performing nicely maybe because it rings about a higher sensitivity for the vessel's edges.

#### 4. The InflateSAR Campaign

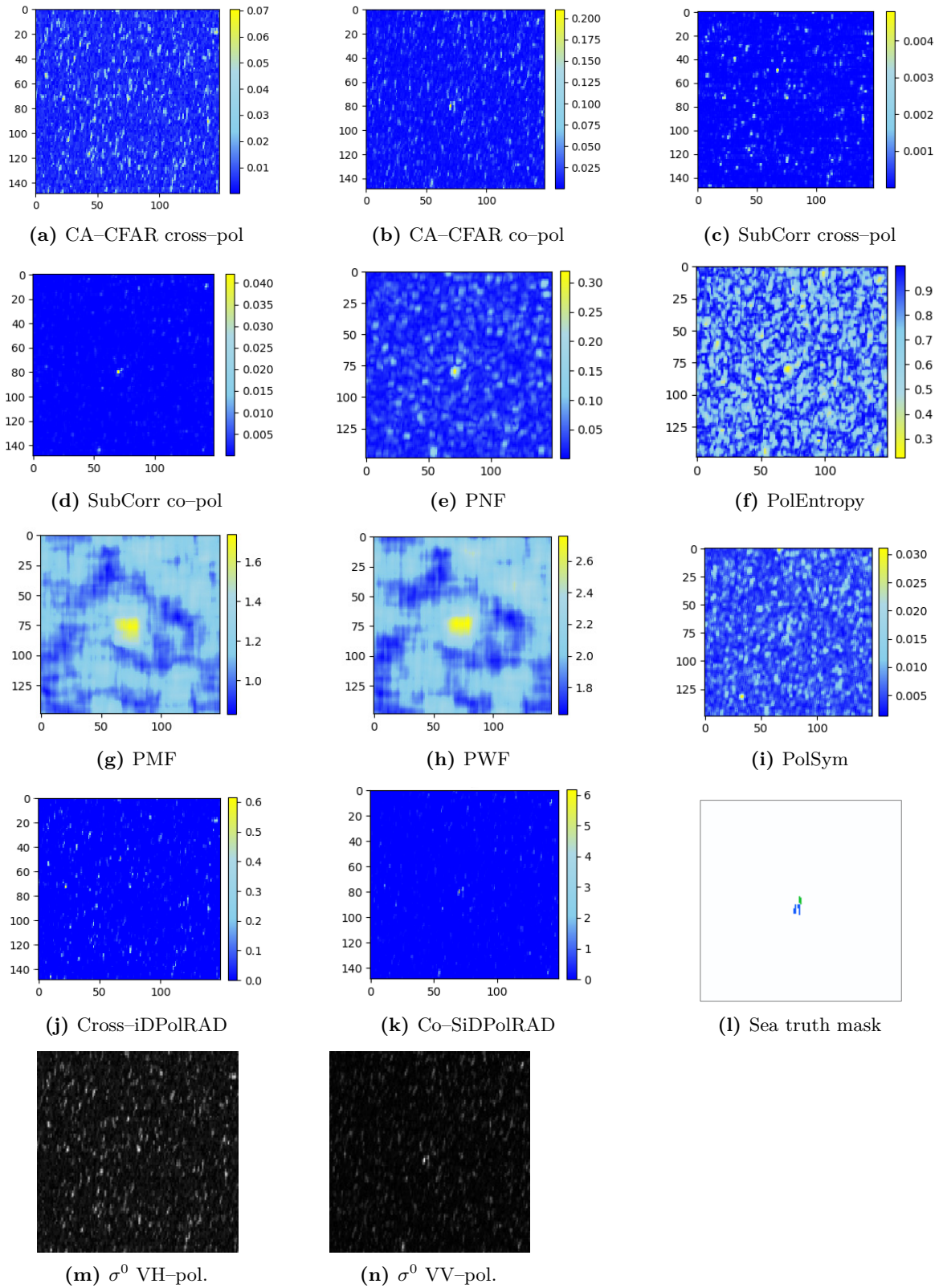


**Figure 4.28:** Incidence angle: high; boat: inclined; mode: SM; polarisation: dual VH-pol and VV-pol (scale in meters, colour ramps are without units).

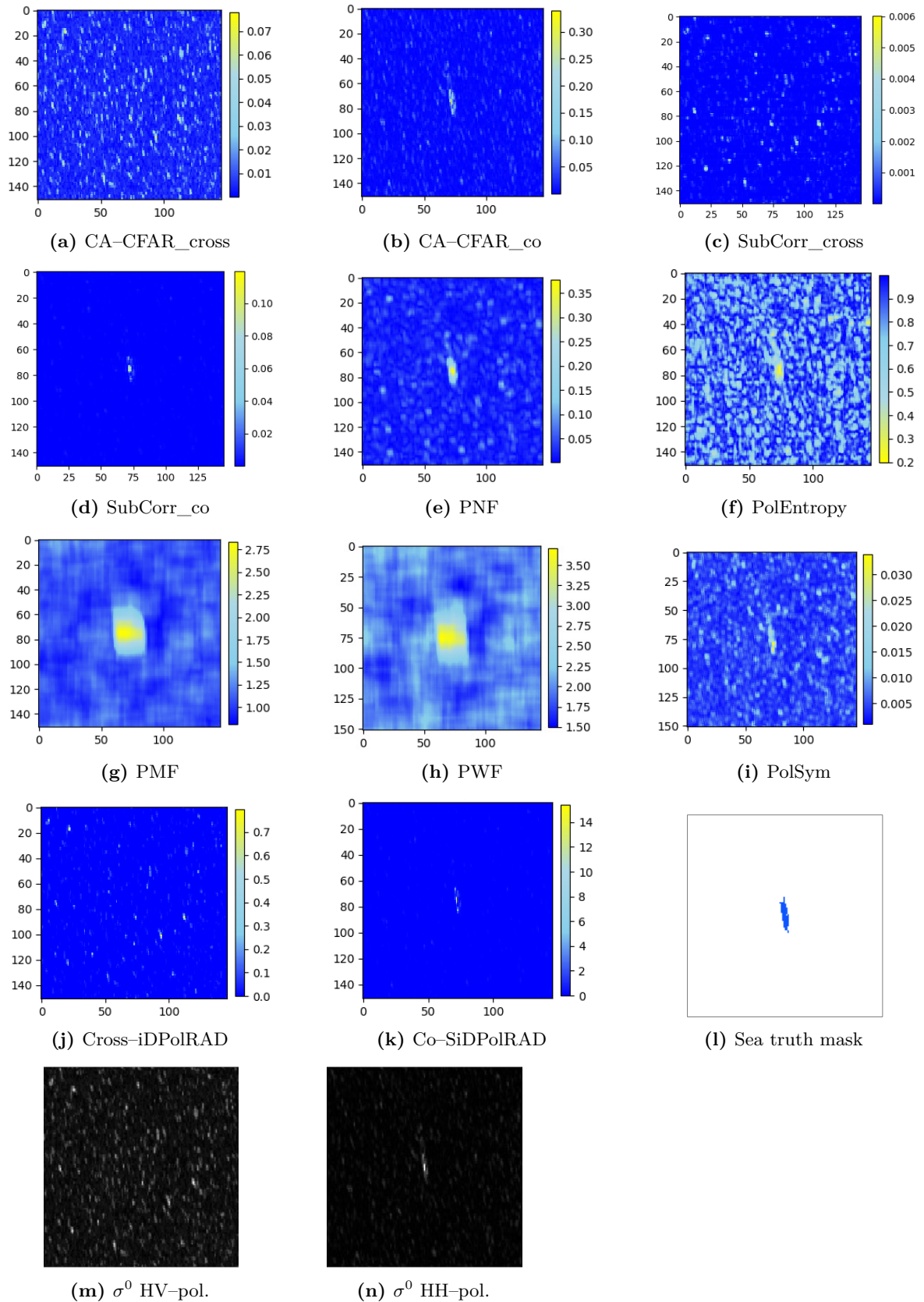


**Figure 4.29:** Incidence angle: high; boat: orthogonal, moving in azimuth; mode: SM; polarisation: dual HV-pol and HH-pol (scale in meters, colour ramps are without units).

#### 4. The InflateSAR Campaign

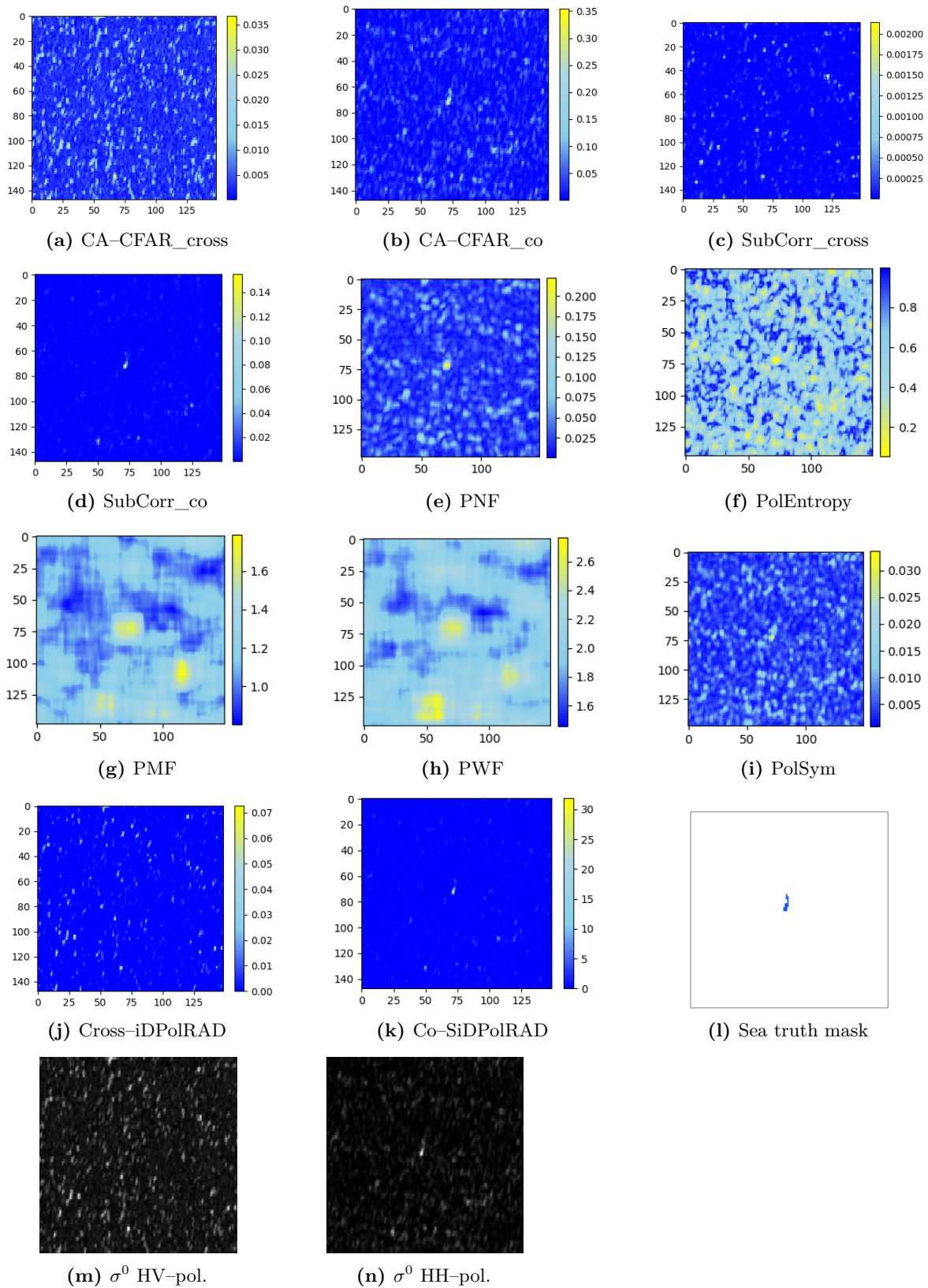


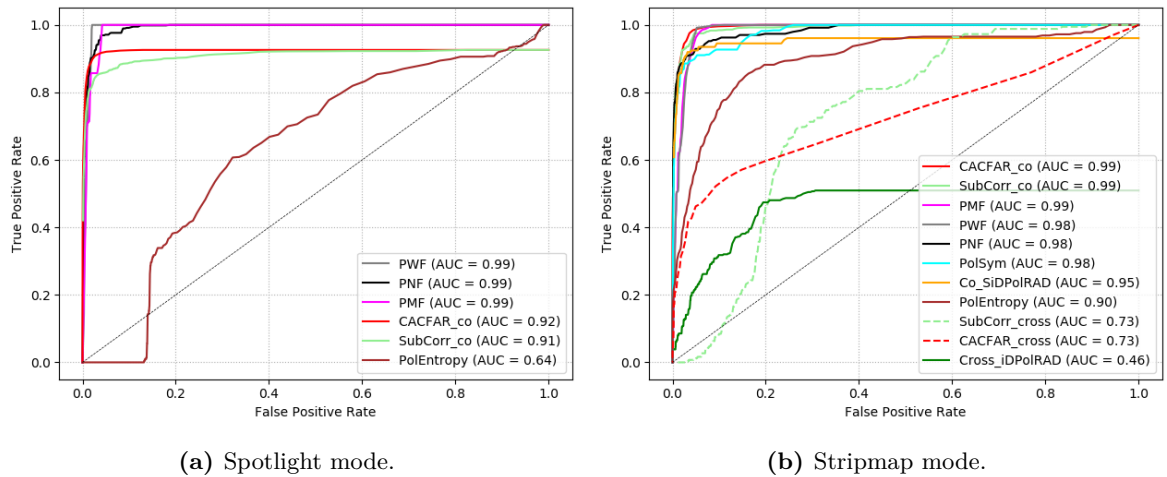
**Figure 4.30:** Incidence angle: low; boat: orthogonal, non-moving; polarisation: low; mode: SM; dual HV-pol and HH-pol (scale in meters, colour ramps are without units).

#### 4.4.3.2 Comparing Well-Known Detectors

This part of the Results section is prepared in such a way that the detectors' performance is extensively tested on TSX data before the background of the main sensor settings (incidence angle, polarimetric property and acquisition mode), the detection approach (pixel-based, object-based with/without buffer) and whether multilooking is switched on or off. The subsequent part describes the benefits of combining two of the algorithms used. Finally, the VDS are tested using S1 data.

#### 4.4.3.3 Comparing Resolution Modes

Figure 4.31 shows the ROC curves for SM and HM with pixel-based evaluation of the TPR and detector perform filtering (multilooking). The dotted black diagonal line represent the worst possible performance when a completely random choice is made.



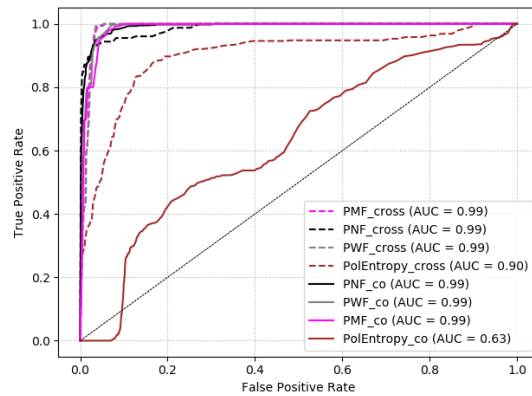
**Figure 4.31:** Comparing resolution: ROC curves for different acquisition modes (Pixel-based, multilooked).

Figure 4.31a presents the result for HS where cross-pol data and therefore some detectors are missing. This ROC shows that the polarimetric detectors PWF, PNF and PMF perform best. The PolEntropy detector, which is set to find low entropy anomalies, provides a very weak performance because the lake has a low backscattering increasing its entropy (strong impact of thermal noise in the signal) and the boat is very small with a dominant scattering mechanism (surface) and occasional volume scattering, therefore it does not have stable entropy values throughout. The SubCorr and the CA-CFAR have discrete performance, but there are some boats that are always missing (TPR remains  $<0.926$ ).

Figure 4.31b shows the SM mode where the full set of algorithms could be tested. Again, the polarimetric detectors did well except for the iDPolRAD volume detector. The SubCorr and the CA-CFAR have low performance, showing that the polarimetric information layer is important for detecting these objects. The very good result of the Co-SiDPolRAD surface detector indicates that surface scattering is dominant at the inflatable. HH VV data seems to support better detection results than HV HH data for the CA-CFAR and the sublook detector. The results of HS modes are not better than the SM mode, indicating that the decisive difference here is rather made by the polarimetric capability than by the resolution.



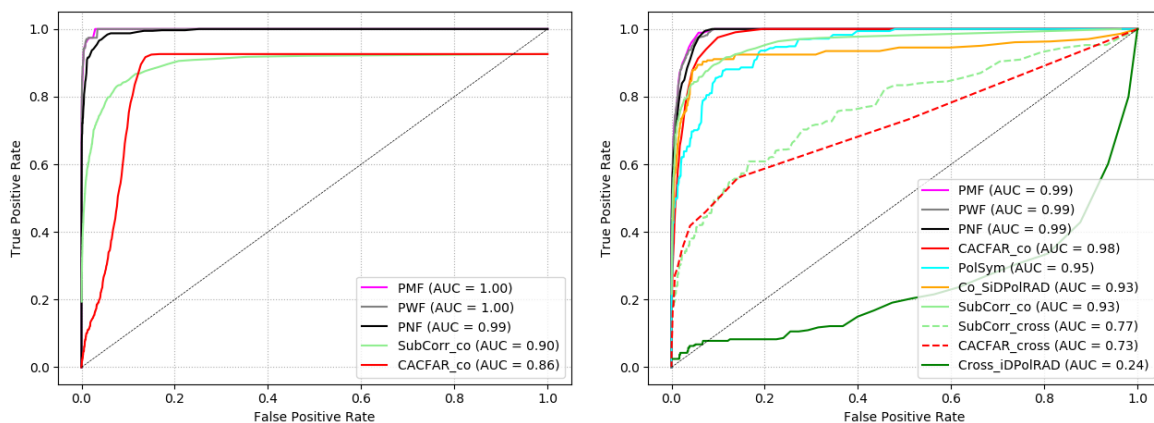
4.4.3.4 Comparing Polarimetric Modes



**Figure 4.32:** Comparing polarimetric modes: ROC curves for dual co-pol and cross-pol data in SM mode (pixel-based, multilooked).

Figure 4.32 extends the comparison between co-pol (HH VV) and cross-pol(HV HH, VH VV) data to cover the polarimetric detectors. It is again a pixel-based approach with filtering and it shows that the detectors' performance are at very similar levels for cross-pol and co-pol data. Again, the PolEntropy detector show a different behaviour being more performant in the cross-pol data domain. It seems that its performance greatly depends on the polarimetry but this is, to a certain extent, misleading. It happens to be that in the data there is a pattern of co-pol data being taken under rather extreme low or high incidence angles. The influence of the incidence angle on the entropy is expected to be even greater than the polarisation mode. Consequently, when we see PMF, PWF and PNF performing very well in this setting, we can assume their robustness with respect to the polarisation but also to the incidence angle.

4.4.3.5 Assessing Filtering (Multilooking)



(a) Spotlight mode.

(b) Stripmap mode.

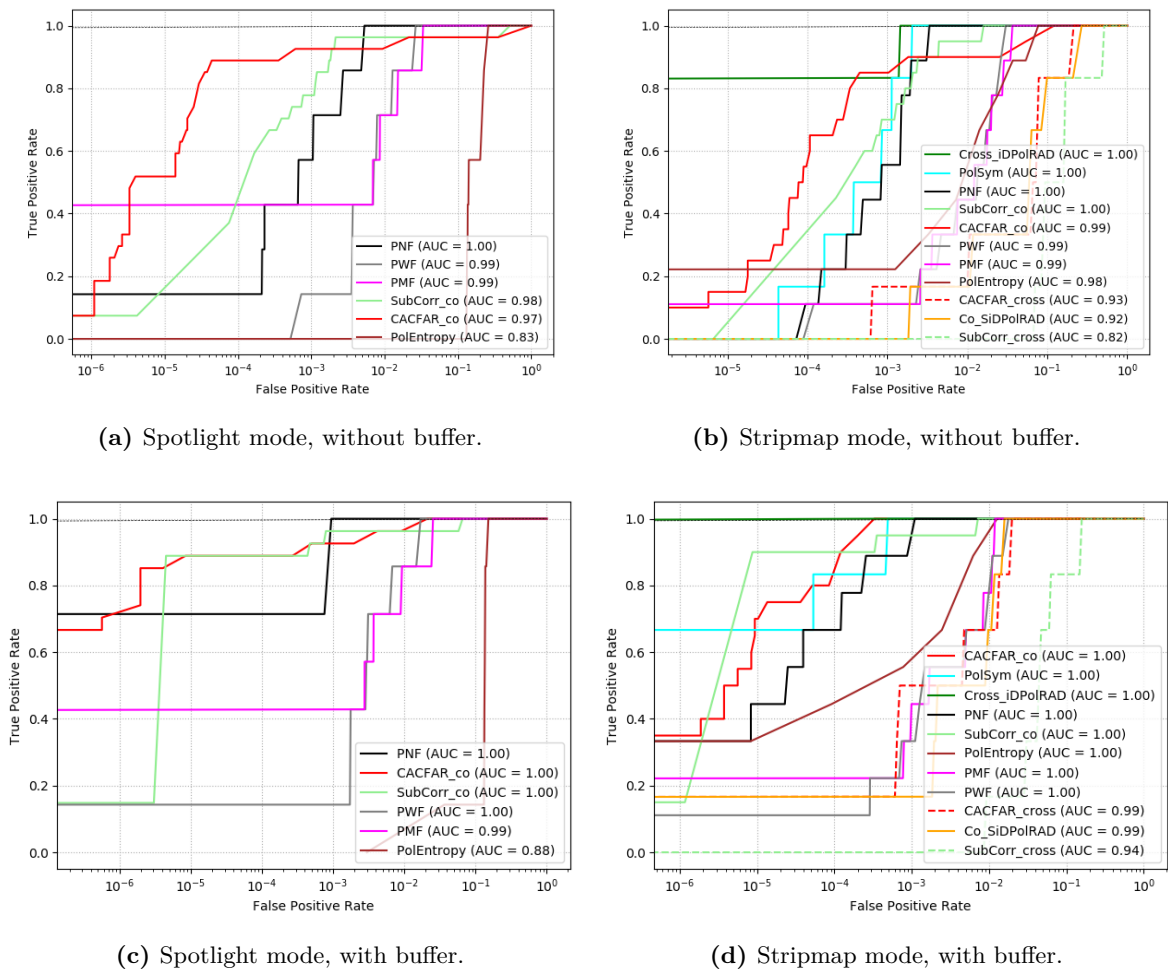
**Figure 4.33:** Assessing multilooking: ROC curves for different TSX-modes (pixel-based, not multilooked).

Figure 4.33 illustrates the performance for all detectors without speckle filtering. The CACFAR and the SubCorr both perform slightly weaker in HS mode but very similar in SM mode.

Only the SubCorr\_cross reaches a clearly higher AUC in this cost-saving mode. Among the polarimetric detectors, the PMF, PWF and PNF manage to maintain similar performance results as with multilooking. The PolSym and the surface detector lose a bit of performance, the volume detector clearly benefits from speckle filtering. The PolEntropy was taken out since its result would be unitary.

#### 4.4.3.6 Counting the Boat as a Single Object

Figure 4.34 shows the results using the object-based approach to count TPR. As expected, the detectors' performance increased since the detection task is less hard than the delineation task. Furthermore, enlarging the object by using a buffer around the boat additionally improves the results of all detectors. Very interestingly, whereas in the pixel-based approach, the Cross-iDPolRAD has the weakest performance, it becomes one of the strongest detectors in the object-based variant. That could be a sign of strong volume scattering processes going on around the inflatable. Their spatial extent seems to be rather small and a little dislocated from the high intensity pixels used for the pixel-based approach. This is a phenomenon in reverse to what was observed in monitoring icebergs [112], where the surrounding pixels showed deeps of the iDPolRAD.

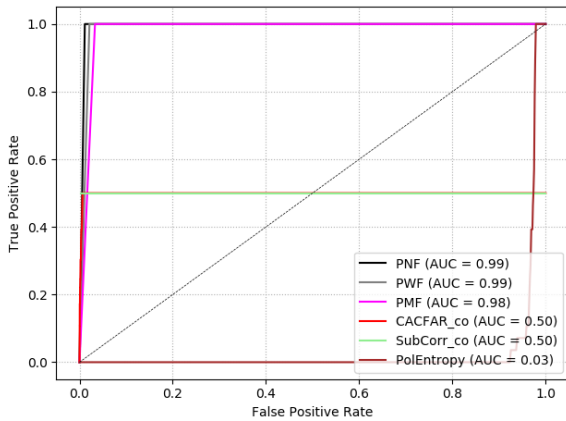


**Figure 4.34:** Object detection: impact of the usage of a buffer around the boat on ROC curves for different TSX-modes (multilooked, false positives in log10 scale).

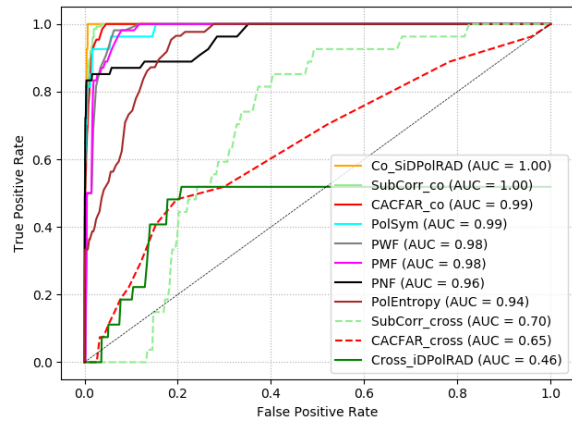
#### 4. The InflateSAR Campaign

This indicates that the edges are stronger for the opposite of the anomaly (i.e., a surface anomaly produces volume anomalies around the edges). Since only the edges of the boat are detected, further future analyses are needed to evaluate the actual usefulness of the iDPolRAD for inflatable boats. This could as well be considered a reason the PolEntropy detector works much better than in pixel-wise mode. The volume scattering occurring around the inflatable changes the relation between the scattering mechanisms at that locations and creates therefore an anomaly in the entropy space. It is notable that the Co-SiDPolRAD do not increase as much as the others. In Spotlight mode the PNF becomes the best detector.

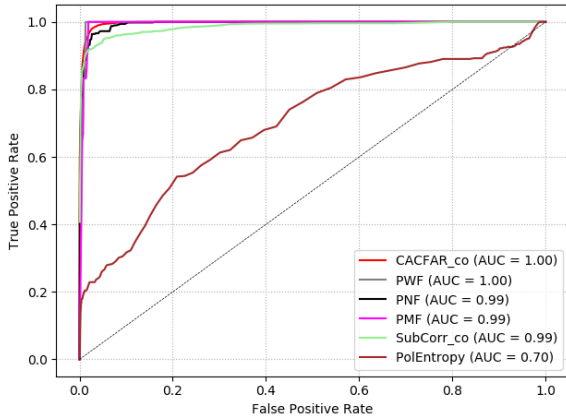
##### 4.4.3.7 Comparing Incidence Angles



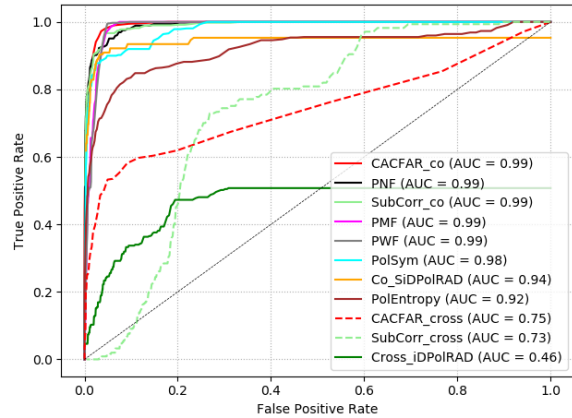
(a) Spotlight mode, low incidence angles.



(b) Stripmap mode, low incidence angles.



(c) Spotlight mode, high incidence angles.



(d) Stripmap mode, high incidence angles.

**Figure 4.35:** Impact of the incidence angle on the ROC curves for different acquisition modes (pixel-based, multilooked).

Figure 4.35 compares the performance of the algorithms with regard to different incidence angles (low  $< 35^\circ <$  high), separated by the acquisition mode. The influence of the incidence angle alone cannot be shown isolated, but it seems that for most algorithms the incidence angle does not influence the detection performance to a great extent. The results of Figure 4.35a has to be taken with precaution due to the very small number of samples.



Lower incidence angles decrease the AUC when cross-pol data is used (Figure 4.35b). A low incidence angle triggers intensified surface scattering mechanisms at the flattened water surface below the inflatable compared to the surrounding water surface and the surface detector Co-SiDPolRAD shows much better results in Figure 4.35b than in Figure 4.35d accordingly. Again, PolEntropy is especially weak at HS mode. Although, when set for anomalies with a low entropy, this detector sometimes could be promising for data acquired under moderate or rather high incidence angles. Figure 4.35a (an entropy detector set to search for high entropy would reach an AUC of 0.97 here) and Figure 4.35d, where it scores an AUC for 0.92 affirms that theory, whereas Figure 4.35b invalidates it. The PolEntropy seems very co-dependent on the polarisation mode and presumably on scene parameters such as weather situation and vessel orientation as well.

#### 4.4.3.8 Combining iDPolRAD Detectors

The combination of iDPolRAD detectors for surface and volume scattering improves the results for the special object as it can be seen in Figure 4.36. It enables the detector to search for surface scattering and volume scattering at the same time.

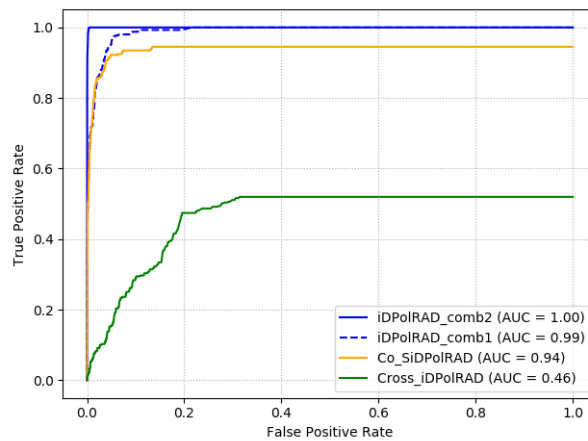


**Figure 4.36:** ROC curves for the iDPolRAD volume detector (green), its surface detecting variant (orange) and the two new combinations in dark blue (pixel-based, multilooked).

Different logical operators are tested in order to create the iDPolRAD\_comb2. It turned out that using the 'or' for the positives and the negatives in the two detectors' detection masks respectively yields the best result. The AUC for using the 'and' operator is at 0.49.

#### 4.4.3.9 Summary of Results Using TerraSAR-X Data

Table 4.8 wraps up all the detectors' performance comparison using TSX data and highlights selected scene parameters such as low incidence angles or cross-pol data which are found as being especially challenging for intensity-based detectors. To compute the overall performance, all available data is used which means that HH VV and HV HH data are put together. In the central three columns, light green cells mark AUCs of 98% or greater whereas dark green cells indicate the detector with the highest AUC for the respective category. Furthermore, the computational cost is added as a factor to the comparison as an expenditure of time

## 4. The InflateSAR Campaign

normalised by the CA–CFAR time and acquired under the same size for the moving windows for all detectors.

It shows, that the CA–CFAR and the sublook detector have the big advantages that only one single polarisation channel is needed, their cost is quite low and their overall performance is quite high. As it is known for the intensity–based CA–CFAR, the SubCorr does not perform well neither in the "challenging" data categories.

**Table 4.8:** Detectors' performance comparison (pixel–based, multilooked).

Detector	Applicability to single–pol mode	Overall performance	Challenges		Cost per step (norm= CA–CFAR)
			Low incidence angle	Cross–pol	
CA–CFAR	✓	95	76	73	1
SubCorr	✓	94	78	75	2.8
PNF	x	98	96	99	3.8
PolEntropy	x	69	63	90	42.3
PMF	x	99	97	99	70.6
PWF	x	99	97	99	14.9
PolSym	x	99	99	98	0.4
Cross–iDPolRAD	x	46	45	46	0.4
Co–SiDPolRAD	x	94	100	94	0.4
iDPolRAD_comb1	x	99	100	99	0.8
iDPolRAD_comb2	x	100	100	100	0.8

From the remaining group of polarimetric detectors, in all of them, except the PolEntropy, the volume scattering detecting iDPolRAD and its surface detecting variant reach very high AUCs in all categories. Of that group of the remaining very high performing detectors, the two new iDPolRAD combinations appeared to perform at least one magnitude faster than the PMF and PWF and almost five times faster than the PNF. None of the polarimetric detectors is especially challenged by low acquisition angles or cross–polarisation data. On the contrary, the PolEntropy manages to extract a way better TCR when having access to the cross–polarisation channel. In terms of computational cost, it shows that the sublook detector SubCorr, the polarimetric detectors PolSym and the group of iDPolRADs perform at the same order of magnitude whereas the PNF with its pixel–wise normalisation is a little bit slower. The PolEntropy, PWF and PMF are more expensive in the scale of one to two orders of magnitude due to the fact that they need to use a for loop for the diagonalization.

### 4.4.3.10 Performance Tests Using Sentinel-1 Data

While having only focused on TSX data so far, an assessment of the detection capabilities of the VDS when using S1 data is added here. The S1 data collection consists of four Interferometric Wide Swath (IW) dual–pol sets with a spatial resolution of about 70 m<sup>2</sup>/pixel. Accordingly, the inflatable now is represented only by very few pixels (between one and five) in the binary masks for the sea truth. The methods used are similar to the workflow involving TSX data. Only, S1's coarse spatial resolution reduced the maximum backscatter intensity from the inflatable. That is why when it came to generate the sea truth masks, the minimum TCR had to be lowered from  $\mu + 3 * \sigma$  of the local clutter which was used for TSX to  $\mu + 2 * \sigma$ . Otherwise the boat would not be visible at all. Finally, the preprocessing needed some extra steps (such as deburst).

Figure 4.37 reveals that under the given circumstances of a calm sea state an automatic detection of the inflatable is possible with S1 data. Similar to the results obtained with TSX,

the iDPolRAD\_comb2 performs best. Similar good results can be seen from the surface detector, the CA-CFAR with co-pol data, the PWF, and the PMF. The PNF, the PolSym, and the SubCorr detector on the other hand seem to suffer more from coarse resolution and show very low AUCs. Due to the fact that the vessel cannot be identified in one of the four datasets, none of the VDS surpass an AUC of 0.75.

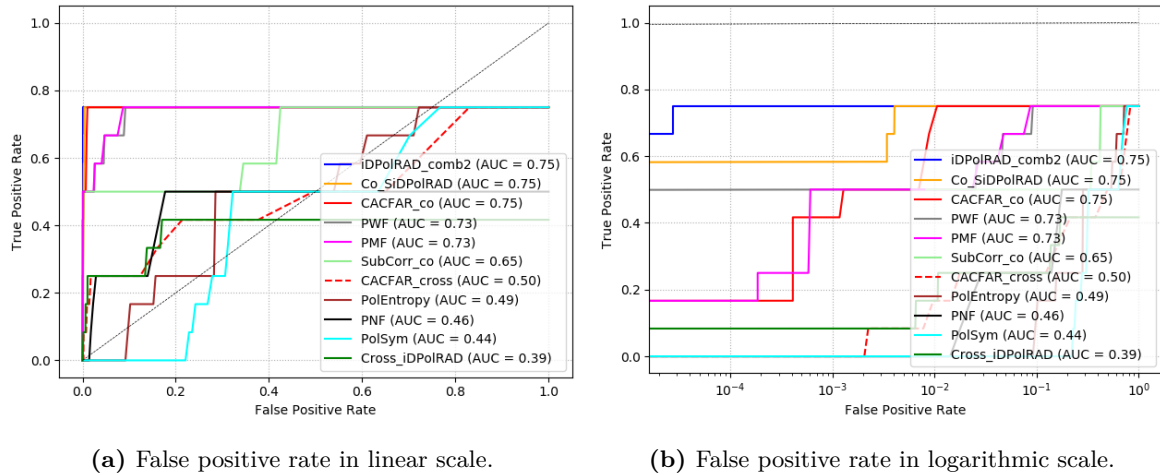


**Figure 4.37:** VDS performance test on S1 data (pixel-based, multilooked).

#### 4.4.4 Section Resume

These experiments show that the detection of very small, non-metallic vessels such as the refugee inflatable is possible with high-resolution SAR data and calm sea states (as represented by the lake experiment). Most of the detectors show very good results under the given presets. As expected, the detection task proved to be easier than the delineation task, which is based on the intensity values. This is questionable, but no other way to deal with the unknown GPS receiver's inaccuracy could be identified.

All of the SAR imagery collected show an empty boat which reflects a more challenging scenario than real applications where these inflatables use to accommodate more than 100 people. The limited availability of a 'full' vessel (30 passengers) can unfortunately not entirely describe the impact of these people on the vessel's radar backscatter behaviour. For the empty boat, surface scattering dominates its inside with only occasional volume scattering presumably at its transom or around the inflatable's tubes. However, in a realistic environment, such boats host tens of people that, reasonably, largely perturb the backscattered signal with respect to an empty boat. In order to accommodate for possible changes of backscattering when there are passengers, a new detector was designed, combining surface and volume scattering.

Furthermore, the author is aware of the fact that the lake only represents calm sea conditions and the detectors could not be tested in higher sea states. It is therefore to be expected that the AUCs will fall in stronger winds and higher swell. In order to extend the validity of these results for higher sea states, future research should aim at gathering more realistic data from the open sea.

This section compares the performance of different ship detection systems for the detection of a small inflatable boat using TerraSAR-X and Sentinel-1 data. The tests are structured such that the influence of different sensor settings can be observed. They have shown that a discrete detection performance is achieved if the clutter is not too strong. Low incidence

angles decrease the performance of many detectors but has little effect on the polarimetric approaches. Cross-pol data has a negative impact on the CA-CFAR and the sublook detector but all polarimetric detectors, except the PolEntropy, reach similar results on cross-pol and on co-pol data. Therefore, polarimetry seems to improve detection especially when it comes to what is defined as more challenging situations. As TerraSAR-X data is concerned, all algorithms perform better on multilooked data. The spatial resolution has a minor impact comparing TerraSAR-X's HS mode (pixel size 1 – 2 m<sup>2</sup>) and SM mode (3 – 5 m<sup>2</sup>) since detectors' performance are quite similar. Lowering the resolution further down to  $\approx 70$  m<sup>2</sup> by using Sentinel-1's Interferometric Wide Swath mode brings about reduced target to clutter ratios, lowers the contrast of edges and hampers vessel detection capabilities and decreases the accuracy of vessel identification through delimitation from bigger ships by correct boat size estimation.

The introduced new version of the iDPolRAD aimed at anomalies in surface scattering worked better on the chosen object than the volume detection algorithm but the best results are delivered by the combination of the two iDPolRADs. That enables volume scattering and surface scattering detection at the same time leading to a further improvement of the detection performance for the chosen rubber inflatable. In the comparison with a range of ship detectors those new combinations proved to be best suited for the test-bed data of small rubber inflatables. This is true for detection performance as well as for the computing costs.

For future research, the impact of the scene settings, for instance the vessel's orientation, speed, heading and superstructure should be addressed. The new combinations of the iDPolRAD reach higher AUCs and it seems to be a promising way to go for further research. Since there are several SAR images of a moving vessel, wake detection and MMT techniques could be explored to increase detection rates. Furthermore, the detector testing should be extended to quad-pol data, to different spatial resolutions (favourably between 5 and 10 meters and to other wavelengths such as C-band RADARSAT-2) and to non-calibrated SAR or compact polarisation SAR (e.g. ALOS-2). Finally, in order to extend this to higher sea states, future campaigns should be planned at sea.

### 4.5 Developing Refugee Vessel Detection Capabilities with Polarimetric SAR

For the research work in this section, a second data collection campaign was organised to create a more realistic scenario by simulating passengers on the vessel and combining it with SAR imagery from the ocean. This enabled the analysis of the SAR vessel-detection capabilities for migrant rubber inflatables for a variety of sensor settings and scene parameters, such as the wave height and wave direction. In addition to a polarimetric analysis of the backscattering behaviour of the fully occupied inflatable boat, a benchmark of various known detectors in relation to different influencing parameters is presented. To improve the detection quality, new versions of the iDPolRAD [112] and the combination of detectors ('detector fusion') were tested. The main parts of this section are also available as a journal paper within Remote Sensing, special issue Remote Sensing for Marine Environmental Disaster Response [304].

### 4.5.1 Materials and Methods

#### 4.5.1.1 The Human Scattering Experiment

This initial experiment evaluated which material was best suited to emulate the presence of humans on a rubber inflatable and was sufficiently durable to remain in the vessel on a lake for several months. During the whole campaign, the material properties that influence the scattering behaviour (roughness, shape, water content and dielectric property) must remain constant. A mobile/handheld radar sensor compared the radar backscatter behaviour of a number of different materials with that of humans at X-band and VV polarisation. The experiments involved:

- four volunteers sitting close to each other on the ground of an empty room. The sitting posture most closely resembles the real situation in the migrant inflatable. The data include different arrangements: four people in a row perpendicular to the sensor line of sight (LoS) ('H4×1'), two rows of two people behind each other ('H2×2') and all four people in one column behind each other parallel to the LoS ('H1×4')
- water-soaked clay pebbles, packed in 30 × 40 cm air-tight plastic bags. The bags themselves are invisible to microwaves and the soaked clay pebbles, as they are roundish objects smaller than the wavelength and with a similar water content to the human body and, thus, should appear similar to the uppermost body parts (heads and shoulders). SAR data was taken from bags perpendicular to the LoS ('C2×1'), two bags parallel to the LoS ('C1×2'), two bags sitting on top of each other ('C1×1×2') and two bags stacked with one large bag ( $\approx 30 \times 60$  cm) standing behind them ('C1×1×2+1')
- steel wool clumped to random 20 cm diameter balls to imitate the top layer of passengers in a boat. The acquisitions involved six balls in two rows ('S2×3') and two balls plus four 5 × 10 × 60 cm (h,w,l) steel wool layers not clumped but stretched out in the front ('S2+4')

The dielectric constant  $\epsilon'$  is an important factor during the interaction with electromagnetic waves. For a given shape, the lower the dielectric constant, the higher the backscatter intensity from volume scattering [199]. A very low dielectric constant, such as air or PVC (all dry) renders them almost invisible to microwaves and increases the penetration depth. The dielectric property is a function of the temperature and the microwave frequency and of course the exact composition of the particular material. Dry clay pebbles would be almost invisible to microwaves due to their very low  $\epsilon'$  (Table 4.9). For this reason, the clay pebbles soaked in water were packed in airtight bags in order to maintain a water content similar to that of the human body (approx. 80%) throughout the entire collection campaign.

#### 4. The InflateSAR Campaign

**Table 4.9:** The dielectric properties for a list of materials involved in the detection scenario at 20°C (\* at 37°C) [413]. The value for sea water, given the typical salinity of the Mediterranean Sea, is about 38 g per kilo [414].

Material	Dielectric Constant $\epsilon'$	Loss Tangent $\tan \delta$
Air	1	depends on weather
Blood *	58	0.27
Fat *	5.5	0.21
Muscle *	49	0.33
Nylon	2.4	0.0083
Polyethylene	2.25	-
Water, fresh [27]	80	-
Sea water [116, 117]	$\approx 70$	-
Sea ice [199]	4	0.5
Sandy soil (dry)	2.55	0.0062
Clay bricks	3.7 – 4.5	-
Metals	infinite	-
Plywood	2.5	-

The loss tangent is the relation between the dielectric constant  $\epsilon'$  and the loss factor  $\epsilon''$  and describes the conductivity of a medium:

$$\tan(\delta) = \frac{\epsilon''}{\epsilon'} \quad (4.7)$$

The dielectric permittivity  $\epsilon_c$  is defined as a complex number:

$$\epsilon_c = \epsilon' - i\epsilon'' \quad (4.8)$$

consisting of the dielectric constant (real) and the loss factor (imaginary). The latter describes the electromagnetic loss of a medium. A low electromagnetic loss generally results in an additional contribution from volume scattering [199].

Fresh water has an  $\epsilon'$  similar to blood or muscle tissue, which justifies/explains the use of water-soaked clay pebbles. Steel wool has, as with all magnetic matter, a very high dielectric constant, and its  $\epsilon_c$  is infinite. Due to that and due to its shape, it is expected to behave similarly to human bodies and to have a strong volume backscattering signal.

Figure 4.38 compares the intensity images of all three test cases. The test objects are placed at the same distance from the sensor (y-axis) whereas the x-axis represents the number of pulses. In this case, 65 consecutive pulses were emitted and recorded. The radar return from H2×2 is speckled in time due to movement, and the signal is more spread out since human bodies occupy a wider space along the LoS than the comparably small test objects (Figure 4.38, left). The wall in the background is more clearly visible in the scenarios with clay pebbles and steel wool since the objects used are much smaller than four people, occupy much less space and produce less occlusion (Figure 4.38, centre and right). To evaluate how many sacks are needed, the intensity values of all pulses of the different materials and the humans were summed up within each scenario. The comparison of these backscattering intensities revealed that approximately 90 bags of soaked clay would emulate 80 occupants.

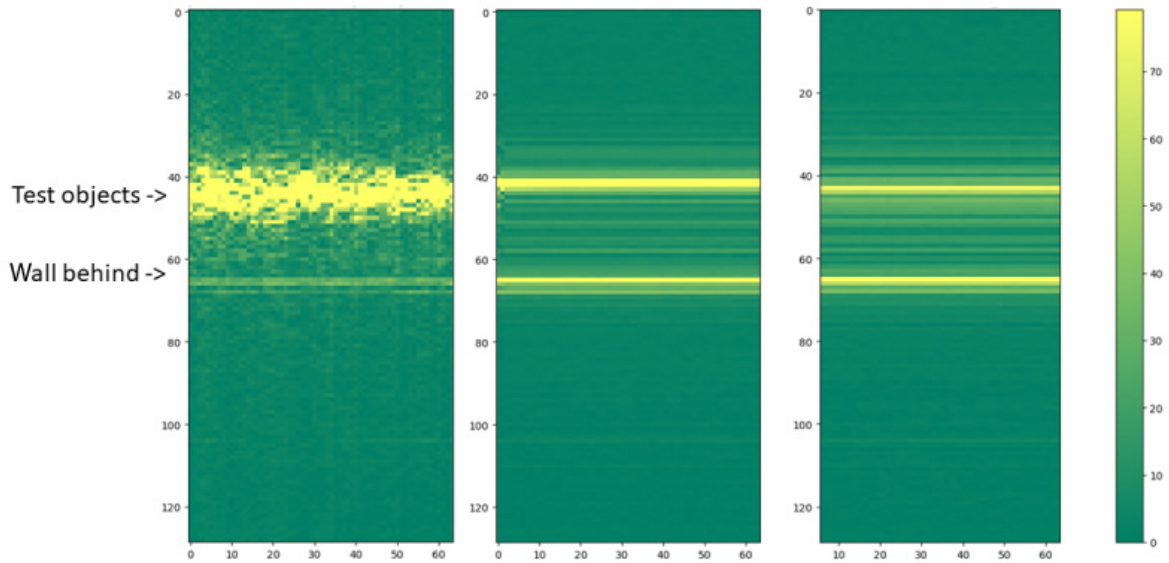
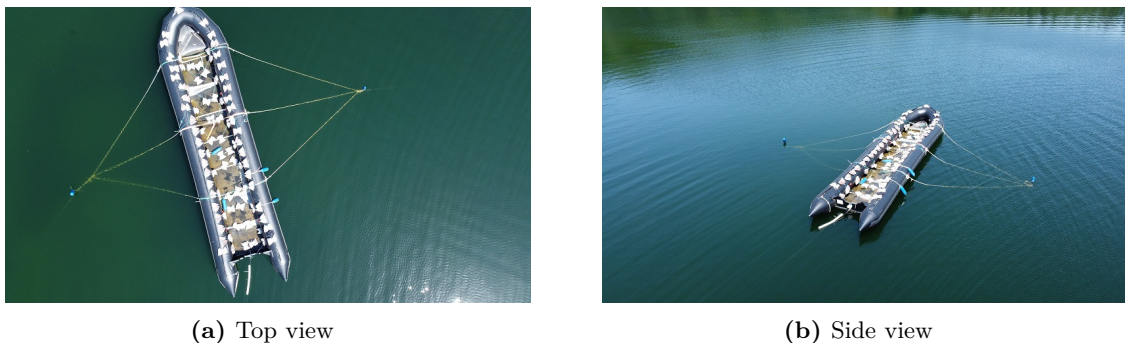


**Figure 4.38:** Example results (in dB) of the human backscattering experiments:  $H2 \times 2$  (left),  $C2 \times 2 \times 2$  (centre) and  $S2 \times 3$  (right). The y-axes show the distance from the sensor in decimetres.

#### 4.5.1.2 Data Campaign and Data Collection

The data campaign was conducted on a small lake in northern Germany in spring 2022. The test object was a  $12 \times 3$  m rubber (1.2 mm PVC) inflatable with a wooden floor and no metal parts at all. Due to its dielectric properties, the boat itself is expected to be hardly visible using microwaves (see Table 4.9; [302]). Finally, the 90 bags of soaked clay pebbles were placed so that they covered the entire surface of the vessel, including the inflated volumes that passengers use to sit on (Figure 4.39).

The bags are expected to leave a similar radar signature compared to a group of 80 people sitting in the boat. First, the bags were expected to simulate the volumetric structure created by many people with their shoulders and heads placed close to each other. Second, the water in the volume-like clay pebbles, preserved over the whole time by air-tight bags, should resemble the water content of the human body. The approach to simulate the backscattering of a human body in different frequencies is supported by similar studies. For example, Ref. [415] used wet sand for Ultra Wide Band (UWB) radar. In the experiment, a stronger intensity signature is expected compared to that of an empty boat (see [303]).



(a) Top view

(b) Side view

**Figure 4.39:** SAR data acquisition setup in the test-bed lake.

#### 4. The InflateSAR Campaign

Thus, prepared, the boat sat on the lake perpendicular to the LoS (in a N–S direction) for the first two months. In a second phase, it was oriented at 45° to the LoS and acquired data for another two months. These two geometries should represent two diametrically different scenarios when it comes to scattering mechanisms. The boat oriented 90° relative to the LoS should generate a strong radar backscattering since it exposes the maximum amount of surfaces facing the LoS and being capable of scattering the EM–waves directly back through double reflections [302]. The boat oriented at 45°, on the other hand, is expected to scatter some of the multiple reflections away from the sensor. This is because the volume scattering expected by the human–equivalent and from the vessel facets (for example in case they are wet) is not fully isotropic.

The data collected comprise full–pol data from CSG, dual–pol Stripmap data in several combinations from TSX and very high–resolution VV–pol data from ICEYE (Table 4.10).

**Table 4.10:** Overview of the data collected for the boat on the lake with 80 simulated people.

Mission	Mode	Average Pixel Size (m <sup>2</sup> )	polarisation	Incidence Angle	Datasets
TerraSAR–X	Stripmap	4.4	Dual–pol: HH VV, HV HH, VH VV	Low, medium and high	46
Cosmo–SkyMed	Spotlight	2.7	Quad–Pol	Medium and high	4
ICEYE	High–res. Spotlight	0.6	Single–Pol: VV	Low and medium	4

The CSG and the TSX data should cover different combinations of sensor and scene setting, such as incidence angle, dual–pol polarisation and the orientation of the boat. This made it possible to analyse the influence of these parameters on the scattering behaviour of the inflatable and on the performance of the detectors.

**Table 4.11:** TSX data parameter matrix of the ‘full’ inflatable on the lake.

	90 Degrees			45 Degrees		
	Low	Medium	High	Low	Medium	High
HH VV	1 (1)	4	3	3 (2)	5	5
HV HH	1	2	2	1 (1)	3	2
VH VV	1	2	1	1 (1)	2	2

Table 4.11 quantifies the available TSX datasets. The categories for the incidence angles are defined as smaller than 28° for ‘low’, from 28° to 43° for ‘medium’ and greater than 43° for ‘high’. The figures list the datasets where an unambiguous identification of the boat on the lake was possible; figures in brackets represent unsuccessful identifications. The reason for the latter was mainly strong Bragg scattering due to low incidence angles. It is called an unambiguous identification when the TCR of at least one of the polarisation channels is larger than three times the clutter standard deviation  $\sigma$  in dB:

$$TCR \geq 3 * \sigma_{clutter} \quad (4.9)$$



where TCR is defined as the ratio between the maximum backscattering of the rubber inflatable and the mean of the backscattering of the local lake clutter. In dB, the ratio has a difference. It is useful to express  $\sigma^0$  in the decibel (dB) scale since it can be statistically modelled with a Gaussian distribution. In linear scale, the fit of a generalised gamma distribution would be much more appropriate and Equ.4.9 would have to be adapted accordingly.

The high variability of the ocean surface due to wind speed, wind direction, swell and other factors has grave implications for its scattering behaviour. The backscattering intensity changes with the water wave height, frequency, form and orientation relative to the LoS of the radar. Moreover, the combination of scattering mechanisms changes with the existence and density of wave features, such as foam or breaking waves [220, 221, 416, 417, 418]. Consequently, higher sea states are expected to hamper the detection task.

Figure 4.40a visualises an example for the increased radar backscattering intensity from 2.1 m waves. On the right, the corresponding detection probability map from the intensity-based cell averaging-constant false alarm rate (CA-CFAR) detector shows how the waves can raise the false positive rate.

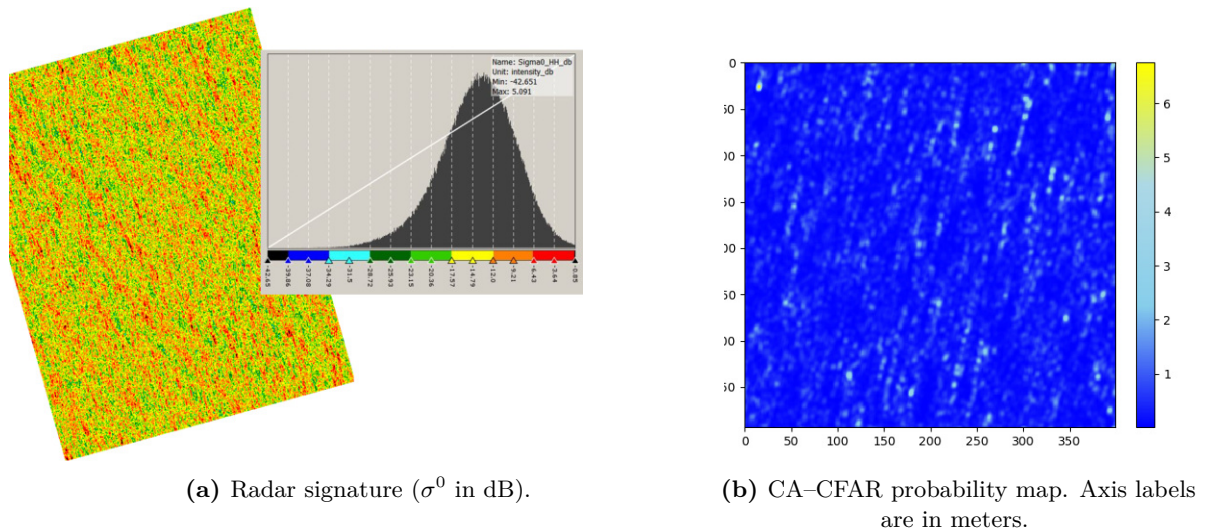


**Figure 4.40:** Radar signature of 2.1 m waves in the up/down direction, HH-pol TSX Stripmap (left) and its implications for the detection task (right) (©DLR 2014).

A collection of SAR data from the ocean was gathered in order to analyse and quantify the influence of the significant wave height  $H_s$  on the performance of the detectors. These ocean data comprise different  $H_s$  for a selection of combinations of wave directions, incidence angles and dual-pol combinations. The collection is categorised by the wave direction (relative to the LoS) in two groups:

- cross-wind waves: these are waves that move perpendicular to the LoS. They move in the direction of the satellite azimuth, which is close to N-S
- up/down-wind waves: here, the waves move in the range direction

The wave direction is — particularly for low wind speed/low waves — an important impact factor for the backscattering behaviour of the water surface (e.g. [205]). The LoS was calculated using the heading of the satellite defined by the azimuth angle, which is  $10.2^\circ$  for TSX. That means a heading of  $349.8^\circ$  for ascending orbits and  $190.1^\circ$  for descending orbits. An average deviation of  $10^\circ$  between the wave direction and the respective directions for up/down wind and cross wind was accepted.

#### 4. The InflateSAR Campaign

The wave direction and  $H_s$  of the TSX–archive datasets were determined with the help of in situ wave–sensor buoys from the Copernicus Marine Environment Monitoring Service In Situ Thematic Assembly Centre (CMEMS In Situ TAC). In fact, only SAR data near in situ buoys for which wave height and wave direction data were available were used. To verify the data, its plausibility was double checked with data from nearby buoys of that network and with estimations from a number of Copernicus wave models covering different ocean areas:

- North Sea: Atlantic–European North–West Shelf–Wave Physics Reanalysis [419]
- Mediterranean Sea and West Gibraltar region: Mediterranean Sea Waves Reanalysis [420]
- Arctic Ocean: Arctic Ocean Wave Hindcast [421]
- all other maritime regions not covered by a high–resolution wave model: Global Ocean Waves Reanalysis WAVERYS [422]

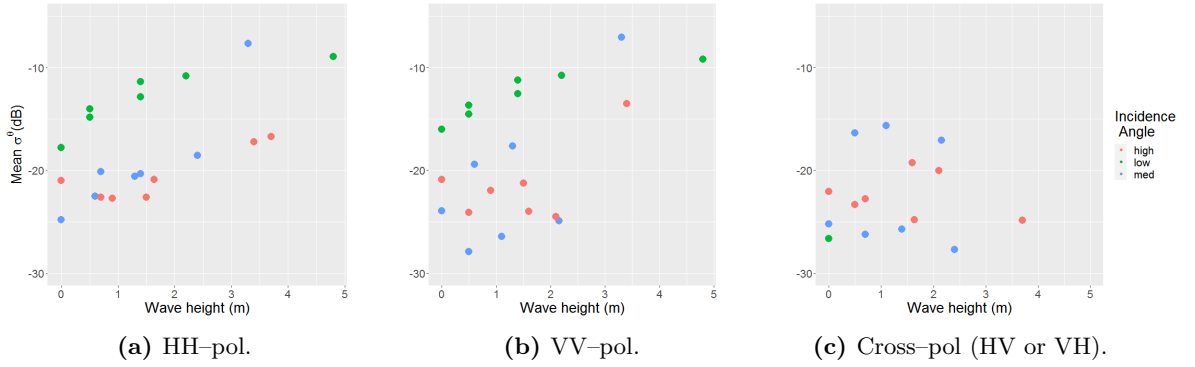
A number of model parameters were extracted and used such as the *sea surface wave significant height* ( $VHM0$  or  $Hm0$  (m)), *significant height of waves*  $H_s$  on the water body ( $VGHS$  (m)) and *average height highest wave* ( $VAVH$ ) for the wave height, *wave principal direction at spectral peak* ( $VPED$ ), *direction from which the waves are coming relative to true north* ( $VDIR$ ), *direction from which the wind is coming relative to true north* ( $WDIR$ ) and the *wave–induced horizontal Eulerian mean current* ( $HCDDT$ ), to determine the main direction of the waves. The latter is useful since the Eulerian mean current is always in the direction of the waves [423].

**Table 4.12:** Collection of TSX dual–pol ocean data, covering different wave directions, wave heights, polarimetric channel combinations and incidence angles.

polarisation Incidence Angle Wave Direction Wave height (m)	HH VV			HV HH		VH VV		
	Low Cross	Low Up/Down	Medium Up/Down	High Up/Down	Medium Up/Down	High Up/Down	Medium Up/Down	High Up/Down
0.4–0.8 (BFT3)	✓	✓	✓	✓	✓	✓	✓	✓
0.8–1.5 (BFT4)	✓	✓	✓	✓	✓		✓	✓
1.5–2.5 (BFT5)		✓			✓	✓	✓	✓
2.5–3.5 (BFT6)			✓	✓				
3.5–4.5 (BFT7)						✓		
4.5–6.5 (BFT8)	✓							

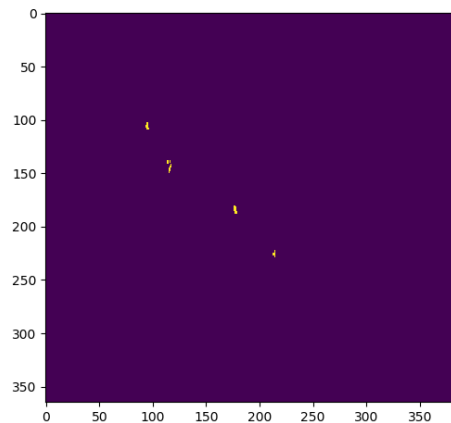
The Beaufort scale (BFT) defines the wave height categories in Table 4.12, and each category corresponds to a specific sea state defined in that scale. This collection enabled the examination the impact of a variety of sea states on the radar backscattering and on the detection task. As Table 4.12 shows, the collection of ocean data was subdivided according to the polarisation, the incidence angle (low, medium and high) and the principal wave direction relative to the LoS (up/down and cross).

Figure 4.41 provides an overview of the collection of TSX archive SAR data of different wave heights and the water surface mean backscattering energy by polarisation. The acquisitions from the lake test bed are included as well ( $H_s = 0$ ). It shows a general trend of stronger backscattering from the water surface with increasing  $H_s$ . Moreover, small incidence angles tend to give very high backscattering intensities due to larger Bragg scattering. In co–pol datasets, VV shows a slightly higher mean intensity value throughout the data collection (HH: –15.5 dB and VV: –14.4 dB). At medium and high incidence angles, the return from the water surface is very low — especially for cross–pol channels.



**Figure 4.41:** TSX dual-pol data collection of different wave heights and their mean backscattering intensity; one diagram for each polarisation.

To facilitate the testing of vessel detector algorithms at different sea states, the pixels of the simulated 'full' inflatable were fused with the datasets showing the ocean. All important sensor parameters (resolution/acquisition mode, incidence angle and polarisation), were considered when replacing the pixels in the images from the ocean with the pixels of the boat. The pixels of the boat on the lake were chosen using an intensity-based approach as described in Formula 4.9. Figure 4.42 shows a ground truth map with four different signatures of the inflatable (yellow) inserted at random positions into the ocean data (purple). This binary mask with yellow pixels represent the 'positive true' case in the following analysis. Again, extra care was taken to only replace pixels where the satellite parameters were similar.



**Figure 4.42:** A  $350 \times 350$  m ground truth map after insertion of the positive true pixels (yellow) of four different acquisitions from the rubber inflatable. Purple pixels represent the ocean surface.

#### 4.5.1.3 Polarimetric Analysis of the Inflatable

Decomposition theorems (DT) provide a physical interpretation of the signals scattered from a target by considering them as a combination of several components. To better understand the scattering mechanisms at the inflatable, quad-pol CSG data was used for a selection of well-known coherent and incoherent polarimetric decompositions as listed in Table 4.13. In this context, the term *coherent* indicates the decomposition of the scattering matrix  $[S]$  (Pauli, Cameron), including the phase information, whereas incoherent decompositions (Yamaguchi, Cloude-Pottier) use the averaging coherency  $[T]$ -matrix or covariance  $[C]$ -matrix [424].

#### 4. The InflateSAR Campaign

The most commonly known coherent model-based decomposition is the Pauli decomposition where the scattering matrix  $[S]$  is the sum of the complex quantities of odd-bounce (e.g. single bounce), even-bounce (e.g. double bounce) and  $45^\circ$  rotated double bounce (see Table 4.13). The Cloude-Pottier decomposition or Entropy/Anisotropy/Alpha decomposition (H/A/ $\bar{\alpha}$ ) [87, 132] proposes the existence of three orthogonal scattering mechanisms. It belongs to the category of eigenvector-based DTs and is especially useful for partial targets. To retrieve its parameters, it is necessary to form the covariance matrix in the Pauli basis.

Working on the assumption of a monostatic system and reciprocity, the Pauli vector is  $k_p = \frac{1}{\sqrt{2}}[HH + VV, HH - VV, 2 * HV]^T$ . This matrix is then called coherency matrix  $[T]$ . In the quad-pol reciprocal scenario, (T) gives three independent scattering mechanisms along its main axis: surface scattering  $T_{11} = \langle k_1 k_1^{*T} \rangle$ , double-bounce scattering  $T_{22} = \langle k_2 k_2^{*T} \rangle$  and volume scattering  $T_{33} = \langle k_3 k_3^{*T} \rangle$ . The three roll-invariant parameters  $H$ ,  $A$  and  $\bar{\alpha}$  can be used to describe the quantitative proportion between the three scattering mechanisms. For the detection task, H was found to be particularly useful.

**Table 4.13:** Polarimetric decompositions and parameters. The Yamaguchi parameters had their orientation removed.

Parameter	Decomposition	Note
Alpha	Cloude-Pottier	
Entropy	Cloude-Pottier	
Single Bounce	Yamaguchi Y4R	
Double Bounce	Yamaguchi Y4R	
Volume Scattering	Yamaguchi Y4R	
Helix Scattering	Yamaguchi Y4R	
Symmetry	Yamaguchi Y4R	Huynen Target Generator A0
Irregularity/Double Bounce	Yamaguchi Y4R	Huynen Target Generator B0-B
Non-symmetry	Yamaguchi Y4R	Huynen Target Generator B0+B
Even bounce	Pauli	HH-VV
Even bounce $45^\circ$ oriented	Pauli	HV
Odd bounce	Pauli	HH+VV
Trihedral	Cameron	
Dipole	Cameron	
Narrow Diplane	Cameron	
Diplane	Cameron	
Left Helix	Cameron	
Right Helix	Cameron	
Cylinder	Cameron	
1/4 Wave Device	Cameron	

The model-based Yamaguchi decomposition [98] added the helix parameter to the Freeman and Durden decomposition [125], adding an asymmetric component to the scattering model. Helix scattering is fully determined by the imaginary part of the  $T_{23}$  element of the coherency matrix. This element is expected to be strong when there is no reflection symmetry, such as in forests or  $45^\circ$  oriented built-up areas.

It is expected to be weak for flat surfaces and parallel built-up areas. Polarimetric reflection symmetry means there is no correlation between the co-pol and the cross-pol channels [286]:

$$\langle S_{HH} S_{HV}^* \rangle = \langle S_{HV} S_{VV}^* \rangle = 0 \quad (4.10)$$

The Cameron decomposition [123] uses the Pauli spin matrices to decompose and to classify  $[S]$  in several steps. The scattering  $[S]$ -matrix is described as the complex sum of these basis matrices. Each of them is associated with one of the elementary scattering mechanisms: single scattering from plane surfaces, diplane scattering from corner reflectors oriented  $45^\circ$  and non-symmetric components. The Cameron decomposition is a multistage procedure.

First, the degree of reciprocity (in Cameron's formula the angle  $\theta$ ) is calculated in order to examine whether the reciprocal components dominate or not by separating the symmetric and non-symmetric parts. For the scattering matrix of reciprocal objects, the elements  $S_{12}$  and  $S_{21}$  are equal. If the reciprocal part is dominant, the reciprocal term is decomposed into symmetric and asymmetric scatterers. Representative  $[S]$ -matrices for asymmetric left and right helices are:

- Left helix:  $S_{hl} = \frac{1}{2} \begin{bmatrix} 1 & i \\ i & -1 \end{bmatrix}$
- Right helix:  $S_{hr} = \frac{1}{2} \begin{bmatrix} 1 & -i \\ -i & -1 \end{bmatrix}$

If the  $[S]$ -matrix exhibits asymmetry, its share of left helix and right helix is calculated. In a final step, if the matrix is symmetric, it is compared to a list of symmetric scatterers.

- Trihedral:  $\frac{1}{\sqrt{2}} \begin{bmatrix} 1 & 0 \\ 0 & 1 \end{bmatrix}$
- Cylinder:  $\frac{1}{\sqrt{5}} \begin{bmatrix} 2 & 0 \\ 0 & 1 \end{bmatrix}$
- Diplane:  $\frac{1}{\sqrt{2}} \begin{bmatrix} 1 & 0 \\ 0 & -1 \end{bmatrix}$
- Narrow diplane:  $\frac{1}{\sqrt{5}} \begin{bmatrix} 2 & 0 \\ 0 & -1 \end{bmatrix}$
- Dipole:  $\begin{bmatrix} 1 & 0 \\ 0 & 0 \end{bmatrix}$
- 1/4 wave device:  $\frac{1}{\sqrt{2}} \begin{bmatrix} 1 & 0 \\ 0 & i \end{bmatrix}$

where, according to Cameron, a symmetric scatterer has an axis of symmetry in the plane of the radar line of sight (LoS).

The Cameron decomposition is a coherent DT, such as, for example, the Krogager decomposition [122]. This group of DTs are particularly useful in the case of one dominant scattering mechanism. Cameron's cylinder and narrow diplane scattering can be composed of trihedral, dihedral and dipole scattering. Together with the quarter wave device, they can be called fundamental scattering mechanisms [425].

#### 4.5.1.4 Detector Comparison and Detector Fusion

Nine different vessel-detection systems (VDS; Table 4.14) algorithms were tested and benchmarked using receiver operating characteristic (ROC) curves. ROC curves are plots of the probability of detection ( $P_D$ ) versus the probability of false alarm ( $P_F$ ). To quantify and compare the results from the ROC curves, their area under the curve (AUC) was estimated and grouped for different wave heights and detectors.

ROC curves are computed by varying the threshold between a minimum and a maximum value depending on the histogram of the detector output. The AUC is a value for the classifier's performance: an AUC of 1 is the best achievable result and means 100% detection with no false alarms. An AUC of 0.5 is obtained for detectors making random choices. All VDS were implemented using a sliding window of a specific size (CUT) with a guard window around it and a training window around the guard window.

#### 4. The InflateSAR Campaign

---

**Table 4.14:** Overview of the vessel detection algorithms being tested and their parameterization.

Detector	Cells Under Test (CUT) Window Size	Guard Window Size	Train Window Size
Polarimetric Symmetry Detector (PolSym)	1	2	5
Polarimetric Notch Filter (PNF)	5	12	36
Polarimetric Entropy Detector (PolEntropy)	2	-	10
Polarimetric Match Filter (PMF)	5	12	36
Intensity Dual-pol Ratio Anomaly Detector (iDPolRAD)	1	12	36
Surface Intensity Dual-pol Ratio Anomaly Detector (SiDPolRAD)	1	12	36
Sublook Correlation Detector (SubCorr)	1	-	36
Polarimetric Whitening Filter (PWF)	5	12	36
Cell Averaging Constant False Alarm Rate (CA-CFAR)	1	24	36

In an initial phase of benchmarking and detector tuning, the best performing parameterization was selected for each detector (Table 4.14). PolEntropy and the SubCorr worked better without a guarding window, so it was removed for these two. The iDPolRAD is actually intended for use as a volume detector and designed to work with the cross-polarisation over co-polarisation ratio [112].

As it has been applied to all available combinations of dual-pol data, including HH VV, it is referred to as PolRatio1 when used with cross-pol data and PolRatio3 when used with co-pol data. The same is true for its surface and double-bounce scattering detecting variant SiDPolRAD [303], which was renamed to PolRatio2 when used with cross-pol data and PolRatio4 when used with co-pol data. For VH VV and HV HH, the two detectors are defined as:

$$PolRatio1 : \frac{\langle |cross-pol|^2 \rangle_{test} - \langle |cross-pol|^2 \rangle_{train}}{\langle |co-pol|^2 \rangle_{train}} * \langle |cross-pol|^2 \rangle_{test} \quad (4.11)$$

$$PolRatio2 : \frac{\langle |co-pol|^2 \rangle_{test} - \langle |co-pol|^2 \rangle_{train}}{\langle |cross-pol|^2 \rangle_{train}} * \langle |co-pol|^2 \rangle_{test} \quad (4.12)$$

Applying those two to the HH VV polarisation combination, they are result in:

$$PolRatio3 : \frac{\langle |HH|^2 \rangle_{test} - \langle |HH|^2 \rangle_{train}}{\langle |VV|^2 \rangle_{train}} * \langle |HH|^2 \rangle_{test} \quad (4.13)$$

$$PolRatio4 : \frac{\langle |VV|^2 \rangle_{test} - \langle |VV|^2 \rangle_{train}}{\langle |HH|^2 \rangle_{train}} * \langle |VV|^2 \rangle_{test} \quad (4.14)$$

A possible physical interpretation for PolRatio3 is 'dihedral scattering' since the HH channel is stronger compared to the VV channel when we have a horizontal dihedral. The interpretation for PolRatio4 is 'Bragg scattering' since VV is stronger than HH in the case of Bragg scattering.

At this stage, it was possible to identify the most promising detectors for each dual-polar combination of polarimetric channels against the background of different wave heights. To improve the detection capabilities for the vessel, different combinations of the top-ranking detectors were tested.

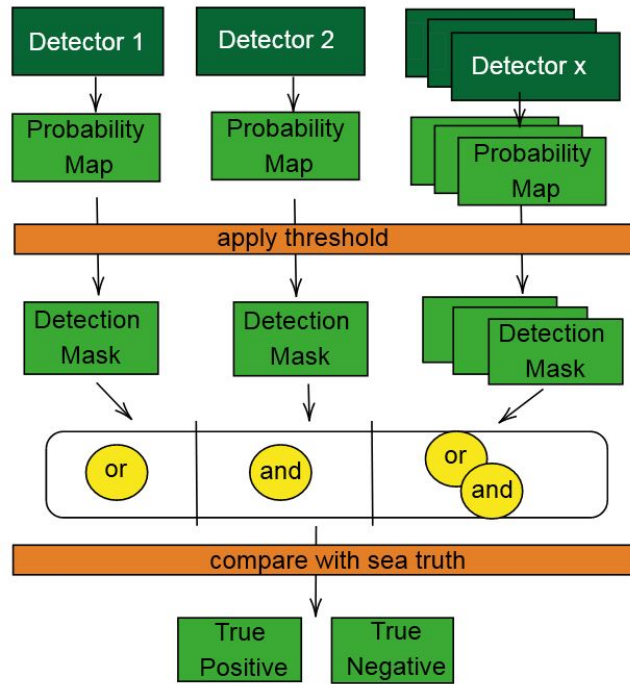


Figure 4.43: Detector melange flow diagram.

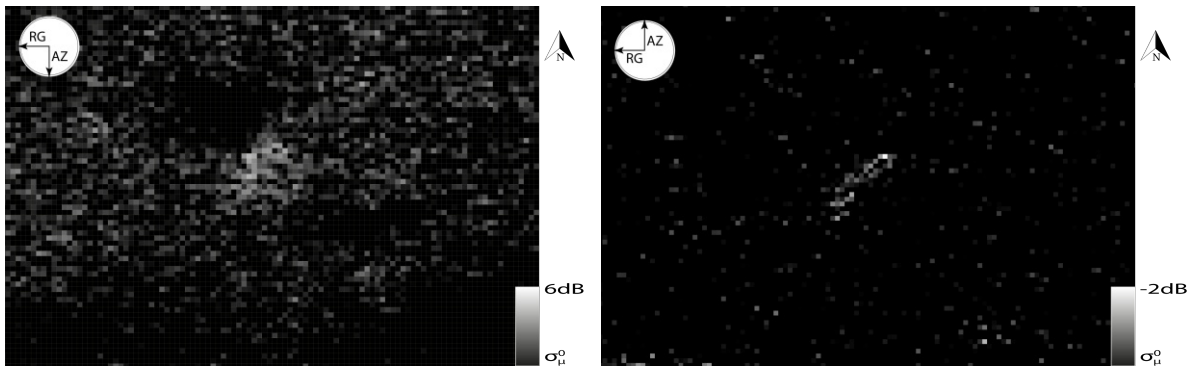
Each detector produces a detection probability map. This map is then classified by applying a threshold to generate the detection mask. This mask is a binary image showing the detector decision at a specific threshold. Each pixel receives either a zero value for 'no boat' or a one value for 'boat detected'. Various combinations of the logical operators 'OR' and 'AND' were tested in order to merge the binary detection masks originating from different detectors (Figure 4.43). Further, detection algorithms that use the intensity and the ratio between the  $T_{11}$  (surface scattering),  $T_{12}$  (compound H- and V-dipoles, [426]) and  $T_{22}$  (double-bounce scattering) elements of the covariance matrix were tested. The double-bounce scattering can come from the side of the inflatable and the passengers inside, which, together with the water surface, form dihedral structures. The term  $T_{22}$  can be expanded as:

$$T_{22} = \frac{1}{2} \langle |S_{HH} - S_{VV}|^2 \rangle = \frac{1}{2} \langle |S_{HH}|^2 \rangle + \frac{1}{2} \langle |S_{VV}|^2 \rangle - \langle \text{Re}\{S_{HH}S_{VV}^*\} \rangle \quad (4.15)$$

In the dihedral scattering, the most significant feature is that the co-polarised components HH and VV are in opposite phase. Therefore,  $T_{22}$  increases to the maximum when the last part of Equation 4.15 becomes smaller than zero.

## 4.5.2 Results

### 4.5.2.1 Qualitative Inspection of High-Resolution Data



(a) Low incidence angle, 45° inclined boat.

(b) Medium incidence angle, 45° inclined boat.

(c) Medium incidence angle, orthogonal boat.

**Figure 4.44:** High-resolution ICEYE VV-pol of the vessel at different scenarios and its mean backscattering intensity with  $\sigma_{\mu}^0$  as the mean backscattering of the lake surface (©ESA 2022).

Figure 4.44 shows the boat with different sensor parameters at a sub-metre resolution of about 0.8 m. These three high-resolution spotlight images from ICEYE single-VV-pol images provide insight into the location and spatial variation of backscattering of the rubber inflatable. All three allow for a good visual identification and a precise size estimation. Strong scattering responses (bright pixels) are almost uniformly spread throughout the vessel. At a low incidence angle (Figure 4.44a), the mean response from the water surface is at about 10 dB and, compared to higher incidence angles, is increased by Bragg scattering. The vessel response is stronger as well; however, that increase is less strong. The wave structure of the water seems to be disturbed by the boat in the southeast — northwest direction, where there are also areas of



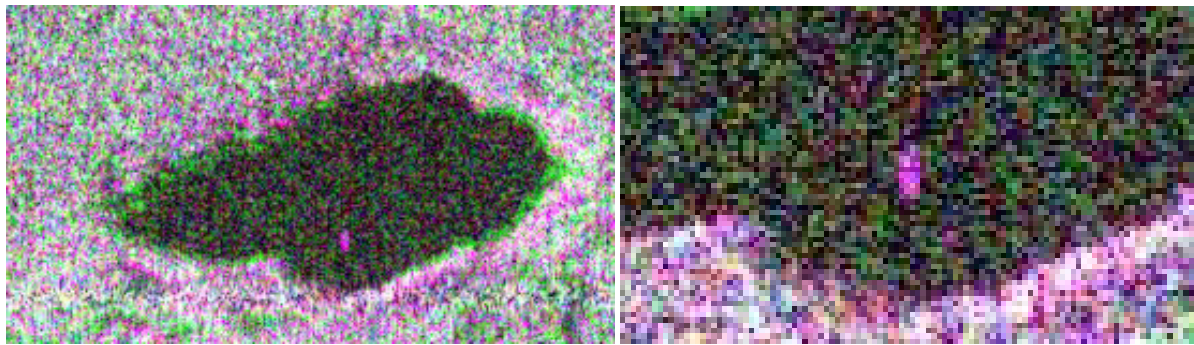
lower backscattering. This theory is backed by recordings from the Deutsche Wetterdienst (DWD) of the wind direction being  $330^\circ$  at the time of acquisition. At medium incidence angles, the mean radar response from the water surface (Figure 4.44b and 4.44c) is around 16 dB, and the TCR is higher. The vessel orientation relative to the LoS is clearly visible.

#### 4.5.2.2 Polarimetric Scattering Analysis

A pixel-wise Pauli RGB image analysis shows that the boat triggers different scattering mechanisms. A relatively small 3x3 window is used for filtering the (C) and (T) matrices in order to maintain the spatial resolution as far as possible. Table 4.15 lists the contributions of scattering mechanisms according to the Pauli decomposition. Double-bounce and single-bounce scattering clearly dominate. Volume scattering plays a minor role across the range of different acquisition parameters and seems to be stronger at low incidence angles.

**Table 4.15:** Pauli scattering mechanisms (dimensionless, comparative quantities, normalized to 0->1).

	Double Bounce	Volume	Single Bounce
low inc. angle, inclined vessel	0.41	0.25	0.41
low inc. angle, orthogonal vessel	0.33	0.17	0.33
medium inc. angle, orthogonal vessel	0.68	0.26	0.73



(a) Pauli RGB from the lake test bed.

(b) Pauli RGB from a section of the lake with the rubber inflatable in the centre.

**Figure 4.45:** Pauli R (double bounce) G (volume scattering) B (single bounce) composites for the orthogonal vessel at a medium incidence angle (©ASI 2022).

The Cloude-Pottier decomposition delivers low entropy at low incidence angles and medium entropy for medium incidence angles (Table 4.16, Figure 4.46). The mean alpha angle varies throughout the three acquisitions, indicating a dominance of surface scattering and double-bounce scattering as well as minor contributions from volume scattering.

#### 4. The InflateSAR Campaign

**Table 4.16:** The results of the Cloude–Pottier decomposition of the inflatable (dimensionless, comparative quantities, normalized to 0->1).

	Double Bounce	Volume	Single Bounce
low inc. angle, inclined vessel	0.41	0.25	0.41
low inc. angle, orthogonal vessel	0.33	0.17	0.33
medium inc. angle, orthogonal vessel	0.68	0.26	0.73

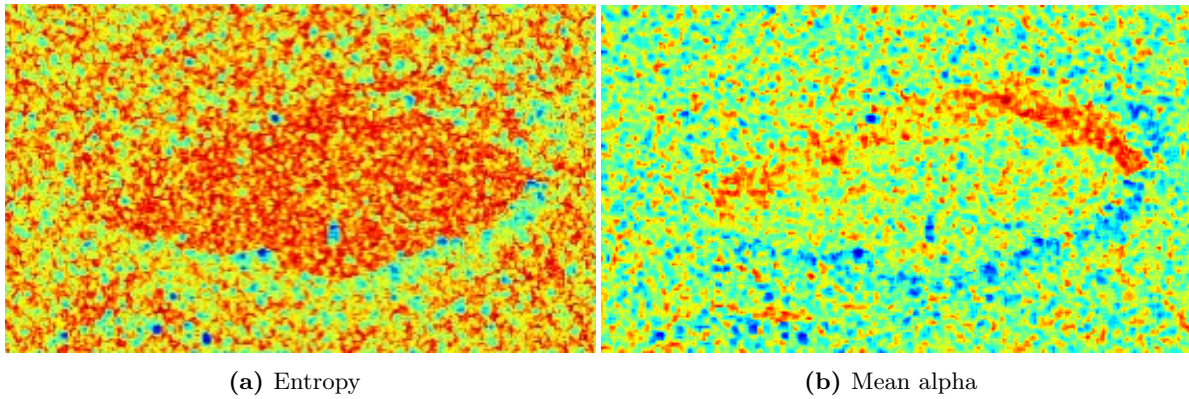


**Figure 4.46:** Cloude–Pottier decomposition results in a scale from red (high) to blue (low) for the orthogonal vessel at a medium incidence angle (©ASI 2022).

The Yamaguchi Y4R decomposition reveals the dominance of single-bounce scattering in the two acquisitions when the vessel was oriented orthogonally (Table 4.17, Figure 4.47). Double-bounce scattering varies to a great extent. Volume and helix scattering do not contribute significantly in any section of the inflatable.

**Table 4.17:** Yamaguchi Y4R decomposition (dimensionless, comparative quantities, normalised to 0->1).

	Helix	Single Bounce	Volume	Double Bounce
Low inc. angle, inclined vessel	0.00	0.07	0.01	0.49
Low inc. angle, orthogonal vessel	0.00	0.48	0.01	0.00
Medium inc. angle, orthogonal vessel	0.00	0.80	0.01	0.39

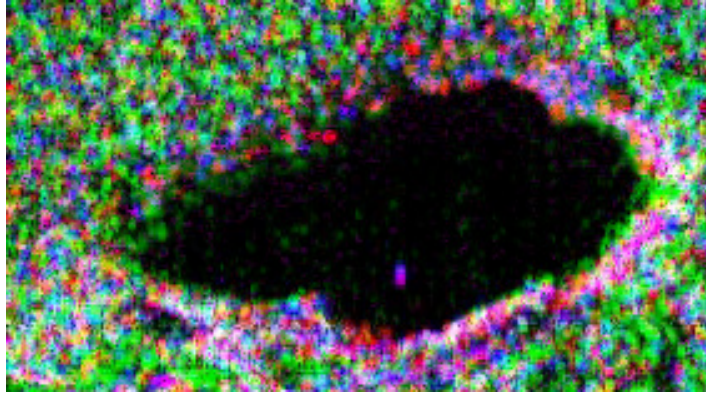


**Figure 4.47:** Yamaguchi Y4R RGB-composite showing symmetric (red), irregular/double-bounce (green) and non-symmetric (blue) scattering of the orthogonal vessel at a medium incidence angle (©ASI 2022).

According to the Cameron decomposition (Table 4.18), the inflatable is dominated by scattering from dipoles with minor contributions from narrow diplanes and scattering from cylinders. It appears that  $\frac{1}{4}$  wave device scattering contributes more at low incidence angles. Trihedral scattering plays a minor role. Asymmetric helix scattering only contributes to a minor extent. There is no direct and simple explanation for the occurrence of these mechanisms; however, they could be related to multiple interactions (in the resolution cell) between the pellet sacks and the water underneath.

**Table 4.18:** Cameron decomposition (dimensionless, comparative quantities, normalised to 0->1).

	Tri- hedral	Di- pole	Narrow Diplane	Di- plane	Cylin- der	1/4 Wave Device	Left Helix	Right Helix
low inc. angle, inclined vessel	0.08	0.47	0.17	0.07	0.26	0.18	0.03	0.01
low inc. angle, orthogonal vessel	0.15	0.53	0.22	0.06	0.11	0.21	0.02	0.01
medium inc. angle, orthogonal vessel	0.06	0.57	0.15	0.06	0.23	0.10	0.00	0.00

All four decompositions show a dominance of surface scattering and double-bounce scattering. Pauli and Cloude-Pottier show that the entropy is at a medium level since, with double-bounce and single-bounce scattering, there are two dominant mechanisms. The result of the Yamaguchi decomposition show an unequal distribution of single-bounce and double-bounce scattering and no double-bounce scattering in one acquisition. This agrees with the Cameron decomposition in showing very little asymmetric helix scattering.

#### 4.5.2.3 Detector Testing

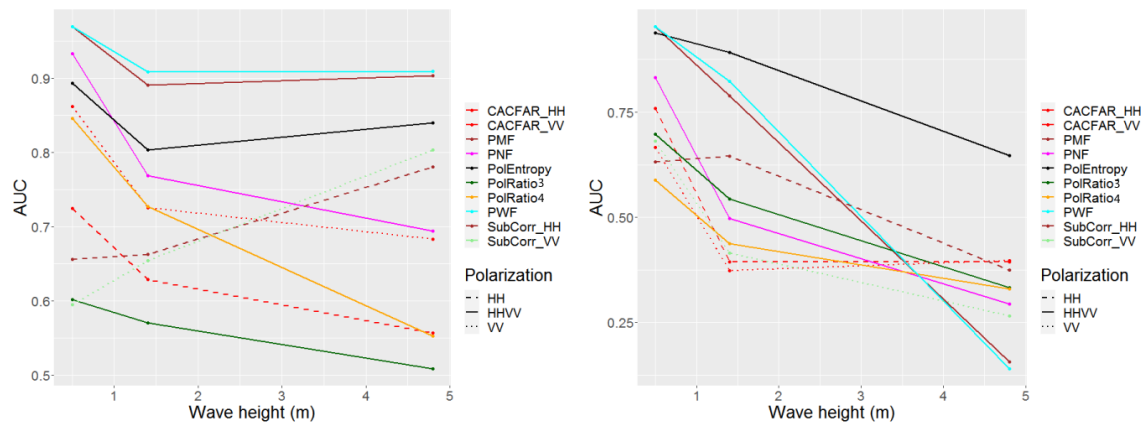
The first results are a comprehensive comparison of the performance of nine detectors for three different categories of incidence angles and three different polarisation channel combinations. For this purpose, the simulated data combining sea and lake observations was used. Figure 4.42 shows an example of a sea truth mask after embedding the boat into the ocean background.

#### 4. The InflateSAR Campaign

The detector testing was done with two different boat orientations and using all the combinations of these sensor parameters with different wave directions and wave heights, according to the availability of ocean data as listed in Table 4.12.

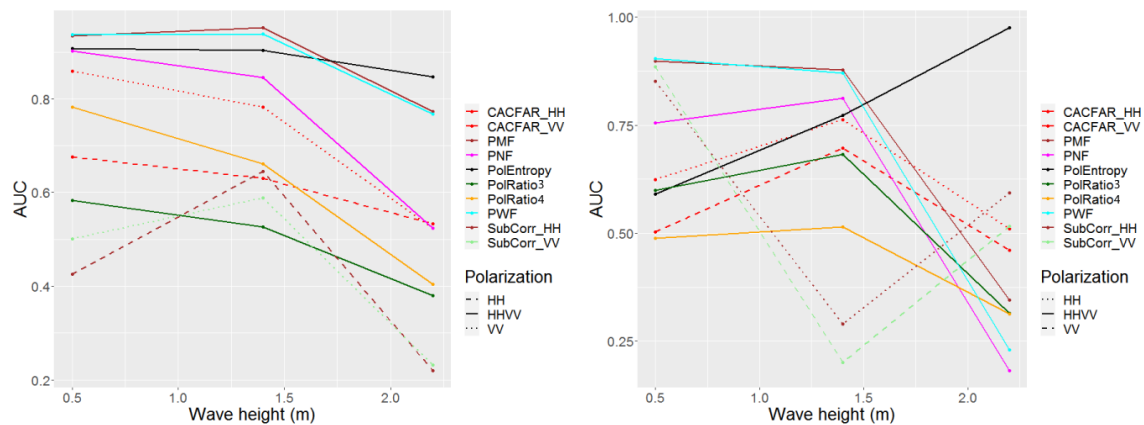
For dual co-pol data, most detectors performed worse with increasing  $H_s$  and decreasing incidence angles. Very interestingly, the PolEntropy had increasing, or at least stable, AUCs for higher sea states. The fact that it searches for high entropy shows that the entropy of the water surface declines with increasing  $H_s$ . This is mostly due to noise floor issues where low sea states produce high entropy backscattering that is close to the noise floor. A high incidence angle can reduce the backscattering even below the noise floor. That is why the PolEntropy detector is the only detector with very low performance at high incidence angles and for calm water surfaces (Figure 4.48g, 4.48h).

The detector performance for HV HH polarisation (Figure 4.49) reveals good and stable performances for most of the detectors at medium incidence angles. The entropy here seems to be less reliable for higher sea states than it is for co-pol data.



(a) Wind: cross, incidence angle: low and boat orientation: 45°.

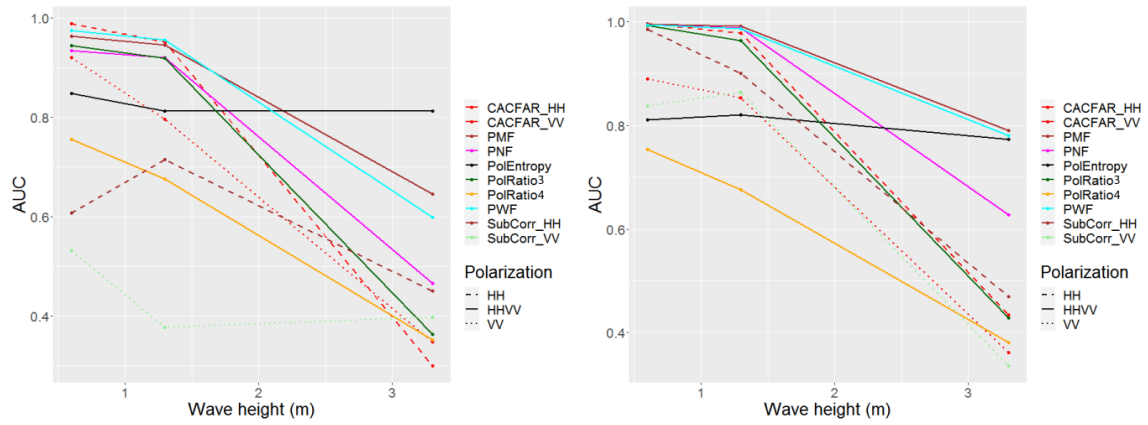
(b) Wind: cross, incidence angle: low and boat orientation: 90°.



(c) Wind: up/down, incidence angle: low and boat orientation: 45°.

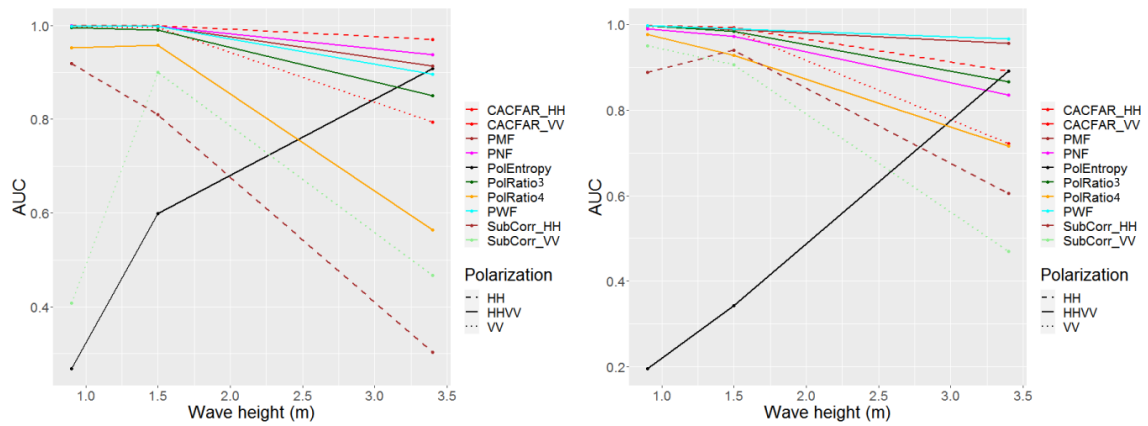
(d) Wind: up/down, incidence angle: low and boat orientation: 90°.

## 4.5 Developing Refugee Vessel Detection Capabilities with Polarimetric SAR



(e) Wind: up/down, incidence angle: medium and boat orientation: 45°.

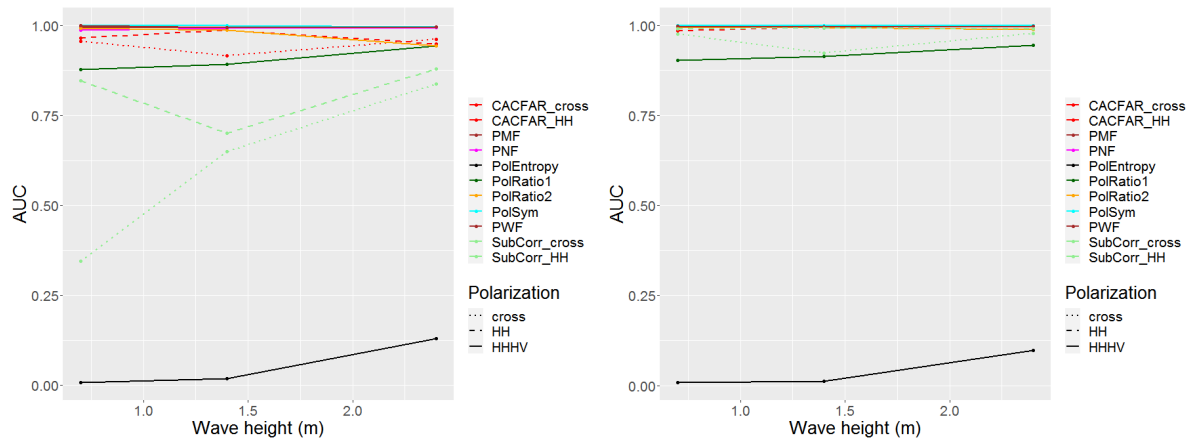
(f) Wind: up/down, incidence angle: medium and boat orientation: 90°.



(g) Wind: up/down, incidence angle: high and boat orientation: 45°.

(h) Wind: up/down, incidence angle: high and boat orientation: 90°.

**Figure 4.48:** Comparison of the detector AUCs for different wave heights for HH VV.



(a) Wind: up/down, incidence angle: medium and boat orientation: 45°.

(b) Wind: up/down, incidence angle: medium and boat orientation: 90°.

#### 4. The InflateSAR Campaign

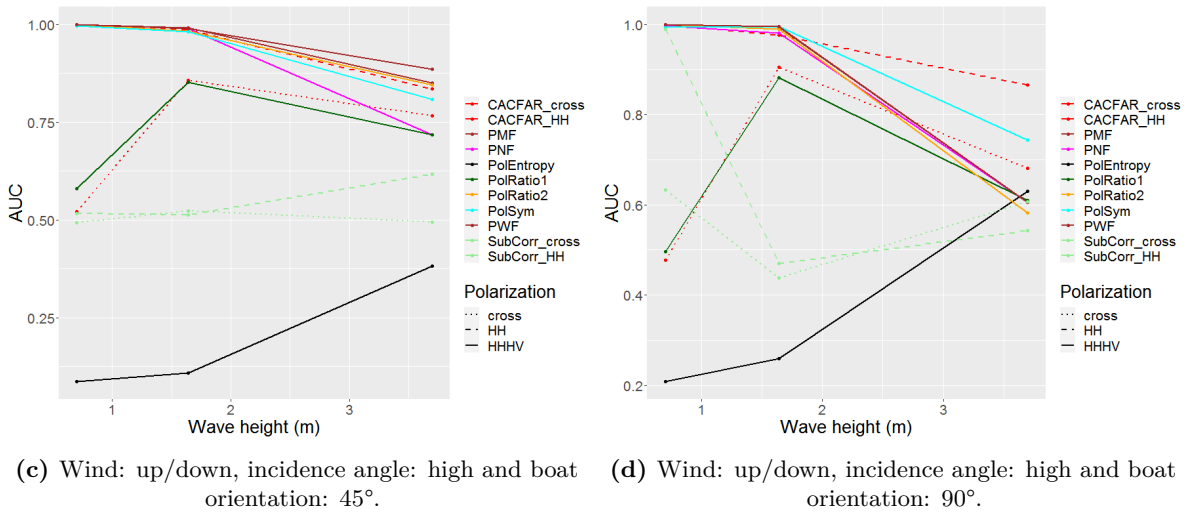


**Figure 4.49:** Comparison of the detector AUCs for different wave height for HV HH.

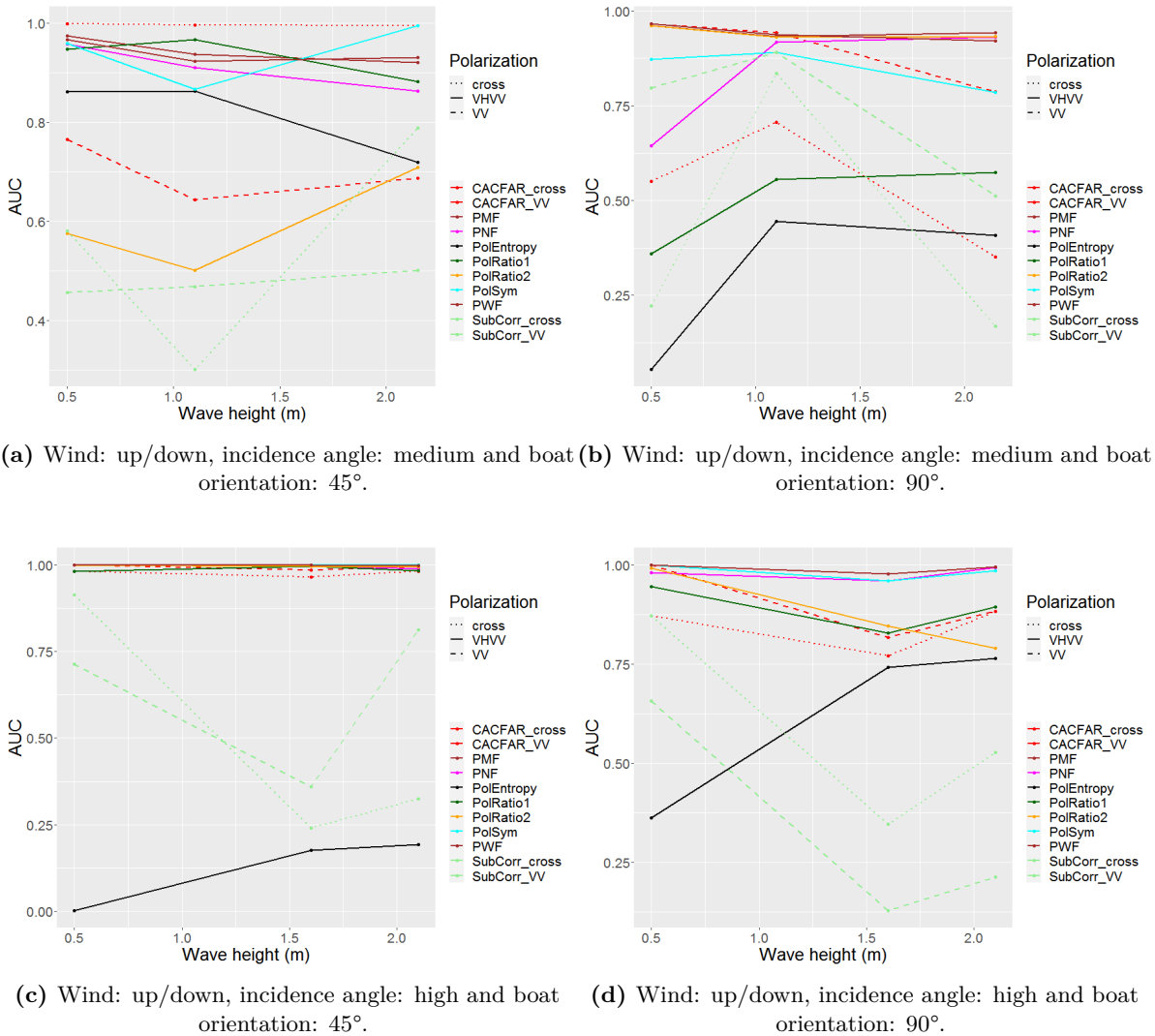


**Figure 4.50:** Comparison of the detector AUCs for different wave heights for VH VV.



In VH VV (Figure 4.50), the detector performance seems to be less dependent on  $H_s$ . The SubCorr and the PolEntropy are not able to match the PWF, the PMF and the PolSym.

Summing up the behaviour of the entropy of the water surface for different polarisations shows that:

- HH VV: the water surface has lower entropy values than the boat except for low sea states and/or high incidence angles
- HV HH: medium angles: the entropy of the water stays higher than that of the boat; high angles: the entropy of water stays higher than that of the boat
- VH VV: the entropy of water is lower than that of the boat

In the following section, one table compares the mean AUCs of all detectors, the next explores the detector performance at higher sea states, and the last visualises the influence of different boat orientations. They also give an indication of the overall influence of the incidence angle and the polarisation.

Table 4.19 compares the overall performance of all detector algorithms. The best detectors, on average, are the PWF, the PMF and the PolSym. Low incidence angles are not a good choice when it comes to maritime object detection, since increased backscattering from the water surface decreases the TCR. Medium and high incidence angles are more useful for detection. The comparison of combinations of polarisations is strongly biased by different sets of wave heights; for example, the category for medium incidence angles in HV HH does not include any data with high waves. The same is true for high incidence angles in VH VV. Nevertheless, we see that all three combinations of polarisation enable detectors to reach high AUCs.

**Table 4.19:** The vessel-detection algorithm AUCs with different sensor parameters.

polarisation Incidence Angle	HH VV			HV HH		VH VV		avg
	Low	Medium	High	Medium	High	Medium	High	
PMF	0.787	0.888	0.976	0.996	0.906	0.945	0.995	<b>0.928</b>
PWF	0.779	0.882	0.975	0.997	0.912	0.941	0.995	<b>0.926</b>
PNF	0.670	0.822	0.956	0.994	0.881	0.871	0.986	<b>0.883</b>
PolEntropy	0.834	0.813	0.534	0.046	0.279	0.559	0.373	<b>0.491</b>
PolRatio1/3	0.529	0.768	0.947	0.913	0.689	0.714	0.939	<b>0.786</b>
PolRatio2/4	0.554	0.599	0.849	0.983	0.900	0.768	0.936	<b>0.799</b>
SubCorr_HH	0.565	0.688	0.744	0.900	0.608			<b>0.701</b>
SubCorr_VV	0.528	0.557	0.684			0.604	0.481	<b>0.571</b>
SubCorr_cross				0.785	0.531	0.483	0.537	<b>0.584</b>
CACFAR_HH	0.600	0.775	0.975	0.980	0.943			<b>0.854</b>
CACFAR_VV	0.628	0.695	0.915			0.798	0.946	<b>0.797</b>
CACFAR_cross				0.972	0.701	0.766	0.909	<b>0.837</b>
PolSym				0.999	0.920	0.895	0.991	<b>0.951</b>
avg	<b>0.647</b>	<b>0.749</b>	<b>0.856</b>	<b>0.869</b>	<b>0.752</b>	<b>0.759</b>	<b>0.826</b>	

As Table 4.20 shows, only results for data with a SPAN greater than  $-17$  dB, it shows that the PMF, the PWF and the PolSym adapt more readily to high sea states. The entropy is more suitable for challenging situations, such as low incidence angles or high seas (high SPAN) at HH VV. For cross-pol, the PolSym seems to be a good choice, and the CACFAR\_HH delivers very good results at high incidence angles. Again, all three combinations enable the detectors to deliver comparably good performances on average. When the SPAN reaches over

#### 4. The InflateSAR Campaign

−5 dB, all detectors except PMF, PWF and entropy fall to a level equivalent to random choice (AUC  $\approx$  0.5).

**Table 4.20:** The vessel detection algorithm AUCs with high sea states (SPAN > −17 dB).

polarisation Incidence Angle	HH VV			HV HH		VH VV		avg
	Low	Medium	High	Medium	High	Medium	High	
PMF	0.787	0.843	0.935		0.728	0.945		<b>0.848</b>
PWF	0.779	0.830	0.932		0.745	0.941		<b>0.846</b>
PNF	0.670	0.750	0.887		0.662	0.871		<b>0.768</b>
PolEntropy	0.834	0.804	0.900		0.506	0.559		<b>0.721</b>
PolRatio1/3	0.529	0.669	0.858		0.664	0.714		<b>0.687</b>
PolRatio2/4	0.554	0.521	0.640		0.714	0.768		<b>0.639</b>
SubCorr_HH	0.565	0.634	0.455		0.580			<b>0.558</b>
SubCorr_VV	0.528	0.494	0.468			0.604		<b>0.523</b>
SubCorr_cross					0.551	0.483		<b>0.517</b>
CACFAR_HH	0.600	0.666	0.931		0.850			<b>0.762</b>
CACFAR_VV	0.628	0.590	0.758			0.798		<b>0.694</b>
CACFAR_cross					0.723	0.766		<b>0.745</b>
PolSym					0.776	0.895		<b>0.835</b>
avg	<b>0.647</b>	<b>0.680</b>	<b>0.776</b>		<b>0.682</b>	<b>0.759</b>		

Table 4.21 shows which detectors and sensor parameters deliver better AUCs for the boat when oriented at 45° (blue) or at 90° (orange) relative to the LoS. In general, the two different experimental setups deliver very comparable results, which backs the theory that the inflatable itself is effectively invisible to microwaves and does not scatter at all. This shows, moreover, that the most dominant scatterers are the passengers whose scattering behaviour is less dependent on the orientation. For low incidence angles in HH VV, the inclined boat is more easily detectable for most detectors. At medium angles, an orthogonal vessel seems to be slightly favourable. At high angles, the boat orientation has no impact at all.

**Table 4.21:** The vessel-detection algorithm AUCs with different orientations of the rubber vessel.

polarisation Incidence Angle	HH VV			HV HH		VH VV		avg
	Low	Medium	High	Medium	High	Medium	High	
PMF	0.23	-0.07	-0.01	0.00	0.08	0.00	0.01	<b>0.03</b>
PWF	0.25	-0.08	-0.02	0.00	0.09	0.00	0.01	<b>0.04</b>
PNF	0.22	-0.10	0.05	-0.01	0.04	0.08	0.02	<b>0.04</b>
PolEntropy	0.06	0.02	0.12	0.01	-0.17	0.51	-0.50	<b>0.01</b>
PolRatio1/3	0.00	-0.05	0.00	-0.02	0.05	0.44	0.10	<b>0.07</b>
PolRatio2/4	0.22	-0.01	-0.05	-0.02	0.09	-0.35	0.12	<b>0.00</b>
SubCorr_HH	0.00	-0.19	-0.13	-0.18	-0.12			<b>-0.13</b>
SubCorr_VV	0.07	-0.24	-0.18			-0.26	0.30	<b>-0.06</b>
SubCorr_cross				-0.35	-0.06	0.15	-0.09	<b>-0.09</b>
CACFAR_HH	0.05	-0.06	0.03	-0.03	-0.01			<b>0.00</b>
CACFAR_VV	0.22	-0.01	0.03			-0.20	0.09	<b>0.03</b>
CACFAR_cross				-0.06	0.03	0.46	0.14	<b>0.14</b>
PolSym				0.00	0.02	0.09	0.02	<b>0.03</b>
avg	<b>0.13</b>	<b>-0.08</b>	<b>-0.02</b>	<b>-0.06</b>	<b>0.00</b>	<b>0.08</b>	<b>0.02</b>	<b>0.01</b>



Detectors that use using the cross-pol element (CACFAR\_cross, PolRatio1) work slightly better with an inclined boat. The PolRatio1 is, when applied to VH VV or HV HH, called iDPolRAD. The SubCorr is the only detector for which an orthogonal vessel is preferable.

4.5.2.4 Detector Fusion

Combining detectors can increase the detection performance. The detector fusion was done for dual-pol cross-pol (VH VV and HV HH) and dual-pol co-pol (HH VV) data separately. In the cross-pol case, the combination of PolRatio1 and PolRatio2 was tested. where the logical operator 'OR' was used and the result is called PolRatioOR. This detector reaches an average AUC of 0.91.

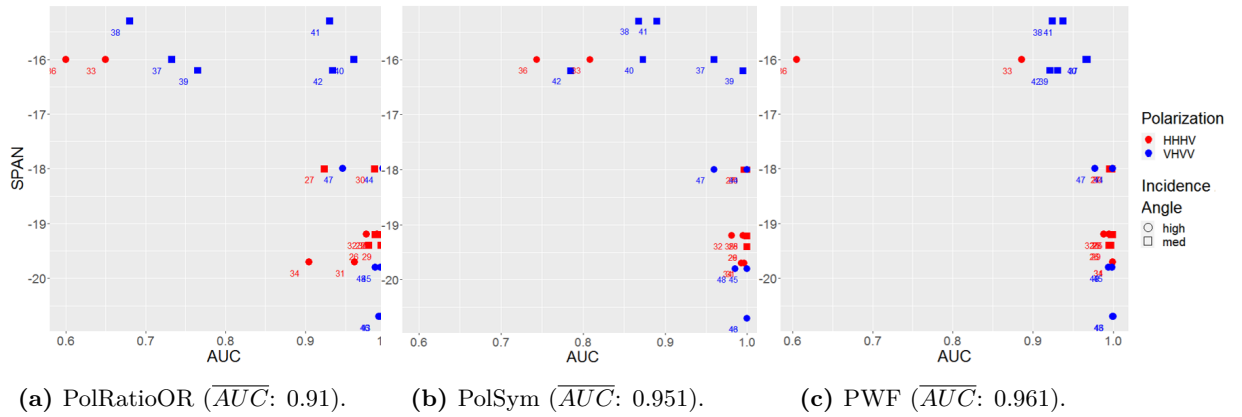


Figure 4.51: Comparison of the mean AUCs for different wave heights at VH VV and HV HH for PolRatioOR, PolSym and PWF.

Thus, this 'surface or volume anomaly detector' approaches the best-performing algorithms PolSym and PWF (Figure 4.51). The PMF reaches similar results such as those of the PWF, and since their mechanisms are quite similar, only the PWF was used for this comparison. To further increase its performance, various combinations of the PolRatioOR, the PolSym, the PWF and the CACFAR were tested but without any further increase in the AUC.

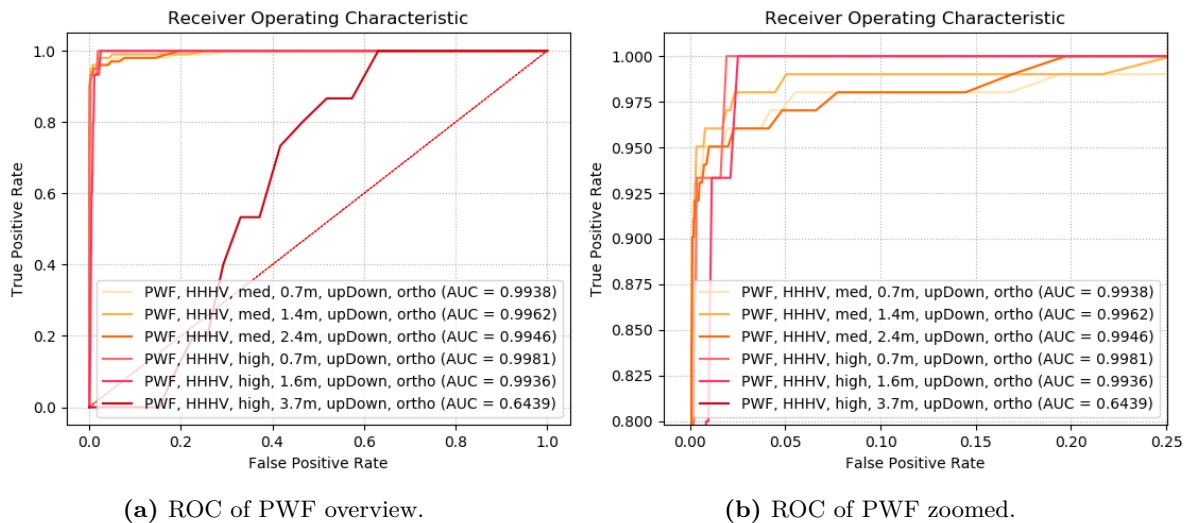
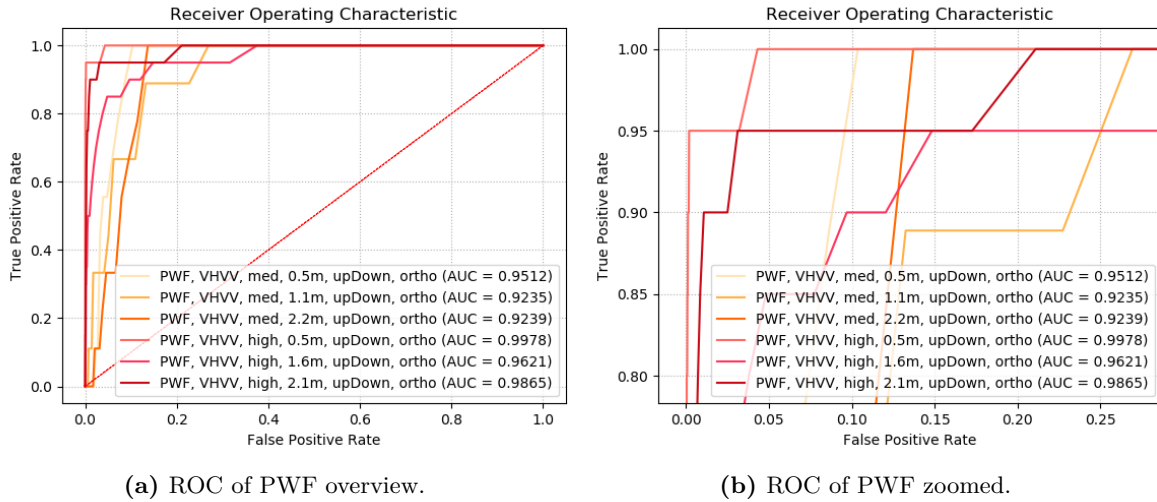


Figure 4.52: ROC curves of the PWF detector for HV HH data with different sea states and the vessel oriented orthogonally to the LoS.

#### 4. The InflateSAR Campaign

The ROC curves for the HV HH dual cross-pol data reveal that wave heights larger than three metres significantly hamper the detection of the inflatable (Figure 4.52). If we only look at acquisitions taken at a medium incidence angle, a  $P_D$  of 90% is possible with a maximum  $P_F$  of 0.11%. These results cover wave heights of up to 2.4 metres or BFT5.



**Figure 4.53:** ROC curves of the PWF detector for VH VV data with different sea states and the vessel oriented orthogonally to the LoS.

The tests with VH VV dual cross-pol imagery give the impression that the PWF delivers better results at high incidence angles (Figure 4.53). Since the results are partly incoherent, it is difficult to express a recommendation regarding the wave height. The best results for the 90% detection rate were found for a wave height of 0.5 metres with a  $P_F$  of 0.12% and for 2.1 metres with a  $P_F$  of 1.07%.

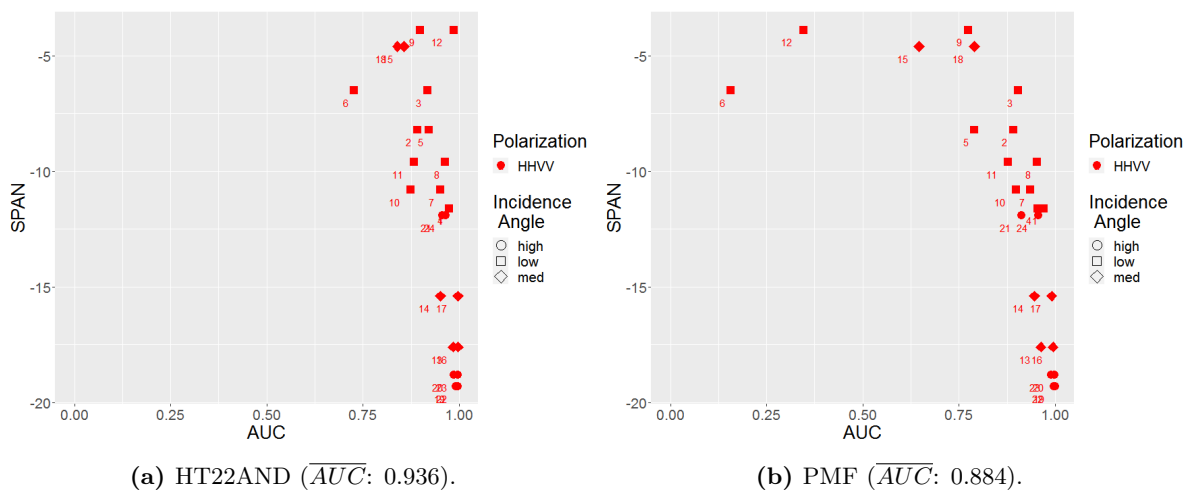


**Figure 4.54:** Comparison of the mean AUCs for different wave heights at HH VV for HT22AND and PMF.

In the co-pol case (HH VV), the combinations of a new double-bounce detector ( $T_{22}$ ), the PolEntropy, the PWF and the CACFAR were examined. Again, the PMF was left out due to its very similar performance results. The  $T_{22}$  yielded an average AUC of 0.914 for HH VV data, thus, making it the best detector — closely ahead of PMF and PWF, each with an AUC of 0.909.

For the co-pol data (HH VV), the combination using the 'AND' operator for  $T_{22}$  and PolEntropy, which is called HT22AND, reached the highest AUC (Figure 4.54). In particular, the results for higher sea states/higher SPANs are promising. This effect can be attributed to the PolEntropy algorithm.

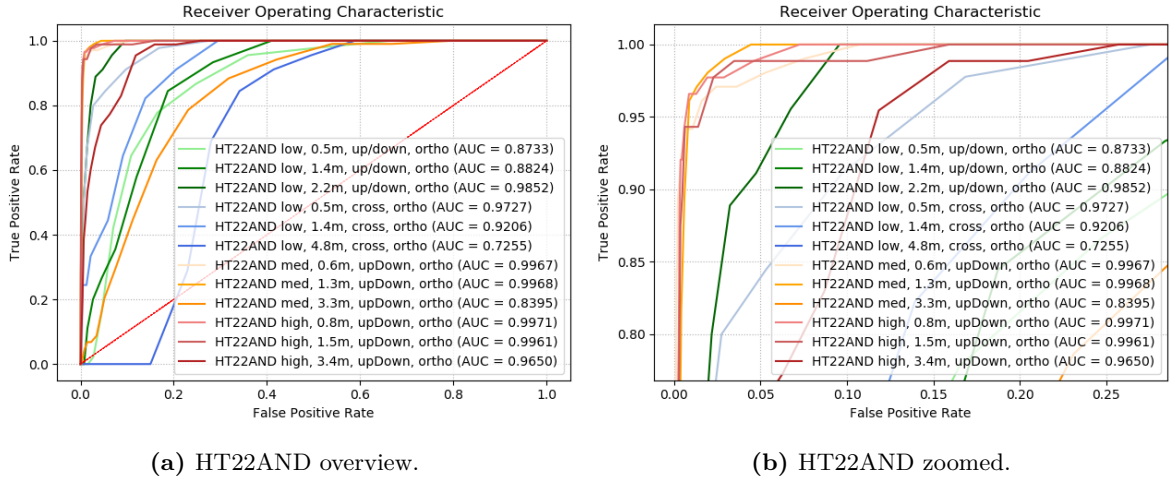


**Figure 4.55:** ROC curves of the HT22AND detector for HH VV data with different sea states and the vessel oriented orthogonally to the LoS.

Figure 4.55a helps to describe the predictive strength of the HT22AND detector. We see very poor detection results at low incidence angles ( $P_F$  20% at a  $P_D$  of 80%). The same is true for wave heights in the range of three metres, with comparably high false alarm rates. If we look at medium and high incidence angles and wave heights below 1.5 m, the HT22AND reaches a  $P_D$  of 90% with a much better  $P_F$  of, at most, 0.59% (Figure 4.55b).

#### 4.5.2.5 Estimation of the Detection Quality

These detection results always include some inherent degree of uncertainty. A metric that gives an estimation of the detection quality would be of great help for the sea rescue teams on the ground. Two appropriate parameters for such a metric would be the estimated vessel size and the TCR. These help with the exclusion of large and strong scatterers, such as large metallic ships. Long high waves could have a TCR similar to the inflatable but could be excluded from the positive true list by virtue of their sheer size. Figure 4.56a shows that the TCR ranges between two and six times the standard deviation of the clutter of the lake. From the TCR, expressed in terms of the standard deviation of the background clutter, a contrast parameter could be calculated (as in [261], called 'significance').

The vessel size estimations in the data range from 30 to 500 m<sup>2</sup> (the true size is 42 m<sup>2</sup>). Low incidence angles seem to increase the overestimation. If only high incidence angles were used, the variation in estimations reduced to between 30 and 180 m<sup>2</sup>. Figure 4.56a further reveals a linear correlation between the TCR and the vessel size estimation. Underlined symbols stand for an orthogonal orientation of the boat, the others mean the boat is inclined at 45°, and the vessel orientation appears to have no significant impact on the detection quality.

#### 4. The InflateSAR Campaign

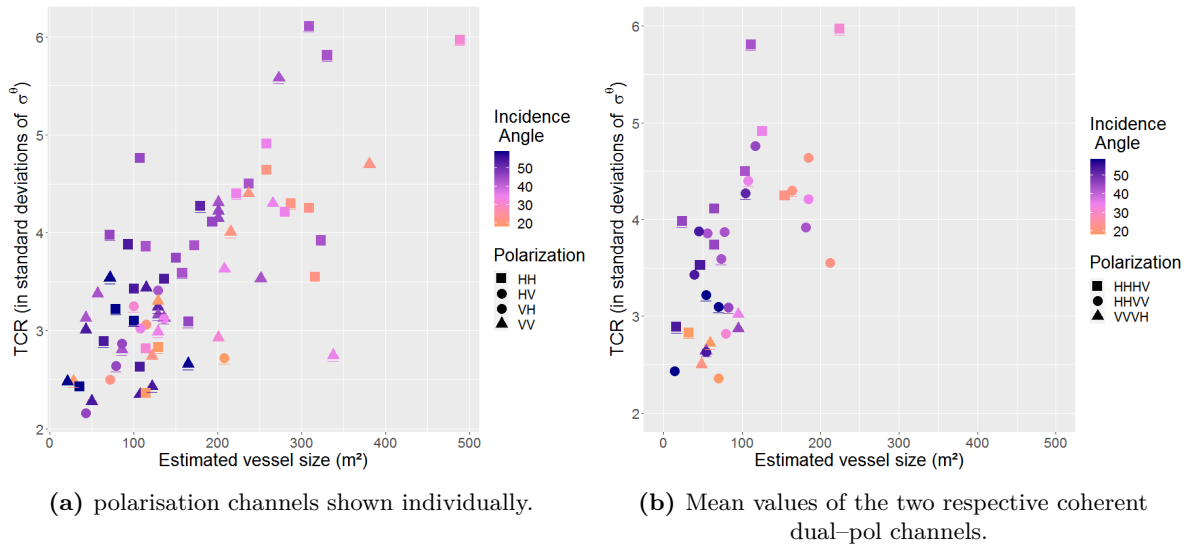


**Figure 4.56:** Detection quality estimation parameters TCR and estimated vessel size on the lake test bed.

The size estimation can be improved by using the mean value of the two dual-pol channels and by the application of a resizing formula from our previous work [302]. Now, the improved size estimations range between 20 and 250  $m^2$ ; for high incidence angles, they stay below 100  $m^2$  (Figure 4.56b). Future work on this could include an analysis of the behaviour of the TCR against the background of different sea states.

# 5

## Discussion and Conclusion

The final chapter tries first to illustrate the results of this thesis considering current research in the field of vessel detection with Synthetic Aperture Radar (SAR). Then follows a general summary of this research and its main findings, followed by a discussion of possible next steps to further enhance the detection capabilities for the special target. The chapter closes with concluding remarks concerning the actual situation of the humanitarian crisis at the European Union's maritime border regions. Parts of this chapter are also available as a journal paper within Remote Sensing [304].

### 5.1 Synthesis in the Context of Existing Literature

The research goal of the automatic detection of small, non-metallic vessels, fully occupied with passengers, represents a special topic in the broader field of ship detection with SAR. Well-known recommendations, which are connected to the radar patterns of the background water surface, could be confirmed with the analyses of the test datasets. Accordingly, it could be confirm that a calm water surface, high incidence angles and HH-pol are generally more suitable for ship detection than high sea states, low incidence angles and VV-pol, since the latter are more affected by clutter and Bragg scattering (e.g. [258, 18, 205, 307, 348, 427]). Further, the quality of the ship detection results depends on the wind speed and the wind direction. The backscattering from the inflatable is assumed to be dependent on the sea state. Especially at rough seas, the surfaces of the vessel will be wetted by foam and spray and the local incidence angle changes constantly according to the wave-induced tilt of the inflatable. The testing of different polarimetric channel combinations revealed that, according to the data and detectors being trialled, co-pol (HH VV) and cross-pol (HV HH and VH VV) channel combinations are similarly well suited and enable comparable detection results — depending on the respective detector algorithm used. The tests with different sea states showed that HH VV and HV HH work better at higher sea states than VH VV. For single-pol data, the co-pol channels are much more favourable than the cross-pol channel.

Due to the lack of comparable data, it was not possible to test the influence of the radar frequency, which has been shown in other studies (e.g. [258, 428, 102, 137]).

The minimal spatial resolution needed is of prime importance and depends on the vessel

size and dielectric properties (e.g. [18]). Using the coarsest resolution possible is important to maximise the swath width and, consequently, maximise the spatial coverage. A number of different acquisition modes were tested such as TerraSAR-X (TSX) Spotlight ( $\approx 1\text{--}2$  m resolution), TSX Stripmap ( $\approx 3\text{--}4$  m resolution) and Sentinel-1 (S1) Interferometric Wide mode ( $\approx 10$  m resolution). Regarding the necessary spatial resolution, this study identified modes such as the TSX Stripmap dual-pol mode as practicable for this detection approach. The inflatable affects at least a small number of pixels in the SAR image and the extra fine mode from RADARSAT-2 could be usable too. The comparison of dual-pol TSX Stripmap mode data and very high resolution imagery from ICEYE ( $\approx 0.25$  m resolution) showed that the maximum target to clutter ratios (TCR) are very similar and mostly independent from the spatial resolution.

Intensity-based detection techniques such as the CA-CFAR have the advantage that only one intensity SAR-image is needed but they are less suitable to detect small, non-metallic objects due to the very small contrast between the ship and its background. Non-metallic vessels, e.g. made of wood or fibreglass have a much smaller Radar Cross Section (RCS) than metal vessels of similar structure and size [128] and are very hard to detect (e.g. [177, 292]). For higher winds, heavy rain and bigger waves, the backscattering intensity from the ocean surface can be even higher than that of small vessels such as refugee rubber inflatables. Ref. [429] experimented with a very small inflatable ( $< 6$  m) and high-resolution X-band and C-band SAR data. Their tests with the detection algorithm Search for Unidentified Maritime Objects (SUMO), which is a CFAR detector, resulted in positive identifications of 30–50% in calm weather conditions. The influence of sea clutter can be reduced by techniques such as spatial filtering [430]. Ref. [382] did experiments with 6–15 m long wooden canoes, equipped with different kinds of corner reflectors to analyse their TCR. They identified the vessel direction as being an important influencing parameter for its detectability; a fact which could confirm for the empty vessel, but not for the full one. Further, they were able to compare the intensity-based vessel identification capabilities of 3 m resolution X-band (TSX, CSG) and C-band (RADARSAT-2) SAR and concluded that X-band delivers a higher TCR; a result that affirms the approach to work mainly with X-band data.

Polarimetric detectors are commonly used for ship detection. For the detection of the small vessel they provided a number of very useful techniques. This research was subject to the limitation of only having access to dual-pol data. Using dual-pol data instead of quad-pol data increases the spatial coverage but reduces the capabilities and the information value of most of the polarimetric detectors. Furthermore, some polarimetric detectors cannot be applied to all dual-pol channel combinations. For the simulated scenario of a fully occupied vessel on the open ocean, the well-known detectors Polarimetric Whitening Filter (PWF) and Polarimetric Match Filter (PMF) (both [264]) perform best with dual cross-pol data. With dual co-pol data, the fusion of the polarimetric entropy detector with the  $T_{22}$  double bounce scattering detector, called HT22AND, achieves the best results. The use of  $T_{22}$  fits very well with SAR ship detection theory which assumes the ship to be dominated by or, at least, have a greater proportion of double bounce scattering (e.g. [268]) compared to the water surface. The HT22AND works in a similar way to the Van-Zyl method [115], which provides information about whether the received signal made an odd or even number of reflections (referred to as bounces), but uses only dual co-pol SAR data [24]. It analyses the occurrence of double bounce scattering (associated with dihedral reflection from structures commonly found on ships) and single bounce scattering (associated with Bragg scattering effects from the ocean) and considers the relative distribution (i.e. the entropy) between these two scattering mechanisms.

There exist a small number of research projects similar to ours. Ref. [431] demonstrates that with Sentinel-2 multi-spectral data, refugee vessel detection is possible in a timely and

consistent manner but may overlook vessels shorter than 20 m. That assessment can be verified by the S1 data from the 12 m long inflatable in section 4.4.3.10. Ref. [432] shows that the S1 SAR data could provide effective results and spatial information on migration routes. The study concentrates on the detection of vessels between 5 m and 30 m in length and uses adaptive thresholding. Ref. [384] uses quad-pol RADARSAR-2 data and a two-parameter constant false alarm rate mechanism with a detector that searches for high ratios between dipole scattering ( $0^\circ$  azimuth angle  $T_{22}$  +  $45^\circ$  azimuth angle  $T_{33}$ ) and surface scattering ( $T_{11}$ ). The study shows good results for small vessels between 8 m and 16 m with RADARSAT-2 Ultrafine mode of about 5 m resolution and is a good example of a possible adaptation of the  $T_{22}$  detector for quad-pol data. Ref. [427] tried to experiment with the identification of different vessel sizes, amongst them vessels smaller than 25 m. They analyse the influence of parameters such as the incidence angle and the wind speed on the detectability of the ships using dual co-pol TSX data. They employ a CFAR with different polarimetric features which they derived from the Kennaugh elements.

Using the Doppler information for small boat detection has been developed using the wavelet transform [261] and different sublook approaches such as the sublook correlation detector [174]. Both can identify the more coherent vessel in the midst of random, incoherent noise and clutter whereas the movement of the boat reduces its coherence and therefore its detectability. Ref. [433] tried to detect 8 – 12 m long fishing vessels, mainly made of fibre reinforced plastics, with L-band PALSAR data. They applied a CFAR to a variety of intensity-based indicators and a Multilook Cross-Correlation (MLCC) detector and concluded that the use of PALSAR data where the size of the ships is comparable with the resolution scale is feasible. The sublook detector yielded good results, but lower detection rates are expected in real scenarios where, in most cases, the refugee inflatables are moving.

Ref. [168] uses the movement of small vessels in a notch filter for CFAR, extended to the dual-channel Along Track Interferometry (ATI) with L-band SAR data. They consider that this method has superior performance to the single channel intensity approaches. Later, Gao et al. combined a method called Oceanic Displaced Phase Center Antenna (ODPCA) for clutter suppression with an ATI-SAR CFAR approach [321]. Here, they used VV-pol data to test the detection capabilities for small sailing boats in different weather conditions. Testing of the single-channel polarimetric notch filter but could not apply ATI methods due to the lack of usable data. Nevertheless, the movement of small vessels is considered to be a very powerful characteristic which can be exploited for detection purposes.

Reflection symmetry has been used as a feature to distinguish between artificial targets and natural environments in ship and vessel detection. (e.g. [267, 88, 434, 100, 381, 102]). The tests with the symmetry detector revealed more about the inflatable scattering behaviour. They showed that, even though there is a small amount of symmetry in the vessel scattering, the water surface generally has, depending on the sea state, in general a much higher degree of symmetry. That corresponds well with the common expectation of a high symmetry in natural scenes and a lower/no symmetry in artificial objects [435].

The entropy (H) is used as a distinguishing factor for ship detection (e.g. [292, 436, 277]). The analysis of the entropy revealed its interesting behaviour with different wind speeds and sea states. The existing literature has a number of basic assumptions which agree with the results:

- for calm wind conditions, the water surface H is higher than that of ships [268]
- the H value of ships is generally larger than that of the sea [437] — the entropy detector was set up based on that assumption

In this approach the spatial resolution had to be preserved as good as possible. Therefore, the degree of spatial averaging was kept relatively low and that gives the entropy a downward bias [278]. It followed the assumption that the impact of that bias on the detection quality is very low, since the bias is true for the water surface and for the vessel as well so that the difference in entropy — and that’s what measured by the entropy detector — is not biased.

### 5.2 Summary

In this project the polarimetric inflatable radar backscattering was analysed, a number of well-known vessel detectors were tested and adapted for the special target and experiments with detector fusion were carried out. To this end, a unique multi-platform SAR dataset from original rubber inflatables was collected in a test-best scenario used in two data acquisition campaigns in 2017 and in 2022. It comprises SAR data from TSX, TanDEM-X (TDX), S1, ICEYE and Cosmo-Skymed Second Generation (CSG).

In the first campaign the vessel was empty during most of the acquisitions; only four times the inflatable was populated with 30 volunteers. This enabled the comparison and analysis of the impact of different scene parameters and sensor parameters on the detection capabilities which gave the opportunity to recommend specific combinations of sensor settings, favourable for the detection quality. The detectors tested include the intensity-based CA-CFAR, one sublook (sublook correlation) approach and six polarimetric-based (Polarimetric Whitening Filter, Polarimetric Match Filter, Polarimetric Notch Filter, entropy detector, symmetry detector and iDPolRAD) algorithms.

In the second campaign, an attempt was made to simulate a more realistic scenario. The ship was prepared in such a way that it appears on the SAR images as being occupied by 80 passengers. For that experiments were conducted with a ground SAR system to identify bags of wet clay pebbles being usable to simulate humans in SAR imagery. During the data acquisition campaign these bags simulated the backscattering of 80 passengers in two different boat orientations (relative to the sensor line of sight) on a small lake. Additionally, a collection of dual co-pol (HH VV) and dual cross-pol (HV HH and VH VV) TSX Stripmap data from the open ocean was created covering a variety of incidence angles, wave heights and wave directions. The two collections were then combined to create a detector testing environment as close as possible to the real situation.

It can be confirm that higher incidence angles are generally more useful for ship detection. Testing two different vessel orientations relative to the radar line of sight revealed no significant impact on the detection of the special target. For dual-pol and HV HH cross-pol data to achieve a 90% probability of detection, the probability of false alarm remains below 1% with wave heights of 1.5–2.5 metres. Above that wave height, the probability rates for false alarms increase sharply. The reason could be that the scattering processes (increased volume and double bounce scattering) from white caps (common at Beaufort (BFT) 5; 2–3 m waves) and from white foam crests (common at BFT6; 3–4 m waves) build a natural limit for the detection of the small rubber inflatable. These results are, to a large extent, in agreement with the estimation in our first paper (see Fig.4.24).

The main hindrance to this research is the lack of real data in the sea; it was not possible to acquire quad-pol imagery from a rubber inflatable, moving along the SAR’s azimuth at a speed of about 10 km/h and occupied by 100 people or more. Therefore, the scattering behaviour of the inflatable and its scattering matrix is not fully known. That lack of real SAR data, holding ground truth of a fully occupied rubber inflatable, and the restricted access to quad-pol data allowed only for shedding some light on the vessel backscattering. Ground



truth SAR data of a moving vessel would additionally be very useful to investigate smearing effects of the boat scattering pattern and displacement effects ('train-off-the-track-effects') on its detectability. The following data was acquired to recreate the real scenario (or come close to it):

- $\approx 45$  single-pol and dual-pol SAR datasets of an empty, non-moving vessel (1<sup>st</sup> campaign)
- two dual-pol acquisitions of an empty, moving vessel (1<sup>st</sup> campaign)
- three single/dual-pol acquisitions from a vessel with 20–30 volunteers (1<sup>st</sup> campaign)
- $\approx 60$  single-pol (ICEYE), dual-pol (TSX) and quad-pol (CSG) datasets from a vessel, simulating 80 passengers (2<sup>nd</sup> campaign)

The greater part of the data collection consists of dual-pol TerraSAR-X data. In addition, single-pol TerraSAR-X data, a small number of images from TanDEM-X, CSG and ICEYE (all X-band) and from S1 (C-band) was collected to answer more specific questions regarding the radar pattern of the inflatable and its detectability.

The initially stated theory of the scattering going on at and around the boat (Fig. 4.4) could be partly confirmed:

- dry, empty boat: should only have single bounce, specular surface scattering and very low backscattering intensity. The test data from the first campaign shows intensity values higher than expected and the second paper also reveals double bounce scattering for which it is difficult to find an explanation or an inversion model
- fully occupied boat: should be high in double bounce, which could be confirmed by the very good performance of the T22 detector with the data of an 'occupied' vessel (from the second campaign) and the polarimetric decompositions (see section 4.5)

The approach of testing and benchmarking different vessel detection algorithms revealed a number of interesting properties of the vessel backscattering pattern:

- intensity-based detector: the rubber inflatable is sufficiently visible in calm water surfaces, even if it is dry and empty
- sublook coherence detector: the inter-look coherence of the vessel is higher than that of the uncorrelated water surface [174]. It can be confirm that for a non-moving vessel. In the real scenario where, in most cases, the inflatables are moving at a speed of about 10 km/h, the inter-look coherence of the vessel is significantly lower than that of a stationary one. That could decrease the usefulness of this approach for detection
- entropy detector: the inflatable seems to show similar entropy when there is very low backscattering from the water surface (no or very little waves and/or high incidence angles). This could be due to the random noise floor becoming the dominant contribution. With increasing backscattering from the ocean, its entropy decreases and the entropy-generated contrast to the vessel increases
- intensity Dual Depolarisation Ratio Anomaly Detector (iDPolRAD) and its variants: this group of detectors, used with dual cross-pol data, reveals that the vessel scattering is dominated by volume and/or multiple scattering and surface scattering. Or, at least, that these scattering mechanisms occur in a significantly different proportion and/or intensity at the vessel compared to the scattering pattern of the water surface
- symmetry detector: there is a small amount of symmetry in the vessel scattering but its symmetry is, in general, lower than that of the water surface. The inflatable's non-symmetric components enable a detection.

The results of the polarimetric decompositions (see chapter 4.5) could confirm these findings. Nevertheless, the results are only valid under a number of assumptions. This approach combines maritime SAR data with a simulated fully occupied inflatable by pasting the vessel pixels

into the ocean background. That enabled this research to create test data that very closely resemble the real situation. The main assumptions in this operation were that

- the resolution was high enough to resolve the boat pixels separately from the ocean to a large extent
- the interactions between the vessel and the water surface (flattening of the water surface below the vessel and those caused by the wind shadow on the lee side) were the same in the simulation and in the real situation
- the wetness of the boat (e.g. salty spray on the inflatable and water inside the boat) were the same in the simulation and in the real situation
- the air-tight freezer bags full of wet clay pebbles produce a similar scattering behaviour to humans. Since these sacks are much smaller in height than the human upper body, more dihedral scattering and a stronger signal from the torsos of the passengers is expected in the real scenario. Therefore, the volume scattering detecting iDPolRAD and the T22 detector are expected to deliver better results in the real scenario
- the wind is a homogeneous phenomenon. In reality, wind streaks or shifting wind directions can occur close to each other in one location. The numerous interactions in the marine atmospheric boundary layer and their impact on the backscattering of the ocean surface were disregarded

As a minor effect, the fact that the rolling of the boat on the ocean (yaw, pitch and roll) induced by waves might change the backscattering of the vessel was neglected. Further, the definition of positive true was achieved using the intensity values. That approach biases all results as it helps the intensity-based detectors to perform better compared to the others.

The backscattering of the ocean waves and its polarimetric properties depend on the angle between the viewing direction and the orientation of the waves [24]. Since only data with wind directions parallel to the SAR's line of sight ('up/down wind') were available, it remained unknown to which extent changes of this angle affect the detectors.

Another noteworthy difference is that in the real situation the refugee vessels are moving, albeit slowly. This movement of the vessel triggers certain interactions with the water surface. Since the database has only SAR imagery of a stationary vessel, its movement could not be used and tested as a detection mechanism. Therefore, maritime moving target indication (MMTI) methods such as along track interferometry (ATI; [296]), which attempt to discriminate non-moving from moving contributions by estimating a velocity-dependent attribute, could be used in the future to improve the effectiveness of migrant boat detection.

The SAR-data collections enabled this research to test existing detectors and to develop new variants that were specifically tailored for fully occupied rubber inflatables. To visualise and compare the detectors' performance the binary classification scheme called Receiver Operator Characteristics (ROC) was used. To quantify and compare the results from the ROC curves, the area under the curve (AUC) was estimated. To further increase the detection capabilities, different combinations of detectors ('detector fusion') were experimented with. For dual cross-pol data, a new combination of the volume-detecting Intensity Dual-polarisation Ratio Anomaly Detector (iDPolRAD) and its surface-detecting variant was tested. It reached an overall AUC of 0.91. For dual co-pol data, the combination of the volume-scattering detector with the polarimetric entropy detector (HT22AND) delivered the best results with an overall AUC of 0.94. The latter is especially interesting, since it seems to be less compromised by high sea states, and this is mainly caused by the polarimetric entropy detector.

A deeper analysis of the best detectors resulted in a better estimation of their capabilities. If the  $P_D$  should be at least 80% and the  $P_F$  should not exceed 1%, the HT22AND (HH VV) works with wave heights of up to 1.5 m and the PWF works with wave heights up to 2.4 m

with HV HH and up to 0.5 m with VH VV.

At a probability of detection  $P_D = 90\%$  the tests showed that:

- with dual cross-pol channel combinations, the polarimetric match filter (PWF) was the best-performing detector
- with HV HH, the PWF had, at medium incidence angles, a probability of false alarm of only  $P_F = 0.12\%$ . The data support the assumption that the PWF can be used up to a maximum wave height of about 2.4 metres
- with VH VV data, the PWF had a maximum false detection rate of 1.07% up to 2.1 m wave height
- for dual co-pol data, the HT22AND was the best detection algorithm with  $P_F = 0.59\%$ . This is true for wave heights of up to 1.5 m and medium or high incidence angles

The polarimetric match filter (PMF) delivered equivalent results to those of the PWF throughout all the test data. Although the false alarm rates presented here are not yet good enough to support an efficient detection system for high sea states, the study builds a basis for further research and development.

## 5.3 Outlook

Future work could focus on testing the influence of the spatial resolution of the SAR data on the different detectors that were proposed. Further, different SAR frequencies (e.g. L-band and C-band) should be added to the test dataset. The method used to generating the ground truth masks may be improved by exploiting more detectors. The collection of real polarimetric SAR data from a fully occupied refugee inflatable would enable this research to identify the target scattering matrix. This data collection should cover the vessel both moving and stationary, with different orientations, different incidence angles and different wave heights/sea state conditions. The detectors presented here would gain more confidence if it was possible to test them against data with real sea truth obtained from refugee boats.

More ways to improve the detection performance could be:

- the introduction of filtering of the detected objects by size (see section 4.5.2.5)
- the false alarm rate could be lowered with the help of filters that exclude single pixels as well as very large and very bright false detections
- the implementation of an a-priori wind field estimation to enable more informed choices about which detector(s) to use and to better interpret the detection results
- satellite sensor synergy with optical remote sensing data could be helpful to identify inflatables and deliver ground truth for SAR-based detections add information from other sensors/systems such as the Automatic Identification System (AIS)

The impact of the direction of the local wind and the waves relative to the LoS on the polarimetry and the backscattering intensity of the water surface is well-known. Since it was only possible to collect ocean data with up/down wind, future research in this field should embrace data with different wind directions.

The availability of training data permitting machine learning techniques such as support vector machines or random forest could be used for tasks such as finding the best combination of detectors for detector fusion. Deep learning is at the moment out of reach for inflatable refugee vessels of that type due to its large data requirements.

Furthermore, techniques and approaches which try to make use of micro Doppler (e.g. emitted by the vibration of the outboard engine) such as micro-motion target indication should be tested in the future (e.g. [438]). The movement of the vessel can be explored with maritime moving target indication (MMTI) techniques such as space–time adaptive processing (STAP; e.g. [439]).

### 5.4 Concluding Remarks

According to the envisioned early warning architecture (Fig. 1.5), affordable and fast accessible satellite–based SAR imagery with the shortest possible revisit time and sufficient spatial resolution (e.g. Stripmap mode) is essential. The combined use of different SAR constellations can help to achieve a more persistent temporal coverage. Based on the current situation in the central Mediterranean, the search and rescue zone (i.e. the zone where refugee vessels in distress can be found), is currently about 450 km in North-South and about 350 km in East-West direction. This vast spatial expanse means that a satellite–based approach is appropriate but still costly. The current development gives hope that the increase in satellite–based SAR missions in both the agency sector and the private sector will result in more widely–available and more affordable SAR data.

The humanitarian crisis at the southern European borders is severe and costs human lives almost every day. The general public in Europe became more aware of this situation in 2015, but it has persisted for at least 20 years now. In recent years, it spread to the Aegean Sea and later to the British Channel. Anthropologically generated climate change and its consequences are very likely a strong driving force for migration, expulsion and the flight of millions in the near future. Especially in regions where it has its greatest and most immediate impact, such as the Sahel zone where desertification is accelerating.

To stop migrants and refugees from encountering distress at sea and from drowning, this work explored SAR’s potential for detecting the small rubber inflatables which are most often used to cross the Mediterranean Sea. It is an appeal to the international community to recognise the situation at Europe’s maritime borders as a humanitarian disaster. That could pave the way to release funds to continuously acquire satellite–based SAR data and to facilitate the monitoring of the main search and rescue areas. The proposed refugee vessel detection system is intended to assist search and rescue assets on the ground in their search for people in distress at sea. Further, it would act as a monitoring tool to ensure that other (local) actors are willing and able to implement human rights laws. The International Convention on Maritime Search and Rescue, the UN charter, the European Convention on Human Rights, the Geneva Refugee Convention, European laws such as the European Charter of Fundamental Rights and national right of the ships’ flag state are all in place and provide an adequate legal framework for the rescue of people in distress and their transfer to a safe port.

For many years, the European Union has failed to organise search and rescue missions and to uphold, respect and observe basic human rights and the fundamental freedoms of migrants and refugees along its southern maritime borders. Quite on the contrary, the EU supports the so called ‘Libyan Coast Guard’ and supplies it with ships and equipment. This organisation regularly commits refoulement<sup>1</sup> and push–backs by intercepting migrant vessels and forcefully returning migrants and refugees to Libya. Furthermore, EU member states obstruct and hinder

---

<sup>1</sup>non–refoulement is a fundamental principle of international law that forbids a country receiving asylum seekers to return them to a country in which they would be in probable danger of persecution based on ‘race, religion, nationality, membership of a particular social group or political opinion’

NGOs who take up governmental responsibilities such as Search and Rescue operations. They do it by blocking their ports for rescue ships when they are searching for a safe port for refugees which they just rescued from distress. Another tactic is to confiscate rescue ships on specious grounds and to criminalise the act of saving lives of people in distress at sea. A new law from the 24<sup>th</sup> of February 2023, the Italian government decided to limit search and rescue missions by NGOs to just one rescue operation per mission and to force them on multiple-day journeys by opening up only ports which are further north. This wastes the NGO assets' precious time which is then no longer available for search and rescue activities, leads to a higher death toll — a fact confirmed by the latest current statistics from 2023. This dire situation gave rise to the birth of the InflateSAR campaign and its desire to support these NGOs on the ground in their difficult task of finding small refugee vessels in distress at sea.



# Bibliography

- [1] UN-SPIDER. *Risks and Disasters | UN-SPIDER Knowledge Portal*. June 2023. URL: <https://www.un-spider.org/risks-and-disasters> (visited on 06/26/2023).
- [2] Philippe Fargues and Sara Bonfanti. “When the Best Option Is a Leaky Boat: Why Migrants Risk Their Lives Crossing the Mediterranean and What Europe Is Doing about It.” In: (2014), p. 16.
- [3] IOM. *Missing Migrants Project*. 2023. URL: <https://missingmigrants.iom.int/region/mediterranean> (visited on 03/19/2023).
- [4] IOM. *Displacement Tracking Matrix*. 2023. URL: <https://dtm.iom.int/europe/arrivals> (visited on 03/19/2023).
- [5] UNHCR. *Mediterranean Situation*. 2023. URL: <https://data.unhcr.org/en/situations/mediterranean> (visited on 03/19/2023).
- [6] Elias Bierdel. *Ende Einer Rettungsfahrt: Das Flüchtlingsdrama Der Cap Anamur*. Liebe, 2006.
- [7] Paolo Cuttitta. “Repoliticization Through Search and Rescue? Humanitarian NGOs and Migration Management in the Central Mediterranean”. In: *Geopolitics* 23.3 (July 3, 2018), pp. 632–660.
- [8] Matt Wood and Matthew Flinders. “Rethinking Depoliticisation: Beyond the Governmental”. In: *Policy & Politics* 42.2 (Apr. 2014), pp. 151–170.
- [9] Didier Fassin. *Humanitarian Reason: A Moral History of the Present*. Univ of California Press, 2011.
- [10] Michael N. Barnett. “Humanitarian Governance”. In: *Annual Review of Political Science* 16.1 (May 11, 2013), pp. 379–398.
- [11] Silja Klepp. *Europa zwischen Grenzkontrolle und Flüchtlingsschutz: eine Ethnographie der Seegrenze auf dem Mittelmeer*. Kultur und soziale Praxis = Culture and social practice. Bielefeld: Transcript, 2011. 424 pp.
- [12] Silja Klepp. “A Contested Asylum System: The European Union between Refugee Protection and Border Control in the Mediterranean Sea”. In: *European journal of migration and law* 12.1 (2010), pp. 1–21.
- [13] Julia Schulze Wessel. *Grenzfiguren-Zur Politischen Theorie Des Flüchtlings*. transcript-Verlag, 2017.
- [14] Brian Tomaszewski et al. “Geographic Information Systems for Disaster Response: A Review”. In: *Journal of Homeland Security and Emergency Management* 12.3 (Jan. 1, 2015).
- [15] Xianwei Wang and Hongjie Xie. “A Review on Applications of Remote Sensing and Geographic Information Systems (GIS) in Water Resources and Flood Risk Management”. In: *Water* 10.5 (May 7, 2018), p. 608.

## BIBLIOGRAPHY

---

- [16] Brian Tomaszewski. *Geographic Information Systems (GIS) for Disaster Management*. 2nd ed. New York: Routledge, Oct. 28, 2020. 482 pp.
- [17] Armando Marino. *A New Target Detector Based on Geometrical Perturbation Filters for Polarimetric Synthetic Aperture Radar (POL-SAR)*. Berlin, Heidelberg: Springer Berlin Heidelberg, 2012.
- [18] David J Crisp. *The State-of-the-Art in Ship Detection in Synthetic Aperture Radar Imagery*. Edinburgh, S.A., Australia, May 2004: Intell., Surveillance and Reconnaissance Div., Inf. Sci. Lab., Def., Sci. Technol. Org., 2004, p. 136.
- [19] Jakob J. Van Zyl. *Synthetic Aperture Radar Polarimetry*. Vol. 2. John Wiley & Sons, 2011.
- [20] Carl Wiley. “Synthetic Aperture Radars”. In: *IEEE Transactions on Aerospace and Electronic Systems* AES-21.3 (May 1985), pp. 440–443.
- [21] Fotios Stathopoulos, Christoph Lenzen, and Falk Mrowka. “Adapting the Battery Model in the Mission Planning System of Ageing Satellites”. In: *2018 SpaceOps Conference*. 2018 SpaceOps Conference. Marseille, France: American Institute of Aeronautics and Astronautics, May 28, 2018.
- [22] C. Lenzen. *Implementation of Power and Thermal Constraints in Mission Planning*. TD-MOS-TN-3043, GSOC, DLR, Project internal document, 2010.
- [23] S.R. Cloude. “Lie Groups in Electromagnetic Wave Propagation and Scattering”. In: *Journal of Electromagnetic Waves and Applications* 6.7 (Jan. 1, 1992), pp. 947–974.
- [24] Iain H Woodhouse. *Introduction to Microwave Remote Sensing*. CRC press, 2005.
- [25] Jullis Adams Stratton. *Electromagnetic Theory*. New York: McGraw-Hill, 1941.
- [26] ESA. *Satellite Frequency Bands*. 2022. URL: [https://www.esa.int/Applications/Telecommunications\\_Integrated\\_Applications/Satellite\\_frequency\\_bands](https://www.esa.int/Applications/Telecommunications_Integrated_Applications/Satellite_frequency_bands) (visited on 09/21/2022).
- [27] Jakob J. Van Zyl, Motofumi Aarii, and Yunjin Kim. “Model-Based Decomposition of Polarimetric SAR Covariance Matrices Constrained for Nonnegative Eigenvalues”. In: *IEEE Transactions on Geoscience and Remote Sensing* 49.9 (2011), pp. 3452–3459.
- [28] J. A. Johannessen and F. Collard. “SAR Instrument Principles and Processing”. In: *3rd ESA Advanced Training on Ocean Remote Sensing, Cork, Ireland* (2013).
- [29] Robert M. O’Donnell. “Introduction to Radar Systems”. In: *Massachusetts Institute of Technology: MIT OpenCourseWare, Primavera* (2007).
- [30] Floyd M. Henderson and Anthony J. Lewis. *Principles and Applications of Imaging Radar. Manual of Remote Sensing, Volume 2*. John Wiley and sons, 1998.
- [31] John A. Richards. *Remote Sensing with Imaging Radar*. Signals and Communication Technology. Berlin, Heidelberg: Springer Berlin Heidelberg, 2009.
- [32] Bassem R Mahafza. “Chapter 12: Synthetic Aperture Radar”. In: 2000, p. 29.
- [33] Cristian J. Silva-Perez. “Crop Development Monitoring from Synthetic Aperture Radar (SAR) Imagery”. In: (2021).
- [34] John C Curlander and Robert N McDonough. *Synthetic Aperture Radar*. John Wiley & Sons New York, NY, USA, 1991.
- [35] Ian G Cumming and Frank H Wong. *Digital Processing of Synthetic Aperture Radar Data*. Vol. 1. 2005.
- [36] Maria J. Sanjuan-Ferrer. “Detection of Coherent Scatterers in SAR Data: Algorithms and Applications”. ETH Zurich, 2013.



- [37] Bu-Chin Wang. *Digital Signal Processing Techniques and Applications in Radar Image Processing*. Vol. 91. John Wiley & Sons, 2008.
- [38] M. Y. Bhanumurthy and Y. Mallikarjuna Reddy. “SAR Data Processing with Range Cell Migration”. In: *International Journal of Engineering Science and Technology* 3.1 (2011).
- [39] Giorgio Franceschetti and Riccardo Lanari. *Synthetic Aperture Radar Processing*. CRC press, 1999.
- [40] John R. Klauder et al. “The Theory and Design of Chirp Radars”. In: *Bell System Technical Journal* 39.4 (1960), pp. 745–808.
- [41] Chris Oliver and Shaun Quegan. *Understanding Synthetic Aperture Radar Images*. SciTech Publishing, 2004.
- [42] Irena Hajnsek and Yves-Louis Desnos, eds. *Polarimetric Synthetic Aperture Radar: Principles and Application*. Vol. 25. Remote Sensing and Digital Image Processing. Cham: Springer International Publishing, 2021.
- [43] Fawwaz Tayssir Ulaby et al. *Microwave Radar and Radiometric Remote Sensing*. Vol. 4. University of Michigan Press Ann Arbor, 2014.
- [44] RK Raney et al. “A Plea for Radar Brightness”. In: Proceedings of IGARSS’94-1994 IEEE International Geoscience and Remote Sensing Symposium. Vol. 2. IEEE, 1994, pp. 1090–1092.
- [45] David Small. “Flattening Gamma: Radiometric Terrain Correction for SAR Imagery”. In: *IEEE Transactions on Geoscience and Remote Sensing* 49.8 (Aug. 2011), pp. 3081–3093.
- [46] R. L. Cosgriff. *Analysis Of Radar Return From Random Surfaces Relative To Motion Between Surface And Radar*. Ohio State Univ Research Foundation Columbus Antenna Lab, 1960.
- [47] Donald K. Atwood, David Small, and Rüdiger Gens. “Improving PolSAR Land Cover Classification With Radiometric Correction of the Coherency Matrix”. In: *IEEE Journal of Selected Topics in Applied Earth Observations and Remote Sensing* 5.3 (June 2012), pp. 848–856.
- [48] Jakob J. van Zyl and Yunjin Kim. “Synthetic Aperture Radar”. In: *Encyclopedia of Physical Science and Technology (Third Edition)*. Ed. by Robert A. Meyers. New York: Academic Press, Jan. 1, 2003, pp. 451–465.
- [49] M. Eineder et al. “TerraSAR-X Ground Segment Basic Product Specification Document (TX-GS-DD-3302), 1.5”. In: *Cluster applied remote sensing, DLR (German Aerospace Center), Wessling, Germany* (2008).
- [50] Airbus. “Radiometric Calibration of TerraSAR-X Data - Beta Naught and Sigma Naught Coefficient Calculation”. In: 2014.
- [51] Ahmed S. Mashaly and Tarek A. Mahmoud. “A Survey on Speckle Noise Reduction for Sar Images”. In: *Machine Learning and Big Data Analytics Paradigms: Analysis, Applications and Challenges* (2021), pp. 281–302.
- [52] Fawwaz Tayssir Ulaby. “Microwave Remote Sensing Active and Passive”. In: *Rader remote sensing and surface scattering and emission theory* (1982), pp. 848–902.
- [53] J. W. Goodman. “Some Fundamental Properties of Speckle”. In: *Journal of the Optical Society of America* 66.11 (Nov. 1, 1976), p. 1145.
- [54] J.-C. Souyris, Caroline Henry, and Frédéric Adragna. “On the Use of Complex SAR Image Spectral Analysis for Target Detection: Assessment of Polarimetry”. In: *IEEE Transactions on Geoscience and Remote Sensing* 41.12 (2003), pp. 2725–2734.

- [55] C. Oliver and S. Quegan. *Understanding Synthetic Aperture Radar Images* (Boston: Artech House). Inc, 1998.
- [56] F. Lombardini. “Analysis of Non-Gaussian Speckle Statistics in High-Resolution SAR Images”. In: *Proceedings. 2005 IEEE International Geoscience and Remote Sensing Symposium, 2005. IGARSS '05*. Proceedings. 2005 IEEE International Geoscience and Remote Sensing Symposium, 2005. IGARSS '05. Vol. 2. July 2005, pp. 1337–1340.
- [57] E. Rignot and R. Chellappa. “Maximum a Posteriori Classification of Multifrequency, Multilook, Synthetic Aperture Radar Intensity Data”. In: *Journal of the Optical Society of America A* 10.4 (Apr. 1, 1993), p. 573.
- [58] Stian Normann Anfinssen, Anthony Paul Doulgeris, and Torbjørn Eltoft. “Estimation of the Equivalent Number of Looks in Polarimetric SAR Imagery”. In: *Geoscience and Remote Sensing Symposium, 2008. IGARSS 2008*. IEEE International. Vol. 4. IEEE, 2008, pp. IV–487.
- [59] J. S. Lee, M. R. Grunes, and G. De Grandi. “Polarimetric SAR Speckle Filtering and Its Impact on Classification”. In: *IGARSS'97. 1997 IEEE International Geoscience and Remote Sensing Symposium Proceedings. Remote Sensing-A Scientific Vision for Sustainable Development*. Vol. 2. IEEE, 1997, pp. 1038–1040.
- [60] Andrew J. Roscoe and Steven M. Blair. “Choice and Properties of Adaptive and Tunable Digital Boxcar (Moving Average) Filters for Power Systems and Other Signal Processing Applications”. In: *2016 IEEE International Workshop on Applied Measurements for Power Systems (AMPS)*. 2016 IEEE International Workshop on Applied Measurements for Power Systems (AMPS). Aachen, Germany: IEEE, Sept. 2016, pp. 1–6.
- [61] Jong-Sen Lee et al. “Speckle Filtering of Polarimetric SAR Interferometry Data”. In: *IEEE International Geoscience and Remote Sensing Symposium*. IEEE International Geoscience and Remote Sensing Symposium. Vol. 2. June 2002, 832–834 vol.2.
- [62] Jong-Sen Lee. “Digital Image Enhancement and Noise Filtering by Use of Local Statistics”. In: *IEEE transactions on pattern analysis and machine intelligence* 2 (1980), pp. 165–168.
- [63] Jong-Sen Lee. “Refined Filtering of Image Noise Using Local Statistics”. In: *Computer graphics and image processing* 15.4 (1981), pp. 380–389.
- [64] Steffen Suchandt, Hartmut Runge, and Ulrich Steinbrecher. “Ship Detection and Measurement Using the TerraSAR-X Dual-Receive Antenna Mode”. In: *Geoscience and Remote Sensing Symposium (IGARSS), 2010 IEEE International*. IEEE, 2010, pp. 2860–2863.
- [65] Sune RJ Axelsson. “Position Correction of Moving Targets in SAR Imagery”. In: *SAR Image Analysis, Modeling, and Techniques VI*. Vol. 5236. International Society for Optics and Photonics, 2004, pp. 80–93.
- [66] Martin Kirscht. “Estimation of Velocity, Shape, and Position of Moving Objects with SAR”. In: *Proceedings of the 4th International Airborne Remote Sensing Conference and Exhibition, Ottawa, ON, Canada*. Vol. 2124. 1999.
- [67] C. A. Balanis. *Advanced Engineering Electromagnetics Wiley*. John Wiley & Sons, 1989.
- [68] James Clerk Maxwell. “A Dynamical Theory of the Electromagnetic Field”. In: *Proceedings of the Royal Society of London* 13 (1864), pp. 531–536.
- [69] A. Marino, S. R. Cloude, and I. H. Woodhouse. “Detecting Depolarized Targets Using a New Geometrical Perturbation Filter”. In: *IEEE Transactions on Geoscience and Remote Sensing* 50.10 (Oct. 2012), pp. 3787–3799.
- [70] Wolfgang-M. Boerner. “Use of Polarization in Electromagnetic Inverse Scattering”. In: *Radio Science* 16.6 (1981), pp. 1037–1045.

- [71] W. M. Boerner. *Basics of Radar Polarimetry, RTO SET Lecture Series*. 2004.
- [72] Heein Yang et al. “Circular Polarization Implementation on Synthetic Aperture Radar”. In: *Information and Communication Technology Convergence (ICTC), 2014 International Conference On*. IEEE, 2014, pp. 991–994.
- [73] Shane Cloude. *Polarisation: Applications in Remote Sensing*. Oxford University Press, 2009.
- [74] Jong-Sen Lee and Eric Pottier. *Polarimetric Radar Imaging: From Basics to Applications*. CRC press, 2009.
- [75] Edward Collett. “Field Guide to Polarization”. In: Spie Bellingham, WA, 2005.
- [76] R.C. Jones. “A New Calculus for the Treatment of Optical Systems. I. Description and Discussion; II. Proof of the Three General Equivalence Theorems; III. The Stokes Theory of Optical Activity”. In: *Journal of the Optical Society of America* (1941), pp. 488–503.
- [77] Ernst LÜNEBURG. “Principles of Radar Polarimetry”. In: *IEICE Transactions on Electronics* 78.10 (1995), pp. 1339–1345.
- [78] S. R. Cloude. “Polarimetry: The Characterisation of Polarisation Effects in EM Scattering”. University of Birmingham, 1987.
- [79] George Gabriel Stokes. “On the Composition and Resolution of Streams of Polarized Light from Different Sources”. In: *Transactions of the Cambridge Philosophical Society* 9 (1852), p. 399.
- [80] J. J. Gil. “Polarimetric Characterization of Light and Media: Physical Quantities Involved in Polarimetric Phenomena”. In: *The European Physical Journal Applied Physics* 40.1 (Oct. 2007), pp. 1–47.
- [81] J. M. Bennett. “Polarization| Introduction”. In: *Encyclopedia of Modern Optics* (2005), pp. 190–204.
- [82] F. T. Ulaby and C. Elachi. *Radar Polarimetry for Geoscience Applications*. Norwood, 1990.
- [83] Eric Pottier. “Dr. J. R. Huynen’s Main Contributions in the Development of Polarimetric Radar Techniques and How the ‘Radar Targets Phenomenological Concept’ Becomes a Theory”. In: San Diego ’92. Ed. by Harold Mott and Wolfgang-Martin Boerner. San Diego, CA, Feb. 12, 1993, p. 72.
- [84] Y. Dong and B. Forster. “Understanding of Partial Polarization in Polarimetric SAR Data”. In: *International Journal of Remote Sensing* 17.12 (1996), pp. 2467–2475.
- [85] Roger H. Lang. “Electromagnetic Backscattering from a Sparse Distribution of Lossy Dielectric Scatterers”. In: *Radio Science* 16.01 (1981), pp. 15–30.
- [86] Howard A. Zebker and Jakob J. Van Zyl. “Imaging Radar Polarimetry: A Review”. In: *Proceedings of the IEEE* 79.11 (1991), pp. 1583–1606.
- [87] Shane R. Cloude and Eric Pottier. “A Review of Target Decomposition Theorems in Radar Polarimetry”. In: *IEEE transactions on geoscience and remote sensing* 34.2 (1996), pp. 498–518.
- [88] S. V. Nghiem et al. “Symmetry Properties in Polarimetric Remote Sensing”. In: *Radio Science* 27.05 (1992), pp. 693–711.
- [89] Shane R. Cloude. “Eigenvalue Parameters for Surface Roughness Studies”. In: *Polarization: Measurement, Analysis, and Remote Sensing II*. Vol. 3754. International Society for Optics and Photonics, 1999, pp. 2–13.

## BIBLIOGRAPHY

---

- [90] A. Freeman. “Fitting a Two-Component Scattering Model to Polarimetric SAR Data”. In: *IEEE 1999 International Geoscience and Remote Sensing Symposium. IGARSS’99 (Cat. No. 99CH36293)*. Vol. 5. IEEE, 1999, pp. 2649–2651.
- [91] Anthony Freeman and Stephen L. Durden. “A Three-Component Scattering Model for Polarimetric SAR Data”. In: *IEEE transactions on geoscience and remote sensing* 36.3 (1998), pp. 963–973.
- [92] E. J. Rothwell and M. J. Cloud. *Electromagnetics CRC Press LLC*. Boca Raton, FL, 2001.
- [93] Sang-Hoon Hong and Shimon Wdowinski. “Rotated Dihedral and Volume Scattering Behavior in Cross-Polarimetric SAR”. In: *2010 IEEE International Geoscience and Remote Sensing Symposium. IGARSS 2010 - 2010 IEEE International Geoscience and Remote Sensing Symposium*. Honolulu, HI, USA: IEEE, July 2010, pp. 3138–3141.
- [94] Thuy Le Toan. “Introduction to SAR Remote Sensing”. In: *Advanced training course on Land Remote Sensing, esa, Lecture D1La1, PowerPoint presentation* 74 (2021).
- [95] Fei Teng et al. “An Anisotropic Scattering Analysis Method Based on the Statistical Properties of Multi-Angular SAR Images”. In: *Remote Sensing* 12.13 (July 5, 2020), p. 2152.
- [96] L Ferro-Famil et al. “Analysis of Anisotropic Scattering Behavior Using Sub-Aperture Polarimetric Sar Data”. In: (2003), p. 3.
- [97] Rick Chapman and Richard Gasparovic. *Remote Sensing Physics: An Introduction to Observing Earth from Space*. John Wiley & Sons, 2022.
- [98] Y. Yamaguchi et al. “Four-Component Scattering Model for Polarimetric SAR Image Decomposition”. In: *IEEE Transactions on Geoscience and Remote Sensing* 43.8 (Aug. 2005), pp. 1699–1706.
- [99] Mingfei Gu et al. “PolSAR Target Detection via Reflection Symmetry and a Wishart Classifier”. In: *IEEE Access* 8 (2020), pp. 103317–103326.
- [100] Ferdinando Nunziata, Maurizio Migliaccio, and Carl E Brown. “Reflection Symmetry for Polarimetric Observation of Man-Made Metallic Targets at Sea”. In: *Oceanic Engineering, IEEE Journal of* 37.3 (2012), pp. 384–394.
- [101] S. R. Cloude, K. Papathanassiou, and I. Hajnsek. “An Eigenvector Method for the Extraction of Surface Parameters in Polarmetric SAR”. In: *SAR Workshop: CEOS Committee on Earth Observation Satellites*. Vol. 450. 2000, p. 693.
- [102] Maurizio Migliaccio et al. “A Multifrequency Polarimetric SAR Processing Chain to Observe Oil Fields in the Gulf of Mexico”. In: *IEEE Transactions on Geoscience and Remote Sensing* 49.12 (2011), pp. 4729–4737.
- [103] Domenico Velotto et al. “Dual-Polarimetric Terrasar-x SAR Data for Target at Sea Observation”. In: *Geoscience and Remote Sensing Letters, IEEE* 10.5 (2013), pp. 1114–1118.
- [104] Gui Gao, Xiaoyang Wang, and Min Niu. “Statistical Modeling of the Reflection Symmetry Metric for Sea Clutter in Dual-Polarimetric SAR Data”. In: (2016).
- [105] Yisok Oh, Kamal Sarabandi, and Fawwaz T. Ulaby. “An Empirical Model and an Inversion Technique for Radar Scattering from Bare Soil Surfaces”. In: *IEEE transactions on Geoscience and Remote Sensing* 30.2 (1992), pp. 370–381.
- [106] Brent Minchew, Cathleen E. Jones, and Benjamin Holt. “Polarimetric Analysis of Backscatter from the Deepwater Horizon Oil Spill Using L-band Synthetic Aperture Radar”. In: *IEEE Transactions on Geoscience and Remote Sensing* 50.10 (2012), pp. 3812–3830.

- [107] M. Migliaccio, F. Nunziata, and A. Gambardella. “On the Co-polarized Phase Difference for Oil Spill Observation”. In: *International Journal of Remote Sensing* 30.6 (2009), pp. 1587–1602.
- [108] Jong-Sen Lee et al. “On the Estimation of Radar Polarization Orientation Shifts Induced by Terrain Slopes”. In: *IEEE Transactions on Geoscience and Remote Sensing* 40.1 (2002), pp. 30–41.
- [109] Francesco Mattia et al. “On the Sensitivity of Polarimetric Coherence to Small and Large Scale Surface Roughness”. In: *IGARSS 2003. 2003 IEEE International Geoscience and Remote Sensing Symposium. Proceedings (IEEE Cat. No. 03CH37477)*. Vol. 2. IEEE, 2003, pp. 690–692.
- [110] Dayalan Kasilingam et al. “Modulation of Polarimetric Coherence by Ocean Features”. In: *IEEE International Geoscience and Remote Sensing Symposium*. Vol. 1. IEEE, 2002, pp. 432–434.
- [111] Hiroyuki Wakabayashi et al. “Polarimetric Characteristics of Sea Ice in the Sea of Okhotsk Observed by Airborne L-band SAR”. In: *IEEE Transactions on Geoscience and Remote Sensing* 42.11 (2004), pp. 2412–2425.
- [112] A. Marino, W. Dierking, and C. Wesche. “A Depolarization Ratio Anomaly Detector to Identify Icebergs in Sea Ice Using Dual-Polarization SAR Images”. In: *IEEE Transactions on Geoscience and Remote Sensing* 54.9 (Sept. 2016), pp. 5602–5615.
- [113] Yoshio Yamaguchi et al. “Classification of Terrain by Implementing the Correlation Coefficient in the Circular Polarization Basis Using X-band POLSAR Data”. In: *IEICE transactions on communications* 91.1 (2008), pp. 297–301.
- [114] E. Rodriguez and J. M. Martin. “Theory and Design of Interferometric Synthetic Aperture Radars”. In: *IEE Proceedings F (Radar and Signal Processing)*. Vol. 139. 2. IET, 1992, pp. 147–159.
- [115] Jakob J. Van Zyl. “Unsupervised Classification of Scattering Behavior Using Radar Polarimetry Data”. In: *IEEE Transactions on Geoscience and Remote Sensing* 27.1 (1989), pp. 36–45.
- [116] Lawrence A Klein and Calvin T Swift. “An Improved Model for the Dielectric Constant of Sea Water at Microwave Frequencies”. In: *Antennas and Propagation, IEEE Transactions on* 25.1 (1977), pp. 104–111.
- [117] Chenyu Guo et al. “Scaled Sea Surface Design and RCS Measurement Based on Rough Film Medium”. In: *Sensors* 22.16 (Aug. 21, 2022), p. 6290.
- [118] Jean Richard Huynen. “Phenomenological Theory of Radar Targets”. PhD thesis. Netherlands: Technical University Delft, 1970.
- [119] Subrahmanyam Chandrasekhar and Donna D. Elbert. “The Illumination and Polarization of the Sunlit Sky on Rayleigh Scattering”. In: *Transactions of the American Philosophical Society* 44.6 (1954), pp. 643–728.
- [120] William A. Holm and Richard M. Barnes. “On Radar Polarization Mixed Target State Decomposition Techniques”. In: *Proceedings of the 1988 IEEE National Radar Conference*. IEEE, 1988, pp. 249–254.
- [121] S. R. Cloude. “Uniqueness of Target Decomposition Theorems in Radar Polarimetry”. In: *Direct and Inverse Methods in Radar Polarimetry: Part 1*. Ed. by Wolfgang-M. Boerner et al. NATO ASI Series. Dordrecht: Springer Netherlands, 1992, pp. 267–296.
- [122] E. Krogager. “New Decomposition of the Radar Target Scattering Matrix”. In: *Electronics Letters* 26.18 (1990), pp. 1525–1527.

## BIBLIOGRAPHY

---

- [123] William L. Cameron and Ling K. Leung. “Feature Motivated Polarization Scattering Matrix Decomposition”. In: *IEEE International Conference on Radar*. IEEE, 1990, pp. 549–557.
- [124] R. Touzi. “Speckle Effect on Polarimetric Target Scattering Decomposition of SAR Imagery”. In: *Canadian Journal of Remote Sensing* 33.1 (2007), pp. 60–68.
- [125] Anthony Freeman and Stephen L. Durden. “Three-Component Scattering Model to Describe Polarimetric SAR Data”. In: *Radar Polarimetry*. Vol. 1748. International Society for Optics and Photonics, 1993, pp. 213–224.
- [126] Gulab Singh et al. “Hybrid Freeman/Eigenvalue Decomposition Method with Extended Volume Scattering Model”. In: *IEEE Geoscience and Remote Sensing Letters* 10.1 (2012), pp. 81–85.
- [127] David J Crisp and Nicholas J Redding. “Ship Detection in Synthetic Aperture Radar Imagery”. In: *12th Australasian Remote Sensing and Photogrammetry Conference. Fremantle, Western Australia, 18–22 October (2004)*, p. 10.
- [128] M. Jeremy et al. “Ocean Surveillance with Polarimetric SAR”. In: *Canadian Journal of Remote Sensing* 27.4 (2001), pp. 328–344.
- [129] W.L. Cameron, N.N. Youssef, and L.K. Leung. “Simulated Polarimetric Signatures of Primitive Geometrical Shapes”. In: *IEEE Transactions on Geoscience and Remote Sensing* 34.3 (May 1996), pp. 793–803.
- [130] Eric Pottier, Jong-Sen Lee, and Laurent Ferro-Famil. *Advanced Concepts in Polarimetry. Part 1: Polarimetric Target Description, Speckle Filtering and Decomposition Theorems*. Naval Research Lab Washington Dc, 2005.
- [131] J.R. Huynen. “Measurement of the Target Scattering Matrix”. In: *Proceedings of the IEEE* 53.8 (1965), pp. 936–946.
- [132] Shane Cloude and Eric Pottier. “An Entropy Based Classification Scheme for Land Applications of Polarimetric SAR”. In: *Geoscience and Remote Sensing, IEEE Transactions on* 35 (Feb. 1, 1997), pp. 68–78.
- [133] Shane R Cloude et al. “Unsupervised Image Classification Using the Entropy/Alpha/Anisotropy Method in Radar Polarimetry”. In: (2002), p. 20.
- [134] Eric Pottier and J.-S Lee. “Application of the «H / A / A» Polarimetric Decomposition Theorem for Unsupervised Classification of Fully Polarimetric SAR Data Based on the Wishart Distribution”. In: 450 (Feb. 29, 2000), p. 335.
- [135] Shane R. Cloude. “Polarimetry in Wave Scattering Applications”. In: *Scattering*. Elsevier, 2002, pp. 407–430.
- [136] Kefeng Ji and Yonghui Wu. “Scattering Mechanism Extraction by a Modified Cloude-Pottier Decomposition for Dual Polarization SAR”. In: *Remote Sensing* 7.6 (2015), pp. 7447–7470.
- [137] Laurent Ferro-Famil, Eric Pottier, and Jong-Sen Lee. “Unsupervised Classification of Multifrequency and Fully Polarimetric SAR Images Based on the H/A/Alpha-Wishart Classifier”. In: *IEEE Transactions on Geoscience and Remote Sensing* 39.11 (2001), pp. 2332–2342.
- [138] Sang-Eun Park and Wooil M. Moon. “Unsupervised Classification of Scattering Mechanisms in Polarimetric SAR Data Using Fuzzy Logic in Entropy and Alpha Plane”. In: *IEEE Transactions on Geoscience and Remote Sensing* 45.8 (2007), pp. 2652–2664.
- [139] Cao Fang, Hong Wen, and Wu Yirong. “An Improved Cloude-Pottier Decomposition Using H/ $\alpha$ /Span and Complex Wishart Classifier for Polarimetric SAR Classification”. In: *2006 CIE International Conference on Radar*. IEEE, 2006, pp. 1–4.

- [140] Jong-Sen Lee, Mitchell R. Grunes, and R. Kwok. “Classification of Multi-Look Polarimetric SAR Imagery Based on Complex Wishart Distribution”. In: *International Journal of Remote Sensing* 15.11 (1994), pp. 2299–2311.
- [141] Hossein Aghababae and Mahmood Reza Sahebi. “Wishart Derived Distance Based Clustering of Polarimetric SAR Images Using Support Vector Machines”. In: *Journal of the Indian Society of Remote Sensing* 44.6 (2016), pp. 1003–1010.
- [142] J. S. Lee et al. “Segmentation of Polarimetric SAR Images That Preserves Scattering Mechanisms”. In: *4th European Conference on Synthetic Aperture Radar, EUSAR 2002*. 2002.
- [143] Yuki Yajima et al. “POLARSAR Image Analysis of Wetlands Using a Modified Four-Component Scattering Power Decomposition”. In: *IEEE T. Geoscience and Remote Sensing* 46 (June 1, 2008), pp. 1667–1673.
- [144] Yoshio Yamaguchi, Yuki Yajima, and Hiroyoshi Yamada. “A Four-Component Decomposition of POLSAR Images Based on the Coherency Matrix”. In: *IEEE Geoscience and Remote Sensing Letters* 3.3 (2006), pp. 292–296.
- [145] Bin Zou et al. “A Four-Component Decomposition Model for PolSAR Data Using Asymmetric Scattering Component”. In: *IEEE Journal of Selected Topics in Applied Earth Observations and Remote Sensing* 8.3 (Mar. 2015), pp. 1051–1061.
- [146] Yoshio Yamaguchi et al. “Four-Component Scattering Power Decomposition with Rotation of Coherency Matrix”. In: *IEEE Transactions on Geoscience and Remote Sensing* 49.6 (2011), pp. 2251–2258.
- [147] Gulab Singh, Yoshio Yamaguchi, and Sang-Eun Park. “General Four-Component Scattering Power Decomposition With Unitary Transformation of Coherency Matrix”. In: *IEEE Transactions on Geoscience and Remote Sensing* 51.5 (May 2013), pp. 3014–3022.
- [148] Yi Cui et al. “On Complete Model-Based Decomposition of Polarimetric SAR Coherency Matrix Data”. In: *IEEE transactions on geoscience and remote sensing* 52.4 (2013), pp. 1991–2001.
- [149] Hossein Aghababae and Mahmood Reza Sahebi. “Incoherent Target Scattering Decomposition of Polarimetric SAR Data Based on Vector Model Roll-Invariant Parameters”. In: *IEEE Transactions on Geoscience and Remote Sensing* 54.8 (2016), pp. 4392–4401.
- [150] Avik Bhattacharya et al. “Modifying the Yamaguchi Four-Component Decomposition Scattering Powers Using a Stochastic Distance”. In: *IEEE Journal of Selected Topics in Applied Earth Observations and Remote Sensing* 8.7 (2015), pp. 3497–3506.
- [151] Bin Zou et al. “Eigen-Decomposition-Based Four-Component Decomposition for PolSAR Data”. In: *IEEE Journal of Selected Topics in Applied Earth Observations and Remote Sensing* 9.3 (2016), pp. 1286–1296.
- [152] Shane Cloude. “The Dual Polarization Entropy/Alpha Decomposition: A PALSAR Case Study”. In: *ESASP* 644 (2007), p. 2.
- [153] Jérôme Morio et al. “Application of Information Theory Measures to Polarimetric and Interferometric SAR Images”. In: *PSIP 2007* (2007).
- [154] Philippe Réfrégier and Jérôme Morio. “Shannon Entropy of Partially Polarized and Partially Coherent Light with Gaussian Fluctuations”. In: *JOSA A* 23.12 (2006), pp. 3036–3044.
- [155] I. Hajnsek, E. Pottier, and S.R. Cloude. “Inversion of Surface Parameters from Polarimetric SAR”. In: *IEEE Transactions on Geoscience and Remote Sensing* 41.4 (Apr. 2003), pp. 727–744.

## BIBLIOGRAPHY

---

- [156] Juan M. Lopez-Sanchez et al. “Polarimetric Response of Rice Fields at C-band: Analysis and Phenology Retrieval”. In: *IEEE Transactions on Geoscience and Remote Sensing* 52.5 (2013), pp. 2977–2993.
- [157] Shane Robert Cloude. “Target Decomposition Theorems in Radar Scattering”. In: *Electronics Letters* 21.1 (1985), pp. 22–24.
- [158] R Touzi et al. “A Review of Polarimetry in the Context of Synthetic Aperture Radar: Concepts and Information Extraction”. In: *Canadian Journal of Remote Sensing* 30.3 (2004), pp. 380–407.
- [159] My-Linh Truong-Loi, Pascale Dubois-Fernandez, and Eric Pottier. “Compact Polarimetry Potentials”. In: *2011 IEEE International Geoscience and Remote Sensing Symposium*. IEEE, 2011, pp. 3823–3826.
- [160] Shane R. Cloude, David G. Goodenough, and Hao Chen. “Compact Decomposition Theory for L-Band Satellite Radar Applications”. In: *2012 IEEE International Geoscience and Remote Sensing Symposium*. IEEE, 2012, pp. 5097–5100.
- [161] T.L. Ainsworth, J.P. Kelly, and J.-S. Lee. “Classification Comparisons between Dual-Pol, Compact Polarimetric and Quad-Pol SAR Imagery”. In: *ISPRS Journal of Photogrammetry and Remote Sensing* 64.5 (Sept. 2009), pp. 464–471.
- [162] F J Charbonneau et al. “Compact Polarimetry Overview and Applications Assessment”. In: *Canadian Journal of Remote Sensing* (2010), p. 19.
- [163] R.K. Raney. “Dual-Polarized SAR and Stokes Parameters”. In: *IEEE Geoscience and Remote Sensing Letters* 3.3 (July 2006), pp. 317–319.
- [164] Thomas Jagdhuber, Irena Hajnsek, and Konstantinos P. Papathanassiou. “Soil Moisture Estimation Using Dual-Polarimetric Coherent (HH/VV) TerraSAR-X and TanDEM-X Data”. In: (2013).
- [165] Andreas Schmitt and Brian Brisco. “Wetland Monitoring Using the Curvelet-Based Change Detection Method on Polarimetric SAR Imagery”. In: *Water* 5.3 (3 Sept. 2013), pp. 1036–1051.
- [166] Tobias Ullmann, Andreas Schmitt, and Thomas Jagdhuber. “Two Component Decomposition of Dual Polarimetric HH/VV SAR Data: Case Study for the Tundra Environment of the Mackenzie Delta Region, Canada”. In: (2016).
- [167] Kaupo Voormansik et al. “Towards a Detection of Grassland Cutting Practices with Dual Polarimetric TerraSAR-X Data”. In: *International journal of remote sensing* 34.22 (2013), pp. 8081–8103.
- [168] Gui Gao and Gongtao Shi. “Ship Detection in Dual-Channel ATI-SAR Based on the Notch Filter”. In: *IEEE Transactions on Geoscience and Remote Sensing* 55.8 (Aug. 2017), pp. 4795–4810.
- [169] Ferdinando Nunziata, Antonio Montuori, and Maurizio Migliaccio. “Dual-Polarized COSMO SkyMed SAR Data to Observe Metallic Targets at Sea”. In: *Geoscience and Remote Sensing Symposium (IGARSS), 2011 IEEE International*. IEEE, 2011, pp. 2270–2273.
- [170] Christoph H. Gierull. “Demystifying the Capability of Sublook Correlation Techniques for Vessel Detection in SAR Imagery”. In: *IEEE Transactions on Geoscience and Remote Sensing* 57.4 (Apr. 2019), pp. 2031–2042.
- [171] Armando Marino et al. “Ship Detection with Spectral Analysis of Synthetic Aperture Radar: A Comparison of New and Well-Known Algorithms”. In: *Remote Sensing* 7.5 (Apr. 30, 2015), pp. 5416–5439.



- [172] C. Brekke, S. N. Anfinsen, and Y. Larsen. “Subband Extraction Strategies in Ship Detection With the Subaperture Cross-Correlation Magnitude”. In: *IEEE Geoscience and Remote Sensing Letters* 10.4 (July 2013), pp. 786–790.
- [173] A. Arnaud. “Ship Detection by SAR Interferometry”. In: *IEEE 1999 International Geoscience and Remote Sensing Symposium. IGARSS’99 (Cat. No.99CH36293)*. IEEE 1999 International Geoscience and Remote Sensing Symposium. IGARSS’99 (Cat. No.99CH36293). Vol. 5. IEEE, June 1999, 2616–2618 vol.5.
- [174] K. Ouchi et al. “Ship Detection Based on Coherence Images Derived From Cross Correlation of Multilook SAR Images”. In: *IEEE Geoscience and Remote Sensing Letters* 1.3 (July 2004), pp. 184–187.
- [175] K. Ouchi and Haipeng Wang. “Interlook Cross-Correlation Function of Speckle in SAR Images of Sea Surface Processed with Partially Overlapped Subapertures”. In: *IEEE Transactions on Geoscience and Remote Sensing* 43.4 (Apr. 2005), pp. 695–701.
- [176] K. Ouchi et al. “Nonuniform Azimuth Image Shift Observed in the Radarsat Images of Ships in Motion”. In: *IEEE Transactions on Geoscience and Remote Sensing* 40.10 (Oct. 2002), pp. 2188–2195.
- [177] Armando Marino and Irena Hajnsek. “Statistical Tests for a Ship Detector Based on the Polarimetric Notch Filter”. In: *Geoscience and Remote Sensing, IEEE Transactions on* 53.8 (2015), pp. 4578–4595.
- [178] Richard Bamler and Philipp Hartl. “Synthetic Aperture Radar Interferometry”. In: *Inverse problems* 14.4 (1998), R1.
- [179] Steffen Suchandt and Hartmut Runge. “Motion Detection Using TanDEM-X Along-Track Interferometry”. 2013.
- [180] P. Lombardo, D. Pastina, and F. Turin. “Ground Moving Target Detection Based on MIMO SAR Systems”. In: *IEEE Journal of Selected Topics in Applied Earth Observations and Remote Sensing* 8.11 (Nov. 2015), pp. 5081–5095.
- [181] Stefan Baumgartner and Gerhard Krieger. “Dual-Platform Large Along-Track Baseline GMTI”. In: *IEEE Transactions on Geoscience and Remote Sensing* 54 (Oct. 29, 2015), pp. 1–21.
- [182] Thomas Börner et al. “ATI and GMTI Performance Analysis of Post-Sentinel-1 SAR Systems Based on Simulations Using OASIS”. In: *EUSAR 2014; 10th European Conference on Synthetic Aperture Radar; Proceedings Of. VDE, 2014*, pp. 1–4.
- [183] Steffen Suchandt, Andreas Lehmann, and Hartmut Runge. “Analysis of Ocean Surface Currents with TanDEM-X ATI: A Case Study in the Baltic Sea”. In: *2014 IEEE Geoscience and Remote Sensing Symposium. IGARSS 2014 - 2014 IEEE International Geoscience and Remote Sensing Symposium*. Quebec City, QC: IEEE, July 2014, pp. 3918–3921.
- [184] Roland Romeiser et al. “Quality Assessment of Surface Current Fields From TerraSAR-X and TanDEM-X Along-Track Interferometry and Doppler Centroid Analysis”. In: *IEEE Transactions on Geoscience and Remote Sensing* 52.5 (May 2014), pp. 2759–2772.
- [185] H.A. Zebker and J. Villasenor. “Decorrelation in Interferometric Radar Echoes”. In: *IEEE Transactions on Geoscience and Remote Sensing* 30.5 (1992), pp. 950–959.
- [186] Ridha Touzi et al. “Coherence Estimation for SAR Imagery”. In: *IEEE transactions on geoscience and remote sensing* 37.1 (1999), pp. 135–149.
- [187] S.R. Cloude and K.P. Papathanassiou. “Polarimetric SAR Interferometry”. In: *IEEE Transactions on Geoscience and Remote Sensing* 36.5 (Sept. 1998), pp. 1551–1565.
- [188] Maxim Neumann, Andreas Reigber, and Laurent Ferro-Famil. “PolInSAR Coherence Set Theory and Application”. In: (2006), p. 4.

## BIBLIOGRAPHY

---

- [189] J. Wright. “A New Model for Sea Clutter”. In: *IEEE Transactions on Antennas and Propagation* 16.2 (Mar. 1968), pp. 217–223.
- [190] F. Bass et al. “Very High Frequency Radiowave Scattering by a Disturbed Sea Surface Part I: Scattering from a Slightly Disturbed Boundary”. In: *IEEE Transactions on Antennas and Propagation* 16.5 (Sept. 1968), pp. 554–559.
- [191] Gary S. Brown. “A Comparison of Approximate Theories for Scattering from Rough Surfaces”. In: *Wave motion* 7.2 (1985), pp. 195–205.
- [192] OM Phillips. “Radar Returns from the Sea Surface—Bragg Scattering and Breaking Waves”. In: *Journal of physical oceanography* 18.8 (1988), pp. 1065–1074.
- [193] G. R. Valenzuela and M. B. Laing. “Study of Doppler Spectra of Radar Sea Echo”. In: *Journal of Geophysical Research* 75.3 (1970), pp. 551–563.
- [194] Sushil Kumar Joshi and Stefan V. Baumgartner. “Sea Clutter Model Comparison for Ship Detection Using Single Channel Airborne Raw SAR Data”. In: *Proceedings of the European Conference on Synthetic Aperture Radar, EUSAR*. European Conference on Synthetic Aperture Radar (EUSAR). Aachen, Germany: VDE, June 6, 2018, pp. 731–735.
- [195] J. Yin et al. “The Extended Bragg Scattering Model-Based Method for Ship and Oil-Spill Observation Using Compact Polarimetric SAR”. In: *IEEE Journal of Selected Topics in Applied Earth Observations and Remote Sensing* 8.8 (Aug. 2015), pp. 3760–3772.
- [196] D. Zhao et al. “Sea Clutter Modeling by Statistical Majority Consistency for Ship Detection in SAR Imagery”. In: *2015 IEEE International Geoscience and Remote Sensing Symposium (IGARSS)*. 2015 IEEE International Geoscience and Remote Sensing Symposium (IGARSS). July 2015, pp. 3695–3698.
- [197] Ding Tao, Stian Normann Anfinnsen, and Camilla Brekke. “Ocean Clutter Modeling for Ship Detection”. In: *Proc. SEASAR* (2012), p. 6.
- [198] Vilhelm Gregers-Hansen and Rashmi Mital. “An Improved Empirical Model for Radar Sea Clutter Reflectivity”. In: *IEEE Transactions on Aerospace and Electronic Systems* 48.4 (2012), pp. 3512–3524.
- [199] Benjamin Holt. “SAR Imaging of the Ocean Surface”. In: *Synthetic Aperture Radar Marine User’s Manual*. Ed. by C.R. Jackson and J.R. Apel. Washington, D.C., USA: NOAA/NESDIS, 2004, pp. 25–79.
- [200] Abhilash Singh et al. “Comparison of Different Dielectric Models to Estimate Penetration Depth of L- and S-Band SAR Signals into the Ground Surface”. In: *Geographies* 2.4 (Nov. 28, 2022), pp. 734–742.
- [201] Maen Ishtaiwi, Muna Hajjyahya, and Shahd Habbash. “Electrical Properties of Dead Sea Water”. In: *Journal of Applied Mathematics and Physics* 09.12 (2021), pp. 3094–3101.
- [202] Enrique Vidal-Vijande et al. “Analysis of a 44-Year Hindcast for the Mediterranean Sea: Comparison with Altimetry and in Situ Observations”. In: (2011).
- [203] John R. Apel. *Principles of Ocean Physics*. Academic Press, 1987.
- [204] R. Keith Raney. “Radar Fundamentals: Technical Perspective”. In: *Principals and Applications of Imaging Radar, Manual of Remote Sensing 2* (1998), pp. 9–130.
- [205] Yongzheng Ren et al. “An Algorithm for the Retrieval of Sea Surface Wind Fields Using X-band TerraSAR-X Data”. In: *International Journal of Remote Sensing* 33.23 (Dec. 10, 2012), pp. 7310–7336.
- [206] William J Plant and William C Keller. “Evidence of Bragg Scattering in Microwave Doppler Spectra of Sea Return”. In: *Journal of Geophysical Research: Oceans* 95.C9 (1990), pp. 16299–16310.

- [207] PW Vachon et al. “Ship Detection by the RADARSAT SAR: Validation of Detection Model Predictions”. In: *Canadian Journal of Remote Sensing* 23.1 (1997), pp. 48–59.
- [208] Yury Yu Yurovsky et al. “Ka-Band Dual Copolarized Empirical Model for the Sea Surface Radar Cross Section”. In: *IEEE Transactions on Geoscience and Remote Sensing* 55.3 (2016), pp. 1629–1647.
- [209] Fawwaz T. Ulaby, Richard K. Moore, and Adrian K. Fung. “Microwave Remote Sensing: Active and Passive. Volume 1-Microwave Remote Sensing Fundamentals and Radiometry”. In: (1981).
- [210] George Biddell Airy. *Tides and Waves*. B. Fellowes, 1845.
- [211] R Keith Raney. “Theory and Measure of Certain Image Norms in SAR”. In: *Geoscience and Remote Sensing, IEEE Transactions on* 3 (1985), pp. 343–348.
- [212] Tobias Schneiderhan. “Nutzung Satellitengestützter SAR-Daten Und Des CMOD4-Modells Zur Untersuchung Des Lokalen Windfeldes in Der Umgebung von Offshore-Windparks”. lmu, 2006.
- [213] Adrianus Cornelis Maria Stoffelen. “Scatterometry”. In: *Ph. D. Thesis* (1996).
- [214] R. Z. Schneider et al. “Polarimetric and Interferometric Characterization of Coherent Scatterers in Urban Areas”. In: *IEEE Transactions on Geoscience and Remote Sensing* 44.4 (Apr. 2006), pp. 971–984.
- [215] Valeria Gracheva. “Multichannel Analysis of Medium Grazing Angle Sea Clutter for Airborne Microwave Radar Systems”. 2015.
- [216] Julius Adams Stratton and L. J. Chu. “Diffraction Theory of Electromagnetic Waves”. In: *Physical Review* 56.1 (1939), p. 99.
- [217] Keith D. Ward, Simon Watts, and Robert JA Tough. *Sea Clutter: Scattering, the K Distribution and Radar Performance*. Vol. 20. IET, 2006.
- [218] I. S. Robinson. *Satellite Oceanography; an Introduction for Oceanographers and Remote-Sensing Scientists*. Chichester (UK) Horwood, 1985.
- [219] Physical Sciences Laboratory NOAA. *ESRL Wave Propagation and Remote Sensing Theory Program*. 2022. URL: <https://psl.noaa.gov/psd3/multi/ocean/numerical.html> (visited on 01/14/2023).
- [220] Gaspar R. Valenzuela. “Theories for the Interaction of Electromagnetic and Oceanic Waves—A Review”. In: *Boundary-Layer Meteorology* 13.1 (1978), pp. 61–85.
- [221] Ian S. Robinson. *Measuring the Oceans from Space: The Principles and Methods of Satellite Oceanography*. Springer Science & Business Media, 2004.
- [222] Eric A. Ericson, David R. Lyzenga, and David T. Walker. “Radar Backscatter from Stationary Breaking Waves”. In: *Journal of Geophysical Research: Oceans* 104.C12 (Dec. 15, 1999), pp. 29679–29695.
- [223] A. Voronovich and V. Zavorotny. “A Numerical Model of Radar Scattering from Steep and Breaking Waves”. In: *2006 IEEE International Symposium on Geoscience and Remote Sensing*. 2006 IEEE International Symposium on Geoscience and Remote Sensing. Denver, CO, USA: IEEE, July 2006, pp. 469–472.
- [224] V. U. Zavorotny and A. G. Voronovich. “Comparison of Geometric Optics and Diffraction Effects in Radar Scattering from Steep and Breaking Waves”. In: *2007 IEEE International Geoscience and Remote Sensing Symposium*. 2007 IEEE International Geoscience and Remote Sensing Symposium. Barcelona, Spain: IEEE, 2007, pp. 1350–1353.
- [225] Werner Alpers and Christian Melsheimer. “Rainfall”. In: *Synthetic Aperture Radar Marine User’s Manual*. Ed. by C.R. Jackson and J.R. Apel. Washington, D.C., USA: NOAA/NESDIS, 2004, pp. 353–372.

## BIBLIOGRAPHY

---

- [226] Werner Alpers et al. “Rain Footprints on C-band Synthetic Aperture Radar Images of the Ocean”. In: *Remote Sensing of Environment* 187 (Dec. 2016), pp. 169–185.
- [227] William Henry Bragg and William Lawrence Bragg. “The Reflection of X-rays by Crystals”. In: *Proceedings of the Royal Society of London. Series A, Containing Papers of a Mathematical and Physical Character* 88.605 (1913), pp. 428–438.
- [228] Frank M. Monaldo et al. “Comparison of SAR-derived Wind Speed with Model Predictions and Ocean Buoy Measurements”. In: *IEEE Transactions on Geoscience and Remote Sensing* 39.12 (2001), pp. 2587–2600.
- [229] Klaus Hasselmann et al. “Theory of Synthetic Aperture Radar Ocean Imaging: A MARSEN View”. In: *Journal of Geophysical Research: Oceans* 90.C3 (1985), pp. 4659–4686.
- [230] D. Offiler. “The Calibration of ERS-1 Satellite Scatterometer Winds”. In: *Journal of Atmospheric and oceanic Technology* 11.4 (1994), pp. 1002–1017.
- [231] A. E. Long. “Towards a C-band Radar Sea Echo Model for the ERS-1 Scatterometer”. In: 1985. (1985), pp. 29–34.
- [232] A. Stoffelen, D. Anderson, and C. Gaffard. “From Measurement to Model: ERS-1 Scatterometer Data Assimilation”. In: *Proceedings of IGARSS '93 - IEEE International Geoscience and Remote Sensing Symposium*. IGARSS '93 - IEEE International Geoscience and Remote Sensing Symposium. Tokyo, Japan: IEEE, 1993, pp. 1762–1764.
- [233] H. Hersbach, A. Stoffelen, and S. de Haan. “An Improved C-band Scatterometer Ocean Geophysical Model Function: CMOD5”. In: *Journal of Geophysical Research: Oceans* 112.C3 (2007).
- [234] Ad Stoffelen et al. “The CMOD7 Geophysical Model Function for ASCAT and ERS Wind Retrievals”. In: *IEEE Journal of Selected Topics in Applied Earth Observations and Remote Sensing* 10.5 (May 2017), pp. 2123–2134.
- [235] Ad Stoffelen and David Anderson. “Scatterometer Data Interpretation: Estimation and Validation of the Transfer Function CMOD4”. In: *Journal of Geophysical Research: Oceans* 102.C3 (Mar. 15, 1997), pp. 5767–5780.
- [236] Vincent Kerbaol, Bertrand Chapron, and Paris W Vachon. “Analysis of ERS-1/2 Synthetic Aperture Radar Wave Mode Imagettes”. In: *Journal of Geophysical Research: Oceans* 103.C4 (1998), pp. 7833–7846.
- [237] S. Lehner et al. “Wind and Wave Measurements Using Complex ERS-2 SAR Wave Mode Data”. In: *IEEE Transactions on Geoscience and Remote Sensing* 38.5 (2000), pp. 2246–2257.
- [238] Nicolas Fichaux and Thierry Ranchin. “Combined Extraction of High Spatial Resolution Wind Speed and Wind Direction from SAR Images: A New”. In: *Canadian Journal of Remote Sensing* (2002), p. 8.
- [239] S. Lehner et al. “Mesoscale Wind Measurements Using Recalibrated ERS SAR Images”. In: *Journal of Geophysical Research: Oceans* 103.C4 (Apr. 15, 1998), pp. 7847–7856.
- [240] D.R. Thompson, T.M. Elfouhaily, and B. Chapron. “Polarization Ratio for Microwave Backscattering from the Ocean Surface at Low to Moderate Incidence Angles”. In: *IGARSS '98. Sensing and Managing the Environment. 1998 IEEE International Geoscience and Remote Sensing Symposium Proceedings. (Cat. No.98CH36174)*. IGARSS '98. Sensing and Managing the Environment. 1998 IEEE International Geoscience and Remote Sensing Symposium Proceedings. (Cat. No.98CH36174). Seattle, WA, USA: IEEE, 1998, 1671–1673 vol.3.
- [241] Jochen Horstmann. “Measurement of Ocean Wind Fields with Synthetic Aperture Radar”. Staats-und Universitätsbibliothek Hamburg Carl von Ossietzky, 2001.

- [242] O. Isoguchi and M. Shimada. “An L-Band Ocean Geophysical Model Function Derived From PALSAR”. In: *IEEE Transactions on Geoscience and Remote Sensing* 47.7 (July 2009), pp. 1925–1936.
- [243] P.W. Vachon and F.W. Dobson. “Wind Retrieval from RADARSAT SAR Images: Selection of a Suitable C-Band HH Polarization Wind Retrieval Model”. In: *Canadian Journal of Remote Sensing* 26.4 (Aug. 1, 2000), pp. 306–313.
- [244] Weizeng Shao, Susanne Lehner, and Changlong Guan. “Study on Polarisation Ratio for X-band Using Dual-Polarisation Terra-SAR X Image”. In: *2012 IEEE International Geoscience and Remote Sensing Symposium. IGARSS 2012 - 2012 IEEE International Geoscience and Remote Sensing Symposium*. Munich, Germany: IEEE, July 2012, pp. 3768–3771.
- [245] Xiao-Ming Li and Susanne Lehner. “Algorithm for Sea Surface Wind Retrieval From TerraSAR-X and TanDEM-X Data”. In: *IEEE Transactions on Geoscience and Remote Sensing* 52.5 (May 2014), pp. 2928–2939.
- [246] Donald R. Thompson et al. “Comparison of High-Resolution Wind Fields Extracted from TerraSAR-X SAR Imagery with Predictions from the WRF Mesoscale Model: TERRASAR-X SAR Wind Retrieval”. In: *Journal of Geophysical Research: Oceans* 117.C2 (Feb. 2012), n/a–n/a.
- [247] Jong-Sen Lee et al. “Polarimetric Analysis and Modeling of Multifrequency SAR Signatures from Gulf Stream Fronts”. In: *IEEE Journal of Oceanic Engineering* 23.4 (1998), pp. 322–333.
- [248] D. L. Schuler and J. S. Lee. “A Microwave Technique to Improve the Measurement of Directional Ocean Wave Spectra”. In: *International Journal of Remote Sensing* 16.2 (Jan. 1995), pp. 199–215.
- [249] D.L. Schuler et al. “Measurement of Ocean Wave Spectra Using Polarimetric SAR Data”. In: *IGARSS 2003. 2003 IEEE International Geoscience and Remote Sensing Symposium. Proceedings (IEEE Cat. No.03CH37477)*. IGARSS 2003. 2003 IEEE International Geoscience and Remote Sensing Symposium. Proceedings. Vol. 2. Toulouse, France: IEEE, 2003, pp. 708–710.
- [250] S. M. Kay. *Fundamentals of Statistical Signal Processing-Vol. 2: Detection*. Prentice-Hall, 1998.
- [251] Keinosuke Fukunaga. *Introduction to Statistical Pattern Recognition*. Elsevier, Oct. 22, 2013. 606 pp.
- [252] E.E. Kuruoglu and J. Zerubia. “Modelling SAR Images with a Generalisation of the Rayleigh Distribution”. In: *Conference Record of the Thirty-Fourth Asilomar Conference on Signals, Systems and Computers (Cat. No.00CH37154)*. Conference Record of the Thirty-Fourth Asilomar Conference on Signals, Systems and Computers (Cat. No.00CH37154). Vol. 1. Oct. 2000, 224–228 vol.1.
- [253] Christopher C. Wackerman et al. “Automatic Detection of Ships in RADARSAT-1 SAR Imagery”. In: *Canadian Journal of Remote Sensing* 27.5 (2001), pp. 568–577.
- [254] Jia Xu et al. “Small Target Detection in SAR Image Using the Alpha-stable Distribution Model”. In: (2010), p. 5.
- [255] D.A. Shnidman. “Generalized Radar Clutter Model”. In: *IEEE Transactions on Aerospace and Electronic Systems* 35.3 (July 1999), pp. 857–865.
- [256] Mohamed Adnane Habib et al. “Ca-Cfar Detection Performance Of Radar Targets Embedded In “Non Centered Chi-2 Gamma” Clutter”. In: *Progress In Electromagnetics Research* 88 (2008), pp. 135–148.

## BIBLIOGRAPHY

---

- [257] Felix Totir, S Demeter, and Emanuel Radoi. “Sea Clutter Simulation and Comparative Study of Effects in Radar Imagery”. In: METRA. Bucarest, Romania, 2005.
- [258] Knut Eldhuset. “An Automatic Ship and Ship Wake Detection System for Spaceborne SAR Images in Coastal Regions”. In: *IEEE transactions on Geoscience and Remote Sensing* 34.4 (1996), pp. 1010–1019.
- [259] H. M. Finn and R. S. Johnson. “Adaptive Detection Mode with Threshold Control as a Function of Spatially Sampled Clutter-Level Estimates”. In: *Rca Rev.* 29 (1968), pp. 414–465.
- [260] Gerard Margarit, José A. Barba Milanés, and Antonio Tabasco. “Operational Ship Monitoring System Based on Synthetic Aperture Radar Processing”. In: *Remote Sensing* 1.3 (Aug. 14, 2009), pp. 375–392.
- [261] Mariví Tello, Carlos López-Martínez, and Jordi J Mallorqui. “A Novel Algorithm for Ship Detection in SAR Imagery Based on the Wavelet Transform”. In: *IEEE Geoscience and remote sensing letters* 2.2 (2005), pp. 201–205.
- [262] Richard B. Olsen and Terje Wahl. “The Ship Detection Capability of ENVISAT’s ASAR”. In: *Geoscience and Remote Sensing Symposium, 2003. IGARSS’03. Proceedings. 2003 IEEE International*. Vol. 5. IEEE, 2003, pp. 3108–3110.
- [263] S. Watts, C. J. Baker, and K. D. Ward. “Maritime Surveillance Radar. Part 2: Detection Performance Prediction in Sea Clutter”. In: *IEE Proceedings F (Radar and Signal Processing)*. Vol. 137. 2. IET, 1990, pp. 63–72.
- [264] Leslie M Novak, Michael B Sechtin, and Michael C Burl. “Algorithms for Optimal Processing of Polarimetric Radar Data”. In: *Massachusetts Inst. of Tech Lexington Lincoln Lab* (1989), p. 99.
- [265] C. Liu, P. W. Vachon, and G. W. Geling. “Improved Ship Detection Using Polarimetric SAR Data”. In: *IGARSS 2004. 2004 IEEE International Geoscience and Remote Sensing Symposium*. IGARSS 2004. 2004 IEEE International Geoscience and Remote Sensing Symposium. Vol. 3. 2004, 1800–1803 vol.3.
- [266] Pasquale Iervolino, Raffaella Guida, and Philip Whittaker. *A New GLRT-based Ship Detection Technique in SAR Images*. 2015. URL: <http://ieeexplore.ieee.org/xpls/icp.jsp?arnumber=7326480> (visited on 10/05/2016).
- [267] Giuseppe Ferrara et al. “Generalized-K (GK)-Based Observation of Metallic Objects at Sea in Full-Resolution Synthetic Aperture Radar (SAR) Data: A Multipolarization Study”. In: *IEEE Journal of Oceanic Engineering* 36.2 (Apr. 2011), pp. 195–204.
- [268] R. Touzi et al. “Ship-Sea Contrast Optimization When Using Polarimetric SARs”. In: *IGARSS 2001. Scanning the Present and Resolving the Future. Proceedings. IEEE 2001 International Geoscience and Remote Sensing Symposium (Cat. No. 01CH37217)*. Vol. 1. IEEE, 2001, pp. 426–428.
- [269] Qingshan Jiang et al. “Automatic Detection for Ship Target in SAR Imagery Using PNN-model”. In: *Canadian Journal of Remote Sensing* 26.4 (2000), pp. 297–305.
- [270] K. Ouchi and H. Yaguchi. “Simulation on the Extraction of Ships’ Images Embedded in Speckle Using Cross-Correlation of Multilook SAR Images and Applications to Radarsat Data”. In: *IEEE International Geoscience and Remote Sensing Symposium*. IEEE International Geoscience and Remote Sensing Symposium. IGARSS 2002. Vol. 4. Toronto, Ont., Canada: IEEE, 2002, pp. 2498–2500.
- [271] Vahid Akbari, Anthony Paul Doulgeris, and Camilla Brekke. “Subaperture Analysis of Polarimetric SAR Data for Iceberg Detection”. In: *2016 IEEE International Geoscience and Remote Sensing Symposium (IGARSS)*. IGARSS 2016 - 2016 IEEE International Geoscience and Remote Sensing Symposium. Beijing, China: IEEE, July 2016, pp. 5666–5669.

- [272] V. M. Giacomazzo et al. "Identification of Coherent Scatterers: Spectral Correlation vs. Multi-Chromatic Phase Analysis". In: *IGARSS 2008 - 2008 IEEE International Geoscience and Remote Sensing Symposium*. IGARSS 2008 - 2008 IEEE International Geoscience and Remote Sensing Symposium. Boston, MA, USA: IEEE, 2008, pp. IV - 411-IV -414.
- [273] M. J. Sanjuan-Ferrer, I. Hajnsek, and K. P. Papathanassiou. "Analysis of the Detection Performance of Coherent Scatterers in SAR Images". In: *2012 IEEE International Geoscience and Remote Sensing Symposium*. 2012 IEEE International Geoscience and Remote Sensing Symposium. July 2012, pp. 1457-1460.
- [274] Stian Normann Anfinsen and Camilla Brekke. "Statistical Models for Constant False Alarm Rate Ship Detection with the Sublook Correlation Magnitude". In: *Geoscience and Remote Sensing Symposium (IGARSS), 2012 IEEE International*. IEEE, 2012, pp. 5626-5629.
- [275] WG Zhang, F Liu, and LC Jiao. "SAR Image Despeckling via Bilateral Filtering". In: *Electronics letters* 45.15 (2009), pp. 781-783.
- [276] Bernd Scheuchl et al. "H/A/ $\alpha$ -Based Classification of Sea Ice Using SAR Polarimetry". In: (2001), p. 9.
- [277] R. Touzi. "On the Use of Polarimetric SAR Data for Ship Detection". In: *IEEE 1999 International Geoscience and Remote Sensing Symposium. IGARSS'99 (Cat. No.99CH36293)*. IEEE 1999 International Geoscience and Remote Sensing Symposium. IGARSS'99. Vol. 2. Hamburg, Germany: IEEE, 1999, pp. 812-814.
- [278] Jong-Sen Lee et al. "Evaluation and Bias Removal of Multilook Effect on Entropy/Alpha/Anisotropy in Polarimetric SAR Decomposition". In: *Geoscience and Remote Sensing, IEEE Transactions on* 46 (Nov. 1, 2008), pp. 3039-3052.
- [279] C. Lopez-Martinez, E. Pottier, and S.R. Cloude. "Statistical Assessment of Eigenvector-Based Target Decomposition Theorems in Radar Polarimetry". In: *IEEE Transactions on Geoscience and Remote Sensing* 43.9 (Sept. 2005), pp. 2058-2074.
- [280] A. A. Swartz et al. "Optimal Polarizations for Achieving Maximum Contrast in Radar Images". In: *Journal of Geophysical Research: Solid Earth* 93.B12 (1988), pp. 15252-15260.
- [281] Armando Marino and Matteo Nannini. "Signal Models for Changes in Polarimetric SAR Data". In: *IEEE Transactions on Geoscience and Remote Sensing* 60 (2022), pp. 1-18.
- [282] Armando Marino and Irena Hajnsek. "A Change Detector Based on an Optimization With Polarimetric SAR Imagery". In: *IEEE Transactions on Geoscience and Remote Sensing* 52.8 (Aug. 2014), pp. 4781-4798.
- [283] R D Chaney, M C Burl, and L M Novak. "On the Performance of Polarimetric Target Detection Algorithms". In: (1990), p. 7.
- [284] A. Lopes and F. Sery. "Optimal Speckle Reduction for the Product Model in Multilook Polarimetric SAR Imagery and the Wishart Distribution". In: *IEEE Transactions on Geoscience and Remote Sensing* 35.3 (May 1997), pp. 632-647.
- [285] Guoqing Liu et al. "The Multilook Polarimetric Whitening Filter (MPWF) for Intensity Speckle Reduction in Polarimetric SAR Images". In: *IEEE Transactions on Geoscience and Remote Sensing* 36.3 (May 1998), pp. 1016-1020.
- [286] E. M. Kennaugh and R. W. Sloan. *Effects of Type of Polarization On Echo Characteristics*. Ohio State Univ Research Foundation Columbus Antenna Lab, 1952.
- [287] Armando Marino, Shane R Cloude, and Iain H Woodhouse. "A Polarimetric Target Detector Using the Huynen Fork". In: *IEEE Transactions on Geoscience and Remote Sensing* 48.5 (May 2010), pp. 2357-2366.

## BIBLIOGRAPHY

---

- [288] Armando Marino, Shane R. Cloude, and Juan M. Lopez-Sanchez. “A New Polarimetric Change Detector in Radar Imagery”. In: *IEEE Transactions on Geoscience and Remote Sensing* 51.5 (May 2013), pp. 2986–3000.
- [289] Armando Marino and Irena Hajnsek. “Ship Detection With TanDEM-X Data Extending the Polarimetric Notch Filter”. In: *Geoscience and Remote Sensing Letters, IEEE* 12.10 (2015), pp. 2160–2164.
- [290] A Marino and I Hajnsek. “CFAR Ship Detection With A Notch Filter Using Polarimetric Sar Data”. In: *sea* 2.1 (2013), p. 2.
- [291] A. Marino, S. Cloude, and I. Woodhouse. “Detecting Depolarizing Targets with Satellite Data: A New Geometrical Perturbation Filter”. In: *2010 IEEE International Geoscience and Remote Sensing Symposium*. 2010 IEEE International Geoscience and Remote Sensing Symposium. July 2010, pp. 1847–1850.
- [292] Armando Marino et al. “Validating a Notch Filter for Detection of Targets at Sea with ALOS-PALSAR Data: Tokyo Bay”. In: *Selected Topics in Applied Earth Observations and Remote Sensing, IEEE Journal of* 7.12 (2014), pp. 4907–4918.
- [293] Johnson Bailey, Armando Marino, and Vahid Akbari. “Comparison of Target Detectors to Identify Icebergs in Quad-Polarimetric L-Band Synthetic Aperture Radar Data”. In: *Remote Sensing* 13.9 (9 Jan. 2021), p. 1753.
- [294] Pasquale Iervolino et al. “SAR Ship Detection for Rough Sea Conditions”. In: *IGARSS 2019 - 2019 IEEE International Geoscience and Remote Sensing Symposium*. IGARSS 2019 - 2019 IEEE International Geoscience and Remote Sensing Symposium. Yokohama, Japan: IEEE, July 2019, pp. 505–508.
- [295] Richard Klemm. *Principles of Space-Time Adaptive Processing*. 12. IET, 2002.
- [296] R. K. Raney. “Synthetic Aperture Imaging Radar and Moving Targets”. In: *IEEE Transactions on Aerospace and Electronic Systems* AES-7.3 (May 1971), pp. 499–505.
- [297] Ludger Prünte. “Application of Distributed Compressed Sensing for GMTI Purposes”. In: *Radar Systems (Radar 2012)*, IET International Conference On. IET, 2012, pp. 1–6.
- [298] G. Margarit et al. “Orbital SAR Simulator of Fishing Vessel Polarimetric Signatures Based on High Frequency Electromagnetic Calculations”. In: *IGARSS 2003. 2003 IEEE International Geoscience and Remote Sensing Symposium. Proceedings (IEEE Cat. No.03CH37477)*. IGARSS 2003. 2003 IEEE International Geoscience and Remote Sensing Symposium. Proceedings (IEEE Cat. No.03CH37477). Vol. 7. July 2003, 4459–4461 vol.7.
- [299] Stefan V Baumgartner and Gerhard Krieger. “Ship Detection and Motion Parameter Estimation with TanDEM-X in Large along-Track Baseline Configuration”. In: *ESA Special Publication*. Vol. 709. 2013, p. 18.
- [300] Joachim HG Ender. “Space-Time Processing for Multichannel Synthetic Aperture Radar”. In: *Electronics & Communication engineering journal* 11.1 (1999), pp. 29–38.
- [301] F. Banda, L. Ferro-Famil, and S. Tebaldini. “Polarimetric Time-Frequency Analysis of Vessels in Spotlight SAR Images”. In: *2014 IEEE Geoscience and Remote Sensing Symposium*. 2014 IEEE Geoscience and Remote Sensing Symposium. July 2014, pp. 1033–1036.
- [302] Peter Lanz et al. “The InflateSAR Campaign: Evaluating SAR Identification Capabilities of Distressed Refugee Boats”. In: *Remote Sensing* 12.21 (21 Jan. 2020), p. 3516.
- [303] Peter Lanz et al. “The InflateSAR Campaign: Testing SAR Vessel Detection Systems for Refugee Rubber Inflatables”. In: *Remote Sensing* 13.8 (8 Jan. 2021), p. 1487.
- [304] Peter Lanz et al. “The InflateSAR Campaign: Developing Refugee Vessel Detection Capabilities with Polarimetric SAR”. In: *Remote Sensing* 15.8 (Apr. 10, 2023), p. 2008.



- [305] Johannes Bayer. *Technisches Gutachten: Einsatz Eines Festrumpfschlauchbootes (RHIB) Auf Der Spree*. 2015.
- [306] A. L. Pleskachevsky, Wolfgang Rosenthal, and Susanne Lehner. “Meteo-Marine Parameters for Highly Variable Environment in Coastal Regions from Satellite Radar Images”. In: *ISPRS Journal of Photogrammetry and Remote Sensing* (2016).
- [307] Karen Fletcher. *SENTINEL 1: ESA’s Radar Observatory Mission for GMES Operational Services*. European Space Agency, 2012.
- [308] ESA. *SAR Instrument - Sentinel-1 SAR Technical Guide*. Sentinel Online. 2023. URL: <https://copernicus.eu/technical-guides/sentinel-1-sar/sar-instrument> (visited on 04/12/2023).
- [309] ESA. *COSMO-SkyMed Second Generation*. 2023. URL: <https://earth.esa.int/eogateway/missions/cosmo-skymed-second-generation> (visited on 04/12/2023).
- [310] ICEYE. *Satellite Missions*. 2023. URL: <https://www.iceye.com/satellite-missions> (visited on 04/12/2023).
- [311] ESA. *ICEYE Overview - Earth Online*. 2023. URL: <https://earth.esa.int/eogateway/missions/iceye/description> (visited on 04/12/2023).
- [312] Tonje N Hannevik. “Evaluation of Radarsat-2 for Ship Detection”. In: *Forsvarets Forskningsinstitut, FFI-rapport* Volume 1692 (2011).
- [313] Domenico Velotto, Björn Tings, and Carlos Bentes. “Comparison of Ship Detectability between TerraSAR-X and Sentinel-1”. In: *Research and Technologies for Society and Industry (RTSI), 2017 IEEE 3rd International Forum On*. IEEE, 2017, pp. 1–5.
- [314] Virginia Fernandez Arguedas et al. “Ship Classification in High and Very High Resolution Sar Imagery”. In: *Future Security 2016*. Fraunhofer Verlag, 2016.
- [315] Armando Marino. “A Notch Filter for Ship Detection with Polarimetric SAR Data”. In: *Selected Topics in Applied Earth Observations and Remote Sensing, IEEE Journal of 6.3* (2013), pp. 1219–1232.
- [316] Armando Marino et al. “Comparison of Ship Detectors Using Polarimetric Alos Data: Tokyo Bay”. In: *Geoscience and Remote Sensing Symposium (IGARSS), 2013 IEEE International*. IEEE, 2013, pp. 2345–2348.
- [317] S. Song and J. Yang. “Ship Detection in Polarimetric SAR Images via Tensor Robust Principle Component Analysis”. In: *2015 IEEE International Geoscience and Remote Sensing Symposium (IGARSS)*. 2015 IEEE International Geoscience and Remote Sensing Symposium (IGARSS). July 2015, pp. 3152–3155.
- [318] M. J. Sanjuan-Ferrer et al. “A New Detection Algorithm for Coherent Scatterers in SAR Data”. In: *IEEE Transactions on Geoscience and Remote Sensing* 53.11 (Nov. 2015), pp. 6293–6307.
- [319] Alfredo Renga et al. “Adaptive Threshold and Sub-Look Processing in Ship Detection by SAR”. In: *OCEANS 2015 - Genova*. OCEANS 2015 - Genova. May 2015, pp. 1–8.
- [320] Min Tian et al. “A Method for Active Marine Target Detection Based on Complex Interferometric Dissimilarity in Dual-Channel ATI-SAR Systems”. In: *IEEE Transactions on Geoscience and Remote Sensing* 58.1 (Jan. 2020), pp. 251–267.
- [321] Gui Gao et al. “Ship Detection Based on Oceanic Displaced Phase Center Antenna Technique in Along-Track Interferometric SAR”. In: *IEEE Journal of Selected Topics in Applied Earth Observations and Remote Sensing* 12.3 (Mar. 2019), pp. 788–802.
- [322] Eduardo Makhoul et al. “Multichannel SAR-GMTI in Maritime Scenarios With F-SAR and TerraSAR-X Sensors”. In: *IEEE Journal of Selected Topics in Applied Earth Observations and Remote Sensing* 8.11 (Nov. 2015), pp. 5052–5067.

## BIBLIOGRAPHY

---

- [323] A. H. Oveis and M. A. Sebt. “Dictionary-Based Principal Component Analysis for Ground Moving Target Indication by Synthetic Aperture Radar”. In: *IEEE Geoscience and Remote Sensing Letters* 14.9 (Sept. 2017), pp. 1594–1598.
- [324] Gerard Margarit and Antonio Tabasco. *European Commission : CORDIS : Projects and Results : Final Report Summary - SAGRES (Services Activations for GRowing Eurosur’s Success)*. 2015. URL: [https://cordis.europa.eu/result/rcn/172060\\_en.html](https://cordis.europa.eu/result/rcn/172060_en.html) (visited on 02/13/2018).
- [325] F. Topputo et al. “Space Shepherd: Search and Rescue of Illegal Immigrants in the Mediterranean Sea through Satellite Imagery”. In: *2015 IEEE International Geoscience and Remote Sensing Symposium (IGARSS)*. 2015 IEEE International Geoscience and Remote Sensing Symposium (IGARSS). July 2015, pp. 4852–4855.
- [326] Gerard Margarit. “NEREIDS: New Concepts in Maritime Surveillance for Consolidating Operational Developments”. In: vol. Proceedings of the 2012 Esa’s Seasat Workshop. Tromsø, Norway, June 22, 2012, pp. 18–22.
- [327] Gerard Margarit et al. “Exploitation of Ship Scattering in Polarimetric SAR for an Improved Classification under High Clutter Conditions”. In: *Geoscience and Remote Sensing, IEEE Transactions on* 47.4 (2009), pp. 1224–1235.
- [328] Harold Mott. *Remote Sensing with Polarimetric Radar*. John Wiley & Sons, 2006.
- [329] Steffen Suchandt et al. “Traffic Measurement with TerraSAR-X: Processing System Overview and First Results”. In: Synthetic Aperture Radar (EUSAR), 2008 7th European Conference On. VDE, 2008, pp. 1–4.
- [330] M. Daniela Graziano. “SAR-based Ship Route Estimation by Wake Components Detection and Classification”. In: *2015 IEEE International Geoscience and Remote Sensing Symposium (IGARSS)*. 2015 IEEE International Geoscience and Remote Sensing Symposium (IGARSS). July 2015, pp. 3255–3258.
- [331] F. C. Jackson and D. R. Lyzenga. “Microwave Techniques for Measuring Directional Wave Spectra”. In: *Surface Waves and Fluxes*. Ed. by G. L. Geernaert and W. L. Plant. Dordrecht: Springer Netherlands, 1990, pp. 221–264.
- [332] T. Elfouhaily et al. “A Unified Directional Spectrum for Long and Short Wind-driven Waves”. In: *Journal of Geophysical Research: Oceans* 102.C7 (July 15, 1997), pp. 15781–15796.
- [333] William J. Plant. “Bragg Scattering of Electromagnetic Waves from the Air/Sea Interface”. In: *Surface Waves and Fluxes: Volume II — Remote Sensing*. Ed. by G. L. Geernaert and W. L. Plant. Environmental Fluid Mechanics. Dordrecht: Springer Netherlands, 1990, pp. 41–108.
- [334] D. R. Thompson. “Calculation of Microwave Doppler Spectra from the Ocean Surface with a Time-Dependent Composite Model”. In: *Radar Scattering from Modulated Wind Waves: Proceedings of the Workshop on Modulation of Short Wind Waves in the Gravity-Capillary Range by Non-Uniform Currents, Held in Bergen Aan Zee, The Netherlands, 24–26 May 1988*. Ed. by G. J. Komen and W. A. Oost. Dordrecht: Springer Netherlands, 1989, pp. 27–40.
- [335] W. Alpers. “Imaging Ocean Surface Waves by Synthetic Aperture Radar: A Review”. In: *Satellite microwave remote sensing* (1983), pp. 107–119.
- [336] G. Schwartz et al. “Elimination of False Positives in Vessels Detection and Identification by Remote Sensing”. In: *Geoscience and Remote Sensing Symposium, 2002. IGARSS’02. 2002 IEEE International*. Vol. 1. IEEE, 2002, pp. 116–118.
- [337] Chao Wang et al. “Ship Detection for High-Resolution SAR Images Based on Feature Analysis”. In: *IEEE Geoscience and Remote Sensing Letters* 11.1 (2014), pp. 119–123.

- [338] Stephan Bruschi et al. "Ship Surveillance with TerraSAR-X". In: *IEEE transactions on geoscience and remote sensing* 49.3 (2011), pp. 1092–1103.
- [339] Pasquale Iervolino, Raffaella Guida, and Philip Whittaker. "NovaSAR-S and Maritime Surveillance". In: *Geoscience and Remote Sensing Symposium (IGARSS), 2013 IEEE International*. IEEE, 2013, pp. 1282–1285.
- [340] F. Dell'Acqua, P. Gamba, and G. Lisini. "Rapid Mapping of High Resolution SAR Scenes". In: *ISPRS Journal of Photogrammetry and Remote Sensing* 64.5 (2009), pp. 482–489.
- [341] M. L. Jeremy, G. Geling, and M. Rey. "Results from the Crusade Ship Detection Trial : Polarimetric SAR". In: *IEEE International Geoscience and Remote Sensing Symposium*. IEEE International Geoscience and Remote Sensing Symposium. Vol. 2. June 2002, 711–713 vol.2.
- [342] M. Brizi, P. Lombardo, and D. Pastina. "Exploiting the Shadow Information to Increase the Target Detection Performance in SAR Images". In: *5th International Conference and Exhibition on Radar Systems (Brest, 17-21 Mai 1999, Proceedings)*. 1999.
- [343] Philip B. Chapple et al. "Stochastic Model-Based Processing for Detection of Small Targets in Non-Gaussian Natural Imagery". In: *IEEE Transactions on Image Processing* 10.4 (2001), pp. 554–564.
- [344] Karen S. Friedman et al. "Validation of a CFAR Vessel Detection Algorithm Using Known Vessel Locations". In: *IGARSS 2001. Scanning the Present and Resolving the Future. Proceedings. IEEE 2001 International Geoscience and Remote Sensing Symposium (Cat. No. 01CH37217)*. Vol. 4. IEEE, 2001, pp. 1804–1806.
- [345] Johnny A Johannessen. "Coastal Observing Systems: The Role of Synthetic Aperture Radar". In: *Johns Hopkins APL Technical Digest* 21.1 (2000), p. 9.
- [346] Armand Lopes et al. "Structure Detection and Statistical Adaptive Speckle Filtering in SAR Images". In: *International Journal of Remote Sensing* 14.9 (1993), pp. 1735–1758.
- [347] Nikola S Subotic et al. "Multiresolution Detection of Coherent Radar Targets". In: *IEEE transactions on image processing* 6.1 (1997), pp. 21–35.
- [348] Camilla Brekke. "Automatic Ship Detection Based on Satellite SAR". In: *FFI rapport Volume 84* (2008).
- [349] Steven M. Kay. *Fundamentals of Statistical Signal Processing, Volume 1: Estimation Theory (v. 1)*. PTR Prentice-Hall, Englewood Cliffs, 1993.
- [350] Pierfrancesco Lombardo, Massimo Sciotti, and Lance M. Kaplan. "SAR Prescreening Using Both Target and Shadow Information". In: *Radar Conference, 2001. Proceedings of the 2001 IEEE*. IEEE, 2001, pp. 147–152.
- [351] Khalid El-Darymli et al. "Target Detection in Synthetic Aperture Radar Imagery: A State-of-the-Art Survey". In: *Journal of Applied Remote Sensing* 7.1 (2013), p. 071598.
- [352] Waldo Kleynhans et al. "Ship Detection in South African Oceans Using a Combination of SAR and Historic LRIT Data". In: *Geoscience and Remote Sensing Symposium (IGARSS), 2013 IEEE International*. IEEE, 2013, pp. 1521–1524.
- [353] Pang Fengqian et al. "A Cascaded False-Alarm Elimination Method for Accurate Ship Detection in SAR Images". In: *IET International Radar Conference 2013*. IET International Radar Conference 2013. Xi'an, China: Institution of Engineering and Technology, 2013, pp. 0671–0671.
- [354] Wentao An, Chunhua Xie, and Xinzhe Yuan. "An Improved Iterative Censoring Scheme for CFAR Ship Detection with SAR Imagery". In: *IEEE Transactions on Geoscience and Remote Sensing* 52.8 (2014), pp. 4585–4595.

- [355] Shiqi Huang et al. “A Novel Method for Speckle Noise Reduction and Ship Target Detection in SAR Images”. In: *Pattern Recognition* 42.7 (2009), pp. 1533–1542.
- [356] C. P. Schwegmann et al. “A CA-CFAR and Localized Wavelet Ship Detector for Sentinel-1 Imagery”. In: *2015 IEEE International Geoscience and Remote Sensing Symposium (IGARSS)*. 2015 IEEE International Geoscience and Remote Sensing Symposium (IGARSS). July 2015, pp. 3707–3710.
- [357] Ghada Atteia and Michael J Collins. “Ship Detection Performance Assessment for Simulated RCM SAR Data”. In: *Geoscience and Remote Sensing Symposium (IGARSS)*, 2014 IEEE International. IEEE, 2014, pp. 553–556.
- [358] L. E. Yam, J. J. Mallorqui, and J. M. Rius. “Validation of a Sea Surface Model for Simulations of Dynamic Maritime SAR Images”. In: *2012 IEEE International Geoscience and Remote Sensing Symposium*. 2012 IEEE International Geoscience and Remote Sensing Symposium. July 2012, pp. 2813–2816.
- [359] B. Errasti-Alcala et al. “Realistic Ship Model for Extended Target Tracking Algorithms”. In: *2015 IEEE International Geoscience and Remote Sensing Symposium (IGARSS)*. 2015 IEEE International Geoscience and Remote Sensing Symposium (IGARSS). July 2015, pp. 3135–3138.
- [360] Tonje N Hannevik. “Multi-Channel and Multi-Polarisation Ship Detection”. In: *Geoscience and Remote Sensing Symposium (IGARSS)*, 2012 IEEE International. IEEE, 2012, pp. 5149–5152.
- [361] T.N. Arnesen, Richard B Olsen, and D.J Weydahl. “Ship Detection Signatures in AP Mode Data”. In: *56th International Astronautical Congress of the International Astronautical Federation, the International Academy of Astronautics, and the International Institute of Space Law*. International Astronautical Congress (IAF). Fukuoka, Japan: American Institute of Aeronautics and Astronautics, Oct. 17, 2005.
- [362] Tonje N. Arnesen Hannevik. “Combining Polarimetric Channels for Better Ship Detection Results”. In: *ESA Special Publication*. Vol. Vol. 713. Frascati, Italy, 2013.
- [363] Ross Girshick et al. “Rich Feature Hierarchies for Accurate Object Detection and Semantic Segmentation”. In: *2014 IEEE Conference on Computer Vision and Pattern Recognition*. 2014 IEEE Conference on Computer Vision and Pattern Recognition (CVPR). Columbus, OH, USA: IEEE, June 2014, pp. 580–587.
- [364] Ross Girshick. “Fast R-Cnn”. In: *Proceedings of the IEEE International Conference on Computer Vision*. 2015, pp. 1440–1448.
- [365] Shaoqing Ren et al. “Faster R-CNN: Towards Real-Time Object Detection with Region Proposal Networks”. In: *Advances in Neural Information Processing Systems 28*. Ed. by C. Cortes et al. Curran Associates, Inc., 2015, pp. 91–99.
- [366] Jianwei Li, Changwen Qu, and Jiaqi Shao. “Ship Detection in SAR Images Based on an Improved Faster R-CNN”. In: *2017 SAR in Big Data Era: Models, Methods and Applications (BIGSARDATA)*. 2017 SAR in Big Data Era: Models, Methods and Applications (BIGSARDATA). Beijing: IEEE, Nov. 2017, pp. 1–6.
- [367] Shaoming Zhang et al. “R-CNN-Based Ship Detection from High Resolution Remote Sensing Imagery”. In: *Remote Sensing* 11.6 (Mar. 15, 2019), p. 631.
- [368] Tianwen Zhang and Xiaoling Zhang. “High-Speed Ship Detection in SAR Images Based on a Grid Convolutional Neural Network”. In: *Remote Sensing* 11.10 (May 21, 2019), p. 1206.
- [369] Joseph Redmon et al. “You Only Look Once: Unified, Real-Time Object Detection”. In: *2016 IEEE Conference on Computer Vision and Pattern Recognition (CVPR)*. 2016 IEEE Conference on Computer Vision and Pattern Recognition (CVPR). Las Vegas, NV, USA: IEEE, June 2016, pp. 779–788.

- [370] Yang-Lang Chang et al. “Ship Detection Based on YOLOv2 for SAR Imagery”. In: *Remote Sensing* 11.7 (Apr. 2, 2019), p. 786.
- [371] Mohammad Rostami et al. “Deep Transfer Learning for Few-Shot SAR Image Classification”. In: *Remote Sensing* 11.11 (June 8, 2019), p. 1374.
- [372] Andrey Pleskachevsky et al. “Synergy and Fusion of Optical and Synthetic Aperture Radar Satellite Data for Underwater Topography Estimation in Coastal Areas”. In: *Ocean Dynamics* 61.12 (2011), pp. 2099–2120.
- [373] G. E. Atteia and Michael J. Collins. “On the Use of Compact Polarimetry SAR for Ship Detection”. In: *ISPRS Journal of Photogrammetry and Remote Sensing* 80 (2013), pp. 1–9.
- [374] Susanne Lehner et al. “Ship Surveillance with High Resolution Terrasar-X Satellite in African Waters”. In: *Remote Sensing of the African Seas*. Springer, 2014, pp. 285–313.
- [375] Hao Zhou et al. “Wind and Current Dependence of the First-Order Bragg Scattering Power in High-Frequency Radar Sea Echoes”. In: *IEEE Geoscience and Remote Sensing Letters* 14.12 (2017), pp. 2428–2432.
- [376] T. N. Hannevik. “Automatic Ship Detection in Sar Images Using Aegir”. In: *2010 IEEE International Geoscience and Remote Sensing Symposium*. 2010 IEEE International Geoscience and Remote Sensing Symposium. July 2010, pp. 3712–3715.
- [377] Morton J. Canty. *Image Analysis, Classification and Change Detection in Remote Sensing: With Algorithms for ENVI/IDL and Python*. Crc Press, 2014.
- [378] Paris W. Vachon. “Ship Detection in Synthetic Aperture Radar Imagery”. In: *Proc. OceanSAR*. 2006, pp. 1–10.
- [379] Armando Marino et al. “PolSAR-Ap: The Use of Polarimetric SAR to Improve Detection of Targets at Sea”. In: *Proceedings of ESA Living Planet Symposium*. ESA Living Planet Symposium 2013. Edinburgh, Scotland: ESA, Sept. 9–13, 2013.
- [380] Armando Marino, Nick Walker, and Iain Woodhouse. “Ship Detection Using SAR Polarimetry. The Development Of A New Algorithm Designed To Exploit New Satellite Sar Capabilities For Maritime Surveillance.” In: *Proc. SeaSAR* (2010), p. 9.
- [381] F Nunziata, M Migliaccio, and C E Brown. “A Physically-Based Approach to Observe Ships in Dual-Polarized Sar Data”. In: *IEEE International Geoscience and Remote Sensing Symposium* (2010), p. 3.
- [382] John Stastny et al. “Application of RADAR Corner Reflectors for the Detection of Small Vessels in Synthetic Aperture Radar”. In: *IEEE Journal of Selected Topics in Applied Earth Observations and Remote Sensing* 8.3 (2014), pp. 1099–1107.
- [383] Juanping Zhao et al. “A Coupled Convolutional Neural Network for Small and Densely Clustered Ship Detection in SAR Images”. In: *Science China Information Sciences* 62.4 (2019), p. 42301.
- [384] Genwang Liu, Xi Zhang, and Junmin Meng. “A Small Ship Target Detection Method Based on Polarimetric SAR”. In: *Remote Sensing* 11.24 (24 Jan. 2019), p. 2938.
- [385] S. Watts. “A Practical Approach to the Prediction and Assessment of Radar Performance in Sea Clutter”. In: *Proceedings International Radar Conference*. IEEE, 1995, pp. 181–186.
- [386] A. Parthiban et al. “Modeling and Simulation of Radar Sea Clutter Using K-distribution”. In: *2004 International Conference on Signal Processing and Communications, 2004. SPCOM'04*. IEEE, 2004, pp. 368–372.
- [387] K. D. Ward, C. J. Baker, and S. Watts. “Maritime Surveillance Radar. Part 1: Radar Scattering from the Ocean Surface”. In: *IEE Proceedings F (Radar and Signal Processing)*. Vol. 137. 2. IET, 1990, pp. 51–62.

## BIBLIOGRAPHY

---

- [388] Christoph H. Gierull and Ishuwa Sikaneta. “A Compound-Plus-Noise Model for Improved Vessel Detection in Non-Gaussian SAR Imagery”. In: *IEEE Transactions on Geoscience and Remote Sensing* 56.3 (2018), pp. 1444–1453.
- [389] Harm Greidanus et al. “The SUMO Ship Detector Algorithm for Satellite Radar Images”. In: *Remote Sensing* 9.3 (Mar. 7, 2017), p. 246.
- [390] Martina Aiello, Renata Vezzoli, and Marco Gianinetto. “Object-Based Image Analysis Approach for Vessel Detection on Optical and Radar Images”. In: *Journal of Applied Remote Sensing* 13.01 (Jan. 11, 2019), p. 1.
- [391] Shengli Song et al. “Ship Detection in SAR Imagery via Variational Bayesian Inference”. In: *IEEE Geoscience and Remote Sensing Letters* (2016), pp. 1–5.
- [392] Irena Hajnsek et al. “PolSAR-Ap: Exploitation of Fully Polarimetric SAR Data for Application Demonstration”. In: POLINSAR 2013, Workshop on Applications of SAR Polarimetry and Polarimetric Interferometry. 2013.
- [393] D. Velotto, M. Soccorsi, and S. Lehner. “Azimuth Ambiguities Removal for Ship Detection Using Full Polarimetric X-Band SAR Data”. In: *IEEE Transactions on Geoscience and Remote Sensing* 52.1 (Jan. 2014), pp. 76–88.
- [394] G. Margarit, J.J. Mallorqui, and X. Fabregas. “Single-Pass Polarimetric SAR Interferometry for Vessel Classification”. In: *IEEE Transactions on Geoscience and Remote Sensing* 45.11 (Nov. 2007), pp. 3494–3502.
- [395] Canbin Hu, Laurent Ferro-Famil, and Gangyao Kuang. “Ship Discrimination Using Polarimetric SAR Data and Coherent Time-Frequency Analysis”. In: *Remote Sensing* 5.12 (2013), pp. 6899–6920.
- [396] Pasquale Iervolino, Raffaella Guida, and Philip Whittaker. “A Novel Ship-Detection Technique for Sentinel-1 SAR Data”. In: *2015 IEEE 5th Asia-Pacific Conference on Synthetic Aperture Radar (APSAR)*. 2015 IEEE 5th Asia-Pacific Conference on Synthetic Aperture Radar (APSAR). Singapore, Singapore: IEEE, Sept. 2015, pp. 797–801.
- [397] Jian Yang and Yi Cui. “A Novel Method for Ship Detection in Polarimetric SAR Images Using Gopce”. In: *2009 IET International Radar Conference*. 2009 IET International Radar Conference. Apr. 2009, pp. 1–5.
- [398] Armando Marino and Nick Walker. “Ship Detection In Variable Sea States And Depolarized Sea Clutter: A Polarimetric Notch Filter”. In: *PolinSAR 2011, Science and Applications of SAR Polarimetry and Polarimetric Interferometry* 695 (2011), p. 8.
- [399] B. Zhang et al. “Compact Polarimetric Synthetic Aperture Radar for Marine Oil Platform and Slick Detection”. In: *IEEE Transactions on Geoscience and Remote Sensing* 55.3 (Mar. 2017), pp. 1407–1423.
- [400] Joachim HG Ender, Christoph H. Gierull, and Delphine Cerutti-Maori. “Improved Space-Based Moving Target Indication via Alternate Transmission and Receiver Switching”. In: *IEEE Transactions on Geoscience and Remote Sensing* 46.12 (2008), pp. 3960–3974.
- [401] Shen Chiu and Chuck Livingstone. “A Comparison of Displaced Phase Centre Antenna and Along-Track Interferometry Techniques for RADARSAT-2 Ground Moving Target Indication”. In: *Canadian Journal of Remote Sensing* 31.1 (Jan. 2005), pp. 37–51.
- [402] Delphine Cerutti-Maori and Ishuwa Sikaneta. “Optimum GMTI Processing for Space-Based SAR/GMTI Systems-Theoretical Derivation”. In: *8th European Conference on Synthetic Aperture Radar*. VDE, 2010, pp. 1–4.
- [403] Dirk Werle. “RADARSAT SAR Azimuth Ambiguity Patterns - The Ghost Fleet of Halifax Harbour and Implications for Applications”. In: *Int. Symp. Geomatics in the Era of RADARSAT (GER'97)* (1997), p. 10.

- [404] Canbin Hu et al. “SAR Azimuth Ambiguities Removal for Ship Detection Using Time-Frequency Techniques”. In: *Geoscience and Remote Sensing Symposium (IGARSS)*, 2014 IEEE International. IEEE, 2014, pp. 982–985.
- [405] Corrado Avolio et al. “A Method for the Reduction of Ship-Detection False Alarms Due to SAR Azimuth Ambiguity”. In: *Geoscience and Remote Sensing Symposium (IGARSS)*, 2014 IEEE International. IEEE, 2014, pp. 3694–3697.
- [406] W. Alpers, R. Romeiser, and I. Hennings. “On the Radar Imaging Mechanism of Kelvin Arms of Ship Wakes”. In: *IGARSS '98. Sensing and Managing the Environment. 1998 IEEE International Geoscience and Remote Sensing. Symposium Proceedings. (Cat. No.98CH36174)*. IGARSS '98. Sensing and Managing the Environment. 1998 IEEE International Geoscience and Remote Sensing. Symposium Proceedings. (Cat. No.98CH36174). Seattle, WA, USA: IEEE, 1998, 1932–1934 vol.4.
- [407] Björn Tings et al. “Extension of Ship Wake Detectability Model for Non-Linear Influences of Parameters Using Satellite Based X-Band Synthetic Aperture Radar”. In: *Remote Sensing* 11.5 (Mar. 7, 2019), p. 563.
- [408] Maria Graziano, Marco D’Errico, and Giancarlo Rufino. “Wake Component Detection in X-Band SAR Images for Ship Heading and Velocity Estimation”. In: *Remote Sensing* 8.6 (June 14, 2016), p. 498.
- [409] Oktay Karakuş, Igor Rizaev, and Alin Achim. “Ship Wake Detection in SAR Images via Sparse Regularisation”. In: *IEEE Transactions on Geoscience and Remote Sensing* 58.3 (Mar. 2020), pp. 1665–1677.
- [410] Tianqi Yang, Oktay Karakuş, and Alin Achim. “Detection of Ship Wakes in SAR Imagery Using Cauchy Regularisation”. 2020.
- [411] Miao Kang et al. “Contextual Region-Based Convolutional Neural Network with Multilayer Fusion for SAR Ship Detection”. In: *Remote Sensing* 9.8 (2017), p. 860.
- [412] Foroogh Sharifzadeh, Gholamreza Akbarizadeh, and Yousef Seifi Kaviani. “Ship Classification in SAR Images Using a New Hybrid CNN–MLP Classifier”. In: *Journal of the Indian Society of Remote Sensing* 47.4 (Apr. 1, 2019), pp. 551–562.
- [413] Microwaves101. *Miscellaneous Dielectric Constants*. 2022. URL: <https://www.microwaves101.com/encyclopedias/miscellaneous-dielectric-constants> (visited on 09/03/2022).
- [414] European Space Agency. *Mediterranean Sea Salinity*. ESA. 2023. URL: [https://www.esa.int/ESA\\_Multimedia/Images/2017/05/Mediterranean\\_Sea\\_salinity](https://www.esa.int/ESA_Multimedia/Images/2017/05/Mediterranean_Sea_salinity) (visited on 03/06/2023).
- [415] Melika Hozhabri, Per Olov Risman, and Nikola Petrovic. “Comparison of UWB Radar Backscattering by the Human Torso and a Phantom”. In: *2018 IEEE Conference on Antenna Measurements & Applications (CAMA)*. 2018 IEEE Conference on Antenna Measurements & Applications (CAMA). Västerås: IEEE, Sept. 2018, pp. 1–4.
- [416] A. G. Voronovich and V. U. Zavorotny. “Theoretical Model for Scattering of Radar Signals in Ku- and C-bands from a Rough Sea Surface with Breaking Waves”. In: *Waves in Random Media* 11.3 (July 2001), p. 247.
- [417] A. A. Mouche, B. Chapron, and N. Reul. “A Simplified Asymptotic Theory for Ocean Surface Electromagnetic Wave Scattering”. In: *Waves in Random and Complex Media* 17.3 (June 6, 2007), pp. 321–341.
- [418] Vladimir Kudryavtsev et al. “A Semiempirical Model of the Normalized Radar Cross-Section of the Sea Surface 1. Background Model”. In: *Journal of Geophysical Research: Oceans* 108.C3 (2003), FET 2-1-FET 2–24.

## BIBLIOGRAPHY

---

- [419] E.U. Copernicus Marine Service Information (CMEMS). Marine Data Store (MDS). *Atlantic- European North West Shelf- Wave Physics Reanalysis*. 2023. URL: [https://data.marine.copernicus.eu/product/NWSHELF\\_REANALYSIS\\_WAV\\_004\\_015/description](https://data.marine.copernicus.eu/product/NWSHELF_REANALYSIS_WAV_004_015/description) (visited on 01/30/2024).
- [420] E.U. Copernicus Marine Service Information (CMEMS). Marine Data Store (MDS). *Mediterranean Sea Waves Reanalysis*. 2023. URL: [https://data.marine.copernicus.eu/product/MEDSEA\\_MULTIYEAR\\_WAV\\_006\\_012/description?view=-&product\\_id=-&option=-](https://data.marine.copernicus.eu/product/MEDSEA_MULTIYEAR_WAV_006_012/description?view=-&product_id=-&option=-) (visited on 01/31/2024).
- [421] E.U. Copernicus Marine Service Information (CMEMS). Marine Data Store (MDS). *Arctic Ocean Wave Hindcast*. 2023. URL: [https://data.marine.copernicus.eu/product/ARCTIC\\_MULTIYEAR\\_WAV\\_002\\_013/description](https://data.marine.copernicus.eu/product/ARCTIC_MULTIYEAR_WAV_002_013/description) (visited on 01/31/2024).
- [422] E.U. Copernicus Marine Service Information (CMEMS). Marine Data Store (MDS). *Global Ocean Waves Reanalysis*. 2023. URL: [https://data.marine.copernicus.eu/product/GLOBAL\\_MULTIYEAR\\_WAV\\_001\\_032/description](https://data.marine.copernicus.eu/product/GLOBAL_MULTIYEAR_WAV_001_032/description) (visited on 01/31/2024).
- [423] Jan Erik H. Weber. “Vertically Varying Eulerian Mean Currents Induced by Internal Coastal Kelvin Waves”. In: *Journal of Geophysical Research: Oceans* 122.2 (2017), pp. 1222–1231.
- [424] Lamei Zhang et al. “Comparison of Methods for Target Detection and Applications Using Polarimetric SAR Image”. In: *Progress in Electromagnetics Research Symposium, Hangzhou, China* 1 (2008).
- [425] Konstantinos Karachristos and Vassilis Anastassopoulos. “Land Cover Classification Based on Double Scatterer Model and Neural Networks”. In: *Geomatics* 2 (Aug. 24, 2022), pp. 323–338.
- [426] Gulab Singh et al. “Physical Scattering Interpretation of POLSAR Coherency Matrix by Using Compound Scattering Phenomenon”. In: *IEEE Transactions on Geoscience and Remote Sensing* 58.4 (Apr. 2020), pp. 2541–2556.
- [427] Domenico Velotto and Bjoern Tings. “Detecting Small Ships in TerraSAR-X/TanDEM-X Acquisitions at Large Grazing Angle and Moderate Metocean Conditions”. In: *EUSAR 2018; 12th European Conference on Synthetic Aperture Radar*. VDE, 2018, pp. 1–4.
- [428] S Angelliaume et al. “Ship Detection and Sea Clutter Characterisation Using X&L-Band Full-Polarimetric Airborne SAR Data”. In: *ESA Special Publication*. Vol. 709. 2013, p. 15.
- [429] Harm Greidanus. “JRC-Frontex Spaceborne SAR Small Boat Detection Campaign–Italy & Spain”. In: (2011).
- [430] Xiangguang Leng et al. “A Bilateral CFAR Algorithm for Ship Detection in SAR Images”. In: *IEEE Geoscience and Remote Sensing Letters* 12.7 (July 2015), pp. 1536–1540.
- [431] Urška Kanjir. “Detecting Migrant Vessels in the Mediterranean Sea: Using Sentinel-2 Images to Aid Humanitarian Actions”. In: *Acta Astronautica* 155 (Feb. 1, 2019), pp. 45–50.
- [432] George Melillos et al. “The Use of Remote Sensing for Maritime Surveillance for Security and Safety in Cyprus”. In: *Detection and Sensing of Mines, Explosive Objects, and Obscured Targets XXV*. Detection and Sensing of Mines, Explosive Objects, and Obscured Targets XXV. Ed. by Jason C. Isaacs and Steven S. Bishop. Online Only, United States: SPIE, Apr. 24, 2020, p. 30.
- [433] Kazuo Ouchi et al. “Ability of Detecting Small Fishing Boats by ALOS-PALSAR Based on CFAR and Multi-Look Cross-Correlation Techniques”. In: (2007).
- [434] Domenico Velotto et al. “A Robust Symmetry-Based Approach to Exploit TerraSAR-X Dual-Pol Data for Targets at Sea Observation”. In: *POLinSAR 2013* (2013), p. 77.



- [435] Hendrik Christoffel Hulst and Hendrik C. van de Hulst. *Light Scattering by Small Particles*. Courier Corporation, 1981.
- [436] Jiong Chen, Yilun Chen, and Jian Yang. “Ship Detection Using Polarization Cross-Entropy”. In: *IEEE Geoscience and Remote Sensing Letters* 6.4 (Oct. 2009), pp. 723–727.
- [437] Gui Gao et al. “Adaptive Ship Detection in Hybrid-Polarimetric SAR Images Based on the Power–Entropy Decomposition”. In: *IEEE Transactions on Geoscience and Remote Sensing* 56.9 (Sept. 2018), pp. 5394–5407.
- [438] Bin Deng et al. “SAR/MMTI: An Extension to Conventional SAR/GMTI and a Combination of SAR and Micro-Motion Techniques”. In: *2009 IET International Radar Conference*. 2009 IET International Radar Conference. Apr. 2009, pp. 1–4.
- [439] Valeria Gracheva and Delphine Cerutti-Maori. “Multi-Channel Analysis of Sea Clutter for STAP Applications”. In: *EUSAR 2012* (2012).





# Dissemination Activities

## Posters

CSE Symposium 2017, Oldenburg, Germany. <https://uol.de/cse>  
AGIT 2018 & GI\_Forum 2018, July 3 – 6 2018, Salzburg, Austria  
NEOCONF 2018, September 4 – 7 2018, University of Birmingham, UK  
ESA Living Planet Conference, May 13 – 17 2019, Milano, Italy.

## Presentations

FOSSGIS 2018, March 21 – 24, Bonn, Germany  
ESA POLInSAR 2019, 28 January – 1 February, Frascati, Italy  
SeaSAR 2023, May 2 – 6, Svalbard, Norway  
POLInSAR 2023, June 19 – 23, Toulouse, France  
TerraSAR-X / TanDEM-X Science Team Meeting 2023, October 18 – 20, Oberpfaffenhofen, Germany

## Publications

Lanz, P., Marino, A., Brinkhoff, T., Köster, F., & Möller, M. (2020). The InflateSAR Campaign: Evaluating SAR Identification Capabilities of Distressed Refugee Boats. *Remote Sensing*, 12(21), Article 21. <https://doi.org/10.3390/rs12213516>

Lanz, P., Marino, A., Brinkhoff, T., Köster, F., & Möller, M. (2021). The InflateSAR Campaign: Testing SAR Vessel Detection Systems for Refugee Rubber Inflatables. *Remote Sensing*, 13(8), Article 8. <https://doi.org/10.3390/rs13081487>

Lanz, P., Marino, A., Simpson, M. D., Brinkhoff, T., Köster, F., & Möller, M. (2023). The InflateSAR Campaign: Developing Refugee Vessel Detection Capabilities with Polarimetric SAR. *Remote Sensing*, 15(8), 2008. <https://doi.org/10.3390/rs15082008>